Postglacial sea-level change: novel insights from physical and statistical modelling

YUCHENG LIN

Postglacial sea-level change: novel insights from physical and statistical modelling

Yucheng Lin

PhD Thesis

A thesis submitted for the Degree of Doctor of Philosophy

in the Department of Geography, Durham University

October 2023

Abstract

Developing accurate projections of future sea-level change is a key challenge for the entire science community under the current warming climate. Due to the fact that modern instrumental sea-level observations are only available since the 19-20th century, sea-level projections based on them can only capture short-term effects, leaving physical processes that dominate over longer timescales underestimated. Therefore, an essential step towards accurate and robust long-term sea-level projections is to investigate the physical processes that impact the spatio-temporal evolution of sea-level change over centennial to millennial timescales. Due to sometimes scarce and often noisy palaeo sea-level observations, mechanisms of sea-level change over geological timescales are still not well-understood, with many outstanding questions to be resolved. This thesis develops novel physical and statistical models to better understand the mechanisms behind postglacial sea-level change. Specifically, this thesis focuses on three outstanding problems that are not only important in postglacial sea-level change but also in understanding past ice sheet dynamics and palaeoclimate change.

Firstly, a statistical framework is developed to invert the sources of meltwater pulse 1A, the largest and most rapid global sea-level rise event of the last deglaciation, with sophisticated treatment of uncertainties associated with sea-level reconstructions and geophysical modelling. The results suggest there were contributions from North America, 12.0 m (5.6-15.4 m; 95% probability), Scandinavia, 4.6 m (3.2-6.4 m), and Antarctica, 1.3 m (0-5.9 m), giving a total global mean sea-level rise of 17.9 m

(15.7-20.2 m) in 500 years.

Secondly, the missing ice problem (distinctive imbalance between observed global mean sea-level rise and the reconstructed amount of ice-sheet melt) is revisited by including an extra physical process (sediment isostatic adjustment, SIA) which has not been considered in this problem before. In particular, this thesis investigates the impact of SIA on local RSL variation across the Great Barrier Reef (GBR), the world's largest mixed carbonate-siliciclastic sediment system. Based on a Bayesian calibration method, SIA can contribute up to 1.1 m relative sea-level rise in the outer shelf of the southern central GBR from 28 ka to present. Because the SIA-induced RSL rise is unrelated to ice mass loss, failing to correct for this signal will lead to systematic overestimation of grounded ice volume. Therefore, incorporating the SIA process will reduce the global grounded ice volume estimate for the Last Glacial Maximum (LGM), which can help to mitigate the missing ice problem.

Lastly, robust global barystatic sea-level maps with minimum dependency on the detailed geometry of past ice sheet change are reconstructed. Estimating such maps requires physical simulation of relative sea-level corresponding to thousands of different ice histories, which is computationally prohibitive. To improve this situation, this thesis develops a statistical emulator which can mimic the behaviour of a physics-based model and is computationally much cheaper to evaluate. The results highlight the Seychelles as an exceptionally good place to map barystatic sea level throughout the last deglaciation because RSL at this location only slightly departs from global barystatic sea level, with minor dependency on the assumed ice history.

Together, these physical and statistical models present powerful tools to yield novel insights into postglacial sea-level change mechanisms and hence they have the potential to yield more robust, accurate and trust-worthy sea-level change projections.

Acknowledgements

First and foremost, I would like to express my gratefulness to my supervisors, Pippa Whitehouse and Sarah Woodroffe, for their guidance, support and endless patience for me to play around different fields over the last three and a half years. It is not only about their time, ideas and knowledge on sea-level change but also love for the nature, I am much appreciated for many unforgettable climbing sessions, I can never imagine a better PhD experience.

None of my research can be done without the supports from my wonderful collaborators. A special thanks to Fiona Hibbert and Ian Shennan for guiding me through sea-level reconstruction and chronology; Sarah Bradley and Anthony Purcell for supports on ice and glacial isostatic adjustment modelling; Gustavo Hinestrosa and Jody Webster for mentoring me on sedimentology and geomorphology in the Great Barrier Reef; Andrew Valentine for his knowledge on data science and statistical emulation. I want to particularly thank Glenn Milne and Chris Clark for sharing their GIA and ice model with me, Richard Jones and Juliet Sefton for showing me impact of Antarctic Ice Sheet on Holocene sea-level change. I'm also very thankful to other professors and researchers in the department who kindly share their knowledge with me, particularly Mike Bentley, Ian Evans, Luke Jackson, Stewart Jamieson, Erin McClymont and Chris Stokes.

I was immensely grateful to Durham-China scholarship council joint scholarship who funded my PhD research; and the following people and organisations that funded me to attend international conferences, workshops and training schools, which are highly

valuable experiences to me where I met lots of great people: Pippa Whitehouse (2022 AGU and many others), International Glaciological Society (for 2022 Karthaus glaciology summer school), World Climate Research Programme (for 2022 WCRP sea-level meeting), PALSEA (for 2022 PALSEA meeting), IQUA (for 2022 Bayesian Statistics ECR Workshop); Scottish Universities Environmental Research Centre (for 2022 short course on geochronology), Department of Geography, Durham University (for 2022 and 2020 QRA), American Geophysical Union (for 2021 AGU meeting), European Space Agency (for 2021 3D Earth training school), Scientific Committee on Antarctic Research (for 2019 GIA training school).

The community in the Department of Geography at Durham University provided a welcoming and engaging atmosphere to me from the very first day, including many chats in the Antarctic group and ice and climate reading group. I want to thank Kathy Wood and Lianne Percival and other staffs for making my life as easy as possible. Manley Room has always been the best place for me to learn new things and gain some peaceful mind, thank you to Jenny Arthur, Cristina Balaban, Ritwika Basu, Jiao Chen, Lianchao Chen, Qinren Chen, Thale Damm-Johnsen, Cheng Fang, Burag Gurden, Ellie Honan, Ruizhe Hong, Huixuan Huang, Muyeol Jung, Danae Kontou, Daisy Lee-Browne, Joshua Leigh, Yu-Kai Liao, María-Paz Lira, Ivo Pink, Yu Qiao, Amy Robson, Leonard Schliesser, Xinquan Wu, Holly Wytiahlowsky, Jingshu Xia, Sheng Xuan, Xiaochen Yu, Yuzhe Zang, Liping Zhang Xiaoxi Zhu and Yuanyuan Zhang for sharing great time there.

Massive thanks to my lovely and supportive friends in Durham for countless memories in pubs, common rooms, cinemas, restaurants, living rooms, climbing walls, gyms, basketball courts, riversides, grasslands and mountains, Durham can never be a place called home without you. Lastly, I want to thank my parents for being the most important people in my life, not only for their selfless support both mentally and financially but being my best inspiration and shield through my ups and downs.

Contents

Declaration

I confirm that no part of the material presented in this thesis has previously been submitted by me or any other persons for a degree in this or any other university. In all cases, where is relevant, material from the work of others has been acknowledged.

Yucheng Lin

Department of Geography
Durham University
April 2023

List of Figures

List of Tables

List of abbreviations

AIS	Antarctic Ice Sheet
BIIS	British-Irish Ice Sheet
BP	Before present
BSL	Barystatic sea level
CI	Confidence interval
CPU	Central processing unit
ESL	Eustatic sea level
GIA	Glacial isostatic adjustment
GPU	Graphics processing unit
GBR	Great Barrier Reef
GMSL	Global mean sea level
healpix	Hierarchical Equal Area isoLatitude Pixelization
HYD	Hydrographer's Passage
ka	Thousand years
LGM	Last Glacial Maximum
MAE	Mean absolute error
MC	Monte Carlo
MIS	Marine Isotope Stage

MSE	Mean squared error
MWP-1A	Meltwater Pulse 1A
NAIS	North American Ice Sheet
NN	Neural network
NOG	Noggin Pass
PC	Principal component
PSNR	Peak signal-to-noise ratio
RSL	Relative sea level
SCNN	Spherical convolutional neural network
SSIM	Structural similarity index measure
SH	Spherical harmonic
SIA	Sediment isostatic adjustment
SIS	Scandinavian Ice Sheet
SLE	Sea level equivalent
SLIP	Sea-level index point
wPCA	Weighted Principal Component Analysis

CHAPTER 1

Introduction

1.1 Context

Sea-level rise is a growing threat caused by the warming of the Earth's climate and it poses great socio-economic risk to coastal communities, causing coastal flooding, coastal erosion, permanent submergence and loss and change of coastal ecosystems (Oppenheimer et al., 2019). This is highlighted by the devastating flooding event induced by Hurricane Sandy in 2012, which caused over $60 billion economic loss in the United States (Strauss et al., 2021). This socio-economic risk motivates the Earth science community to reduce the uncertainty of future sea-level rise projections for vulnerable regions, and hence, foster better coastal management, protection and migration plans to mitigate the impact caused by rising sea level (Kopp et al., 2019). To achieve an accurate spatio-temporal sea-level rise projection, a robust understanding of the different driving mechanisms of relative sea-level (RSL; distance between the ocean surface and the solid Earth surface) change and their relationship with climate forcing is a prerequisite (Figure 1.1a). However, because modern instrumental and satellite sea-level observations have only been available since the 19-20th century (Figure 1.1b), sea-level projections based on these can only capture short-term effects (e.g., steric and ocean dynamic effects; Figure 1.1a) while other physical processes that may dominate RSL change over a longer timescale will be strongly underestimated (Gregory et al., 2019). In this context, to reliably project multi-centennial sea-level change, it is necessary to investigate the physical processes that impact the spatio-temporal evolution of sea-level change over a longer timescale (Clark et al., 2016). The importance of understanding long-timescale processes have been highlighted by recent works that use palaeo sea-level data to constrain the ice dynamic model parameters that were used to project future sea-level change (DeConto et al., 2021; Garbe et al., 2020; Gregoire et al., 2012), estimate modern land deformation in response to past glacial cycles (Caron et al., 2018; Love et al., 2016; Peltier et al., 2015) and evaluate the relationship between global sea level and temperature (Kopp et al., 2016). To this end, this thesis aims to constrain long-term physical processes by developing novel physical and statistical modelling approaches based on observed postglacial sea-level change.

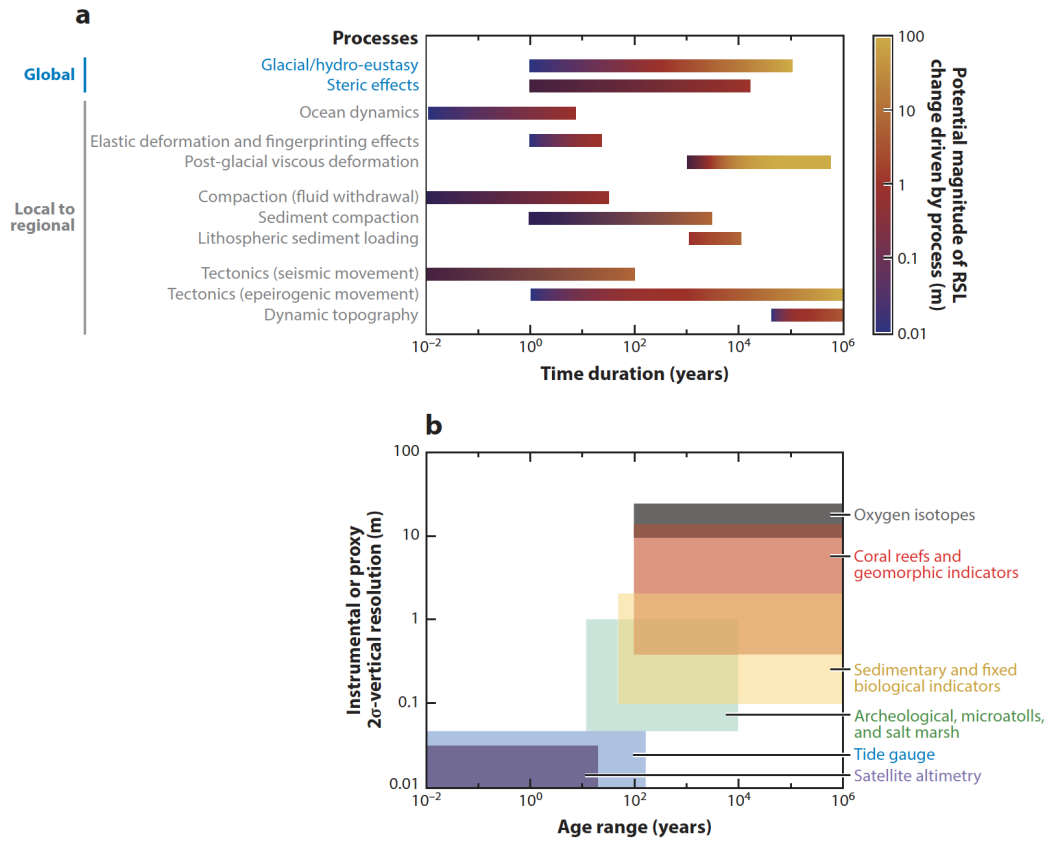

Figure 1.1: (a) Sea-level drivers on different timescales based on available estimates. (b) The uncertainty of instrumental and proxy recorders of sea level. Figure reproduced from Horton et al. (2018).

1.2 Background

Compared with the sea-level change observed in the modern era, long-term sea-level change over a postglacial timescale of 10^3-10^5 years is dominated by different physical processes (Figure 1.1a). At a global scale, the dominant driver of global mean sea-level (GMSL) change is the barystatic effect (i.e., eustasy in Figure 1.1a) caused by ice-ocean mass exchange related to the wax and wane of continental scale ice sheets, which lowered GMSL by >100 m during the Last Glacial Maximum (LGM, ~21 ka BP). On a regional scale, RSL change varies from place to place as a result of perturbations to the shape of the gravitational field, perturbations to Earth's rotational vector, and visco-elastic solid Earth deformation, which all arise due to surface mass redistribution (Whitehouse, 2018) and are often referred to as the gravitational, rotational and deformational (GRD) effects (Frederikse

et al., 2020, corresponding to elastic deformation and fingerprinting effects, and post-glacial viscous deformation in Figure 1.1). Additionally, similar to ice-ocean mass exchange, sediment mass redistribution due to glaciation- or river-induced erosion and deposition processes can also trigger GRD effects (or sediment isostatic adjustment) which can alter local RSL by >100 m since the last interglacial (∼120 ka BP; Jungdal-Olesen et al., 2023; Ruetenik et al., 2020). Lastly, land deformation related to tectonic movement and dynamic topography (surface undulations induced by mantle flow) can also produce >10 m RSL change at some locations over the last 100 ka (Horton et al., 2018; Austermann et al., 2017).

To better understand the postglacial sea-level variability caused by different driving processes, geological proxies of past sea-level change provide valuable information to test our knowledge about physical processes and validate physical models built upon this knowledge. Ideally, a general agreement between proxy-based sea-level observations and physical model predictions can be used to confirm our understanding of the causes of long-term sea-level change and hence be used to produce long-term sea-level predictions and coastal management plans. However, noticeable disagreements often exist between RSL observations and model predictions, which can lessen our confidence in future sea-level predictions. The reason for this disagreement can be attributed to deficiencies in both physical models and observational records.

Glacial isostatic adjustment (GIA) modelling is a commonly used method to describe the barystatic and GRD effects triggered by water mass redistribution between the oceans and the ice sheets. Generally, there are two major components for a GIA model to compute: solid Earth deformation and purtabations to the global gravitational field, both of which can produce spatially variable sea-level change. This section provides a brief summary of the processes represented within a GIA model and the numerical methods used to replicate those process. For full reviews of GIA processes and modelling approaches, the reader can refer to Peltier et al. (2022); Whitehouse (2018).

For GIA studies, the solid Earth response to a changing ice/water load is usually regarded as a visco-elastic process, consisting of an instantaneous elastic response and a viscous deformation that can last for thousands of years. During glacial conditions,

the pressure produced by the growth of large continental ice sheets, such as those which previously existed in North America and Scandinavia, causes gradual land subsidence beneath the ice sheets (i.e., in the near field). This subsidence, in turn, triggers the outward flow of mantle material and the formation of uplifted 'peripheral bulge' regions around the boundary of the ice sheet (i.e., isostatic adjustment; Figure 1.2a). When global climate transitions to an interglacial period, ice sheet melting releases the accumulated pressure, resulting in the back flow of mantle material and peripheral bulge collapse. Glacially-triggered isostatic adjustment is one of the few geophysical processes that can be readily observed on human timescales. For example, RSL in parts of North America is still changing by more than 2 cm/yr due to ongoing land rebound (Lambeck et al., 2017; Peltier et al., 2015).

Solid Earth deformation can also occur outside near-field regions. For example the peripheral bulges produced by large continental ice sheets can extend hundreds of kilometres away from the ice sheet margin (Austermann et al., 2013). When the formation and collapse of these bulges happens within an oceanic area (Figure 1.2b), this alters the capacity of the ocean basins and the mean height of the sea surface (so-called ocean siphoning effect, Mitrovica and Milne (2002)). During a glacial lowstand, many continental shelves far away from large ice sheets will be sub-aerially exposed. Following GMSL rise caused by ice sheet melting, such areas will be submerged and loaded by the ocean causing them to be flexed downwards while the margins of the continents are flexed upwards (Lambeck and Nakada, 1990). By modelling the ocean siphoning and continental levering effects, the majority of the global sea-level highstand observed during the mid-Holocene can be explained without invoking a substantial change in global ice volume (Mitrovica and Milne, 2002).

Calculating the gravitational change caused by water and mantle mass redistribution is another component of a GIA model, which can change the shape of the geoid (the equipotential ocean surface in the absence of dynamic forcing by atmospheric and oceanic circulation). As shown in Figure 1.2a, continental ice sheets can exert a large gravitational force, causing water in the adjacent ocean to be pulled towards them, which increases RSL in the near field of the ice sheets and reduces RSL in the far-field.

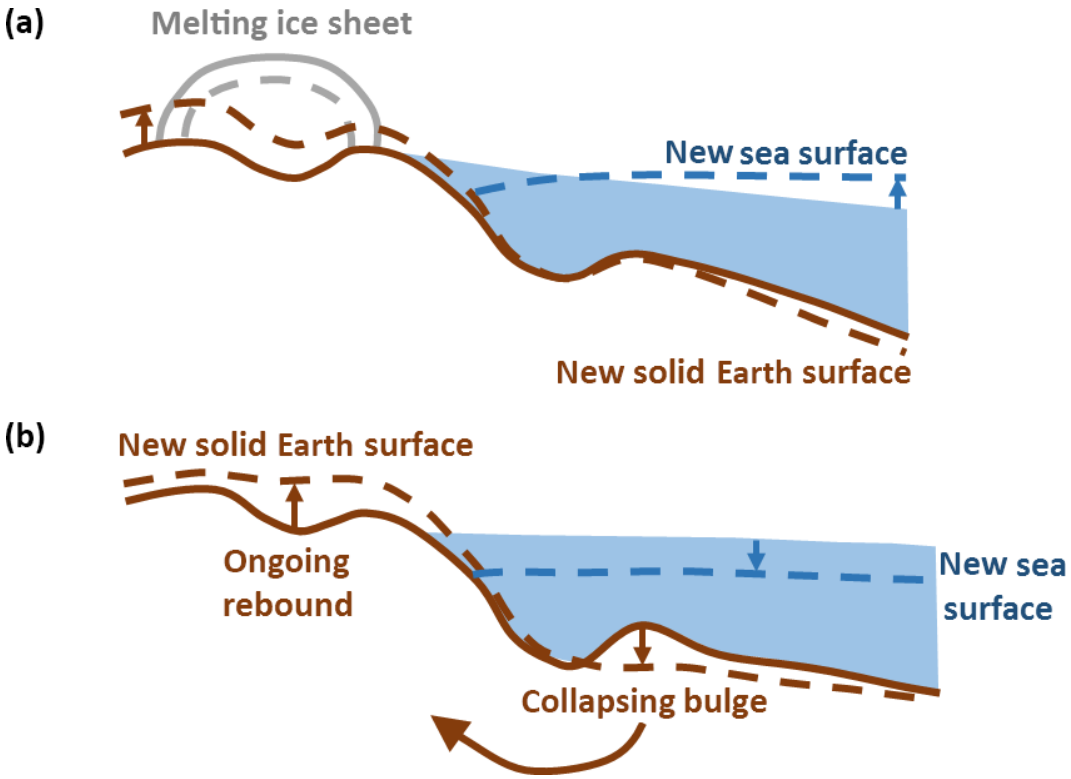

Figure 1.2: Solid Earth deformation and sea-level change. (a) Ice sheet losing mass results in solid Earth rebound and a decrease in sea surface height due to the decreased gravitational attraction of the ice sheet. Both processes cause near-field relative sea-level fall. Relative sea level rises in the far field due to the addition of meltwater to the ocean. (b) Ongoing solid Earth relaxation after disappearance of the ice sheet. Ocean syphoning is the process whereby peripheral bulge subsidence increases the capacity of the ocean; the result is a fall in mean sea surface height. Solid lines indicate original positions; dashed lines indicate new positions. Figure reproduced from Whitehouse (2018).

Conversely, when an ice sheet starts to melt, the near-field geoid will fall due to a reduction in the gravitational pull of the ice, causing net water movement from the near field to the far field. Large water/mantle mass movement also causes Earth's rotation axis to move towards the region of mass loss (i.e., rotational feedback, see Figure 1.3). Such movement of the rotational axis can substantially alter the geoid (Mitrovica and Milne, 1998) and generate elastic deformation (Han and Wahr, 1989), both of which drive azimuthal asymmetric sea-level change (Gomez et al., 2015). It should be noted that, although we describe solid Earth deformation and gravity change induced sea-level change separately, they are convoluted and can iteratively impact each other (Spada et al., 2011).

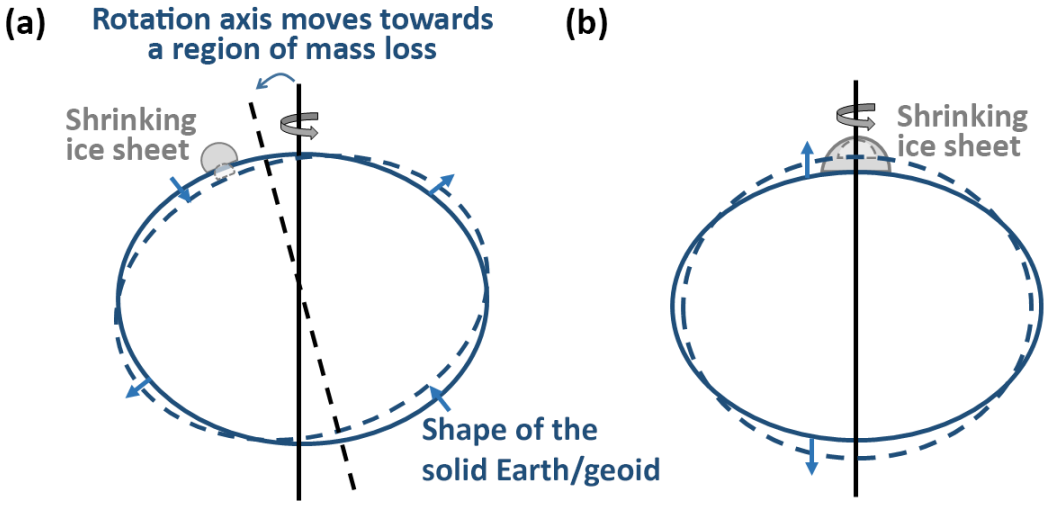

Figure 1.3: Rotational feedback. (a) Earth's rotation vector moves towards a region of mass loss, causing a change in the shape of the solid Earth and the geoid. Relative sea level rises and falls in opposing quadrants of the Earth. (b) Polar ice loss results in a decrease in the oblateness of the Earth. Solid lines indicate original positions; dashed lines indicate new positions. Figure reproduced from Whitehouse (2018).

Numerical modelling of solid Earth deformation and gravitational field variation started in the 1970's when Peltier (1974) used Green's functions and the viscoelastic correspondence principle to formally establish a spherically symmetric, self-gravitating, non-rotating and radially stratified Earth model with a Maxwell-viscoelastic rheology to calculate solid Earth deformation in response to a changing surface load. This theory was then applied by Farrell and Clark (1976) to solve for gravitational field variation (the so-called sea-level equation) assuming a non-rotating Earth with fixed ocean area, which defines the gravitationally self-consistent redistribution of meltwater across the ocean. Thus, given the global ice load history and solid Earth rheology, spatially varying RSL history can be uniquely determined by solving the sea-level equation. Following these seminal investigations, extensive theoretical development of the sea-level equation has been conducted in the following decades to incorporate time-varying shoreline migration (Johnston, 1993; Lambeck and Nakada, 1990; Wu and Peltier, 1984), Earth rotational feedback (Mitrovica et al., 2011; Kendall et al., 2005) and to account for floating ice in shallow basins (Lambeck et al., 2003; Milne and Mitrovica, 1996).

Although the theory of the sea-level equation has been benchmarked by multiple groups (Martinec et al., 2018; Spada et al., 2011) and validated by modern geodetic

observations (Coulson et al., 2022; Peltier et al., 2015; Steffen and Wu, 2011), accurate modelling of past sea-level change remains challenging due to poorly-understood solid Earth rheology and global ice history. Since the 1970s, a radially stratified (i.e., 1-D) Maxwell body has been widely-used to represent solid Earth rheology due to its adequate performance and great efficiency. However, due to un-explainable misfits between sea-level records and GIA model predictions that assume a 1-D Maxwell rheology (e.g., Baril et al., 2023), the sea-level community has recently started to develop more advanced representations of the solid Earth, including models with laterally heterogeneous viscosity and lithspheric thickness profiles and alternative rheological properties (e.g., Burgers/extended Burgers rheology, Ivins et al., 2022; Caron et al., 2017; non-Newtonian rheology, Kang et al., 2022; and composite rheology van der Wal et al., 2015). It is not yet confirmed which rheology is the most suitable solution for modelling past sea-level change and some of them might require large computational resources that prohibit ensemble based sampling to test uncertain model parameters like ice history (Peltier et al., 2022). In addition, the erosive nature of ice means that much of the geological evidence relating to past ice extent has been destroyed by subsequent ice flow, making ice sheet history arguably the most uncertain parameter for a GIA model (Tarasov et al., 2012). These outstanding issues strongly impede the robustness of the resulting RSL predictions produced by a GIA model. Additionally, there has been very limited success in quantifying the spatio-temporal pattern of RSL change due to other physical processes (e.g., sediment, steric and ocean dynamic effects; Gebbie et al., 2019; Pico, 2020) primarily as a result of limited observations, leaving some components of observed RSL variability unexplained by numerical models (Simms et al., 2019).

In addition to the challenges of modelling RSL change, the interpretation and dating of geological sea-level indicators, which can be used to constrain physical models, are subject to complicated uncertainties. To reconstruct past sea level, a prerequisite is building a robust relationship between a proxy and the concurrent sea level, which is often referred to as the "indicative meaning" (Shennan et al., 2018; Horton et al., 2018). For example, fossil corals and microfossil assemblages (e.g., intertidal diatoms or foraminifera) can only provide a maximum/minimum estimate of the elevation of

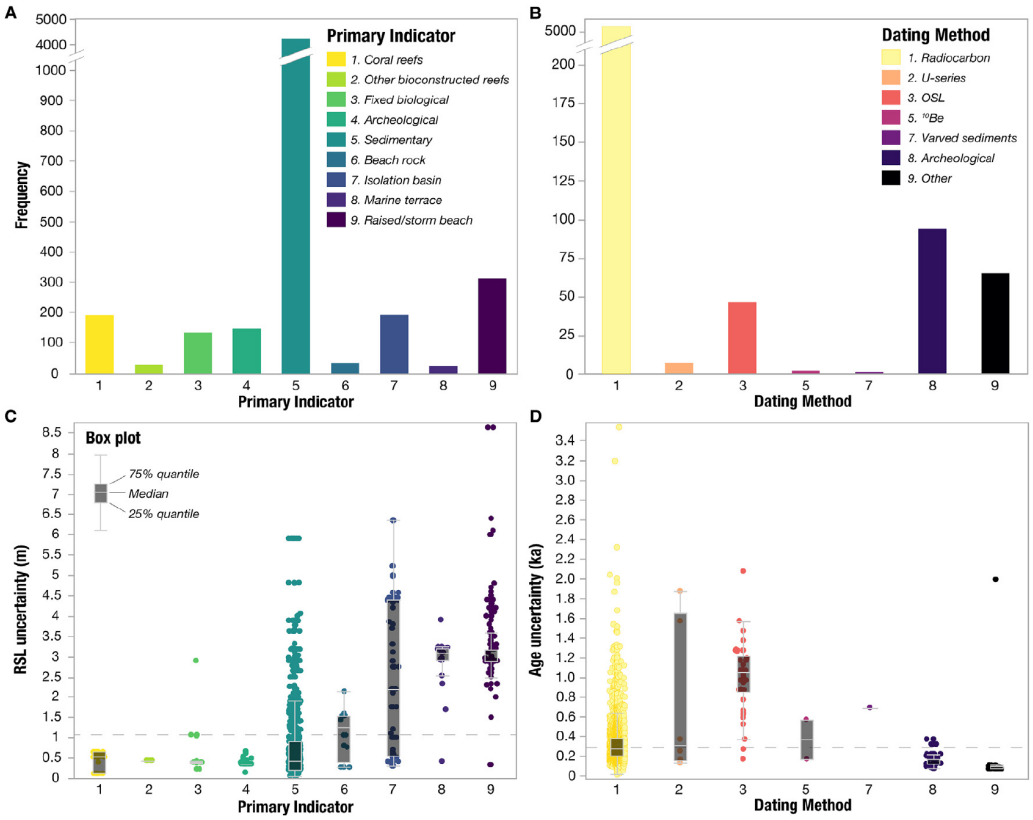

Figure 1.4: Sea-level indicators and their associated frequency, dating methods and uncertainties, which are based on the current dataset amassed by the HOLSEA working group (Khan et al., 2019). (a) Frequency of sea-level indicators, (b) chronological dating methods and (c,d) their associated uncertainties. Note: the coral reef uncertainties shown here primarily relate to shallow water corals which formed during the late Holocene, while many of the coral reef records used in Chapter 2 are deep-water coral (e.g., P. *porties*) that present much larger uncertainties (e.g., >10 m). Figure reproduced from Khan et al. (2019).

concurrent sea level, and to systematically quantify palaeo sea level by these records, it is necessary to establish their depth-habitat distribution relative to mean tidal level (i.e., their indicative ranges; Hibbert et al., 2018). These relationships are often reconstructed by field-based surveys in modern environments and formalized through an appropriate numerical technique (e.g., transfer function, Kemp and Telford, 2015). Although great efforts have been made to carefully interpret the indicative meaning for each proxy species, sea-level reconstructions are often based on a common assumption that modern analogues are representative of the past. Such an assumption, although appropriate given the great difficulty in quantifying the uncertainty due to environmental change, will inevitably produce some uncertainties

that are hard to measure (Khan et al., 2019; Hibbert et al., 2016).

Providing an accurate chronology for the RSL reconstruction is another sophisticated task depending on the specific dating technique employed (Figure 1.4). Taking radiocarbon dating as an example, to account for temporally variable atmospheric and oceanic carbon storage in the Northern and Southern Hemisphere, different calibration curves are needed to convert conventional radiocarbon age measurements into a calibrated calendar year (Reimer et al., 2020, 2013). The resulting radiocarbon age distributions are often multimodal and asymmetric, which further complicates the data-model comparison process (Blaauw and Christen, 2011).

The above-mentioned poorly-constrained physical models along with the observational data that are subject to complicated uncertainties therefore lead to numerous non-negligible data-model misfits. These misfits are highlighted by the following outstanding questions which are not only important in sea-level research, but also in understanding palaeoclimate change and ice-sheet dynamics:

1. **Meltwater Pulse 1A sources**: Meltwater pulse 1A is the largest and most rapid global sea-level rise event of the last deglaciation, characterised by ∼18 m GMSL rise within 340 years (Deschamps et al., 2012). It was driven by the collapse of vulnerable ice sheet sectors and was concurrent with rapid Northern Hemispheric warming and disruptions in oceanic and atmospheric circulation (Fogwill et al., 2017; Buizert et al., 2014). However, the sources of this rapid GMSL rise event remains elusive with ice sheets from North America, Scandinavia and Antarctica all having been proposed as the major contributor (Brendryen et al., 2020; Yeung et al., 2020; Liu et al., 2016; Gregoire et al., 2016; Gomez et al., 2015; Tarasov et al., 2012; Gregoire et al., 2012; Bassett et al., 2005; Weaver et al., 2003). This disagreement therefore precludes any firm understanding of the ice-ocean-climate feedbacks operating during this period of abrupt climate change (Ivanovic et al., 2018; Menviel et al., 2011).

2. **Missing ice problem**: This refers to the distinctive imbalance between observed GMSL rise and the reconstructed amount of ice-sheet melt (Clark and Tarasov, 2014) since the LGM. Simms et al. (2019) suggest this imbalance

is 15.6 ±9.6 m sea-level equivalent, even when additional physical processes, including steric effects and groundwater exchange between the continents and the ocean, have all been considered. More recently, Gowan et al. (2022, 2021) conclude that a new ice model with a different spatial distribution of ice may be able to reconcile this imbalance and therefore solve the missing ice problem. However, their results have been disputed by Yokoyama et al. (2022) and Yokoyama and Purcell (2021) who suggest that the RSL data have been misinterpreted. These active debates reemphasise the importance of reconciling the missing ice problem, not least because ice sheet height at the LGM is a fundamental boundary condition which significantly impacts atmospheric and oceanic circulation and global temperature (Clark and Tarasov, 2014; Clark et al., 2009).

3. **Barystatic sea-level map**: A long-standing goal of the palaeo sea-level modelling community is to locate areas where local RSL approximates global barystatic sea-level (or GMSL) at a certain time, thus providing guidance to the field community as they seek to select ideal locations to reconstruct palaeo GMSL, and thus global grounded ice volume. However, to date, only limited efforts have been made to examine how the above-mentioned uncertainty in global ice history impacts the corresponding barystatic sea-level map (Milne and Mitrovica, 2008). If uncertainties have been underestimated, this can fundamentally impede the robustness of the resulting barystatic sea-level reconstruction and the inferred global ice volume.

To better understand the above-mentioned problems associated with post-glacial sea-level change, this thesis tries to make improvements at three modelling levels which account for uncertainties associated with geophysical models and sea-level reconstructions. Firstly, 'process level' describes the level at which the phenomenon of interest is modelled or decomposed. For postglacial sea-level change, the majority of previous studies only used a GIA model to explain the observed sea-level variability across the globe (Gowan et al., 2021; Peltier et al., 2015; Lambeck et al., 2014). However, as shown in Figure 1.1, there are other physical processes that can substantially alter local RSL, hence, efforts should be made to estimate the mag-

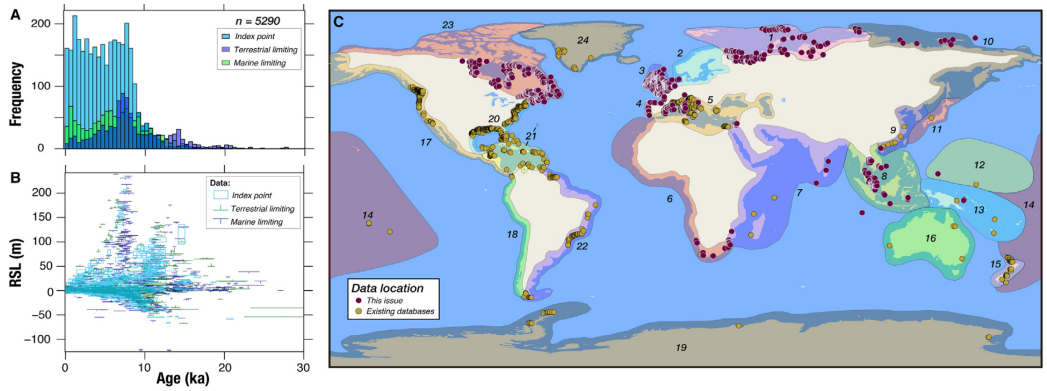

Figure 1.5: Temporal and spatial distribution of the current dataset amassed by the HOLSEA working group (Khan et al., 2019). (a) Histogram showing the temporal distribution of different types of index points and limiting data since the LGM. (b) RSL variability exhibited in the global dataset since the LGM. (c) Spatial distribution of the global dataset. Note 'this issue' in this figure refers to a special issue of global sea-level data compilation by the HOLSEA project (Khan et al., 2019). Figure reproduced from Khan et al. (2019).

nitude of each physical process contributing to the recorded RSL change variability. Secondly, 'data level' characterises the relationship between the phenomenon to be modelled and the observed data, incorporating measurement, inferential and dating uncertainty. Because geological records of past sea-level change are derived using a range of different proxies and dating techniques, each record is subject to different uncertainties. Aside from that, geological RSL data are often unevenly distributed across space and time (Figure 1.5), not considering which may strongly bias the calibration of physical models (Frederikse et al., 2020; Hay et al., 2015). To mitigate these problems, a well-designed statistical framework is required to consider each uncertainty source, and the unevenly distributed data density, separately within the final estimations. Thirdly, 'parameter level' captures key attributes of the process and data levels through unobserved physical model parameters (Ashe et al., 2019). Since the physical model parameters are often not directly observable, to robustly optimise the model parameters with reliable error quantification, a thorough sampling of physical model parameters is required. However, this is often prohibited by high-dimensional parameter spaces and limited computational resources. In this case, efficient optimisation algorithms or alternative modelling approaches (e.g., simplified physical models or surrogate models) should be developed accordingly (Tarasov et al.,

2012).

1.3 Research aims, questions and objectives

Based on the science questions and modelling challenges described above, the overall aim of this thesis is to ***develop novel physical and statistical modelling approaches to improve understanding at process, data and parameter levels and therefore resolve outstanding postglacial sea-level change questions relating to MWP-1A sources, the missing ice problem, and the spatio-temporal evolution of barystatic sea-level***. To achieve this aim, three specific research questions, and their associated objectives are outlined below and framed in the context of the three modelling levels defined above.

RQ1 How much did the North American, Scandinavian and Antarctic Ice Sheets contribute to Meltwater Pulse 1A?

(a) Process Level: Use a sea-level fingerprinting approach to translate the MWP-1A sources detection problem into a series of linear inversion problems.

(b) Data Level: Build probability density distributions for each sea-level change indicator that account for uncertainty from each source, including measurement, inferential and dating uncertainty.

(c) Parameter Level: Perform large ensemble modelling using a range of parameter combinations in order to rigorously quantify the uncertainty associated with the modelling process.

(d) Compare our sea-level based inversion results with previously published regional ice-sheet reconstructions.

(e) Investigate the implications of the inferred Meltwater Pulse 1A sources for palaeoclimate and ice-sheet dynamics.

RQ2 Can we mitigate the missing ice problem by incorporating another physical process (sediment isostatic adjustment) that has not been considered before?

(a) Process Level: Develop a sediment deposition model to estimate the SIA impact on sea-level change using the Great Barrier Reef as an example.

(b) Data Level: Design a platform that incorporates different data sources (e.g., sea-level data and sediment thickness data) into final sediment deposition history and SIA signal estimation via a sophisticated error propagation algorithm.

(c) Parameter Level: Perform large ensemble modelling using a range of ice, sediment and Earth model parameter combinations in order to rigorously quantify the uncertainty related to each modelled process.

(d) Quantify the spatio-temporal RSL change signal associated with sediment erosion and deposition across the Great Barrier Reef.

(e) Investigate the implications of considering sediment-induced sea-level change for the missing ice problem.

RQ3 Where might we find sea-level records that closely approximate barystatic sea-level change regardless of the detailed geometry of past ice sheet change?

(a) Process Level: Build a statistical emulator (i.e., surrogate model) that mimics the behaviour of a physics-based GIA model (i.e., calculate global RSL change based on a given ice history) to enable fast and thorough sampling of the impact of ice history uncertainty on the spatio-temporal distribution of barystatic sea level.

(b) Data Level: Collate a set of global ice history models from previous studies that provide plausible spatio-temporal distributions of global ice variation. Based on these distributions, create an ensemble of possible ice histories for training the statistical emulator.

(c) Parameter level: Based on the trained statistical emulator, perform global RSL emulations using a large ensemble of possible ice histories in order to identify an ice-history-insensitive barystatic sea-level map.

(d) Obtain a robust barystatic sea-level map with uncertainty quantification.

1.4 Thesis structure

The thesis comprises six chapters following the Introduction. **Chapters 2, 3, and 4** are based on separate research papers that have been either published in, or submitted to, international peer-reviewed journals. The papers have been reformatted for self-consistency within the thesis but are otherwise identical to the published versions. This involved incorporating supplementary information from the published manuscripts into the last section of each thesis chapter. Some figures within supplementary information have been moved in the main text for better readability and some of the figure layouts have been re-arranged for better visibility. Note, compared with Chapter 3 and 4, Chapter 2 has a slightly different structure, with the methods section being placed at the end of main text (i.e., section 2.5), to fit the journal requirement. Although the result section (i.e., section 2.3) in Chapter 2 includes some essential information about the method, readers should refer to section 2.5 for full details of method. All of the papers are co-authored and the contributions of the authors are noted clearly below, with an emphasis on what my role and contributions were in each paper. A critical discussion of the key findings of this thesis in relation to the research questions posed in Section 1.2 is presented in **Chapter 5 (Discussion)**, along with a discussion of the implications of these findings for further work on postglacial sea-level change. Finally, the key findings of this body of work are presented in **Chapter 6 (Conclusions)**.

Chapter 2

Lin, Y., Hibbert, F.D., Whitehouse, P.L., Woodroffe, S.A., Purcell, A., Shennan, I. and Bradley, S.L., 2021. A reconciled solution of Meltwater Pulse 1A sources using sea-level fingerprinting. Nature communications, 12(1), p.2015. doi: 10.1038/s41467-021-21990-y.

This chapter presents a data-driven inversion approach that employs a glacial isostatic adjustment model to invert the sources of Meltwater Pulse 1A (MWP-1A) using sea-level data from six geographically distributed sites. Our results suggest there were contributions from Antarctica, 1.3 m (0-5.9 m; 95% probability), Scandinavia, 4.6 m (3.2-6.4 m), and North America, 12.0 m (5.6-15.4 m), giving a total global mean sea-level rise of 17.9 m (15.7-20.2 m) in 500 years (**RQ1**). Compared with previous sea-level inversion studies, we include near-field isolation basin data from northwest Scotland, which enables us to refute an Antarctic-dominant scenario for MWP-1A. Our inversion results based on sea-level data show good agreement with most recent regional ice-sheet reconstructions, and may lead to a reconciled solution of MWP-1A sources. Because our inversion algorithm includes sophisticated treatment of uncertainties associated with sea-level data and geophysical modelling processes, the results can readily be used as boundary conditions to describe the global pattern of meltwater discharge during MWP-1A, which may yield novel insights into the sequencing of ice-ocean-climate interactions during this recent abrupt climate change event. A copy of the published paper is supplied in Appendix A.

In this paper, Y.L. led the research, performed the GIA modelling, generated the sea-level fingerprints, and designed and implemented the statistical inversion framework and sensitivity analysis. Y.L, F.D.H., P.L.W. and S.A.W conceived the scope and design of the research. Y.L., P.L.W., S.A.W and F.D.H. led the writing of the manuscript. P.L.W., A.P. and S.L.B. advised Y.L. in performing GIA modelling. F.D.H., S.A.W and I.S. advised Y.L. in sea-level and field data analysis. Y.L. produced the first draft of the manuscript. All authors contributed ideas and to the editing of the manuscript. The paper was edited by Jasper Franke and reviewed by three anonymous reviewers.

Chapter 3

Lin, Y., Whitehouse, P., Hibbert, F., Woodroffe, S., Hinestrosa, G. and Webster, J., 2023. Relative sea level response to mixed carbonate-siliciclastic sediment loading along the Great Barrier Reef margin. Earth and Planetary Science Letters. doi: 10.1016/j.epsl.2023.118066

This chapter investigates the impact of sediment isostatic adjustment (SIA) on local RSL variation across the Great Barrier Reef (GBR), the world's largest mixed carbonate-siliciclastic sediment system. To estimate the SIA-induced RSL signal, we use a GIA model to develop an ensemble-based sediment deposition history for the GBR since Marine Isotope Stage 2. We further develop a Bayesian framework to calibrate the sediment history ensemble and GIA model parameters conditioned using a high-quality sea-level database. According to our results, 1853.7 Gt (1613.1-2078.7 Gt; 95% confidence interval) of sediment have been deposited across the GBR since Marine Isotope Stage 2, causing spatially variable RSL change with the highest magnitude (0.9-1.1 m) found in the outer shelf of the southern central GBR. Because the SIA-induced RSL change is unrelated to ice mass change, failing to correct for this signal will lead to systematic overestimation of grounded ice volume during the LGM by up to $\sim 4.3 \times 10^5$ km ^{3}. Therefore, it is important to consider the SIA signal when interpreting postglacial sea-level records recovered from locations adjacent to large sediment systems, as this can partially mitigate the missing ice problem (**RQ2**). A copy of the published paper is supplied in Appendix B.

In this paper, Y.L. designed and led the research, performed the GIA and SIA modelling, created the sediment accumulation models, and designed and implemented the physical model calibration framework using a statistical SIA emulator. P.L.W., F.D.H. and S.A.W provided feedback on the scope and design of the research. Y.L., P.L.W., F.D.H. and S.A.W led the writing of the manuscript. G.H and J.M.W guided Y.L. in building the sediment model. P.L.W. advised Y.L. in performing GIA and SIA modelling. F.D.H., S.A.W, G.H and J.M.W advised Y.L. in sediment data analysis. Y.L. produced the first draft of the manuscript. All authors contributed ideas and to the editing of the manuscript. The paper was edited by Yemane Asmerom and reviewed by two anonymous reviewers.

Chapter 4

Lin, Y., Whitehouse, P., Valentine, A.P., and Woodroffe, S., 2023. GEORGIA: a Graph neural network based EmulatOR for Glacial Isostatic Adjustment. Geophysical Research Letters (submitted). This chapter documents the first attempt to build a statistical emulator that can mimic the behaviour of a physics-based GIA model and is computationally cheap to evaluate. Specifically, our emulator is based on state-of-the-art graph-based convolutional neural network algorithms, it shows good emulation accuracy on 150 out-of-sample testing data with 0.54 m mean absolute error, and it has a fast emulation time (<0.5 seconds). Making use of these two ideal properties, we build a probabilistic barystatic sea-level map by emulating 10,000 random synthetic global ice models. Our results highlight the Seychelles as an ideal place to map barystatic sea level throughout the last deglaciation because RSL at this location only slightly departs from global barystatic sea level, with minor dependency on the assumed ice history (**RQ3**). Please note that we focus on providing a proof-of-concept for building a GIA emulator in this chapter, more information about the barystatic sea-level map will be provided in Chapter 5. A copy of the submitted paper is supplied in Appendix C.

In this paper, Y.L. designed and led the research, performed the GIA modelling, generated the ice history ensembles and implemented the deep-learning framework for GEORGIA. P.L.W. and A.P.V. provided feedback on the scope and design of the research. A.P.V guided Y.L. in building the statistical model. P.L.W. advised Y.L. in performing GIA modelling. A.P.V. and P.L.W. helped Y.L. design the testing experiments. P.L.W. and S.A.W. supported Y.L. in creating example emulator applications. Y.L. produced the first draft of the manuscript. All authors contributed ideas and to the editing of the manuscript. The paper has been submitted to Geophysical Research Letters.

CHAPTER 2

A reconciled solution of Meltwater Pulse 1A sources using sea-level fingerprinting

Lin, Y., Hibbert, F.D., Whitehouse, P.L., Woodroffe, S.A., Purcell, A., Shennan, I. and Bradley, S.L., 2021. A reconciled solution of Meltwater Pulse 1A sources using sea-level fingerprinting. Nature communications, 12(1), p.2015. doi: 10.1038/s41467-021-21990-y.

2.1 Abstract

The most rapid global sea-level rise event of the last deglaciation, Meltwater Pulse 1A (MWP-1A), occurred ∼14,650 years ago. Considerable uncertainty regarding the sources of meltwater limits understanding of the relationship between MWP-1A and the concurrent fast-changing climate. Here we present a data-driven inversion approach, using a glacio-isostatic adjustment model to invert for sources of MWP-1A via sea-level constraints from six geographically distributed sites. The results suggest contributions from Antarctica, 1.3 m (0-5.9 m; 95% probability), Scandinavia, 4.6 m (3.2-6.4 m) and North America, 12.0 m (5.6-15.4 m), giving a global mean sea-level rise of 17.9 m (15.7-20.2 m) in 500 years. Only a North American dominant scenario successfully predicts the observed sea-level change across our six sites and an Antarctic dominant scenario is firmly refuted by Scottish isolation basin records. Our sea-level based results therefore reconcile with field-based ice-sheet reconstructions.

2.2 Introduction

Meltwater Pulse 1A (MWP-1A) was the largest and most rapid global sea-level rise event of the last deglaciation, characterised by ∼20 m global mean sea-level (GMSL) rise within 500 years (Deschamps et al., 2012; Lambeck et al., 2014). It was driven by the collapse of vulnerable ice sheet sectors, and was concurrent with rapid Northern Hemispheric warming and disruptions in oceanic and atmospheric circulation (Buizert et al., 2014; Fogwill et al., 2017). The ice-ocean-climate feedbacks operating during this period are not well understood largely due to a lack of consensus on the sources of MWP-1A (Menviel et al., 2011; Ivanovic et al., 2018), which, in turn, were likely to be a key driver in stimulating rapid deglacial climate change (Liu et al., 2009; Ivanovic et al., 2017; Obase and Abe-Ouchi, 2019).

Two major techniques have been used to constrain the sources of MWP-1A. The first uses physics-based models, constrained by field-based glacio-geological evidence, to simulate regional ice sheet change during the last deglaciation (Tarasov et al., 2012; Gregoire et al., 2012; Golledge et al., 2014). This approach is restricted by large

uncertainties regarding palaeo ice-sheet boundary conditions, climatic conditions, and ice-sheet model parameters. Ice histories derived using this approach do not always match sea-level observations (Gregoire et al., 2012). Conversely, the second method seeks to reconcile ice-sheet change with spatially variable records of sea-level change using a glacio-isostatic adjustment (GIA) model (Bassett et al., 2005; Deschamps et al., 2012; Liu, 2013; Liu et al., 2016), an approach often termed 'sea-level fingerprinting' (Mitrovica et al., 2001; Clark et al., 2002). The primary limitation of sea-level fingerprinting is the spatial and temporal scarcity of sea-level records across MWP-1A. Commonly, only three sites are used (Tahiti, Barbados and Sunda Shelf), resulting in an under-constrained problem and strongly non-unique solutions (Clark et al., 2002; Gomez et al., 2015; Liu et al., 2016). Other techniques, e.g., analysis of the oceanographic (Weaver et al., 2003; Ivanovic et al., 2017; Yeung et al., 2020) or isotopic (Wickert et al., 2013) effects of specific meltwater sources, add further constraints, but the primary source of MWP-1A remains controversial with three ice sheets proposed as the major contributor, namely, the North American Ice Sheet, including Greenland (NAIS, Tarasov et al., 2012; Lambeck et al., 2014; Peltier et al., 2015), the Antarctic Ice Sheet (AIS, Bassett et al., 2005; Deschamps et al., 2012) and the Scandinavian and the Barents Sea Ice Sheet (henceforth denoted together as SIS, Brendryen et al., 2020). The reason why Greenland is included as part of the NAIS is because previous modelling studies suggest that Greenland only made a minor contribution to MWP-1A (Peltier et al., 2015; Lambeck et al., 2014) and adding it as an independent source of ice melt would significantly amplify the non-uniqueness problem.

In this work, we combine a new data-driven inversion approach with sea-level fingerprinting to simultaneously derive probability distributions for the magnitude and sources of MWP-1A based on sea-level records from six geographically distributed sites. The results indicate a 17.9 m (15.7-20.2 m; 95% probability) of global mean sea-level rise over 500 years during MWP-1A, which consists of a dominant NAIS contribution (accounting for 35-85% of total MWP-1A magnitude), a substantial SIS contribution (20-35%) and a minor AIS contribution (0-35%). Unlike previous sea-level fingerprinting studies (Liu et al., 2016; Bassett et al., 2005), our results

show good agreements with recent regional ice-sheet reconstructions (Tarasov et al., 2012; Peltier et al., 2015; Lambeck et al., 2017; Brendryen et al., 2020; Gomez et al., 2020; Albrecht et al., 2020), which may lead to a reconciled solution of MWP-1A sources.

2.3 Results

2.3.1 Sea-level fingerprint approach

To robustly fingerprint the sources of MWP-1A, three main challenges need to be overcome. First, the above-mentioned non-uniqueness problem. Previously, only three sea-level sites showed sufficient temporal resolution for fingerprinting studies across MWP-1A (Gomez et al., 2015; Liu et al., 2016), namely, coral reef records from Tahiti (Bard et al., 1996; Deschamps et al., 2012) and Barbados (Fairbanks, 1989; Fairbanks et al., 2005; Abdul et al., 2016) and sedimentary indicators from Sunda Shelf (Hanebuth et al., 2000). The geographical distributions of these sites do not permit the separation of meltwater sources from the AIS and SIS (Figure 2.1). Second, the relationship between coral living depth and environmental conditions, as well as the link between reef accretion and sea level change (Neumann, 1985; Woodroffe and Webster, 2014), is not straightforward and may differ between different localities (Chappell, 1980; Bard et al., 2016; Hibbert et al., 2016). This can add considerable complexity when interpreting coral sea-level indicators. Third, most previous fingerprinting studies assumed a minor SIS contribution to MWP-1A (1-2.5 m) (Bassett et al., 2005; Deschamps et al., 2012; Gomez et al., 2015; Liu et al., 2016). This is challenged by a recent chronological reinterpretation of the SIS ice history that proposes the SIS was a major MWP-1A contributor (Brendryen et al., 2020). Such a large SIS contribution has not yet been tested using sea-level fingerprinting.

We address these challenges via three major methodological advances. First, we increase the number of sea-level sites, with data from extensive coral and coralline algae deposits on the Great Barrier Reef at Hydrographer's Passage (HYD) and Noggin Pass (NOG; Webster et al., 2018; Yokoyama et al., 2018), and isolation

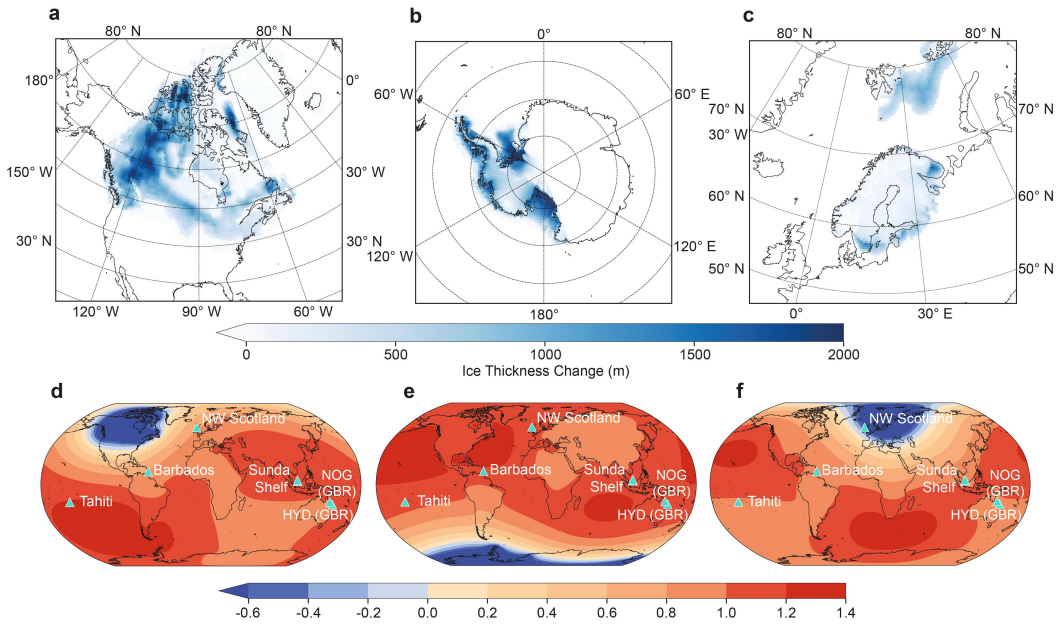

Figure 2.1: Ice melt geometries and normalised sea-level fingerprints used in this study, associated with ice mass loss from (a,d) the NAIS, (b,e) the AIS and (c,f) the SIS. (a,c) The reconstructed MWP-1A ice melt geometries from Lambeck et al. (2017) and BRITICE-CHRONO Bradley et al., 2018. (b) The LGM-to-present West AIS melt geometry from Whitehouse et al. (2012a) (see section 2.5 for details). The cyan triangles and text denote the location and name of each sea-level site. HYD = Hydrographer's Passage, NOG = Noggin Pass, both from the Great Barrier Reef; NW Scotland = Northwest Scotland.

basin stratigraphies from Northwest Scotland (Figure 2.1, Shennan et al., 1996, 1994, 2000). Where necessary, a standardisation is applied to ensure that the sea-level index points (SLIPs) only reflect the sea-level fingerprint of MWP-1A (see section 2.5). Second, based on these standardised SLIPs, we estimate the local rate and magnitude of relative sea-level (RSL) change across MWP-1A at each of our six sites using a Monte Carlo (MC) linear regression approach to capture the vertical and chronological uncertainties of the sea-level indicators. Third, these local MWP-1A magnitudes of RSL change are used to invert for the global magnitude, and regional partitioning via fingerprinting of NAIS, AIS, and SIS change.

Our approach relies on the assumption that SLIPs can be used to map out the fingerprint of ice-sheet change. A sea-level fingerprint reflects the global geoid variation and instantaneous elastic solid Earth response to ice mass change (Mitrovica et al., 2001; Clark et al., 2002), also known as the elastic component of RSL change

(Gomez et al., 2015). Assuming the NAIS, AIS and SIS were the only contributors to MWP-1A, the global pattern of RSL change caused by melt from these ice sheets can be identified as a linear combination of three spatially variable sea-level fingerprints (Figure 2.1d-f), each scaled by the eustatic contribution from the related ice sheet (Clark et al., 2002). Before using SLIPs to map out the fingerprint of MWP-1A, three issues must be addressed (i.e., our standardisation). The first only affects our Northwest Scotland data. RSL change here contains a large local GIA signal associated with changes to the British-Irish Ice Sheet (BIIS). We determine a local GIA correction for all these SLIPs to isolate the GIA signal associated with non-local ice sheet change (see section 2.5, Figure 2.2f; Bradley et al., 2011; Liu, 2013). The second issue concerns the spatial gradient of the sea-level fingerprint between coring locations within one site (e.g., >10km wide; Liu et al., 2016). This affects the Sunda Shelf and Northwest Scotland data and is accounted for by subtracting the time-specific sea-level gradient between each SLIP and a reference location. The corrected SLIPs represent RSL at a single locality (red stars in Figure 2.2c,f and Figure S2.2, see section 2.5). Lastly, for all SLIPs, we remove the age- and location-specific viscous component of RSL change. This correction accounts for the viscous solid Earth response to changes in surface loading and the accompanying change in geoid height caused by ice-sheet variation prior to and during MWP-1A (see section 2.5). We determine all three corrections using the mean of a GIA model ensemble that accounts for uncertainties associated with global ice history and mantle properties (see section 2.5). Because we focus on the centennial timescale of MWP-1A, our GIA corrections are not strongly sensitive to choice of mantle properties (see Figure S2.3), and hence neglect of heterogeneity (i.e., 3-D Earth structure; Austermann et al., 2013) should not bias our results.

2.3.2 Estimating local sea-level change across MWP-1A

The standardised SLIPs constrain local MWP-1A magnitude at each site. We use a conservative time window of 14.65-14.00 ka BP to select SLIPs at each site that clearly mark the initiation and termination of MWP-1A, enabling us to capture the full magnitude of MWP-1A sea-level rise. Ideally, only records with mean

ages within this window will be selected, but for sites with insufficient temporal coverage we include records whose 2σ age error bars extend into it. We estimate local MWP-1A magnitude from the SLIPs using a MC linear regression method, which captures any asymmetric depth and age uncertainties of different types of sea-level indicators by randomly sampling their uncertainty distributions. We use two approaches to represent indicative depth distributions of coral sea-level indicators; an empirically-derived distribution from modern coral analogues (the empirical scenario) and a uniform distribution, using palaeo-water depths from original publications (the uniform scenario; Hibbert et al., 2016, 2018). For non-coral SLIPs, both scenarios adopt a uniform indicative depth distribution based on original publications. The MC sampling process also accounts for the error propagation associated with any GIA correction that is appiled, the elevation measurements, and the tectonic correction uncertainties (see section 2.5). We calculate chronological probability distributions following the methodology of Hibbert et al. (2018), accounting for multimodal, asymmetric ^{14}C age distributions and age reliability screening (see section 2.5).

MC linear regression, using randomly selected data points and a weighted least square method, determines the local MWP-1A RSL rise rate at each site (see section 2.5). We integrate this linear rate to determine the magnitude of RSL change over the assumed duration of MWP-1A (500 years in this study). We exclude, as implausible, regressions producing a reverse slope (i.e., a sea-level fall). Repeating this process 20,000 times (excluding the implausible iterations) produces distributions of local MWP-1A magnitude for each site (Figure 2.2 and 2.3a). Because our results are derived from the averaged sea-level rise rate throughout MWP-1A, they are linearly scalable to any assumed duration of MWP-1A.

The viscous component of RSL change has a significant effect on local sea-level change during MWP-1A. Far-field localities (Tahiti, Sunda Shelf, HYD and NOG) will have experienced local sea-level fall associated with the redistribution of water to regions experiencing peripheral bulge subsidence and due to the ocean load-induced continental levering effect (i.e., we refer to the combined effect as 'ocean siphoning', Mitrovica and Milne, 2002; Figure S2.3 and S2.4). Not considering this effect leads to $\sim$1 m underestimate of the local RSL magnitude. Conversely, Northwest Scotland

will have experienced 0.8 m local RSL rise during MWP-1A mainly due to subsidence of the SIS peripheral bulge. Being an intermediate-field site, Barbados experienced both ocean siphoning and peripheral bulge subsidence during MWP-1A. The effects of these two signals roughly balance each other (Figure S2.3 and S2.4). It should be noted that given the exponential-like form of postglacial decay, the non-linear viscous signal associated with ice melt during MWP-1A is approximately double the linear pre-MWP-1A viscous signal (see section 2.5), a point largely unconsidered in previous work (Liu et al., 2016). We recommend both viscous signals be considered in future meltwater source inversion studies.

At Tahiti, our inversion is tightly constrained by samples containing vermetid gastropods (yellow error bars in Figure 2.2a) that indicate very shallow environments ($<$ 5 to 6 m (Cabioch et al., 1999; Camoin et al., 2012; Deschamps et al., 2012)). Most of the other Tahiti coral samples were identified as *Porites* sp. (Deschamps et al., 2012). Modern analogues (the empirical scenario) suggest a bimodal depth-habitat distribution concentrated at 0-15 m and 40-50 m (Hibbert et al., 2018). This bimodal empirical distribution was generated from a global compilation, and given insufficient modern observations at Tahiti, we consider it a 'maximum' vertical depth-range for this species. Comparatively, the palaeo-water depths derived from coral-algal assemblages (our uniform scenario) suggest depths of 0-10 m or even 0-20 m (Camoin et al., 2007, 2012). Therefore our empirical scenario yields a larger uncertainty range for the MWP-1A magnitude (13.6-30.9 m for a 500-year duration; 95% confidence interval; CI) than the uniform scenario (15.5-26.6 m, see uniform scenario results in Figure S2.6). Under a 340-year duration, our result suggests a 14.5 m sea-level rise (18.7 m if only using the vermetid gastropods records), similar to a previous estimate of 12-22 m (Deschamps et al., 2012).

Because the two Great Barrier Reef sites experienced reef demise and landward migration across MWP-1A, SLIPs from HYD and NOG only show a rapid $\sim$10 m sea-level rise $\sim$14.6-14.4 ka BP with no clear post-MWP-1A marker until the initiation of new coral reefs at $\sim$13.0 ka BP (Figure 2.2d,e, Webster et al., 2018; Yokoyama et al., 2018). To estimate the MWP-1A magnitude at these sites, we determined RSL at 14.0 ka BP by extrapolating back from the large number of

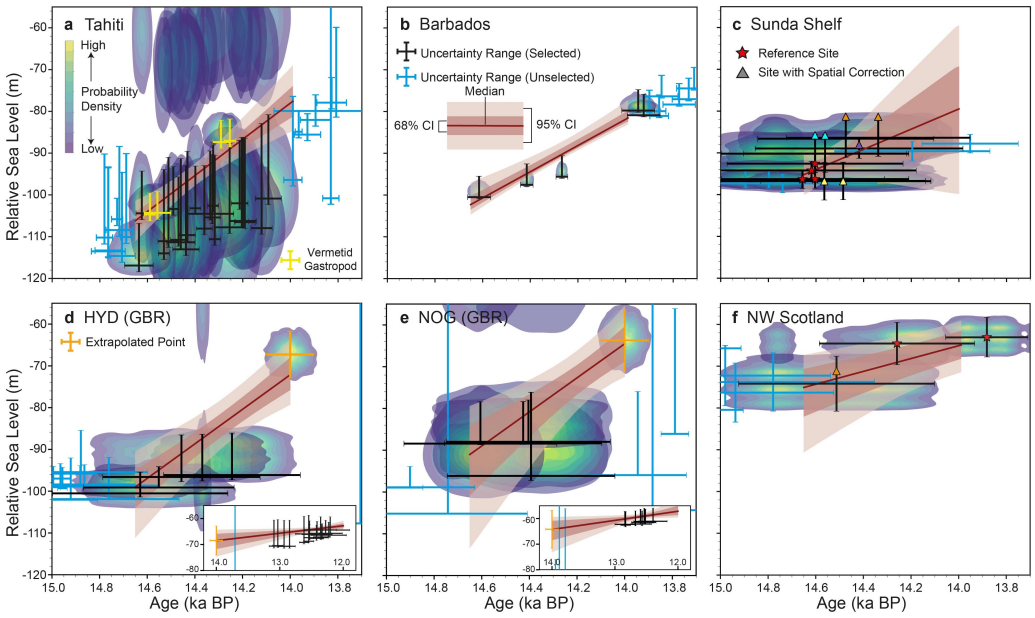

Figure 2.2: Estimated local MWP-1A sea-level rise trend at six selected sites using our 'empirical' scenario. Blue-green-yellow shading indicates the data-point-specific probability density accounting for age and depth uncertainties. The depth uncertainty for coral-based SLIPs (a,b,d,e) was determined using modern ecological data (the empirical scenario), some of which present a bimodal habitat depth, resulting in complex data clouds. For the uniform scenario, see Figure S2.6. The median and 95/68% confidence interval (CI) were determined by 20,000 MC simulations (see main text). Black/cyan error bars reflect uncertainty ranges associated with viscous and spatial signal corrections applied to SLIPs that were selected/unselected to train the MC model. Vertical and horizontal bars indicate combined depth uncertainty and 2σ age error. (a) The selected coral samples containing vermetid gastropods highlighted in yellow. (c, f) A spatial sea-level gradient correction was applied to ensure all SLIPs represent sea level at a single locality (reference site, denoted by red stars) in Sunda Shelf and Northwest Scotland. Triangles with different colours correspond to different localities, their vertical position indicates the original elevation prior to spatial gradient correction. (d, e) Orange error bars indicate the extrapolated point, the extrapolation process is shown in the subplot. (f) SLIPs have been corrected for the local GIA signal using the BRITICE-CHRONO ice model with 120 Earth models. GIA modelling uncertainty is incorporated into the error bars and data clouds.

SLIPs between ~13.0 and 12.0 ka BP (see section 2.5 and Figure S2.5). Based on the extrapolated points, our bimodal empirical distribution yields larger MWP-1A uncertainty ranges of 12.0-32.7 m and 7.3-37.7 m for HYD and NOG (95% CI; 500 years) than the counterpart generated by the uniform scenario (9.3-31.9 m and 11.5-28.2 m, Figure 2.3a), with both showing good agreement with Tahiti.

At Sunda Shelf, temporally clustered SLIPs with ~0.4 ka age uncertainties (2σ;

Figure 2.2c) provide a poor constraint on RSL rise, with ∼35% of MC simulations producing a reverse slope. We therefore only use weighted least square (without MC simulation) to calculate the local MWP-1A RSL magnitude, fitting to the mean of the age/depth distribution of each SLIP, which was assumed to be normally distributed. We exclude one data point, from site 18302 (cyan error bars in Figure 2.2c), because it is inconsistent with other SLIPs from this region (dated ∼14.2 ka BP but suggests 5 m lower RSL than SLIPs at 14.4 ka BP) and would strongly bias the local MWP-1A magnitude estimation. These modified regression conditions, combined with the 2-5 m between-site sea-level gradient corrections (Figure S2.2), produce a large uncertainty range for the MWP-1A magnitude, 0-35.7 m (95% CI, median 15.5 m). Compared with MWP-1A magnitude estimates for other far-field sites, this median value is slightly lower (Figure 2.3a), likely due to SLIPs from site 18301 (yellow triangles in Figure 2.2c) indicating 10-15 m lower RSL than other SLIPs of a similar age. The RANSAC outlier detection algorithm (Fischler and Bolles, 1981) suggests, with >90% probability, that these index points are outliers, and excluding them yields a ∼21.7 m MWP-1A magnitude. However, we choose to retain them for our analysis, and the large uncertainty range, because the MWP-1A partitioning results do not strongly depend on the local MWP-1A magnitude at Sunda Shelf (see section S2.2).

At Barbados, a recent coral-based sea-level reconstruction (Abdul et al., 2016) significantly improved the temporal control on local RSL at the termination of MWP-1A; two samples at ∼14.0 ka BP in Figure 2.2b were not available to former studies (Deschamps et al., 2012; Liu et al., 2016). Constrained by these new SLIPs, both empirical and uniform scenarios yield a tight 95% confidence range of 12.1-20.0 m and 12.8-18.2 m with a common median of ∼15.5 m (500-year MWP-1A duration; Figure 2.3a). Linearly scaling to 340 years yields a median of 10.7 m, which is lower than previous estimates of ∼15 m (Deschamps et al., 2012) or 9.7-33.6 m (Liu et al., 2016), and lower than our estimated MWP-1A magnitudes at other far-field sites.

A low MWP-1A magnitude is also observed in Northwest Scotland. After correcting for the local GIA signal and the spatial sea-level gradient, we identify an 8.6 m MWP-1A magnitude (500-year duration) within a 95% confidence range of 3.9-17.3 m

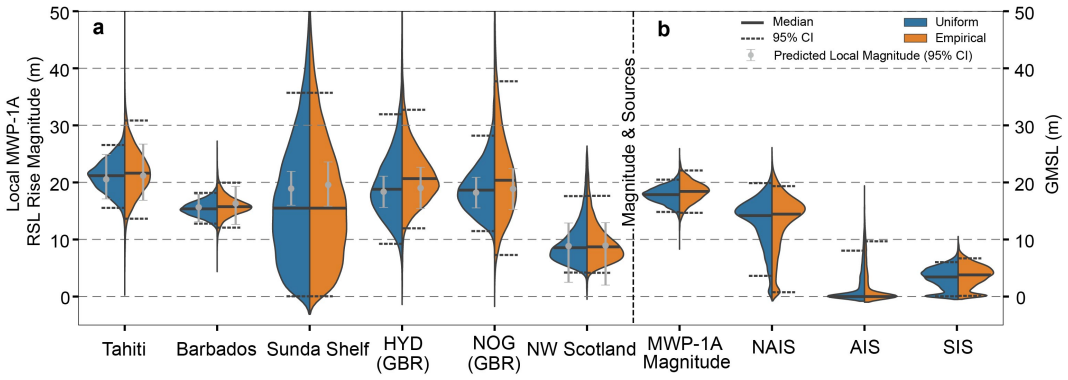

Figure 2.3: Probability distributions of (a) local MWP-1A magnitudes, (b) total MWP-1A magnitude and contribution from each ice sheet, assuming a 500-year duration. The two sides of each violin plot correspond to the empirical (orange) and uniform (blue) scenarios used to represent coral living depths. For non-coral SLIPs (Sunda Shelf and Northwest Scotland), both scenarios adopt a uniform distribution, small differences between the two sides are associated with different viscous signal corrections. Grey error bars in (a) represent the predicted local MWP-1A magnitude (95% probability) calculated using the inverted MWP-1A sources in (b). All probability density functions derived by Gaussian kernel density estimation, and all inversion results are exclusively non-negative.

(Figure 2.3a). The majority of this uncertainty is associated with the three ice models used to determine the local GIA signal, ANU (Lambeck and Purcell, 2001; Lambeck et al., 2014), PATTON2017 (Patton et al., 2016, 2017) and BRITICE-CHRONO (Clark et al., 2018), with only minor uncertainty associated with Earth parameters (see section 2.5 and Figure S2.7). Although the three BIIS models yield relatively large differences regarding the magnitude of the local GIA signal, they provide good consensus on the local elastic-induced MWP-1A sea-level rise magnitude: 9.0 m for ANU, 8.9 m for PATTON2017 and 7.7 m for BRITICE-CHRONO (see section S2.1). The low MWP-1A magnitude observed in Barbados and Northwest Scotland indicate a dominant contribution to MWP-1A from their nearby ice sheets (i.e., the SIS and NAIS, see Figure 2.1).

2.3.3 MWP-1A source inversion

For each of our 20,000 MC simulations of local MWP-1A magnitude, we adopted a non-negative weighted least square algorithm (Lawson and Hanson, 1995) to optimise the contribution of the NAIS, AIS and SIS to MWP-1A based on sea-level fingerprints

generated using realistic deglaciation geometries (Figure 2.1a-c; see section 2.5; Whitehouse et al., 2012a; Hughes et al., 2016; Lambeck et al., 2017; Clark et al., 2018). The use of a non-negative least square algorithm is appropriate here because we assume that ice sheet growth during MWP-1A would be implausible. We also tested alternative sea-level fingerprints based on MWP-1A ice melt geometries from ICE6G_C (Peltier et al., 2015), GLAC-1D (Tarasov et al., 2012) and G12 (Gregoire et al., 2012; Gomez et al., 2015) for the NAIS and PATTON2017 (Patton et al., 2016, 2017) for the SIS, which results in a negligible difference to our results (Table S2.3). The optimisation process was repeated six times, each time removing one site from the six-site database to quantify the bias associated with data over-dependency and assess the consistency of the overall results (i.e., jackknife resampling). We achieve a bias-corrected inversion of MWP-1A magnitude and sources by subtracting the bias (i.e., difference between overall jackknife ensemble mean and original results) from the original inversion result (Figure 2.3b). The averaged 95% CI of the empirical and uniform scenarios gives GMSL rise during MWP-1A between 15.6 and 20.3 m (mean 17.9 m, Figure 2.3b). The SLIPs prefer a dominant NAIS contribution to MWP-1A of 13.1 m (6.0-18.3 m), a substantial contribution from the SIS of 3.3 m (0.5-6.0 m) and a small contribution from the AIS of 1.5 m (0-6.9 m). The jackknifing results (i.e., inversion results when each site is excluded in turn) are generally in agreement (Figure S2.8), pointing to a dominant NAIS contribution and a minor AIS contribution, but they highlight the non-uniqueness of the solution when near-field sites are excluded (section S2.2).

Our GMSL rise magnitude is primarily constrained by data from Tahiti, Sunda Shelf, HYD and NOG because they are relatively insensitive to the origins of the meltwater (Figure 2.1), in contrast to Barbados and Northwest Scotland. For Barbados, melt from the NAIS is the only scenario that produces a considerably reduced local sea-level rise (20% less than the global mean, Figure 2.1d). A dominant NAIS contribution is therefore required to produce ∼15.5 m sea-level rise at Barbados under a 17.9 m GMSL rise scenario. NAIS melting also results in reduced RSL rise in Northwest Scotland (25% less than the global mean), but to match the observed 8.6 m sea-level rise at this site (<50% of the GMSL magnitude) requires a significant

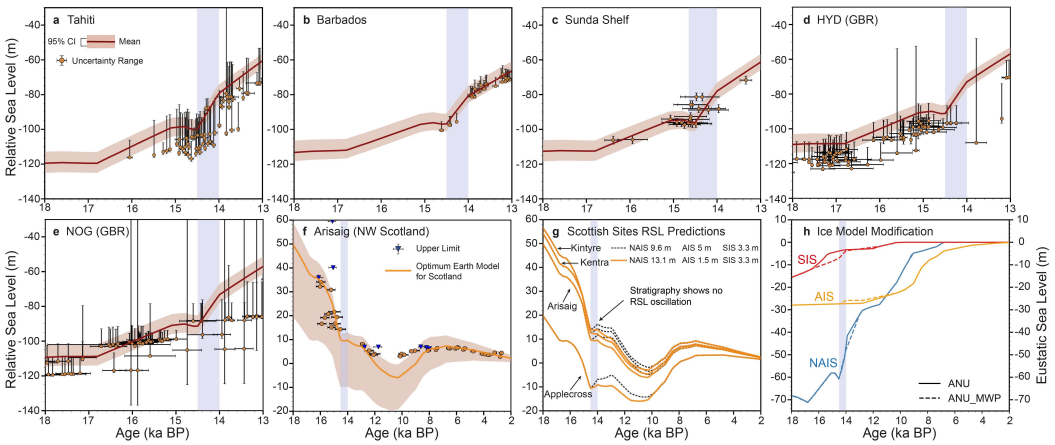

Figure 2.4: RSL predictions using the modified ANU model (ANU_MWP) compared with published sea-level index points. Error bars show depth range and 2σ age uncertainties provided by original studies. The vertical band indicates the duration of MWP-1A assumed in the ANU ice model (14.5-14.0 ka BP). (f) Orange solid line indicates the RSL prediction generated using the optimum Earth model (65 km lithospheric thickness, $4/200 \times 10^{20}$ Pa s upper/lower mantle viscosity) instead of the ensemble mean as in a-e. By combining our MWP-1A solution with this optimum Earth model in Scotland, we achieve a good fit to RSL data and meanwhile avoid a local RSL oscillation. (g) RSL predictions for four Northwest Scotland sites generated using the optimum Earth model in combination with two MWP-1A scenarios with: one that uses the ensemble mean inversion result of this study (orange solid lines) and one where the AIS contributes 5 m to MWP-1A (black dashed lines). The isolation basin stratigraphies indicates no RSL oscillation in Northwest Scotland during MWP-1A. (h) Ice history modifications, solid and dashed lines represent the ANU and ANU_MWP model, respectively. Note the different axis.

MWP-1A contribution from the SIS. Our inversion approach for the partitioning of melt between the NAIS, AIS, and SIS, successfully reproduces the local MWP-1A magnitude at our six sites (Figure 2.3a, grey error bars).

Our inversion results are used to predict deglacial RSL change at our six sites by incorporating our new MWP-1A ice history into the ANU ice model (denoted the ANU_MWP model, Figure 2.4h; see section 2.5). The RSL predictions (Figure 2.4a-f) show good fit to the data at all six sites. In particular, predictions at four sites across Northwest Scotland show monotonic sea-level fall during MWP-1A (Figure 2.4g), which is supported by the stratigraphic interpretation of isolation basins that were isolated shortly before or during MWP-1A, and where no RSL oscillation is recorded (Figure S2.11 and S2.12; Shennan et al., 1994, 1996, 2000, 2018). This condition of no RSL oscillation during MWP-1A can only be achieved if the rate of

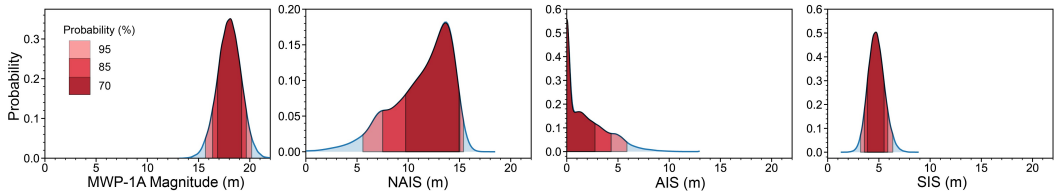

Figure 2.5: Probability density functions of the averaged inversion result of the empirical and uniform scenarios after applying the sea-level oscillation limit. Shaded areas indicate 95/85/70% probability range.

RSL rise due to far-field melt did not outpace land uplift due to local GIA (detailed interpretation in section S2.3). Modelling of the local GIA signal suggests the largest plausible rate of land uplift at Arisaig (one of the sites in Northwest Scotland) is 9.8 m in 500 years (section S2.3). After accounting for 0.8 m sea-level rise caused by the viscous effects of GIA, to avoid a local sea-level oscillation, the RSL fingerprint of MWP-1A cannot exceed ∼9 m within 500 years. We refer to this as the 'sea-level oscillation limit'. Under the scenario of 17.9 m GMSL rise, this 9 m limit is exceeded for any substantial AIS contribution because sea-level rise due to melt from the AIS is amplified by 10% across Scotland (Figure 2.1e). We assessed the potential consequence of a 5 m AIS contribution to MWP-1A (with the NAIS contribution equivalently reduced, see section 2.5). This produces a distinct 2,000-year RSL oscillation following the start of MWP-1A (black dashed lines in Figure 2.4g). The stratigraphic evidence firmly refutes such an oscillation (Shennan et al., 2018). In summary, the isolation basin evidence supports a minor AIS, a substantial SIS and a dominant NAIS contribution scenario.

We recalculate uncertainty ranges for our inversion results by imposing a 9 m upper limit on the local MWP-1A magnitude in Northwest Scotland to avoid a local sea-level oscillation. The resulting 95% probability range of the averaged empirical and uniform scenarios suggests a total GMSL rise of 17.9 m (15.7-20.2 m), which consists of a dominant NAIS contribution of 5.6-15.4 m (accounting for 35-85% of total MWP-1A magnitude), a substantial SIS contribution of 3.2-6.4 m (20-35%) and a minor AIS contribution of 0-5.9 m (0-35%) with median values of 12.0, 4.6 and 1.3 m, respectively (Figure 2.5).

2.4 Discussions

Our estimates show good agreement with recent field-based ice-sheet reconstructions for the NAIS and AIS (Table S2.2). Conversely, most SIS regional reconstructions propose a 1-2.5 m contribution (Lambeck et al., 2014; Hughes et al., 2016; Patton et al., 2017), considerably lower than our estimate. A possible reason for this discrepancy is previous studies are commonly based on radiocarbon chronology that assumes a temporally constant Scandinavian marine radiocarbon reservoir age, which suggests the southern Barents Sea sector collapsed well before MWP-1A (see Figure 2.4h). A recent study adopts a temporally varying Scandinavian marine radiocarbon reservoir age to reinterpret the chronology of SIS retreat and suggests the southern Barents Sea sector may have collapsed during MWP-1A, accompanied by marginal retreat of the Scandinavian Ice Sheet, contributing 4.0-7.4 m to GMSL rise (we calculate the eustatic contribution by subtracting the volume of ice below flotation, as defined in the PATTON2017 ice model, Patton et al., 2017, from the total ice volume change, Brendryen et al., 2020), similar to our estimate. We suggest a substantial SIS contribution is essential to reconcile the gap between regional ice-sheet reconstructions and global sea-level fingerprinting (see Table S2.2), and thus close the MWP-1A global sea-level budget. Such a substantial freshwater input to the Nordic Sea ($\sim$0.12 sverdrup), combined with NAIS freshwater routed along the Mackenzie River into the Arctic, may have contributed to a weakening of this 'limb' of the Atlantic Meridional Overturning Circulation (McManus et al., 2004), potentially helping to explain the termination of Bølling warming and the initiation of the Older Dryas stadial (Weaver et al., 2003; Swingedouw et al., 2009; Ivanovic et al., 2017).

Based on our inversion results, we hypothesise that MWP-1A was triggered by rapid disintegration of Northern Hemispheric ice sheets, which account for at least 65% (95% probability) of GMSL rise during this period. Rapid disintegration of the NAIS and SIS has been proposed to be consistent with the operation of ice-sheet saddle collapse (Gregoire et al., 2012, 2016) and unstable ice grounding line retreat (Mercer, 1978; Pollard et al., 2015) forced by abrupt Northern Hemispheric atmospheric and

oceanic warming (McManus et al., 2004; Buizert et al., 2014). However, the detailed ice dynamic behaviour of these two ice sheets remains elusive. Although most recent studies suggest that saddle collapse between the Western Laurentide and Cordilleran Ice Sheets was a major contributor to MWP-1A (Gregoire et al., 2012; Tarasov et al., 2012; Peltier et al., 2015; Gomez et al., 2015; Lambeck et al., 2017), a recent study based on the Bering Strait flooding history suggests this saddle collapse did not operate until the Younger Dryas and the NAIS contribution to MWP-1A solely originated from the Eastern Laurentide Ice Sheet (Pico et al., 2020). Similarly, for the SIS, the new southern Barents Sea sector collapse chronology proposed by Brendryen et al. (2020) is yet to be validated.

To test the sensitivity of our inversion results to alternative ice melt configurations, we separated the NAIS into the Western and Eastern NAIS (separated by 110° W, as defined in Pico et al., 2020) and generated two sea-level fingerprints using the ICE6G_C model (Peltier et al., 2015). We solve for the contribution of these two NAIS sectors to MWP-1A separately along with the AIS and SIS. The results yield 4.4 m (0-12.5 m; 95% CI) and 8.7 m (0-16.8 m) contributions from the Western and Eastern NAIS, respectively, with little change to the AIS and SIS contributions (Table S2.3). The total NAIS contribution is similar to our original inversion and this NAIS partitioning is consistent with recent NAIS reconstruction studies (Tarasov et al., 2012; Peltier et al., 2015; Gowan et al., 2016a; Lambeck et al., 2017), but due to the limited sea-level sites available, we cannot robustly determine the relative contribution from these two NAIS sectors. For the SIS, we replace the adopted SIS sea-level fingerprint (Figure 2.1f, reflecting ice melt from northern Barents Sea and eastern Fennoscandia) with a fingerprint generated using an ice melt geometry that is predominantly sourced from the southern Barents Sea (from the PATTON2017 model, Patton et al., 2017). The impact on the inferred MWP-1A contribution from each ice sheet is < 0.3 m (Table S2.3). Therefore, our results are not strongly sensitive to the assumed ice melt geometry.

Our results suggest the AIS was relatively stable during the concurrent Antarctic Cold Reversal (Parrenin et al., 2007), which is consistent with recent AIS modelling studies (Gomez et al., 2018; Albrecht et al., 2020; Gomez et al., 2020). Based on

our melt geometries, MWP-1A induced 15-18 m local RSL rise across the AIS. This may have started to destabilise the AIS (Gomez et al., 2018; Whitehouse et al., 2019; Gomez et al., 2020), eventually leading to substantial AIS retreat from 13 ka BP (Anderson et al., 2014).

Our inversion, which includes sophisticated treatment of uncertainties associated with sea-level data and geophysical modelling processes, provides the first calibration of MWP-1A contributions from the NAIS, AIS and SIS that is consistent with both sea-level constraints and regional ice-sheet reconstructions. In particular, our MWP-1A partitioning is supported by Scottish isolation basin stratigraphies, which can only be fit by a minor Antarctic contribution. Use of our results to prescribe the global pattern of meltwater discharge during MWP-1A (Ivanovic et al., 2016) may yield novel insights into the sequencing of ice-ocean-climate interactions during this recent abrupt climate change event.

2.5 Methods

2.5.1 Inversion strategy

We solve for the meltwater contributions from the NAIS, AIS, and SIS that best fit observations of relative sea-level (RSL) change across MWP-1A (ΔRSL_{Obs}). RSL change takes place due to changes in the shape of the solid Earth and the sea surface, with the latter being defined by the shape of Earth's gravity field. Because the solid Earth behaves viscoelastically over the timescale of interest, RSL change at location φ can be divided into a component that reflects the instantaneous response of the solid Earth and sea surface to an influx of meltwater ($\Delta RSL_{Elastic}$) and a component that reflects ongoing perturbations to these surfaces due to past surface load change ($\Delta RSL_{Viscous}$):

$$\Delta RSL_{Obs}(\varphi) = \Delta RSL_{Viscous}(\varphi) + \Delta RSL_{Elastic}(\varphi) \tag{2.1}$$

The elastic term can be further decomposed into:

$$\begin{aligned}\Delta RSL_{Elastic}(\varphi) = ESL_{NAIS} \times F_{NAIS}(\varphi) + ESL_{AIS} \times F_{AIS}(\varphi) \\ + ESL_{SIS} \times F_{SIS}(\varphi)\end{aligned} \tag{2.2}$$

where the three ESL terms represent eustatic sea-level (ESL) contributions from the NAIS, AIS, and SIS ice sheets and the $F(\varphi)$ terms denote ice-sheet-specific, site-specific sea-level fingerprint values. The term 'sea-level fingerprint' describes the normalised elastic component of RSL change triggered by a given pattern of ice loss (Mitrovica et al., 2001; Clark et al., 2002). The $F_i(\varphi)$ terms are insensitive to the value of the ESL_i terms and the choice of Earth rheology (Clark et al., 2002; Mitrovica et al., 2011). Therefore, it can be calculated using existing ice sheet reconstructions and treated as a known parameter (see section 2.5.3). The three *ESL* terms are the unknown parameters in our inversion. We assume that the NAIS, AIS, and SIS are the only contributors to MWP-1A, where any Greenland contribution is included in the NAIS.

The viscous component of RSL change can also be decomposed into two terms:

$$\Delta RSL_{Viscous}(\varphi) = \Delta RSL_{PreViscous}(\varphi) + \Delta RSL_{DurViscous}(\varphi) \tag{2.3}$$

where $\Delta RSL_{PreViscous}(\varphi)$ and $\Delta RSL_{DurViscous}(\varphi)$ are the changes associated with the viscous effects of ice melt prior to and during MWP-1A respectively (see section 2.5.6).

Substituting equation 2.3 in to equation 2.1 yields an expression for the elastic component of RSL change at each field site:

$$\begin{aligned}\Delta RSL_{Elastic}(\varphi) &= \Delta RSL_{Obs}(\varphi) - \Delta RSL_{PreViscous}(\varphi) - \Delta RSL_{DurViscous}(\varphi) \\ &= ESL_{NAIS} \times F_{NAIS}(\varphi) + ESL_{AIS} \times F_{AIS}(\varphi) \\ &\quad + ESL_{SIS} \times F_{SIS}(\varphi)\end{aligned} \tag{2.4}$$

By deriving estimates of $\Delta RSL_{Elastic}$ at our six field sites we create a set of equations that can be inverted to yield the ESL contribution to MWP-1A from each of the three ice sheets considered here.

Monte Carlo linear regression is used to estimate the probability distribution of the $\Delta RSL_{Elastic}$ at each site by computing the fit to probability distributions of all viscous-corrected sea-level index points (SLIPs) at that site that lie within MWP-1A (see section 2.5.7). Prior to carrying out the linear regression, the SLIPs are also

corrected for any local GIA effects (see section 2.5.4) and any spatial gradient of RSL that exists between sites that are combined to estimate sea-level change at a single location (see section 2.5.5). We assume the thermosteric contribution to RSL change during MWP-1A is negligible.

Because $\Delta RSL_{PreViscous}(\varphi)$ is controlled by ice melt prior to MWP-1A it can be calculated using an existing global ice model (see below). In contrast, $\Delta RSL_{DurViscous}(\varphi)$ depends on the unknown ESL parameters, which makes equation 2.4 an implicit equation that must be solved iteratively. We employ the following approach (see Figure S2.1): (*i*) Calculate a first approximation of $\Delta RSL_{Elastic}(\varphi)$ at six sea-level sites (see main text) using a Monte Carlo linear regression method (see details below) that assumes $\Delta RSL_{DurViscous}(\varphi)$ is zero. (*ii*) Invert for the three ESL values using the $\Delta RSL_{Elastic}(\varphi)$ values calculated in step i (for the first iteration) or step v (for all other iterations). (*iii*) Correct the bias within the inversion results using jackknife resampling (see details below). (*iv*) Calculate $\Delta RSL_{DurViscous}(\varphi)$ using the bias-corrected ESL inversion from step *iii* (see details below). (*v*) Computing $\Delta RSL_{Elastic}(\varphi)$ using the $\Delta RSL_{DurViscous}(\varphi)$ values obtained in step *iv*. (*vi*) Repeat step *ii*-*v* until convergence of ESL values has been achieved, i.e., when the updated inversion results show less than 0.3 m difference compared with the previous iteration.

2.5.2 GIA modelling

Sea-level change and the solid Earth response to changes in surface loading are computed using the CALSEA software package (Lambeck et al., 2003; Purcell et al., 2016), which uses a gravitationally self-consistent theory that accounts for migrating shorelines and Earth rotational feedback (Milne and Mitrovica, 1996; Kendall et al., 2005; Mitrovica et al., 2005; Mitrovica and Wahr, 2011). The Earth is represented by a spherically symmetric, radially stratified (i.e., 1-D), self-gravitating Maxwell body comprising an elastic lithosphere, and an upper and lower mantle extending to 670 km and from 670 km to the core-mantle boundary, respectively. The elastic and density structure of the Earth is derived from the Preliminary Reference Earth Model (Dziewonski and Anderson, 1981). GIA modelling is used to calculate sea-level

fingerprints, the local GIA signal in Northwest Scotland, spatial sea-level gradients, and the viscous component of sea-level change.

2.5.3 Sea-level fingerprint

The sea-level fingerprint for each ice sheet is obtained by calculating the normalised global pattern of RSL change associated with melt from a specific ice sheet over a finite time interval. Because sea-level fingerprints are sensitive to the geometry of ice melt (Mitrovica et al., 2011), we use realistic melt geometries across MWP-1A from two recent regional ice-sheet reconstructions of Lambeck et al. (2017) and the BRITICE-CHRONO project (with SCEAN1D scenario, S. Bradley, personal communication) for the NAIS and SIS, respectively (Figure 2.1a,c). The latter is constrained using geomorphological data compiled in Hughes et al. (2016) and Clark et al. (2018), and reconstructed using a plastic ice-sheet model (Gowan et al., 2016b). We also used some alternative NAIS and SIS melt geometries from ICE6G_C (Peltier et al., 2015), GLAC-1D (Tarasov et al., 2012) and G12 (Gregoire et al., 2012) for the NAIS and PATTON2017 (Patton et al., 2016, 2017) for the SIS to test the dependence of the inversion results on the assumed ice melt geometries. This leads to essentially unchanged inversion results (see Table S2.3). For the AIS, due to the lack of geological constraints, the melt geometry across MWP-1A remains largely unknown. Since East Antarctica is estimated to have contributed only ∼1 m to post-Last Glacial Maximum eustatic sea-level rise, with this melt most likely to have occurred after MWP-1A (Mackintosh et al., 2014), any Antarctic contribution to MWP-1A is likely to have come from the West AIS. We therefore generate the AIS sea-level fingerprint using the Last Glacial Maximum-to-present pattern of ice loss across West Antarctica adopted by the W12 ice model (Whitehouse et al., 2012a) (Figure 2.1b). Because all our six sea-level sites are far away from the AIS, their AIS sea-level fingerprint values are not sensitive to the assumed West AIS melt geometry.

2.5.4 Local GIA signal in Northwest Scotland

As demonstrated in previous studies (Bradley et al., 2011; Liu, 2013; Shennan et al., 2018), RSL change across Northwest Scotland can be described in terms of a local GIA signal caused by the growth and decay of the British-Irish Ice Sheet (BIIS) and a non-local GIA signal associated with the growth and decay of other ice sheets around the world. If the local GIA signal can be estimated and removed from the SLIPs, the remaining signal will be the non-local GIA signal associated with changes to the NAIS, AIS, and SIS.

Ice history and Earth rheology are not perfectly known for the British Isles. Therefore, we test 360 parameter sets when computing the local GIA signal. Specifically, we use three different BIIS models: BRITICE-CHRONO (Clark et al., 2018), PATTON2017 (Patton et al., 2016, 2017) and ANU (Lambeck, 1993; Lambeck and Purcell, 2001; Lambeck et al., 2014), and combine each with 120 Earth models. Because these BIIS models were constructed based on different principles (geomorphological reconstruction guided by GIA modelling for BRITICE-CHRONO, thermomechanical ice modelling for PATTON2017 and GIA modelling for ANU) they provide conservative estimates on ice history uncertainties. These ice models were combined with Earth parameters that reflect the rheological properties beneath the British Isles (denoted as near-field rheology). Specifically, we use elastic lithospheric thicknesses of 65, 72 and 80 km, upper mantle viscosities of 4, 4.5, 5, 5.5 and 6 $\times$ 10^{20} Pa s and lower mantle viscosities of 1, 1.5, 2, 3, 4, 5, 7 and 10 $\times$ 10^{22} Pa s. These ranges are constrained by previous GPS analysis and are largely independent to the assumed ice history (Bradley et al., 2009). We calculate the age-specific local GIA signal for each SLIP and subtract this from the original RSL reconstruction to give the non-BIIS GIA signal. The uncertainty for this procedure is considered within the inversion strategy by sampling the 360 local GIA correction values (each applied to 20,000 Monte Carlo simulations, see details below) and adding the standard deviation of the corrections to the original depth uncertainty in quadrature. After removing the local GIA signal, there is a distinct RSL jump recorded between 14.5 and 14.2 ka BP, which is consistent with the MWP-1A signal observed in far-field sea-level records (Figure S2.7).

2.5.5 Spatial sea-level gradient

Due to the large geographical spread of the SLIPs from Sunda Shelf and Northwest Scotland, there will be a non-negligible time-dependent difference in the RSL recorded at the different localities (i.e., a spatial sea-level gradient (Liu et al., 2016)). We apply a correction for this spatial gradient that enables us to determine the RSL change across MWP-1A at a single locality for each region. We quantify this gradient by testing 240 parameter combinations to incorporate uncertainties associated with ice history and Earth rheology. Specifically, we combine the two global ice models ICE6G_C (Peltier et al., 2015) and ANU (Lambeck et al., 2014) with 120 different Earth models. The Earth models each have an elastic lithospheric thickness of 60, 72 or 90 km, an upper mantle viscosity of 1, 3, 5, 6 or 7 $\times$ 10^{20} Pa s, and a lower mantle viscosity of 0.1, 0.2, 0.3, 0.5, 0.6, 0.7, 0.9 or 1 $\times$ 10^{22} Pa s for ICE6G_C, or 0.7, 0.9, 1, 1.5, 3, 4, 5 or 7 $\times$ 10^{22} Pa s for the ANU model (we made different choices for lower mantle viscosity because the two ice models have different preference ranges). Because the local GIA signal in Northwest Scotland is removed separately we do not include the BIIS component of ICE6G_C and ANU when calculating the spatial gradient for Northwest Scotland to avoid a double correction. The ensemble mean of the 240 parameter combinations is used to determine the time-dependent data-specific spatial sea-level gradient (Figure S2.2). Site 18300 and Applecross are defined as reference sites for Sunda Shelf and Northwest Scotland respectively (red stars in Figure 2.2 and Figure S2.2), to which all other sites are corrected. As for the local GIA signal correction, the uncertainty in this procedure is added to the original depth uncertainty in quadrature.

2.5.6 Viscous component of sea-level change

To correct for the viscous signal across MWP-1A, we estimate the viscous contribution of RSL change to each SLIP, accounting for their specific age and location. Given that the viscous response to ice melt prior to MWP-1A ($\Delta RSL_{PreViscous}$) will be approximately linear over MWP-1A (Gomez et al., 2015; Liu et al., 2016), we quantify this linear rate by considering the viscous response to ice sheet change between the

end of the last interglacial and the start of MWP-1A (14.65 ka BP). We assume no melting after 14.65 ka BP and calculate the linear rate of RSL change during the following 1,000 years (Figure S2.3). This linear rate is used to determine the $\Delta RSL_{PreViscous}(\varphi)$ signal that is specific to the age and location of each SLIP, assuming the viscous contribution is 0 at the initiation of MWP-1A (14.65 ka BP). For all sites except Northwest Scotland we use the mean value derived from a 240-member GIA model ensemble, as described in the previous section. For Northwest Scotland, since the dominant viscous signal here relates to SIS-induced peripheral bulge subsidence (roughly 90% of the signal), which primarily depends on the local rheology of the British Isles, we use the near-field Earth parameters described in the section on Northwest Scotland. Again, to avoid a double correction, we did not include the BIIS in the global ice model when calculating $\Delta RSL_{PreViscous}(\varphi)$ for Northwest Scotland.

Because the $\Delta RSL_{DurViscous}(\varphi)$ terms depend on the ESL values in equation 2.4, which are unknown during the first iteration, we neglect this component of RSL change during the first iteration. Since these terms are relatively small compared to $\Delta RSL_{Elastic}(\varphi)$ (less than 10%), neglecting them will not significantly alter the inversion result during the first iteration. Beginning from the second iteration, we scale the ice melt geometries that are used to generate the sea-level fingerprints (main text Figure 2.1) according to the bias-corrected ESL values determined in the previous iteration (details below). The pattern of $\Delta RSL_{DurViscous}(\varphi)$ is then calculated assuming a linear rate of ice melt throughout MWP-1A. A range of Earth models are used, as for $\Delta RSL_{PreViscous}(\varphi)$ above, and the ensemble mean of each set is used to determine the $\Delta RSL_{DurViscous}(\varphi)$ terms, accounting for the age and location of each SLIP (see Figure S2.4).

2.5.7 Monte Carlo linear regression

To quantify the elastic-induced local MWP-1A magnitude at each site ($\Delta RSL_{Elastic}(\varphi)$ in equation 2.4), we use a Monte Carlo (MC) linear regression technique to estimate the distribution of local sea-level rise rates recorded by selected SLIPs at that site. The MC simulation approach is used to capture the potentially asymmetric age and

depth uncertainties of different types of sea-level indicators by randomly sampling each sea-level index point's depth and chronological distribution. These distributions are calculated following the methodology of Hibbert et al. (2016, 2018), assuming no auto-correlation existed between different sea-level records.

For the coral sea-level indicators, we test two methods for representing their indicative depth distributions. First, we use an empirically-derived taxon-specific depth-habitat distribution for each coral-based sea-level indicator (Hibbert et al., 2018), which is obtained using the modern coral analogue from the Ocean Biogeographical Information System (www.iobis.org). This method is denoted as the 'empirical scenario'. Alternatively, we use the coral palaeo-water depth determinations (i.e., upper/lower limit of living range) from the original publications for different coral species. For this method, we assume a uniform distribution, in that the indicator may occur equally anywhere within the given range (Hibbert et al., 2018). We denote this method as the 'uniform scenario'. For non-coral SLIPs (including coral samples additionally constrained by vermetid gastropods in Tahiti), we use the indicative range or facies formation range as determined by the original authors, which is also assumed to be uniformly distributed. At Tahiti and Barbados, a correction to account for local tectonic induced RSL change is applied (Hibbert et al., 2018). Furthermore, when sampling the depth distributions of all SLIPs, we considered the error distribution associated with each of the GIA corrections described above and elevation measurement uncertainties due to coring, levelling and tectonic correction if necessary. We exclude any data explicitly stated as not *in situ* by the original authors.

The chronological probability distributions depend on the method used to date each SLIP. For samples that are radiocarbon dated, we use OxCal version 4.4 (Ramsey, 2009) to obtain the calibrated age probability distribution by recalibrating the conventional radiocarbon age and uncertainty using the latest calibration curves: IntCal20 (Reimer et al., 2020) for Northern Hemisphere terrestrial samples; SHCal20 (Hogg et al., 2020) for Southern Hemisphere terrestrial samples and Marine20 (Heaton et al., 2020) for all marine samples. For marine samples, we apply appropriate, updated (i.e., calculated using Marine20) local marine reservoir corrections (ΔR;

http://calib.org/marine). For all other samples, U-series ages have been recalculated where necessary, assuming a closed system with the latest decay constants (Cheng et al., 2013). Only U-series ages passing the following "age reliability" screening criteria (calcite $< 2\%$, $[^{232}\mathrm{Th}] \leq 2\,‰$, $\delta^{234}\mathrm{U}_{initial} = 147 \pm 5\,‰$) are considered. A normal distribution is adopted for U-series ages, whereas our radiocarbon ages use the full age probability distribution (Hibbert et al., 2018). For any replicated ages, we use the inverse weighted mean value/distribution of each replicate group.

For each of our six sites, we use MC simulation to randomly sample the age and depth distributions of each selected SLIP, and for each MC sampling, we use a weighted least square method to compute an optimum straight line to fit the randomly sampled points. The slope of this line is the averaged RSL rate across MWP-1A (units m/ka), which is assumed to be temporally linear throughout MWP-1A. Note that, since the lack of temporal resolution and uneven temporal distribution of sea-level data prohibit our ability to capture the maximum rates of sea-level rise at each site, our results should be interpreted as the averaged rate of RSL change at each site across our MWP-1A time-window (14.65-14.0 ka BP). Within each weighted least square calculation, the weighting factor w for each SLIP is calculated by:

$$w = 1/\sqrt{\sigma_y^2 + (dy/dx)^2\sigma_x^2} \tag{2.5}$$

where σ_y and σ_x are standard deviations estimated from the depth and age distributions, respectively, and dy/dx is the gradient of global sea-level change at the sampled age obtained from Lambeck et al. (2014). The last term is used to convert the effective contribution of age uncertainty into depth uncertainty. Regressions that produce a reverse slope (i.e., a sea-level fall) are excluded as implausible. The process is repeated 20,000 times (excluding the implausible iterations) to produce a distribution of local MWP-1A sea-level rise rates for each site. Lastly, the local MWP-1A magnitude is obtained by scaling this linear rate to the MWP-1A duration. We use a 500-year MWP-1A duration in this study since it leads to more comparable results with the MWP-1A magnitude from regional ice-sheet reconstructions, but our inversion results can be linearly scaled to any assumed MWP-1A duration for comparison.

2.5.8 Data extrapolation

For HYD and NOG, the SLIPs only show a rapid ∼10 m sea-level rise between 14.6-14.4 ka BP with no clear post-MWP-1A SLIP until the initiation of new coral reefs at ∼13.0 ka BP, showing another 20-25 m sea-level rise. This sequence is identified as "rapid growth then drowning and further landward migration" (Webster et al., 2018, p.420; see their Figure 4a). In order to constrain RSL at the end of MWP-1A, we adopt a data extrapolation approach that uses the large number of SLIPs between ∼13.0 and 12.0 ka BP at the two sites to extrapolate RSL backwards in time. To ensure the accuracy of the data extrapolation we only use SLIPs that pertain to a shallow, high-energy/exposed reef edge environment (the cA coral-algal assemblage, Webster et al., 2018), i.e. SLIPs which have a relatively small depth uncertainty. The data extrapolation was implemented using the same MC linear regression method as above, in combination with the uniform scenario (Figure S2.5) as the empirical depth distribution for some SLIPs contains a bimodal habitat depth, resulting in over-large extrapolation uncertainty. The depth uncertainty of the extrapolated data point is defined by the extrapolation process, and it was assigned an age uncertainty of 0.1 ka assuming a normal distribution.

2.5.9 Inversion for MWP-1A sources

Based on the site-specific elastic-induced local MWP-1A magnitude distributions ($\Delta RSL_{Elastic}(\varphi)$) estimated above, the inversion for MWP-1A sources can be made by identifying the optimum *ESL* parameters in equation 2.4 for each of the 20,000 MC iterations. This is achieved using a weighted non-negative least square method using the Lawson−Hanson algorithm (Lawson and Hanson, 1995) since we assume that ice sheet growth during MWP-1A would be implausible. The weighting factor for each site is given by $w(\varphi) = 1/\sigma(\varphi)^2$ where $\sigma(\varphi)$ is the standard deviation estimated from the local MWP-1A magnitude distributions.

2.5.10 Jackknife resampling

After each iteration of our method (i.e., each time we invert for the sources of MWP-1A, see Figure S2.1), we adopt a jackknife resampling technique to correct for any bias associated with data over-dependency. Specifically, we invert for the sources of MWP-1A six times, each time removing one site from the six-site database. The difference between the mean jackknife inversion result and the original inversion result is defined as the bias contained in the original inversion result. Subtracting this bias from the original result yields a bias-corrected inversion of MWP-1A sources.

2.5.11 Relative sea-level prediction

We modified the deglaciation history during MWP-1A in the ANU ice model (Lambeck et al., 2014) and used this revised model to predict RSL variation at the six sea-level sites used in this study. This revised model (denoted as the ANU_MWP model) was created by leaving the ice history prior to MWP-1A unchanged, but assuming that ice loss during MWP-1A followed the magnitude and spatial pattern of ice loss represented by the mean of our inversion result: 13.1 m NAIS, 3.3 m SIS, and 1.5 m AIS. The rate of ice melt during MWP-1A was assumed to be linear. In the original ANU model, there is not enough ice for the SIS to melt 3.3 m during MWP-1A. We therefore decrease the rate of ice melt between 16.5 and 14.5 ka BP (the latter is the time of MWP-1A initiation in the ANU model) to ensure there is enough ice to provide 3.3 m ESL melt during MWP-1A (Figure 2.4h). The synthetic test of a larger AIS contribution to MWP-1A adopted the same pre-MWP-1A ice geometries as in the ANU_MWP model but used different MWP-1A sources: 9.6 m NAIS, 3.3 m SIS and 5 m AIS. The modified ice models were combined with the 120 ANU-specific Earth models to produce RSL curves from the last interglacial to present.

S2 Supplementary Information

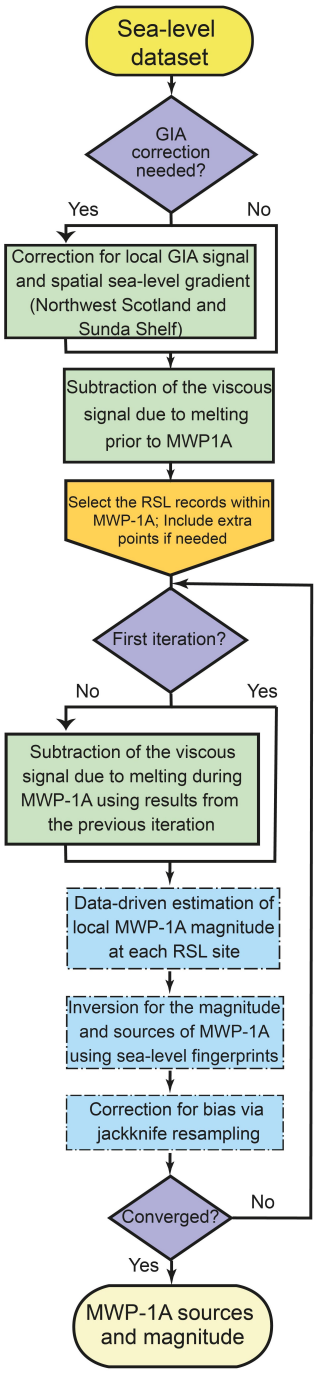

Figure S2.1: Flow chart of the iterative inversion procedure adopted in this study. Green boxes denote steps where GIA modelling is used to isolate the fingerprint signal, blue boxes represent steps in the data-driven statistical inversion, and purple boxes are conditional statements.

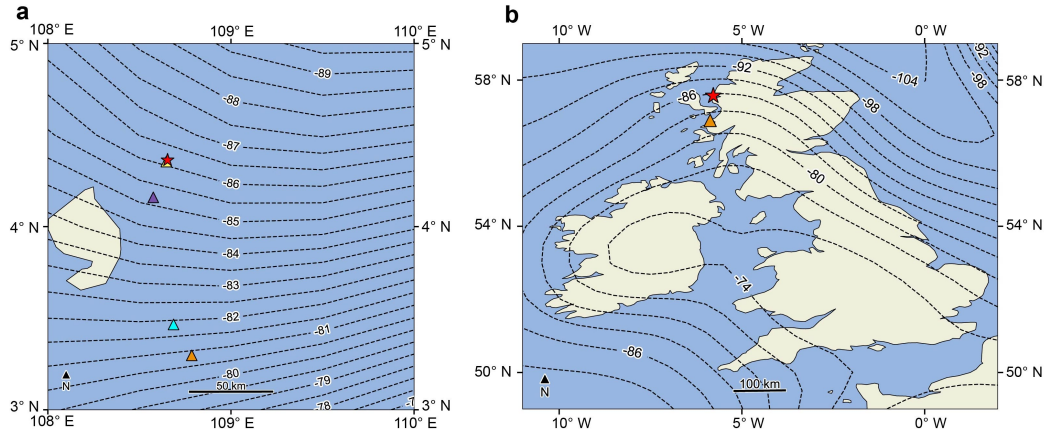

Figure S2.2: Spatial distribution of RSL across (a) Sunda Shelf (at 14.5 ka BP) and (b) Northwest Scotland (at 14.53 ka BP) due to far-field ice loss. The contour lines are determined from the mean of 240 GIA models. Red stars denote the location of site 18300 (Sunda Shelf) and site Applecross (Northwest Scotland), to which all other sites are referenced when correcting for the sea-level spatial gradient. Triangles with different colours are the different coring sites, Sunda Shelf: site 18301 (yellow), site 18302 (purple), site 18309 (cyan) and site 18308 (orange); Northwest Scotland: Arisaig (orange). Colours correspond to those used in Figure 2.2c-f. The RSL prediction shown in (b) is derived using the global ice models of ICE6G_C and ANU without the British-Irish Ice Sheet component.

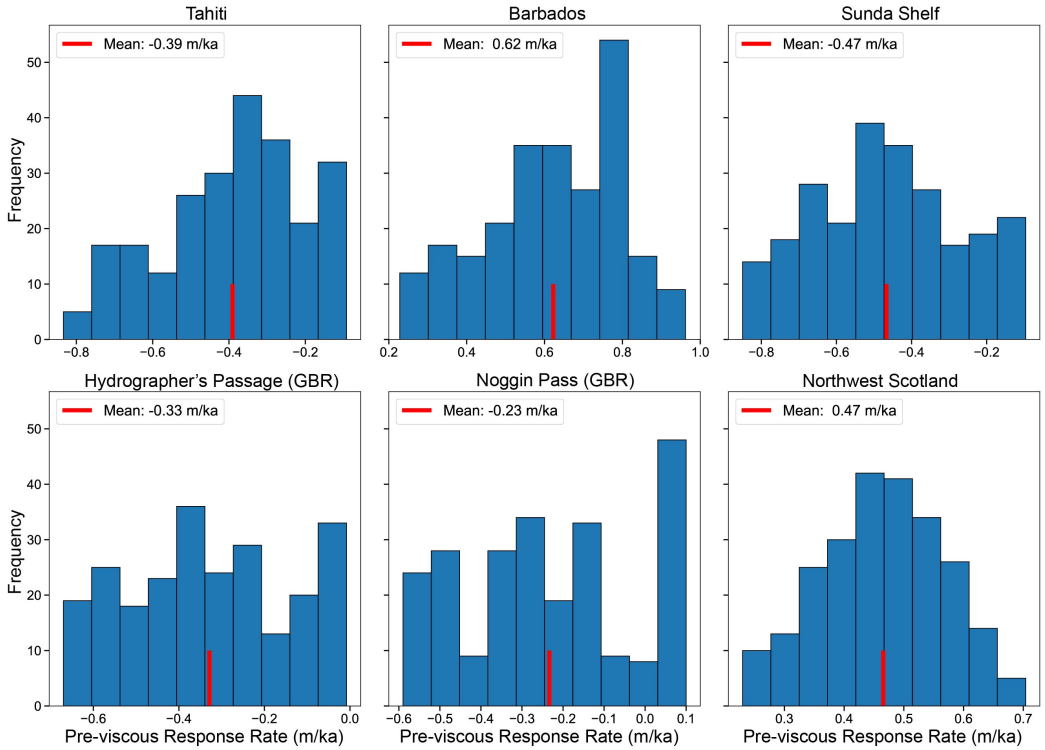

Figure S2.3: Distribution of the pre-MWP-1A viscous contribution to sea-level change at our six sites based on 240 GIA model parameter combinations.

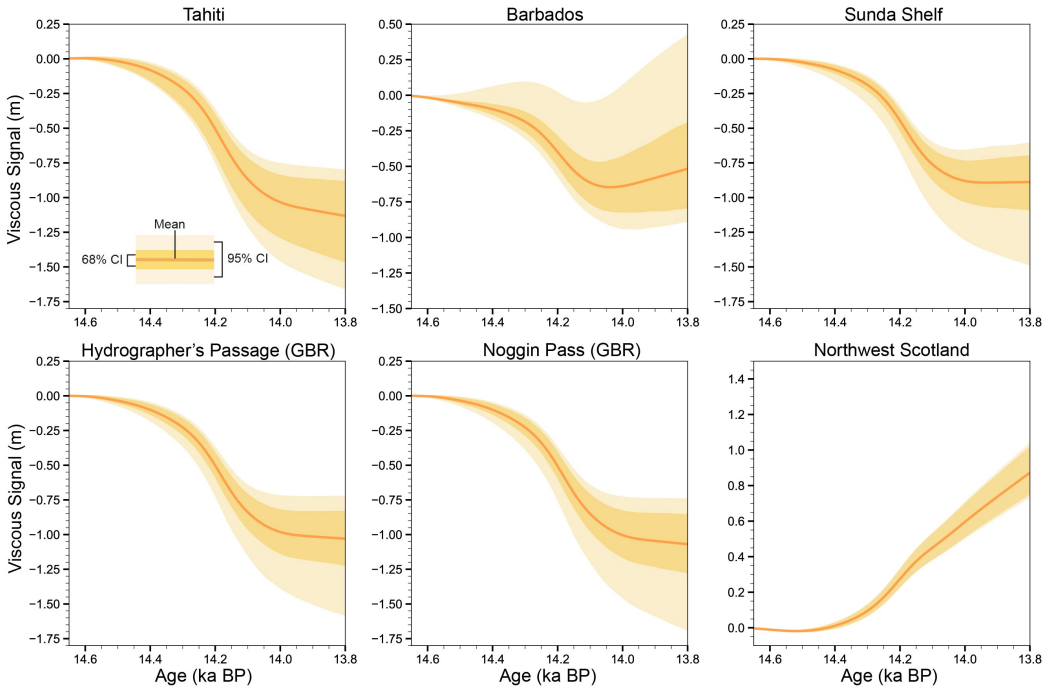

Figure S2.4: The viscous signal at our six sites due to far-field ice melt during MWP-1A. The results shown here are derived by combining 240 Earth models with the MWP-1A ice melt geometries determined by the ensemble mean of our final iteration: 13.1 m NAIS, 1.5 m AIS, and 3.3 m SIS (see section 2.5). CI = confidence interval.

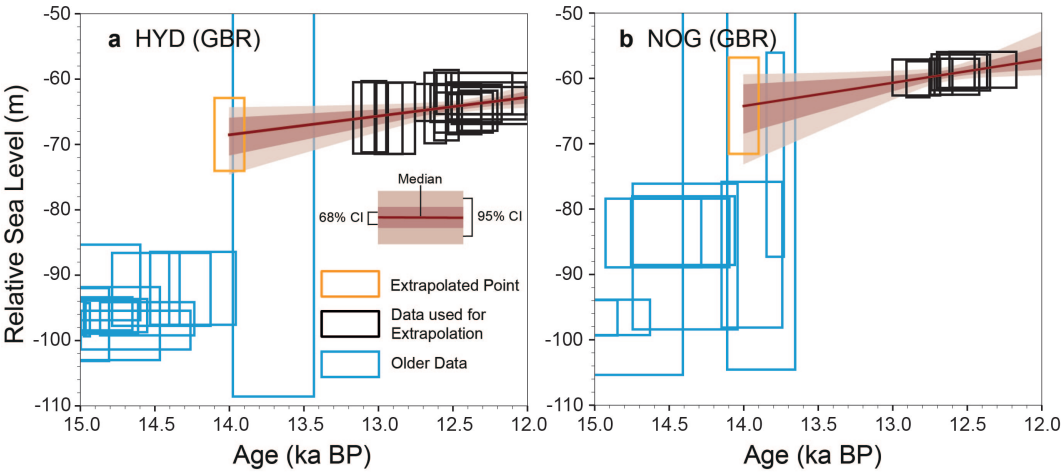

Figure S2.5: Extrapolation of relative sea-level at (a) Hydrographer's Passage and (b) Noggin Pass backwards in time using Monte Carlo linear regression and the uniform scenario for coral-based index points. The sea-level index points are plotted as error boxes indicating the depth range and 2σ age uncertainty. The orange square denotes the extrapolated 2σ depth and age uncertainty.

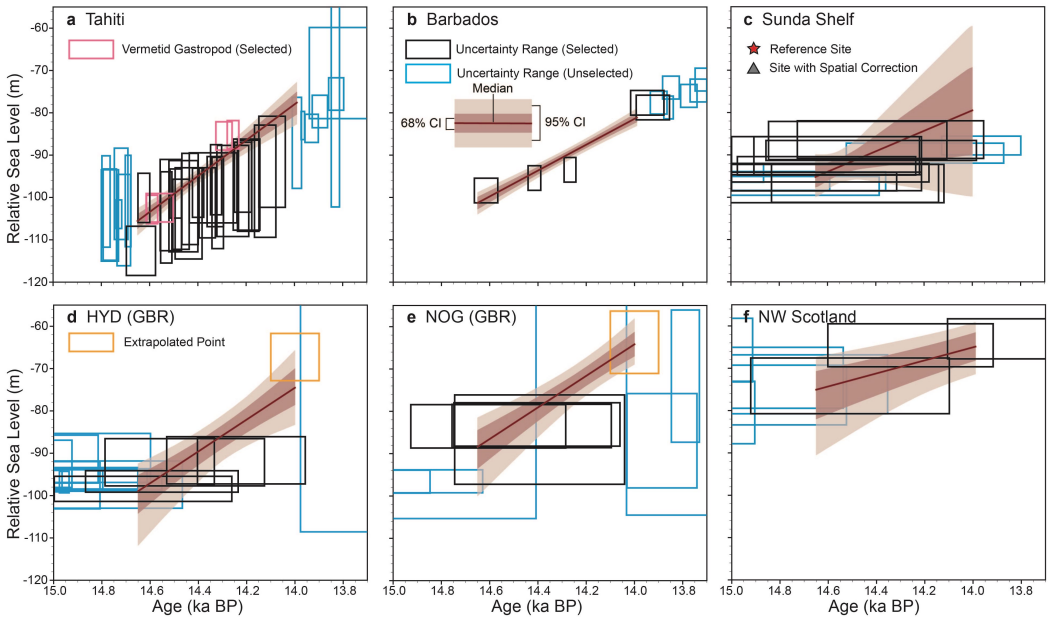

Figure S2.6: Same as Figure 2.2 but using the uniform distribution scenario for coral sea-level indicators.

S2.1 Local GIA Signal in Northwest Scotland

The effects of the local GIA signal caused by variations of the British-Irish Ice Sheet (BIIS) are shown in Figure S2.7. We computed the likely range of the local GIA signal by combining three BIIS ice history models with 120 Earth models (Figure S2.7d-f). By subtracting the mean of the GIA ensemble from the original RSL reconstructions (blue error bars), the non-local ice-sheet induced sea-level rise signal in Northwest Scotland can be obtained (black error bars). These corrected RSL reconstructions are input into the Monte Carlo linear regression and used to estimate the local MWP-1A magnitude (Figure S2.7g-i). There are clear differences between the GIA signals associated with the three BIIS models (up to 15 m) due to differences in local ice thickness and timing of deglaciation (see original publications, Lambeck, 1993; Lambeck et al., 2014; Patton et al., 2016, 2017; Bradley et al., 2018, for details). However, these differences do not impact on our estimate of the local MWP-1A magnitude because this only depends on the gradient of the local GIA signal between the initiation and termination of MWP-1A, which is similar for all three ice models. Consequently, the three ice models result in similar values for the local MWP-1A magnitude (Figure S2.7g-i).

Figs. S2.7g-i show the distributions of the local MWP-1A magnitude estimations produced by carrying out 3,000 Monte Carlo linear regression iterations for each of ice/Earth model combination (white histograms). For each ice model, the distribution of the median result for each Earth model is shown in blue. The uncertainty associated with the choice of Earth model ($\sim$0.5 m) is much smaller than that associated with the choice of ice model, which contributes to up to $\sim$2 m difference.

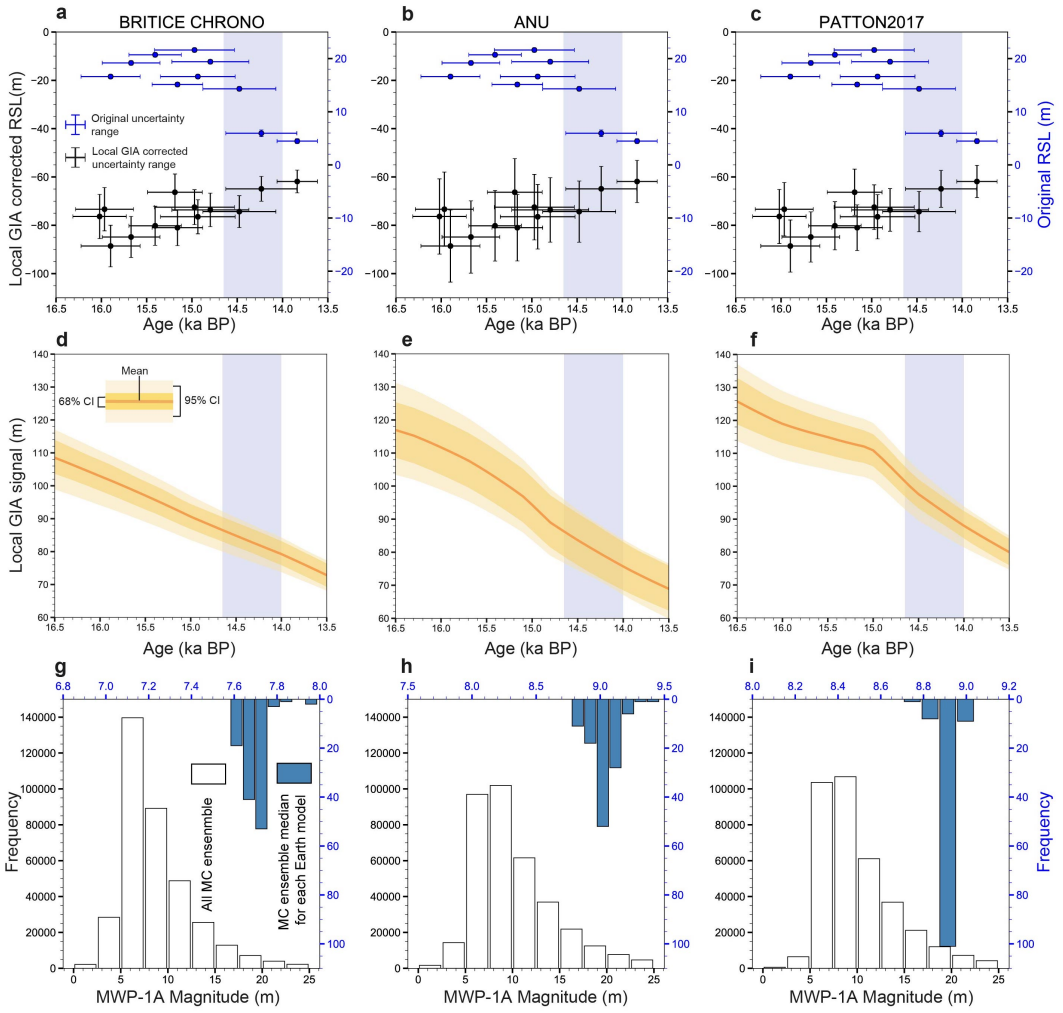

Figure S2.7: Local GIA signal correction and MWP-1A magnitude estimates using three different British-Irish Ice Sheet reconstructions (Bradley et al., 2018; Lambeck et al., 2014; Patton et al., 2017). (a-c) Blue error bars represent the original RSL reconstructions from sites Applecross and Arisaig (Shennan et al., 2018), corresponding to the blue axis shown on the right side of the figure. Black error bars represent the local GIA-corrected RSL reconstructions, with vertical error bars reflecting the uncertainty associated with 120 Earth models (index points from Arisaig have been corrected for spatial sea-level gradient), corresponding to the black axis. (d-f) Uncertainty range of the local GIA signal at Arisaig, determined using 120 Earth models. (g-i) Histograms of local MWP-1A magnitude estimates derived by combining 120 Earth models with each of the three BIIS models. After applying the local GIA signal correction associated with each Earth model, 3,000 iterations of Monte Carlo (MC) linear regression are applied to obtain ensembles of the local MWP-1A magnitude assuming a 500-year duration. A total of 360,000 outputs are shown in each the white histogram (left, black axis). For each Earth model, we calculate the median value of the associated 3,000-member ensemble and combine the results in the blue histograms (right, blue axis).

S2.2 Jackknife Resampling - Robustness of Results

The degree to which our inversion results depend on the choice of RSL sites is assessed by jackknife resampling, which also reveal each site's contribution to the final inversion result. The inversion is repeated six times, each time removing one site from the six-site database. The results (shown in Figure S2.8) are generally consistent, pointing to a dominant NAIS contribution, except for the result obtained by excluding Barbados (third panel in Figure S2.8). When Barbados is excluded, Northwest Scotland becomes the only site that is sensitive to the source of meltwater (all other far-field sites are insensitive; see Figure 2.1). Under this circumstance, due to the proximity of Northwest Scotland to the SIS, the Northwest Scotland MWP-1A magnitude predominantly determines the SIS inversion with the contributions from the NAIS and AIS essentially unconstrained, resulting in large uncertainty ranges (third panel in Figure S2.8). Another important feature is that excluding Northwest Scotland causes the melt contribution from the NAIS to become very large and the contribution from the SIS to become very small. The reason for this is similar, excluding Northwest Scotland leaves Barbados as the only site that is sensitive to the source of meltwater. Since Barbados is mainly sensitive to sources from the NAIS and AIS (main text Figure 2.1), it is possible to partition the contribution from the NAIS and AIS, but not from the SIS. These two features are also reflected in the feasible distributions of our final inversion results shown in Figure S2.9 (same distribution as shown in 2.5 but different data representation). It is clear that the NAIS and AIS contributions to MWP-1A are strongly negatively correlated (R = -0.96), reflecting the Barbados sensitivity to the contributions from these two ice sheets. In contrast, the SIS contribution shows a weak correlation to the NAIS and AIS contributions (R = -0.30 and 0.28), indicating that the inverted SIS contribution is primarily dependent on the isolation basin stratigraphy evidence from Northwest Scotland.

We seek to resolve the ambiguities indicated by the above jackknifing process by re-running the jackknife method but excluding the SIS fingerprint, to allow us to just identify the partitioning of the NAIS and AIS contributions, which were mostly debated to be the dominant source of MWP-1A (Weaver et al., 2003; Peltier, 2004;

Bassett et al., 2005; Deschamps et al., 2012; Gregoire et al., 2012; Tarasov et al., 2012). The results of this test are shown in Table S2.1, which indicates a stable solution with a dominant NAIS source (∼15.5 m) and a small Antarctic contribution (∼2 m). This result provides robust evidence for a NAIS dominant scenario rather than an AIS dominant scenario. However, to obtain a similarly stable jackknife result when inverting sources from three ice sheets, at least one more sea-level data site at a location that is sensitive to the MWP-1A sources is needed.

Sea-level index points from the Argentine Shelf could provide a powerful constraint since local RSL variation will be sensitive to melt from the nearby AIS. However, although shell sediment records from the Argentine Shelf have been dated through the MWP-1A interval (Guilderson et al., 2000), the indicative meaning of shell sea-level indicators remains problematic (see Guilderson et al., 2000). Additionally, RSL change on the Argentine Shelf will be influenced by variations in the adjacent Patagonian Ice Sheet, the deglaciation history of which, though improved by a recent glacial geomorphology data compilation of Davies et al. (2020), has not yet been calibrated with sea-level data. Sea-level index points from locations such as Bonaparte Gulf (Yokoyama et al., 2000; Ishiwa et al., 2019) and Echigo Plain, Japan (Tanabe et al., 2009) are also dated to across MWP-1A, but due to the lack of temporal resolution and their insensitivity to the sources of MWP-1A, they are not particularly useful for our fingerprinting technique. Lastly, using the local GIA correction method introduced in this study, it would be possible to use other near-field sea-level constraints for MWP-1A source inversion (e.g., records from southwest Norway (Vasskog et al., 2019)). However, estimating the local GIA signal requires a well-studied local deglaciation history and sufficient temporal resolution during MWP-1A, which currently is only achieved in Northwest Scotland.

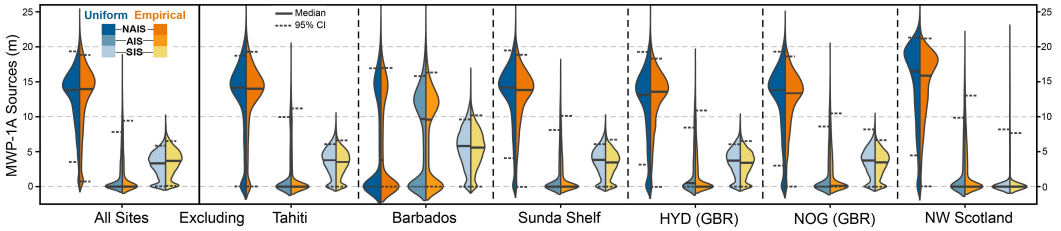

Figure S2.8: A violin plot showing the jackknife resampling results. The first panel shows the MWP-1A source inversion results obtained using all six sites in the database, and the second to seventh panel show the results when excluding each named site from the six-site database. Each panel consists of three violin plots, corresponding to the contribution from each ice sheet: NAIS, AIS, and SIS. The blue/orange tone of the violin plot indicates the result generated using the uniform/empirical scenario for coral records.

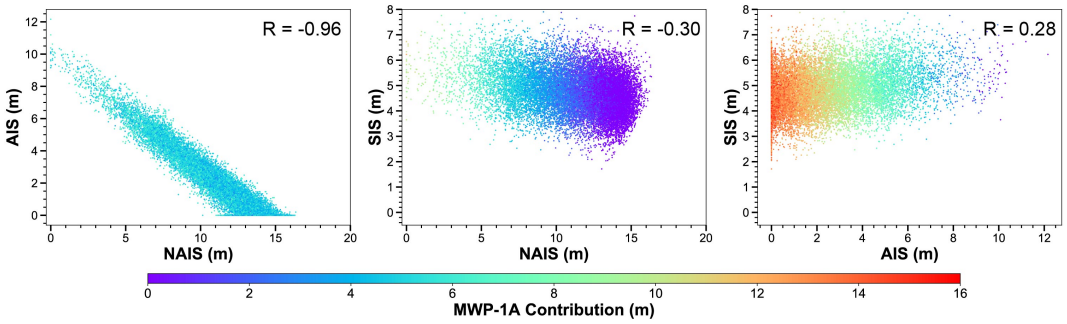

Figure S2.9: Feasible distributions of the averaged inversion result of the empirical and uniform scenarios after applying the sea-level oscillation limit. This is an alternative representation of the information shown in Figure 2.5 of the main text. Each scatter point represents an inversion result from one of 20,000 MC simulations. In each plot, the MWP-1A contribution of the ice sheet that is not listed on the x and y axes is represented by the colour of the dots. The correlation coefficient of each scatter plot is listed within the plot.

Excluded Site	NAIS (m)	AIS (m)
Tahiti	15.48 [10.10-19.61]	2.16 [0-6.13]
Barbados	15.98 [11.52-19.40]	1.26 [0.00-4.31]
Sunda Shelf	15.84 [11.52-19.40]	2.03 [0.00-5.25]
Hydrographer's Passage	14.68 [9.24-18.92]	2.64 [0.00-6.74]
Noggin Pass	15.21 [10.42-19.18]	2.34 [0.00-6.01]
NW Scotland	14.36 [7.61-19.73]	3.83 [0.00-9.10]
Bias-Contained Result	15.57 [11.03-19.28]	2.16 [0.00-5.63]
Jackknife Average	15.26 [11.12-19.05]	2.38 [0.00-4.83]
Bias-Corrected Result	15.89 [11.38-19.60]	1.95 [0.00-5.41]

Table S2.1: Table of jackknife resampling results for the empirical distribution scenario, excluding the Scandinavian Ice Sheet contribution. Rows with site location shown on the left document the inversion results when that site is removed from the six-site database. The last three rows show the bias-contained inversion result, the averaged results of the six jackknife tests, and the bias-corrected result, respectively. The first value in each box is the ensemble mean value of 20,000 iterations of the inversion process, the values in square brackets are the 68% confidence interval.

S2.3 Isolation Basin Evidence

This section provides detailed interpretations of Scottish isolation basin stratigraphy to support the definition of the 'sea-level oscillation limit' used in the main text.

In addition to providing sea-level index points, the isolation basin records from Northwest Scotland provide a unique insight into the magnitude and sources of MWP-1A due to their near-field location and the wealth of information contained within the sedimentation staircase (Shennan et al., 2000). Prior to MWP-1A, the dominant signal recorded by Northwest Scotland sea-level index points is uplift-induced sea-level fall triggered by local ice loss. With this continuous sea-level fall, some basins that were originally connected with the ocean would become isolated. This process is represented by a sediment phase transition from a marine phase (silt/clay) to a freshwater phase (organic mud and peat, Figure S2.10a). During MWP-1A, if the rate of sea-level rise due to melt from the NAIS, AIS and SIS outpaced the local rate of land uplift, it would cause isolation basins in the right height window to reconnect to the ocean, resulting in two isolation events (i.e., marine-freshwater-marine-freshwater, so-called sea-level oscillation), which should be recorded by sediment stratigraphy (Figure S2.10b). However, for all isolation basins at four sites across Northwest Scotland (Applecross, Arisaig, Kentra and Kintyre; main text Figure 2.4g) that were isolated shortly before or during MWP-1A, there is no sea-level oscillation recorded (Figure S2.11 and S2.12). These records therefore provide strong evidence that during MWP-1A the rate of sea-level rise in Northwest Scotland due to far-field ice melt cannot have significantly outpaced the local land uplift rate (i.e., there was no or only a very minor RSL oscillation, Shennan et al., 1994, 1996; Shennan, 1999; Shennan et al., 2000, 2006).

This condition is met by our MWP-1A source partition, the RSL predictions generated by the ANU_MWP ice model (Figure S2.11a,b and S2.12a,b) show a monotonic sea-level fall across MWP-1A and provide good fit to SLIPs at different periods for Arisaig, Kentra and Kintyre. The only minor sea-level oscillation occurs at Applecross where local RSL is underestimated, indicating the adopted ice thickness in this region is too thin in the ANU_MWP ice model.

We place an upper bound on the rate of land uplift (i.e., sea level oscillation limit) at Arisaig during MWP-1A by identifying the largest rate predicted by combining the ANU and BRITICE-CHRONO ice models with 120 Earth models that closely reflect mantle properties beneath the British Isles (Bradley et al., 2009). The maximum rate produces 9.8 m uplift in 500 years obtained by combining the ANU model with the weakest upper and lower mantle model of $4/100 \times 10^{20}$ Pa s, respectively. The PATTON2017 model may produce a larger land uplift rate, but it has not been calibrated to any sea-level records across Scotland and therefore the resulting land uplift rate is less meaningful as a constraint for MWP-1A magnitude.

Several previous studies have used isolation basin evidence to constrain the MWP-1A magnitude and sources (Shennan et al., 1997, 2006, 2018; Liu, 2013). When a regional BIIS model is combined with a global ice model (e.g., a revised version of the model of Bassett et al., 2005) with a dominant AIS contribution to MWP-1A (Bradley et al., 2011; Kuchar et al., 2012), this results in a strong sea-level oscillation across Scotland during MWP-1A (see Figure 10 of Shennan et al., 2018). Because the idea of a substantial SIS contribution has only recently been proposed, previous studies inferred a lower global MWP-1A magnitude to avoid this RSL oscillation, but this is inconsistent with our estimations 20 m sea-level rise in the far field. One way to improve this inconsistency is to estimate MWP-1A magnitude and sources using far-field and near-field data together. Liu (2013) provides a novel method that combines isolation basin evidence with far-field sea-level records from Tahiti, Barbados and Sunda Shelf to infer the MWP-1A sources from the NAIS and AIS. However, the method adopted to remove the local GIA signal for Scotland in that study results in significant uncertainty, which makes the sea-level index points from Scotland less useful for inverting the MWP-1A sources. Liu (2013) therefore was not able to exclusively rule out either a small or large Antarctic contribution.

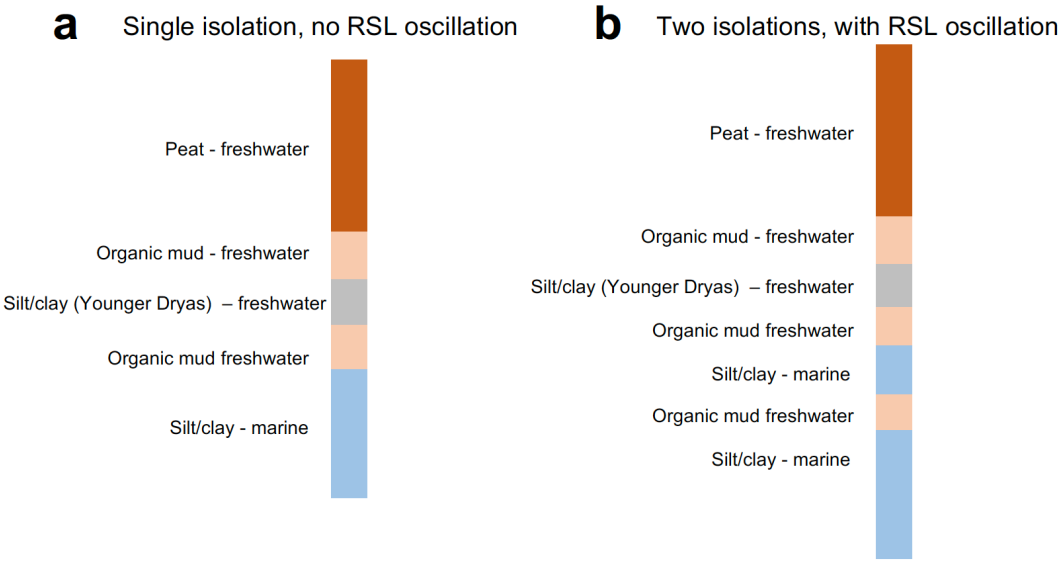

Figure S2.10: Two stratigraphy models of the isolation process. (a) A single isolation process model, indicating no RSL oscillation across MWP-1A; (b) A double isolation process model, indicating an RSL oscillation across MWP-1A.

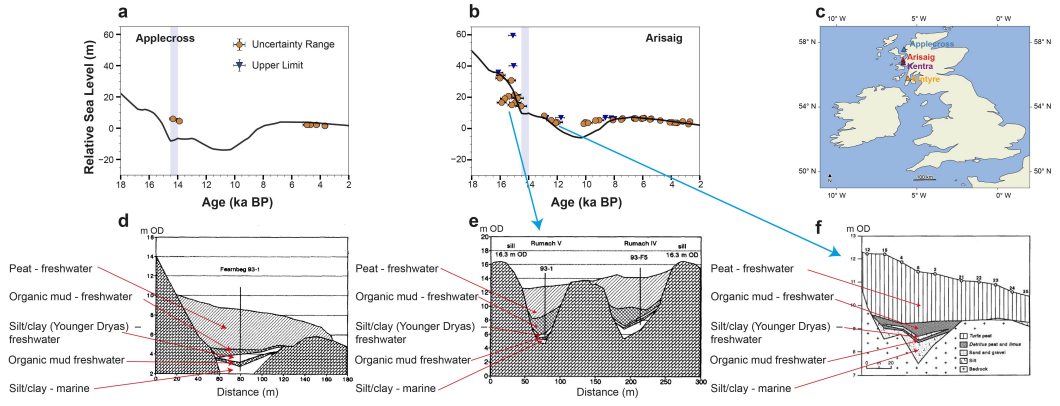

Figure S2.11: Relative sea-level predictions generated using the ANU_MWP model (with optimum Earth model of 65 km lithospheric thickness, $4/200 \times 10^{20}$ Pa s upper/lower mantle viscosity) and isolation basin stratigraphy reconstructions at Applecross and Arisaig, Northwest Scotland. (a,d) RSL prediction and stratigraphy reconstruction at Applecross; (b,e,f) RSL prediction and stratigraphy reconstructions at Arisaig; (c) locations of four Scottish sites, Applecross (blue), Arisaig (red), Kentra (purple) and Kintyre (orange). The stratigraphy figures are reproduced from Shennan et al. (1997, 1993). OD = Ordnance Datum.

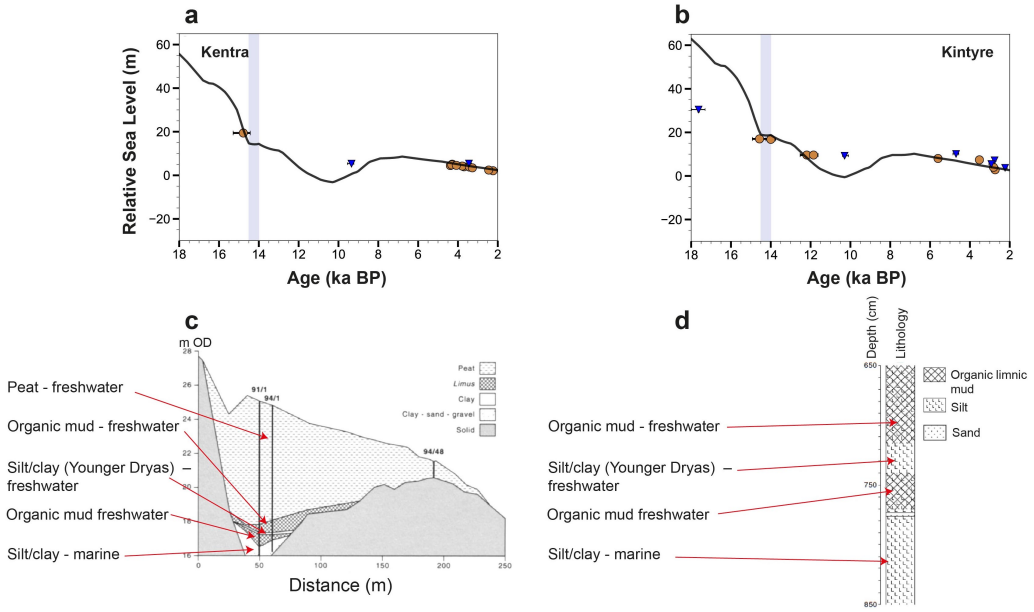

Figure S2.12: Relative sea-level predictions and isolation basin stratigraphy reconstructions at (a,c) Kentra and (b,d) Kintyre, Northwest Scotland. The stratigraphy figures are reproduced from Shennan et al. (1996, 2006). OD = Ordnance Datum.

Ice Sheet	Method	Duration (yrs)	MWP-1A Contribution (m)	Reference
NAIS	Data-driven inversion with GIA modelling	500	5.6-15.4	this study
NAIS	Ice area-volume transition	800	6.7 – 8.7 (SLE)	Carlson and Clark (2012)
NAIS	GIA analysis (ICE-5G)	500	20-20.5	Peltier (2004)
NAIS	GIA analysis (ICE-6G_C)	500	16.5-18	Peltier et al. (2015)
NAIS	3D glacial systems model	500	7.7-10.2	Tarasov and Peltier (2006)
NAIS	Revisited glacial systems model with Bayesian style calibration	500	9.4-13.2	Tarasov et al. (2012)
NAIS	Saddle collapse ice dynamic	340 (500)	5.7-11 (10.4)	Gregoire et al. (2012, 2016); Gomez et al. (2015)
NAIS	GIA and tilting of glacial lake shoreline analysis	600	$\sim$ 18.7	Lambeck et al. (2017)
AIS	Data-driven inversion with GIA modelling	500	0-5.9	this study
AIS	GIA analysis (ICE6G_C)	500	1.5-2	Argus et al. (2014)
AIS	Global sea-level budget analysis	500	$\sim$0.5	Lambeck et al. (2014)
AIS	Ice sheet dynamic modelling	500	0.5/1.5 (W12/W12 S2)	Whitehouse et al. (2012a,b)
AIS	Ice sheet dynamic modelling forced by output from an earth system modelling	500	Up to 2	Golledge et al. (2014)
AIS	Coupled ice-sheet and sea-level modelling	340	1.0-2.0 (SLE)	Gomez et al. (2020)
AIS	GIA analysis of far-field sea-level data within a Bayesian framework	340	Either 4.1-10 or 0-6.9	Liu et al. (2016)
AIS	GIA analysis of far-/near-field sea-level data within a Bayesian framework	340	Either 5-10 or 2-7	Liu (2013)
AIS	GIA analysis of far-field sea-level data	340	At least 7	Deschamps et al. (2012)
AIS	GIA analysis of far-field sea-level data	1000	Preferably 15	Bassett et al. (2005)
SIS	Data-driven inversion with GIA modelling	500	3.2-6.4	this study
SIS	Thermomechanical ice modelling	340	2.5 (SLE)	Patton et al. (2016, 2017)
SIS	GIA analysis (ICE-6G_C)	500	3.5-4	Peltier et al. (2015)
SIS	GIA analysis	500	0.8-1	Lambeck et al. (2014)
SIS	Compilation of large geomorphological dataset; ice area-volume transition	500	1.7-2	Hughes et al. (2016)
SIS	Chronological reinterpretation of SIS ice sheet margin; ice area-volume transition	500	4.5-7.9 (SLE)	Brendryen et al. (2020)
SIS	Ice area-volume transition	1000	4.1-5.7 (SLE)	Carlson and Clark (2012)

Table S2.2: Estimates of the contribution of each ice sheet to MWP-1A. NAIS = North American Ice Sheet; AIS = Antarctic Ice Sheet; SIS = Scandinavian & Barents Sea Ice Sheet. Estimates derived using the ice area-volume transition method are presented in sea-level equivalent (SLE), which includes the contribution from ice that lies below hydrostatic equilibrium (which will not contribute to global sea-level rise); other estimates reflect the eustatic sea level contribution.

Ice Sheet	NAIS[a]	NAIS	NAIS	NAIS	WLIS	ELIS	SIS[a]	SIS	SIS[b]
Ice Model	ANU (Lambeck et al., 2017)	ICE6G_C (Peltier et al., 2015)	GLAC_1D (Tarasov et al., 2012)	G12 (Gregoire et al., 2012; Gomez et al., 2015)	ICE6G_C (Peltier et al., 2015)		BRITICE CHRONO (Bradley et al., 2018)	PATTON2017 (Patton et al., 2017)	PATTON2017 (Patton et al., 2017)
Sea-level fingerprint value									
Tahiti	1.21	1.21	1.22	1.24[c]	1.27	1.19	0.98	0.98	0.99
Barbados	0.82	0.79	0.81	0.85[c]	0.96	0.69	0.97	0.97	0.97
Sunda Shelf	1.08	1.08	1.09	1.09[c]	1.11	1.08	1.00	0.99	1.00
HYD	1.04	1.03	1.04	1.07[c]	1.12	1.00	0.97	0.97	0.98
NOG	1.03	1.02	1.03	1.06[c]	1.10	0.99	0.96	0.97	0.98
NW Scotland	0.75	0.75	0.79	0.82[c]	0.93	0.64	-0.74	-0.76	-0.60
Inversion results									
Total (m)	17.9 [15.6-20.3]	18.1 [15.7-20.6]	17.7 [15.6-20.3]	17.6 [15.4-19.4]	18.1 [15.3-21.3]		17.9 [15.6-20.3]	17.9 [15.6-20.3]	17.8 [15.6-20.3]
NAIS (m)	13.1 [6.0-18.3]	12.9 [5.3-18.0]	12.7 [5.6-17.8]	12.7 [5.8-17.4]	4.4 [0-12.5]	8.7 [0-16.8]	13.1 [6.0-18.3]	13.1 [6.0-18.3]	12.8 [6.0-18.1]
AIS (m)	1.5 [0-6.9]	1.7 [0-7.2]	1.5 [0-6.9]	1.2 [0-6.6]	1.5 [0-6.9]		1.5 [0-6.9]	1.5 [0-6.9]	1.4 [0-6.8]
SIS (m)	3.3 [0.5-6.0]	3.5 [0.7-6.3]	3.7 [0.7-6.4]	3.7 [0.7-6.3]	3.5 [0.4-6.1]		3.3 [0.5-6.0]	3.3 [0.4-5.9]	3.6 [0.5-6.6]

Table S2.3: Sea-level fingerprint values and inversion results associated with using different ice melt geometries. The inversion results shown here have not been constrained by the sea-level oscillation limit. For the inversion results, the first value in each box is the ensemble mean value of 20,000 iterations of the inversion process, the values in square brackets are the 95% confidence interval. WLIS = West Laurentide Ice Sheet, ELIS = East Laurentide Ice Sheet, separated by 110° W. (a) Ice melt geometries used in our inversion. (b) SIS melt geometry associated with Southern Barents Sea sector collapse. (c) Sea-level fingerprints were estimated from Gomez et al. (2015) in their Figure 2.

CHAPTER 3

Relative sea level response to mixed carbonate-siliciclastic sediment loading along the Great Barrier Reef margin

Lin, Y., Whitehouse, P.L., Hibbert, F.D., Woodroffe, S.A., Hinestrosa, G. and Webster, J.M., 2023. Relative sea level response to mixed carbonate-siliciclastic sediment loading along the Great Barrier Reef margin. Earth and Planetary Science Letters. 607, 118066. doi: 10.1016/j.epsl.2023.118066

3.1 Abstract

The continental shelf along northeastern Australia is the world's largest mixed carbonate-siliciclastic passive margin and the location of the Great Barrier Reef (GBR). Following sea-level transgression during the last deglaciation, extensive sediment was deposited along the GBR due to neritic carbonate deposition (including shelf edge reefs, Holocene reefs and *Halimeda* bioherms) and fluvial discharge of terrigenous siliciclastic sediments. Such sediment loading can alter local relative sea level (RSL) by several metres through the sediment isostatic adjustment (SIA) process, a signal that is poorly constrained at the GBR. In this study, we used a glacial isostatic adjustment (GIA) model to develop an ensemble-based sediment loading history for the GBR since Marine Isotope Stage 2 (MIS 2). A Bayesian style framework is adopted to calibrate the sediment history ensemble and GIA model parameters using a sea-level database. According to our results, 1853.7 Gt (1613.1-2078.7 Gt, 95% confidence interval) of sediment have been deposited across the GBR since MIS 2 (28 ka BP), causing spatially variable relative sea-level change with the highest magnitude (0.9-1.1 m) found in the outer shelf of the southern central GBR (18.4-21.6° S). Because the SIA-induced RSL rise is unrelated to ice mass loss, failing to correct for this signal will lead to systematic overestimation of grounded ice volume by up to $\sim 4.3 \times 10^5$ km^3 during the Last Glacial Maximum. Additionally, we found that spatial variation in sediment loading and coastal environment may explain the different RSL history documented by published fossil coral reef records from Noggin Pass and Hydrographer's Passage. These results highlight the importance of considering SIA for any postglacial sea-level studies adjacent to large sediment systems. Lastly, by quantifying both the GIA and SIA signals, we provide a spatially and temporally complete RSL reconstruction that is well-suited to be used as a boundary condition to study the evolution of the GBR shelf and slope sedimentary system.

3.2 Introduction

Located on the world's largest mixed carbonate-siliciclastic passive margin in north-eastern Australia, the Great Barrier Reef (GBR) is an ideal place to study coral reef framework development and terrigenous sediment transportation in response to sea-level variation during glacial cycles (Webster et al., 2018). To accurately understand and model the physical and ecological mechanisms behind the spatio-temporal evolution of this complex sediment system, a key boundary condition is the relative sea-level (RSL) change history, which is by far the most important driver on millennial timescales (Hopley et al., 2007; Woodroffe and Webster, 2014). Previous work suggests strong spatial variability in past RSL along this >2000 km coastline (Lambeck et al., 2002), prompting the need for a comprehensive understanding of the processes controlling sea-level change in this region. Currently, the most commonly-used physical model to explain this variability is a glacial isostatic adjustment (GIA) model, which describes the solid Earth and ocean surface response to changes in surface loading due to ice-ocean mass redistribution. Based on GIA theory, RSL recorded at the far-field location (i.e., far from previous ice sheet margins) of the GBR is primarily a function of solid Earth rheology, the change in global ice volume through time and local shelf morphology (Lambeck et al., 2014), with these factors having previously been invoked to explain different magnitudes of postglacial RSL rise (Yokoyama et al., 2006) and mid-Holocene highstand (Lambeck et al., 2002) along the GBR coastline.

However, recent coral reef records from Noggin Pass (NOG) and Hydrographer's Passage (HYD), two shelf edge sites with similar shelf morphology located 500 km apart from each other, show a consistent RSL offset (reconstructed RSL at NOG is several metres higher than HYD) during the last deglaciation (Yokoyama et al., 2018; Webster et al., 2018) which cannot be explained by a GIA model. To understand this discrepancy, an additional physical process that is able to generate metre scale regional RSL variation within a 10^3-10^5 year timescale is required. For coral reef records from a passive margin, minimally impacted by sediment compaction, the most obvious possibility is RSL change caused by sediment loading (Horton et al.,

2018). Similar to ice loading, sediment loading can lead to isostatic adjustment that changes the local geoid and deforms the land surface depending on the regional load magnitude and Earth rheology (i.e., sediment isostatic adjustment, SIA; Dalca et al., 2013). Previous studies suggest there have been more than 1000 gigaton (Gt) of neritic carbonate sediment (Hinestrosa et al., 2022; Rees, 2005) accumulated across the GBR since the Last Glacial Maximum (LGM) along with a considerable amount of fluvial discharge of terrigenous siliciclastic sediment (Salles et al., 2018). Such sediment loading could be large enough to drive localised RSL variations.

In this study, we aim to simultaneously quantify the ice, ocean and sediment loading impact on RSL variation across the GBR from Marine Isotope Stage (MIS) 2 to present. To quantify the SIA signal, we develop a GIA-model-enabled ensemble-based sediment accretion model, which allows us to reconstruct the spatio-temporal evolution of sediment deposition across the GBR. We then use a Bayesian formalism to calibrate the net RSL history predicted by the GIA and SIA models using a sea-level database. The outputs of our study are a set of high-quality predictions of RSL change and sediment deposition history, with quantified uncertainty (Figure 3.1).

3.3 Methods

The methodology for reconstructing RSL change across the GBR is comprised of three major components: GIA/SIA modelling, sediment deposition history reconstruction and statistical calibration of the first two components using a GBR sea-level database (Figure 3.1).

3.3.1 Glacial/Sediment Isostatic Adjustment Modelling

In this study, we describe RSL variation as a combined signal caused by GIA and SIA (Wolstencroft et al., 2014). We compute GIA-induced RSL change using a gravitationally self-consistent theory that accounts for migrating shorelines and Earth rotational feedback (Kendall et al., 2005; Mitrovica et al., 2005). For SIA, we

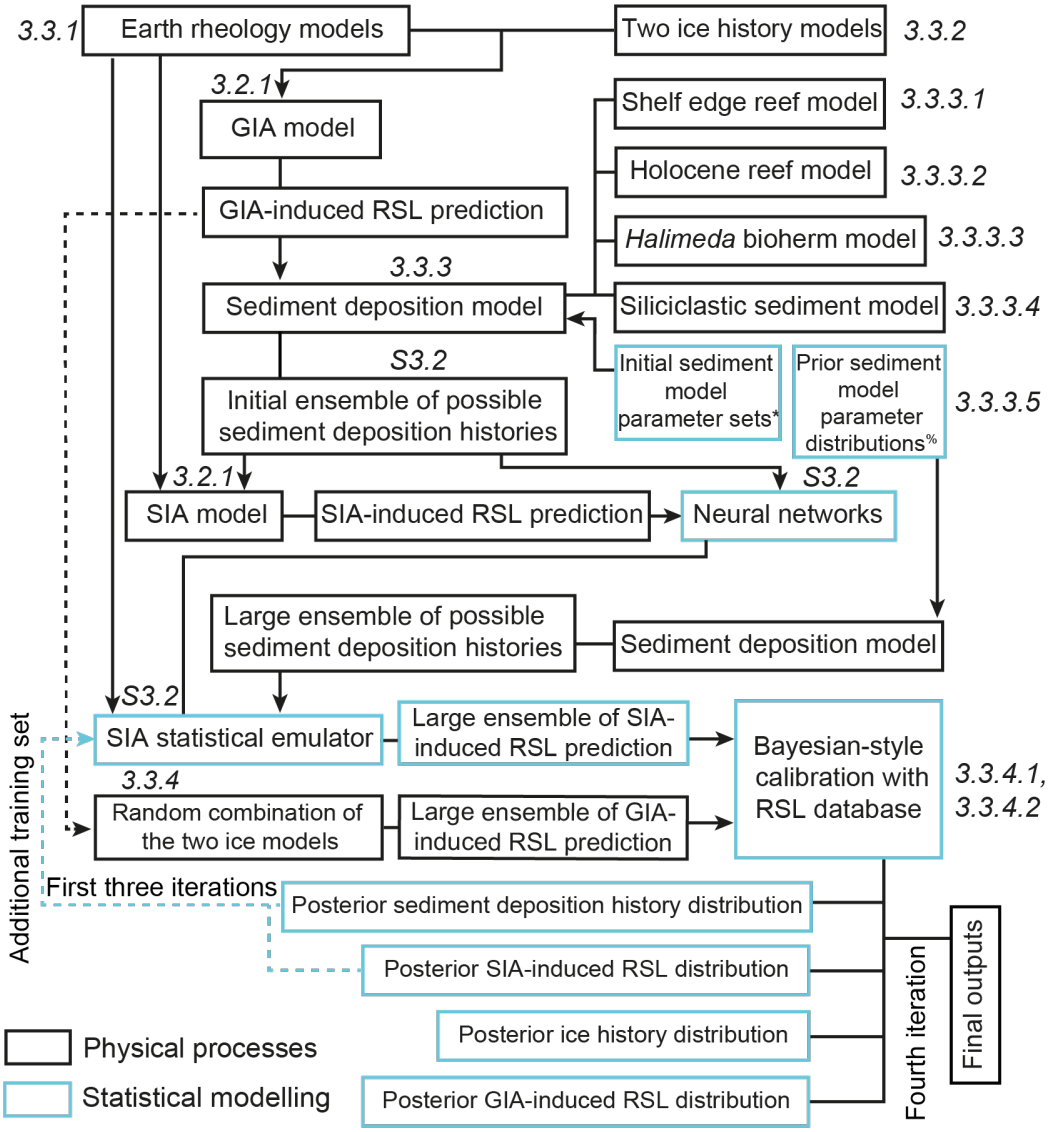

Figure 3.1: Schematic overview of the inversion procedure adopted in this study. The black and blue boxes represent the physical processes and statistical modelling processes and results, respectively. Each arrow indicates that a previous model output acts as the input for the next model. *Initial sediment model parameter sets denote six sediment parameter combinations used to generate sediment models to train a SIA statistical emulator (details in section S3.2). %Prior sediment model parameter distributions are given in Table 3.1, which can be used to create a large ensemble of random sediment models. Note the sediment deposition model appears in multiple places. The annotated italic number beside each box indicates the section that provides detailed descriptions of each modelling procedure, S2.2 indicates Supplementary section 2 (section S3.2 here).

use the methodology of Wolstencroft et al. (2014) which considers the RSL change caused by sediment-driven Earth deformation without considering the sediment

impact on geoid variation, shoreline migration and Earth rotation as they are minor signals (generally accounting for less than 5% of the total SIA caused RSL signal; Ferrier et al., 2018). Although a self-consistent GIA and SIA model has recently been developed (Ferrier et al., 2017), we do not adopt this model here because we wish to rigorously sample the GBR deposition sediment history uncertainty range independently, and solving for the gravitationally self-consistent response to both ice and sediment loading would significantly increase the required computational power.

The Earth model used in this study is represented by a spherically symmetric Maxwell body consisting of an elastic lithosphere, and an upper and lower mantle extending to 670 km and from 670 km to the core-mantle boundary, respectively. The elastic and density structure of the Earth model is derived from the Preliminary Reference Earth Model (Dziewonski and Anderson, 1981). To sample the uncertainty range associated with the rheological properties of the Earth we test lithospheric thickness values of 46, 71 and 96 km and upper and lower mantle viscosity values ranging between 0.05-1 and 1-90 $\times$ 10^{21} Pa s, respectively. The relatively thin lithosphere and weak upper mantle viscosity values that we explore reflect the values constrained by previous GIA studies of the GBR region (Ishiwa et al., 2019; Lambeck et al., 2002) and are supported by a recent global 3D mantle viscosity reconstruction (Austermann et al., 2021). In total, we test 228 Earth model combinations. We use the same Earth model for calculating GIA and SIA in order to produce internally consistent RSL predictions. We perform all calculations using a spherical harmonic truncation of degree and order 512 ($\sim$40 km), which is suitable for calculating long-wavelength (>50 km) SIA and GIA signals. The wavelength of GIA and SIA signals predominantly depends on the lithospheric thickness across the GBR, which is reported to range between 50 and 120 km from previous studies (Austermann et al., 2022; Li et al., 2018).

3.3.2 Ice Model

We use a version of the ANU ice model (denoted as ANU_LGM; Lin, 2019) that has been updated to reflect the early rapid global mean sea-level (GMSL) fall to the LGM lowstand, as revealed by sea-level index points (SLIPs) from NOG and HYD (Yokoyama et al., 2018; Webster et al., 2018). We assume that the majority

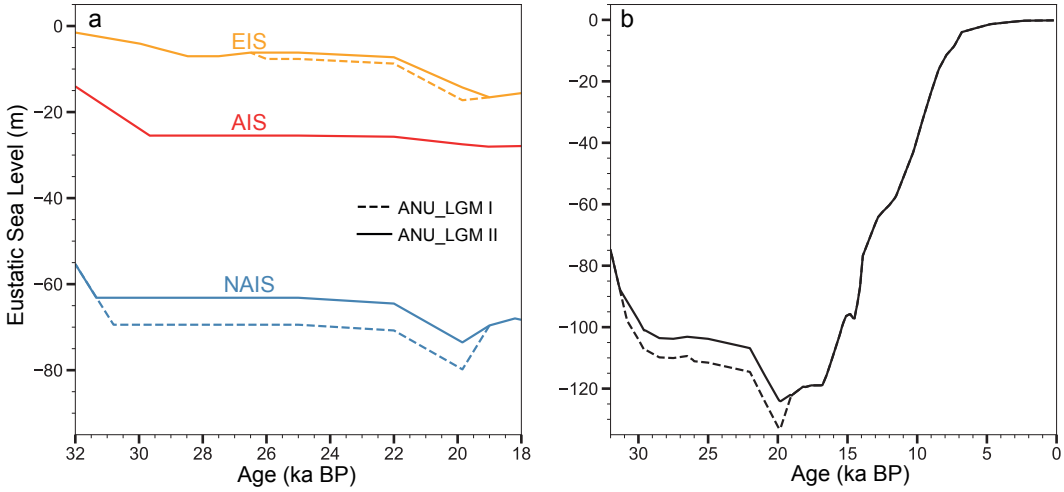

Figure 3.2: Ice history modifications. (a) Pre-LGM ice history modifications for three ice sheets. (b) Modified global ice histories. The dashed and solid lines indicate the scenarios I and II we tested in this study. Note we use the same Antarctic model for both ice loading scenarios. NAIS = North American Ice Sheet; AIS = Antarctic Ice Sheet; EIS = Eurasian Ice Sheet.

(90%) of this GMSL fall was caused by rapid growth of the North American and Eurasian Ice Sheets (Figure 3.2), possibly due to the saddle merger mechanism (Ji et al., 2021). Because GMSL prior to the LGM is poorly-constrained, we test two possible ice loading scenarios, corresponding to a 134 m (scenario I; Lambeck et al., 2014) and a 125 m (scenario II; Yokoyama et al., 2018) GMSL lowstand, which can considered as two end-member scenarios of the LGM GMSL lowstand.

3.3.3 Sediment Model

To reconstruct a complete sediment history for the GBR, we divide its sediment system into four domains: shelf edge reef, Holocene reef, *Halimeda* bioherms (the first three are carbonate sediment) and siliciclastic sediment (Figure 3.3). We then use 456 GIA-induced RSL histories (produced by combining 2 ice models with 228 Earth models) to force simple linear accretion models and reconstruct the sediment history for each domain as an ensemble (Figure 3.1). Sediment accretion is first reconstructed at high spatial resolution by combining the RSL predictions with a 100 m resolution modern GBR digital elevation model (DEM, Beaman, 2010) to create a series of palaeo-DEMs, and hence determine the detailed spatial evolution of

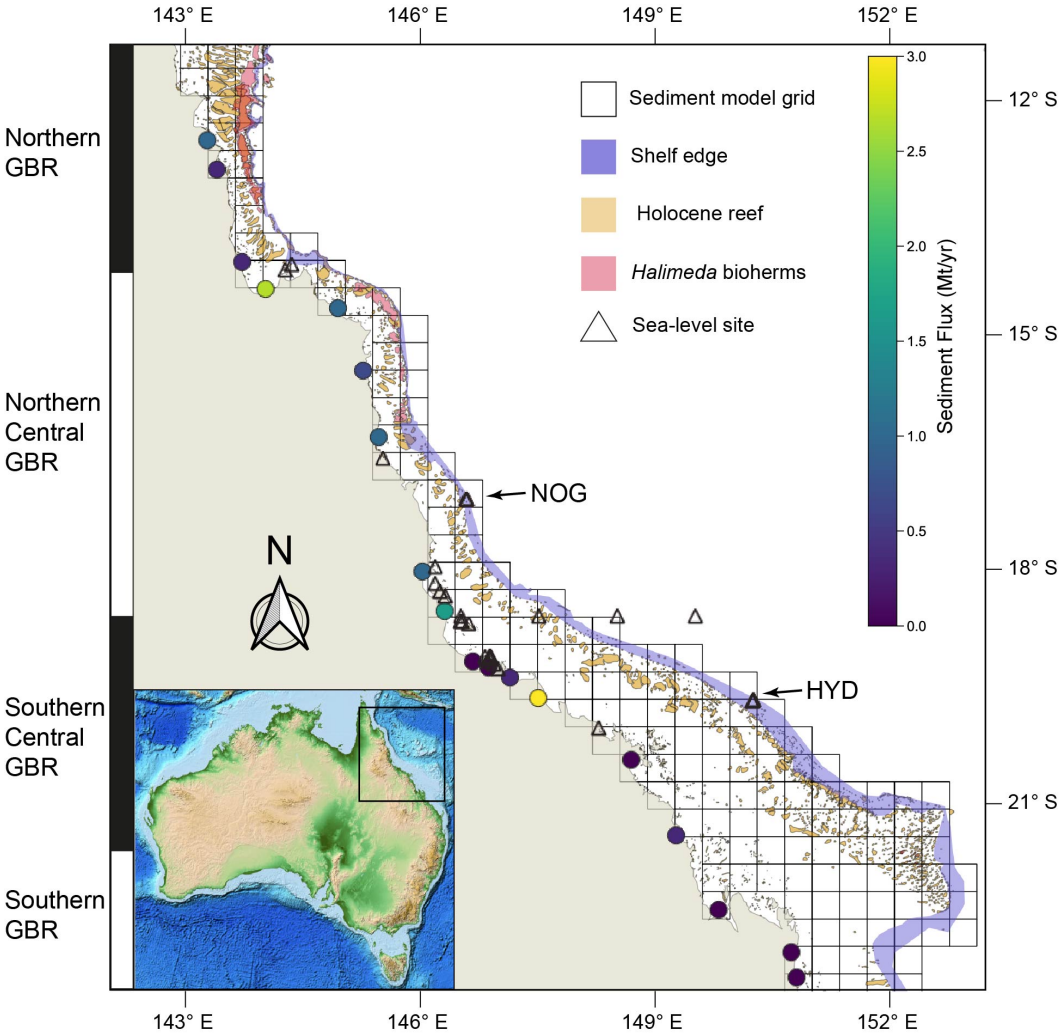

Figure 3.3: Overview of four sediment domains. The orange polygons indicate the locations where Holocene reefs accumulate. The purple polygons outline the domains where shelf edge reefs are likely to have accumulated (shelf edge reefs have not yet been fully mapped along the GBR margin). In the northern GBR, pink polygons show the locations of *Halimeda* bioherms. Coloured dots along the modern coastline indicate the rate of present-day fluvial sediment discharge (Milliman and Farnsworth, 2013). The black triangles are the RSL site locations used to calibrate the sediment loading history. The zebra boxes on the left indicate the four latitudinal GBR regions defined in 3.3.3.5. The sediment loading grid is indicated by the black squares.

inundation and sediment accretion. For the purposes of calculating the SIA response, net sediment load in each ~40 km grid cell of our study region is then summed to produce a loading time series. We do not consider the influence of hydrodynamic effects on sediment distribution because short-wavelength variations in surface load (typically sub-kilometre scale; Dean and Dalrymple, 2004) will have a relatively minor

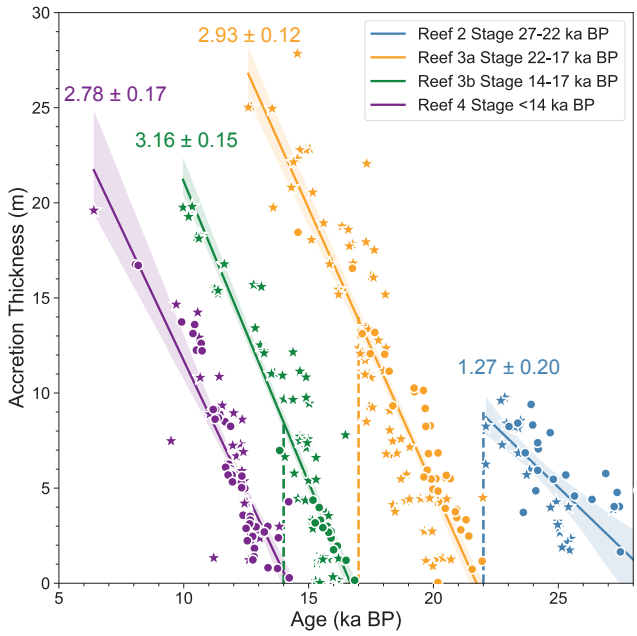

Figure 3.4: Determination of vertical accretion rates across the shelf edge reef. Vertical dashed lines are cut-off ages, used to determine which stage of reef is being formed (see section 3.3.3.1). The linear accretion rate of each reef sequence is given with 1σ uncertainty. The stars and dots indicate data from Hydrographer's Passage and Noggin Pass, respectively.

effect on the SIA signal, which is long-wavelength and is spatially and temporally smooth.

3.3.3.1 Shelf Edge Reef

The shelf edge is defined as the region between the modern outer barrier reef front and the 130 m isobath (Figure 3.3, Beaman, 2010; Abbey et al., 2011). Based on the evidence derived from drill cores at NOG and HYD, the shelf edge reef growth structure can be described by four reef formation-demise sequences: reef 2 (27-22 ka BP; initiation and demise time), reef 3a (22-17 ka BP), reef 3b (17-14 ka BP) and reef 4 (14-10 ka BP; modified from Webster et al., 2018).

To reconstruct the spatio-temporal reef development, we adopt a linear accretion model from Hinestrosa et al. (2022). For this model, the averaged vertical accretion

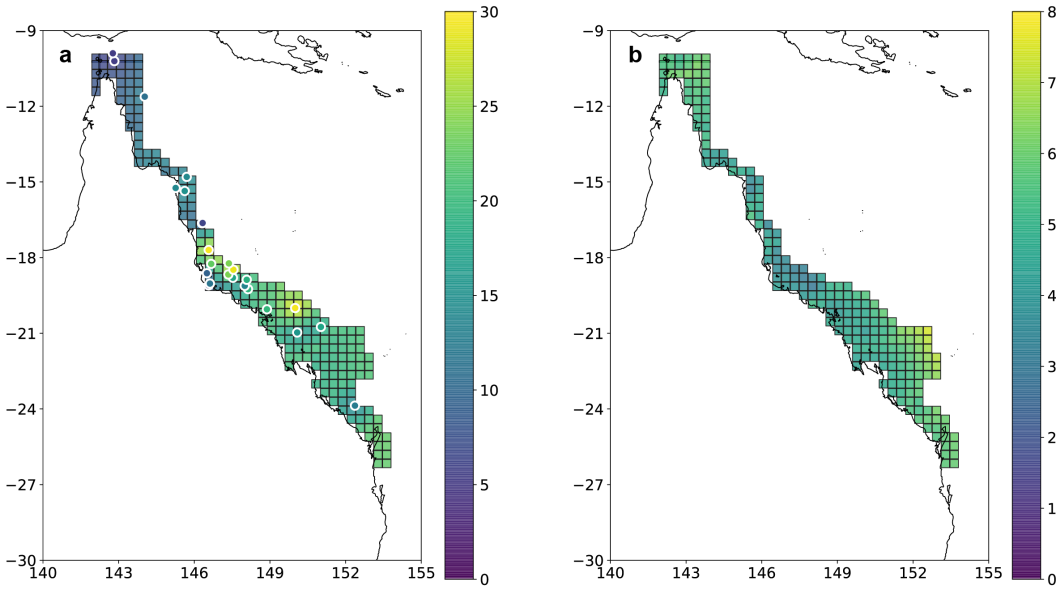

Figure 3.5: Holocene-modern reef accretion thickness kriging results. (a) Background shows the interpolated Holocene-modern reef accretion thickness for each GIA model grid, and the dots indicate the observed sediment accretion thickness from Hinestrosa et al. (2022). (b) 2σ Holocene-modern reef accretion thickness uncertainty associated with the statistical interpolation process.

rate (ν_{se}) and maximum accretion thickness (τ_{se}) are defined for each reef sequence based on the dating of drill core material from HYD and NOG (Figure 3.4). We assume each reef sequence initiates after local inundation, with a time lag (ι_{se}) of between 0 and 1 ka, and that it accumulates uniformly following the rate of ν_{se} until reaching thickness τ_{se}. The 0-1 ka lag between local inundation and reef initiation is defined based on observational evidence from Sanborn et al. (2020). Each reef within the shelf edge polygon (i.e., each DEM grid cell) is classified to one of the four reef sequences (Webster et al., 2018) based on its initiation time, which in turn determines its ν_{se} and τ_{se}. Because constraints on ν_{se} and τ_{se} are currently only available for HYD and NOG, we assume the information derived from them is representative of the southern and northern GBR, respectively.

3.3.3.2 Holocene Reef

The spatial distribution of the Holocene reef has been mapped by modern bathymetric and remote sensing surveys (http://www.gbrmpa.gov.au/). The only variable to

estimate is the spatially-variable Holocene reef accretion thickness, which will vary according to local environmental conditions (Hinestrosa et al., 2022; Hopley et al., 2007). To account for this heterogeneity, we use a kriging method (details in section S3.1) to interpolate the spatial pattern of reef accretion thickness based on a Holocene reef accretion thickness database (Figure 3.5, Hinestrosa et al., 2022). One advantage of this method is that the uncertainty estimation is included in its conceptualisation, hence the interpolation uncertainty can be easily propagated.

Next, to accurately determine the time when the local pre-Holocene substrate was flooded, we create a pre-Holocene GBR DEM by subtracting the interpolated accretion thickness from the modern DEM. We carry out calculations based on this pre-Holocene DEM. We then combine our 456 GIA-induced RSL predictions with this pre-Holocene DEM to create a series of palaeo-DEMs that can be used to determine the timing of local inundation and hence the temporal development of the Holocene reefs. Using interpolated reef accretion thickness estimates as a boundary condition, each Holocene reef is assumed to begin accumulating following local sea-level transgression, with a time lag (ι_{ho}) of between 0 and 1 ka (same as shelf edge reef), and stop accumulating when local RSL is 30 m higher than the modern reef surface (i.e., when the coral reef surface becomes too deep for significant shallow water reef growth). Where the modern water depth is less than 30 m, we assume the reef stops accumulating when local RSL first reaches its maximum value (mid-Holocene highstand or present). Between the defined starting and terminating time, reefs are assumed to grow at a linear rate depending on the interpolated accretion thickness.

3.3.3.3 *Halimeda* bioherms

Halimeda bioherms are a dominant source of inter-reef carbonate deposits for the northern GBR and have been extensively mapped (Figure 3.3, McNeil et al., 2016). McNeil et al. (2020) provide an overall estimate of 55.12 Gt of accumulation, corresponding to a 7.63 m sediment layer across all mapped regions of *Halimeda* bioherms (assumes aragonite density of 2.94 g/m^2 with 0.58 porosity, McNeil et al., 2020). As for the Holocene reef sediment model, we build a pre-Holocene DEM for the

Halimeda bioherms domain by subtracting 7.63 m from the original GBR DEM within the accumulation region (i.e., pink polygons in Figure 3.3). The temporal evolution of the *Halimeda* bioherms is then calculated using the same method as for the Holocene reef model, using a lag parameter ι_{ha}. Although previous studies suggest that other sources of carbonate sediment accumulate across inter-reef regions, such as benthic foraminifera and coralline algae (Hopley et al., 2007), at present there is no comprehensive database which documents the inter-reef carbonate thickness or mass accumulation since MIS 2. We therefore do not consider this possible source of carbonate sediment in our reconstruction.

3.3.3.4 Siliciclastic Sediment

To quantify siliciclastic load, we use a modern global database of fluvial sediment flux measurements (Figure 3.3, Milliman and Farnsworth, 2013) and assume the averaged discharge rate for the whole of the deglacial period is proportional to the modern measurement, with absolute values controlled by a scaling parameter (β) that increases/decreases the modern sediment flux by up to 40%. For each model run, the sediment discharge rate is assumed to be temporally constant. The spatial distribution of siliciclastic sediment deposition will have varied through time due to shoreline migration during postglacial sea-level change. This palaeo shoreline migration is reconstructed by combining a modern DEM with GIA-induced RSL predictions. For each model time step, sediment load is discharged to the nearest palaeo shoreline location relative to the modern river mouth position (Figure 3.3). To conserve mass, we uniformly remove a layer of sediment from the North East Coast drainage basin with a mass equivalent to the siliciclastic sediment deposition in the ocean.

3.3.3.5 Sediment Model Parameters

We use two types of parameter (pattern and magnitude) to represent uncertainties in the sediment history reconstructions. For all sediment domains, Earth and ice model parameters are the primary pattern parameters because they determine the

spatio-temporal pattern of RSL variation, and in turn the sediment accumulation pattern. Additionally, the lag parameters mentioned above (ι_{se}, ι_{ho}, ι_{ha}) allow a delay to the initiation of carbonate sediment accumulation of between 0 and 1 ka after local transgression, which provides additional control on the temporal evolution of the three carbonate sediment domains.

The magnitude parameters control the magnitude of sediment accumulation for each domain. When determining the sediment accretion thickness of the shelf edge reef, we limit the maximum reef accretion thickness for the four reef sequences using the parameters $\tau_{2,3a,3b,4}$ (Table 3.1, values are empirically derived from Hinestrosa et al., 2022). For the Holocene reef, the accretion thickness is subject to spatially variable uncertainty produced by the kriging interpolation, which is described by $\alpha_{ho}(\varphi)$, and varies from -3σ to 3σ. Lastly, the magnitude of the siliciclastic sediment load is controlled by a scaling parameter β (section 3.3.3.4).

The reconstructed sediment accumulation thickness $H(\varphi, t)$ at location φ and time t is converted to a sediment load, $M(\varphi, t)$, by:

$$M_{se}(\varphi, t) = H_{se}(\varphi, t)A(\varphi)\rho_a(1 - \phi_{se})\epsilon_{se} \tag{3.1}$$

$$M_{ho}(\varphi, t) = H_{ho}(\varphi, t)A(\varphi)\rho_a(1 - \phi_{ho})\alpha_{ho}(\varphi) \tag{3.2}$$

$$M_{hb}(\varphi, t) = H_{hb}(\varphi, t)A(\varphi)\rho_a(1 - \phi_{hb}) \tag{3.3}$$

where fixed parameters $A(\varphi)$ and ρ_a indicate bathymetric grid cell area and the density of aragonite (2.94 g/cm^3). ϕ is the averaged sediment porosity for the shelf edge (se), Holocene (ho) and *Halimeda* bioherms (hb) domains; it is allowed to vary from 25% to 45% to represent uncertainty of the overall accumulation magnitude. For the shelf edge reef, one important uncertainty is that only a minor part of our defined shelf edge area (Figure 3.3) is covered by reefal deposit, i.e., significantly thicker sediment than the surrounding area. Therefore, we assign a reefal area percentage parameter (ϵ_{se}), varying between 10-30% (derived from seismic mapping of shelf edge reef structure, Hinestrosa et al., 2016), to describe this uncertainty. Although the non-reefal area shows substantially lower sediment thickness (generally <10 m, Hinestrosa et al., 2016), it covers a much larger proportion of the shelf edge area, meaning it can potentially contribute as much sediment loading as the reefal area.

Therefore, the upper limit of ϵ_{se} is doubled (to 60%) to account for this condition. To reduce computation time, we combine $1-\phi_{se}$ and ϵ_{se} in the shelf edge reef model (as γ_{se}), and $1-\phi_{ho}$ and $\alpha_{ho}(\varphi)$ in the Holocene reef model (as γ_{ho}) together, as they are all scaling parameters.

Due to different climate, local antecedent substrate and shelf physiography, previous studies suggest a contrasting sediment deposition system between the northern and southern GBR (Hinestrosa et al., 2016). Considering this difference, we separate the whole GBR region into northern (10-14.2° S, Figure 3.3), northern-central (14.2-18.4° S), southern-central (18.4-21.6° S) and southern GBR (21.6-26.2° S) sectors based on the definition from Hinestrosa et al. (2019). All sediment parameters are allowed to vary between sectors (Table 3.1), which is indicated by the superscripts 1 (northern), 2 (northern central), 3 (southern central) and 4 (southern). We use the same prior distributions for sediment model parameters across all four regions, except the thickness parameters $\tau_{2,3a,3b,4}$; our compiled database generally shows thicker sediment in the southern GBR (HYD) compared to the north (NOG, Figure 3.4) so we use different prior distributions for these parameters in each region. The prior distributions for all sediment domain parameters are given in Table 3.1 and the resulting sediment loading history prior distributions are given in Figure S3.2.

3.3.4 Statistical Calibration

During the calibration process, to consider uncertainty associated with the poorly-constrained pre-LGM ice history, we allow the ice model to vary between scenarios I and II using a weighting parameter ω. The final RSL predictions are calculated using a weighted combination of the two ice history scenarios. ω therefore indicates the data preference for the assumed pre-LGM ice history. The data used for calibration are sea-level index points (SLIPs). Each SLIP provides information about the age and height of past RSL at a single location, which is assumed to represent the combined signal of GIA and SIA processes. Based on SLIP databases, we use a Bayesian framework to sample the posterior probability density distribution for each model parameter (Table 3.1) conditioned on sea-level data (see Figure 3.1).

Model Component	Parameters and Prior Distribution(s)	Parameter Description
Earth model	LT $\sim U$[46,71,96]	Effective lithospheric thickness with unit kilometre
	$\mu_{up} \sim U$[0.05,0.08,0.1,0.2,0.3,0.5,0.8,1]	Upper mantle viscosity with unit 10^{21} Pa s
	$\mu_{lo} \sim U$[1,2,3,5,8,10,20,30,50,70,90]	Lower mantle viscosity with unit 10^{21} Pa s
Ice model	$\omega \sim U(0,1)$	Relative weighting associated with ice loading scenario II
Shelf edge reef	$\gamma_{se}^{1-4} \sim U(0.055,0.45)$	A combined parameter that describes the uncertainty associated with shelf edge reef formation porosity and reefal area percentage
	$\tau_2^{1-4} \sim U(5,10),\ U(5,10), U(5,15), U(5,15)$	Maximum accretion thickness for shelf edge reef stage 2 with unit metre (same for all maximum accretion thickness parameters below)
	$\tau_{3a}^{1-4} \sim U(10,20), U(10,\ 20), U(15,30), U(15,30)$	Maximum accretion thickness for shelf edge reef stage 3a
	$\tau_{3b}^{1-4} \sim U(5,\ 15), U(5,15), U(10,20), U(10,20)$	Maximum accretion thickness for shelf edge reef stage 3b
	$\tau_4^{1-4} \sim U(5,\ 15), U(5,15), U(10,20), U(10,20)$	Maximum accretion thickness for shelf edge reef stage 4
	$\iota_{se}^{1-4} \sim U$[0,0.2,0.4,0.6,0.8,1]	Lag between local inundation and shelf edge reef initiation with unit ka (same for all lag parameters below)
Holocene reef	$\gamma_{ho}^{1-4} \sim U(-3\sigma,3\sigma)$	A combined parameter that describes the uncertainty associated with reef formation porosity and kriging determined reef depth uncertainty (defined by σ).
	$\iota_{ho}^{1-4} \sim U$[0,0.2,0.4,0.6,0.8,1]	Lag between local inundation and Holocene reef initiation
Halimeda bioherms	$\phi_{ha}^{1-4} \sim U(0.25,0.45)$	*Halimeda* bioherms formation porosity
	$\iota_{ha}^{1-4} \sim U$[0,0.2,0.4,0.6,0.8,1]	Lag between local inundation and *Halimeda* bioherms initiation
Siliciclastic sediment	$\beta^{1-4} \sim U(0.6,1.4)$	Averaged siliciclastic discharge rate relative to present day

Table 3.1: Table of prior sediment model parameters. We assume a uniform prior distribution for all parameters within the defined parameter space. The uniform distributions with parentheses indicate a continuous uniform distribution, those with square brackets indicate a discrete uniform distribution comprising the listed parameters. Superscripts 1 to 4 represent spatially different parameters for the northern, northern central, southern central and southern GBR.

3.3.4.1 Calibration Data

We compile a GBR RSL database following the methodology of Hibbert et al. (2018, 2016). For radiocarbon dated SLIPs we recalibrate the conventional radiocarbon age using the SHCal20 calibration curve (Hogg et al., 2020) for terrestrial samples, and Marine20 (Heaton et al., 2020) with appropriate and up-to-date local marine reservoir corrections (ΔR; http://calib.org/marine) for marine samples. For Uranium-Thorium dated coral samples we recalculate the U-series ages where necessary, assuming a closed system with the latest decay constant (Cheng et al., 2013). We only include the U-series ages that pass the age reliability screening criteria of [^{232}Th] $\leq$ 2 ppb and $\delta^{234}U_{initial} = 147 \pm 5$ ‰. We exclude any SLIPs that are explicitly stated as not being *in situ* by the original paper.

For SLIP depth uncertainty we use local palaeo-water depth determination for each record taken from original publications, assuming that the indicator may occur equally anywhere within the given upper and lower limit (i.e., the uniform distribution scenario, Hibbert et al., 2016, 2018; Lin et al., 2021). Additionally, we consider the elevation measurement uncertainty caused by coring, levelling and tectonic correction when necessary. Overall, our study uses 375 SLIPs (supplementary database; https://github.com/yc-lin-geo/GBR-Sediment/tree/main/Data). To systematically quantify the RSL difference between NOG and HYD, we use a Monte Carlo binning analysis approach to reconstruct the underlying RSL signal at these two sites. The details of this approach are given in section S3.3.

3.3.4.2 Calibration Procedure

The posterior probability distributions are calculated using a simulated annealing algorithm (Kirkpatrick et al., 1983), a probability-based technique which shows good capacity to converge to the global minimum solution. Within a Bayesian framework, a likelihood function describes the joint probability of the observed data as a function of the model parameters. We assume a uniform prior distribution for all model parameters (Table 3.1), meaning the posterior probability is equivalent to the likelihood. In this study we express the likelihood as:

$$p(y|\theta) = exp(-\frac{1}{N}\sum_{n=1}^{N} w_n J_n) \tag{3.4}$$

$$J_n = \sqrt{\frac{(RSL_n^y - RSL_n^m)^2}{\sigma_{RSL,n}^2} + \frac{(t_n^y - t_n^m)^2}{\sigma_{t,n}^2}} \tag{3.5}$$

where θ is the vector of all model parameters, y is the SLIP data set consisting of n samples, each containing information about palaeo RSL height (RSL_n^y) and age (t_n^y) with 1 sigma uncertainties of $\sigma_{RSL,n}$ and $\sigma_{t,n}$, respectively. w_n is a weighting parameter to offset calibration bias due to variable temporal data density using the definition from Tarasov et al. (2012). For each set of model parameters, and for each SLIP location, a RSL curve is produced and we calculate the minimum distance (J_n) between the SLIP and the RSL curve, where RSL_n^m and t_n^m represent the RSL and age of the closest point on the modelled curve (adapted from Love et al., 2016). The

minimum distance data-model comparison metric J provides a unitless measurement of model misfit for both chronological and vertical uncertainties. Because we assume past sea level may occur equally anywhere between the upper and lower limit of each SLIP, we assume no vertical misfit if the model predictions are within the 2 sigma uncertainty range of the observations. Therefore, we express RSL_n^y as:

$$RSL_n^y = \begin{cases} RSL_n^y + 2\sigma_{RSL,n}, & RSL_n^m \geq RSL_n^y + 2\sigma_{RSL,n} \\ RSL_n^m, & {\scriptstyle RSL_n^y - 2\sigma_{RSL,n} < RSL_n^m < RSL_n^y + 2\sigma_{RSL,n}} \\ RSL_n^y - 2\sigma_{RSL,n}, & RSL_n^m \leq RSL_n^y - 2\sigma_{RSL,n} \end{cases} \tag{3.6}$$

Based on this likelihood formulization, we calculate the posterior probability distributions for each model parameter, and to speed up the calibration process, we use a statistical emulator to emulate the SIA process. Details on the implementation of this approach are provided in section S3.2.2.

	P_{max}	Expected Value	Standard Deviation	95% Confidence Interval
LT (km)	96	89.3	11.2	71-96
μ_{up} $(10^{21} Pas)$	1	0.93	0.15	0.5-1
μ_{lo} $(10^{21} Pas)$	30	38.3	11.3	20-50
ω	1	0.98	0.06	0.9-1
$Load_{total}$ (Gt)	1939.6	1853.7	112.4	1613.1-2078.7
$Load_{se}$ (Gt)	559.1	478.8	68.9	330.8-566.3
$Load_{ho}$ (Gt)	797.6	794.2	59.3	630.0-943.4
$Load_{ha}$ (Gt)	47.0	46.7	3.8	46.7-54.1
$Load_{si}$ (Gt)	536.3	534.0	61.3	410.5-659.1
$Load^1$ (Gt)	138.1	167.8	53.1	137.1-271.9
$Load^2$ (Gt)	183.1	229.8	59.3	169.3-361.0
$Load^3$ (Gt)	1007.2	994.6	45.7	905.0-1042.2
$Load^4$ (Gt)	611.3	461.5	98.9	296.2-617.5

Table 3.2: Inversion results. P_{max} indicates the value with the maximum posterior probability (i.e., best-fit value). The load values represent the total sediment load deposited during the last 28 ka BP, subscripts and superscripts are as follows: se = shelf edge reef; ho = Holocene reef, ha = *Halimeda* bioherms, si = siliciclastic discharge, 1= northern GBR, 2 = northern central GBR, 3 = southern central GBR, 4 = southern GBR.

3.4 Results

Based on the posterior probability distributions of the model parameters drawn from the simulated annealing (Table S3.1), we calculate the spatio-temporal field of sediment accumulation and RSL variation for the GBR. We start by presenting the results of the Earth and ice model parameter inversion and describe the resulting GIA-induced RSL predictions. Using these GIA predictions, we illustrate the palaeo GBR shoreline reconstructions and quantify how they affect the sediment accumulation history. Lastly, we present the sediment loading induced RSL change and RSL model-data comparison.

3.4.1 Earth and ice model parameters

The inversion results are given in Table 3.2. For a far-field region like the GBR, post-glacial sea-level change was predominantly driven by ice-ocean mass exchange (causing >100 m RSL change compared to ∼1 m by SIA). Hence, although the Earth model parameters impact the prediction of both GIA- and SIA- induced RSL change, the Earth model parameter distributions are primarily calibrated to replicate the GIA process. The maximum probability fit to the SLIPs is achieved using an Earth model combination of 96 km (71-96 km; 95% confidence interval, CI) lithospheric thickness, and 1 (0.5-1) and 30 (20-70) $\times$ 10^{21} Pa s upper and lower mantle viscosity. These inverted Earth parameters are generally consistent with recent global 3D viscosity field reconstructions (Austermann et al., 2021) but reflect a substantially stronger upper mantle compared with previous estimates based on GIA analysis of Holocene sea-level data from east Australia (0.15-0.3 $\times$ 10^{21} Pa s Lambeck et al., 2002). The main reason for this difference is our inclusion of pre-Holocene coral reef records, which prefer a stronger upper mantle viscosity (details in Figure S3.4).

The ice model weighting parameter predominantly converges to scenario II (Figure 3.2), indicating that a smaller pre-LGM grounded ice volume is preferred by the SLIPs. The blue dashed lines in Figure 3.6 are the expected GIA-induced RSL change for RSL sites with at least five SLIPs; results for other RSL sites are shown in Figure 3.10. It is clear that SLIPs with ages between 19.5 and 21.5 ka BP at NOG represent

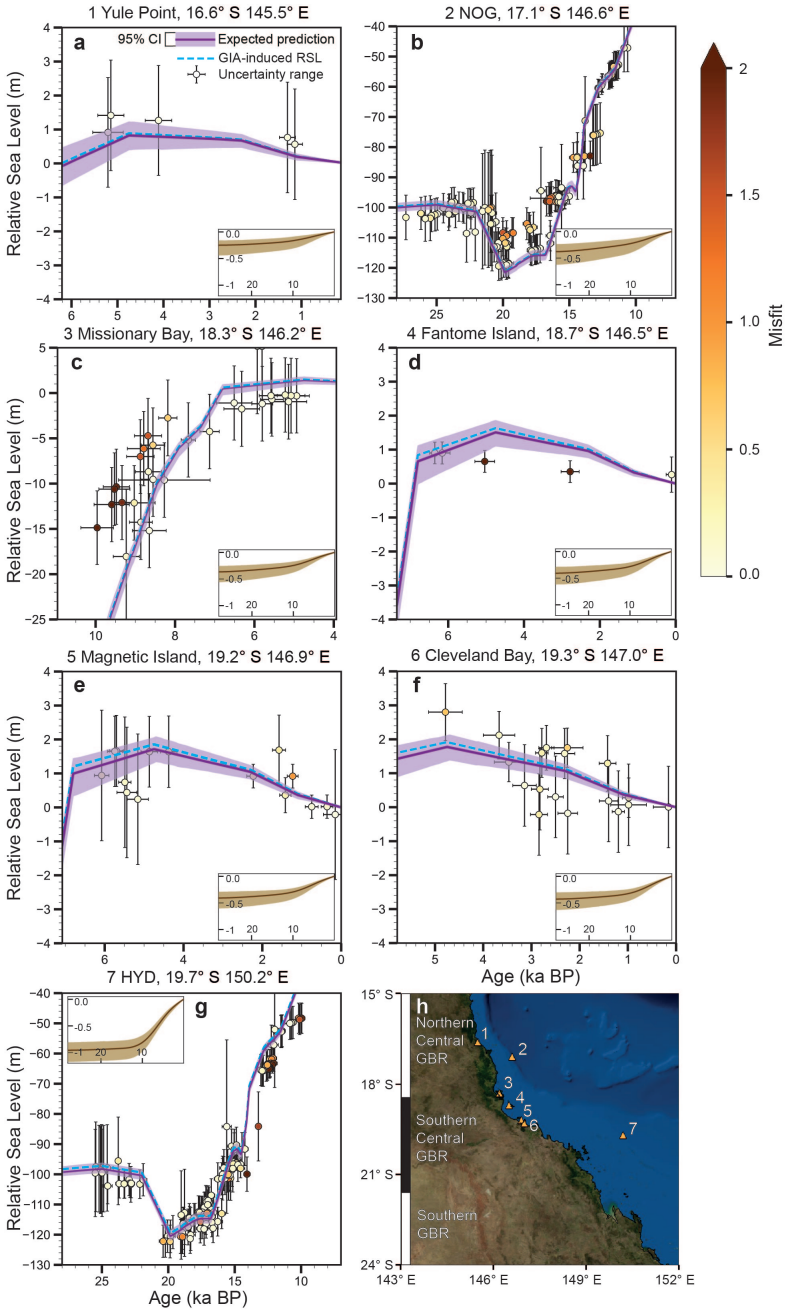

Figure 3.6: Relative sea level data-model comparison. Each error bar shows 2σ vertical and age uncertainties with the coloured dots indicating the unitless data-model misfit (i.e., J in equation 3.5). Note we plot the 2σ vertical uncertainty range of the reconstructed RSL instead of showing the original recorded elevation. The RSL sites are listed from north to south with the site's number, name and coordinates given as the subtitle. The expected SIA-induced RSL change and its associated 95% CI are shown in the subplot within each frame. The last frame shows the RSL site locations and corresponding site numbers. Note the different axes used in each plot.

substantially higher RSL than the prediction produced by the preferred ice loading scenario II. Using scenario I, which has a larger LGM global ice volume, would result in an even lower RSL prediction during this period, therefore further enlarging the data-model misfit, leading to the rejection of this scenario in the inversion.

3.4.2 Sediment Deposition History

3.4.2.1 Temporal Distribution

Using the posterior Earth and ice model parameters, we show detailed palaeo shoreline positions (note that the SIA impact on shoreline migration is minor and is not considered here) for eight key time frames (Figure 3.7). Comparing to the commonly used approach that assumes sea-level rise uniformly follows the GMSL curve (e.g., Hinestrosa et al., 2019), our calculation shows local RSL can significantly depart from GMSL by >10 m depending on local morphology. During early MIS 2 (28-22 ka BP; Figure 3.2), RSL was 90-105 m below present with only part of the shelf edge submerged near the south-eastern Capricorn Channel. The growth of reef stage 2 here (Figure 3.4; Webster et al., 2018) contributed 10% to overall sediment accumulation for this period (Figure 3.8). Comparatively, 19.1 Gt/ka (14.7-23.5 Gt/ka) of siliciclastic sediment was deposited at the continental slope and shelf edge during this period, which dominated the sediment budget (contributing ∼90% of total loading). This siliciclastic proportion became even greater when GMSL dropped to LGM conditions between 22-19.9 ka BP.

After the LGM, local sea level rose gradually prior to 16.5 ka BP and accelerated between 16.5 and 14.65 ka BP, which induced the coastline near the Capricorn Channel to migrate slightly onshore. As a result of the initiation of reef 3b and the continuous growth of reefs 3a and 2 (Figure 3.4), shelf edge reef accumulation increased from 1.6 Gt/ka to 11.1 Gt/ka (Figure 3.9b). Following the start of Meltwater Pulse 1A at 14.5 ka BP, the rate of local sea-level rise exceeded 40 m/ka, which further inundated the Capricorn Channel by hundreds of kilometres and caused the shelf edge accumulation rate to increase to ∼20 Gt/ka. Although the RSL rise rate decreased to ∼15 m/ka after 14.0 ka BP, the coastline continued to retreat

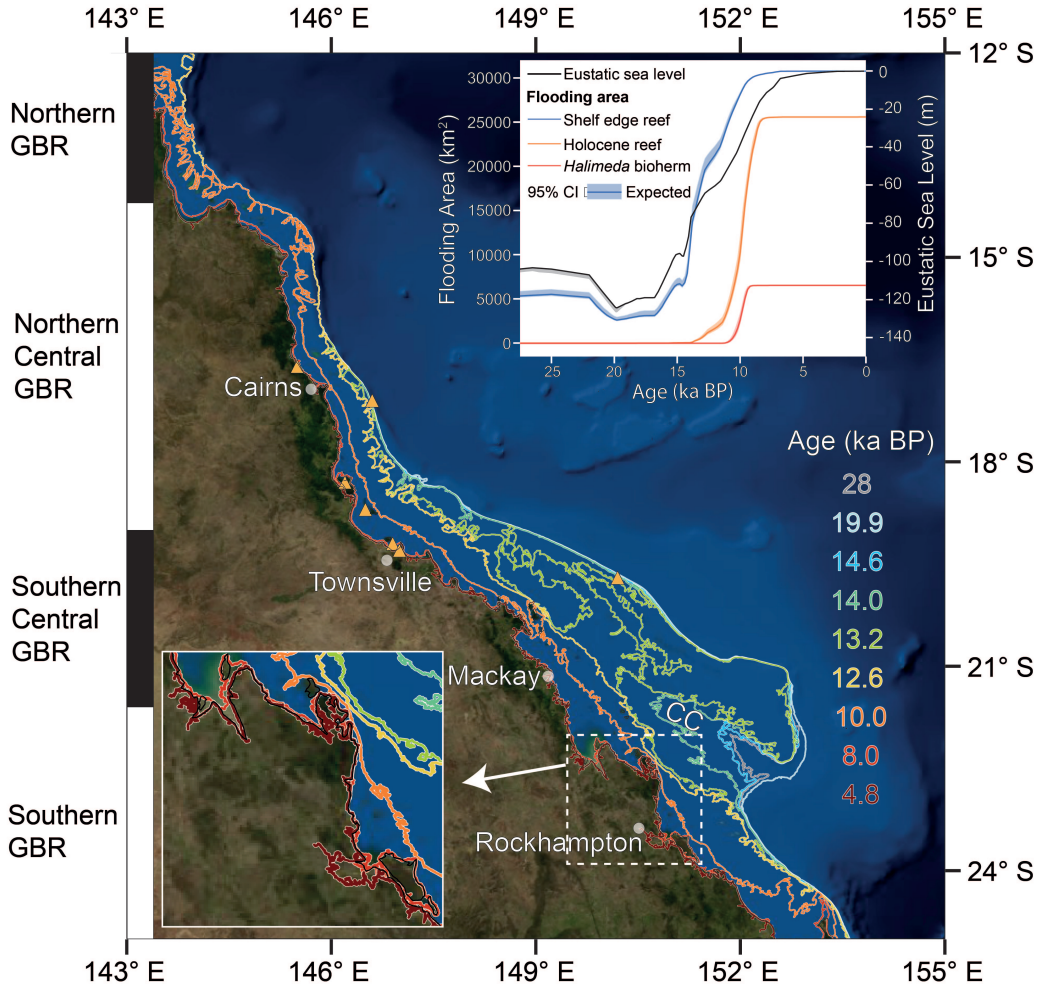

Figure 3.7: Expected GBR postglacial flooding pattern. The eight coloured shoreline reconstructions correspond to the eight time intervals shown on the right. Time series of posterior flooding area for each sediment domain and eustatic sea-level are shown in the subplot in the top-right corner. The subplot in the bottom-left corner shows an enlarged version of the shoreline reconstruction results near Rockhampton. The orange triangles indicate site locations for the sea-level data shown in Figure 3.6. Some key locations are labelled, CC = Capricorn Channel.

significantly in the southern central GBR and less so in the northern central GBR until 13.2 ka BP. Due to the flat morphology of the southern central GBR shelf, a large area of middle shelf near Mackay was flooded at this time, initiating the growth of the Holocene reef. The rest of the outer-middle shelf within the southern central GBR was submerged following ~6.5 m RSL rise leading up to 12.6 ka BP. Meanwhile, north of the southern central GBR, most of the middle shelf and even parts of the shelf edge were still sub-aerially exposed, indicating the strong temporal variability

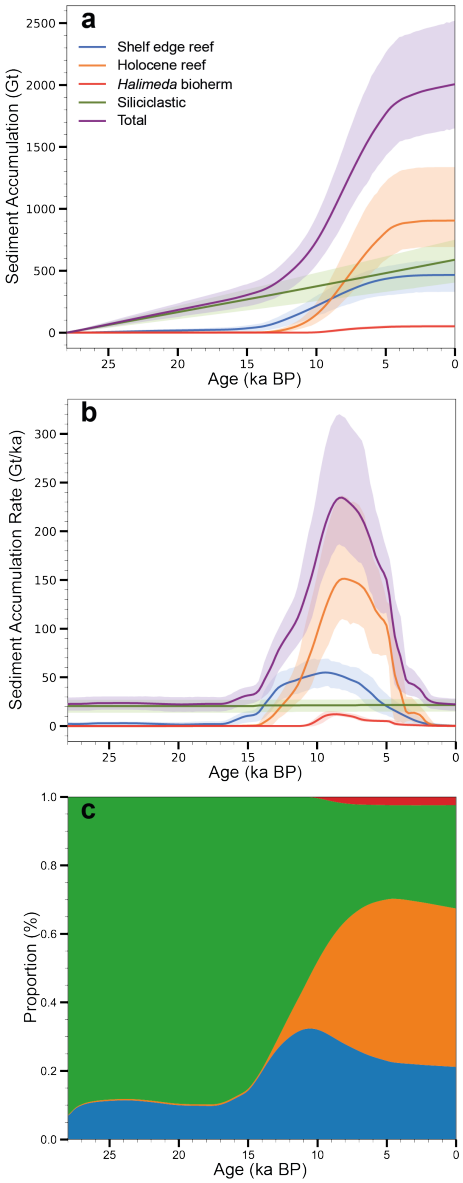

Figure 3.8: GBR posterior sediment mass accumulation history. (a) Total sediment mass accumulation and sediment accumulation associated with each sediment domain. (b) As in (a), but showing the rate of sediment accumulation. The solid lines indicate the expected sediment models and uncertainty ranges denote the 95% confidence intervals. (c) The proportional contribution of each sediment domain to total mass accumulation through time.

in transgression time. The accretion rate of the shelf edge reef along the whole GBR continued to rise until 10 ka BP, when most of the shelf edge had been inundated with its contribution to the sediment budget peaking at 32.3% (Figure 3.9c). Similarly, as the coastline moved across the middle shelf (except in the northern GBR), this accelerated the growth of the Holocene reef and initiated *Halimeda* bioherm growth

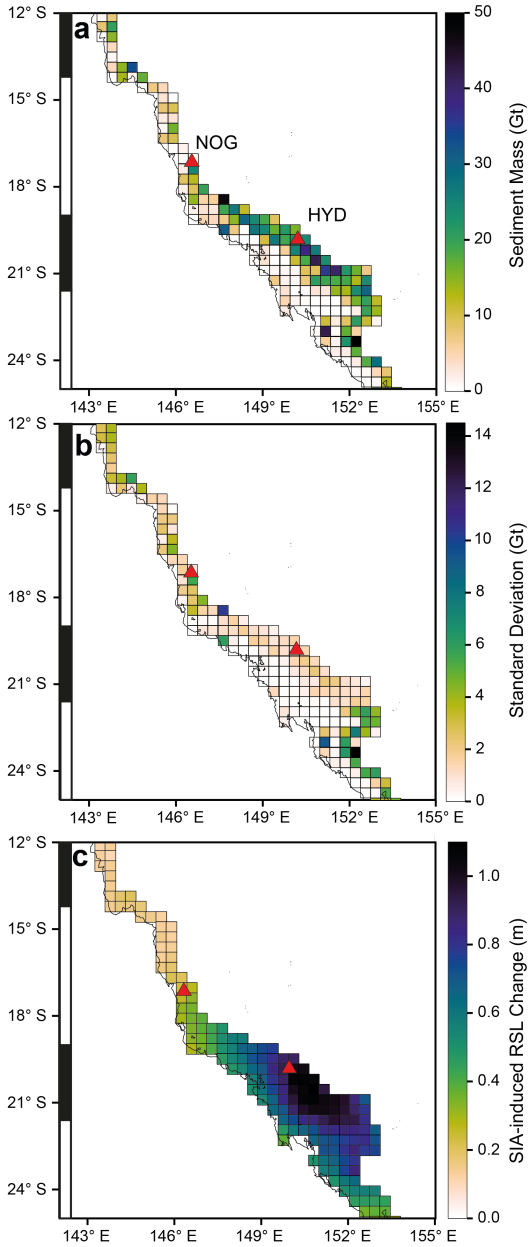

Figure 3.9: Reconstructed spatial distribution of sediment mass accumulated from MIS 2 to present. (a) Expected sediment accumulation mass distribution. (b) One sigma standard deviation of sediment accumulation mass. (c) Expected RSL change due to SIA. The black and white bands on the left define the four GBR latitudinal sectors as in Figure 3.7. The red triangles indicate the locations of NOG and HYD.

at 11 ka BP. This timing agrees well with a recent radiocarbon analysis of inter-reef sediment cores, which suggests *Halimeda* bioherm initiation occurred around 11.1 ka BP in the northern GBR (McNeil et al., 2022).

Between 10-8 ka BP, the shoreline migrated to a geometry similar to present day

and the growth rate of the Holocene reef and *Halimeda* bioherms domains reached their maximum values of 130.5 and 11.2 Gt/ka at 8.2 and 8.8 ka BP, respectively (Figure 3.9b). Concurrently, much of the shelf edge reef had attained its maximum thickness and stopped accreting, therefore, its contribution to the sediment budget was gradually surpassed by the Holocene reef (Figure 3.9c). RSL continued to rise until 4.8 ka BP with the maximum magnitude of the Mid-Holocene highstand (3.2 m) being predicted near Rockhampton and Mackay (Figure 3.7) where the shoreline is estimated to have been up to tens of kilometres inland of its modern position, with the subsequent re-advance being due to the impact of water loading on the adjacent wide continental shelf. The growth rate of carbonate sediment decreased in the late Holocene, with the largest reduction seen in the Holocene reef domain due to the reef surface leaving the photic zone or the cessation of growth following the highstand (section 3.3.3.2). Overall, reconstructed Holocene growth rates for carbonate sediment domains agree well with the theoretical bell-shaped curve (Davies and Hopley, 1983), which suggests a slow growth during reef initiation followed by accelerated growth when the reef is "keeping-up" or "catching-up" to sea level. The final maturation phase exhibits a slow accretion rate mostly due to lack of accommodation space.

Our inversion results indicate the GBR experienced 1853.7 Gt (1613.1-2078.7 Gt) of sediment loading from MIS 2 to present (Figure 3.9a). Three carbonate domains produced 1319.7 Gt (1007.5-1563.8 Gt) of sediment, comparable with previous estimates of 939 Gt (622-1398 Gt, Hinestrosa et al., 2022) and 1709.4 Gt (Rees, 2005). The timing of increased carbonate deposition identified in our study correlates with a period of minor decrease in atmospheric CO_2 (14.3-12.7 ka BP), which is consistent with the idea that coral reef growth played a significant role in the postglacial carbon cycle (Lemieux-Dudon et al., 2010; Kinsey and Hopley, 1991).

3.4.2.2 Spatial Distribution

Figure 3.9 shows the sediment spatial distribution conditioned on the SLIP database. There is a distinct north-south gradient with more sediment accumulated in the southern (central) GBR. This gradient reflects the different physiography of the northern and southern GBR, with the southern GBR having a wider and flatter shelf

morphology. This provides ample accommodation space for carbonate material to grow (Figure 3.3). The SLIPs support this gradient and mostly show higher-than-predicted RSL in the northern (central) GBR and, conversely, lower-than-predicted RSL in the southern central GBR. During sea-level transgression, the GBR sediment system is mostly in a depositional phase, therefore the effect of SIA is to increase the magnitude of post-depositional RSL rise, which results in lower-than-predicted RSL (Figure 3.6). To minimise the misfit to SLIPs, model parameters associated with sediment domains in the northern (central) GBR gradually converged to the lower end of the prior distribution, producing 167.8 Gt and 229.8 Gt of sediment. In contrast, the southern central GBR sediment mass distributions strongly skew to the higher end, producing 994.6 Gt of sediment. Although there are no SLIPs in the southern GBR sector, the larger-than-prior sediment loading results (461.5 Gt) reflect the fact that sediment loading in the southern sector has a long-wavelength impact on RSL change in the southern central GBR.

This north-south distinction is supported by recent seismic mapping of shelf edge reef structures (Hinestrosa et al., 2016, 2014) and a modelling study of the GBR carbonate-siliciclastic systems (Salles et al., 2018), both of which show substantially thicker shelf edge sediment in the southern (central) GBR. The good agreement between RSL observations and these independent studies suggests it is possible to use SLIPs to constrain sediment deposition history. It is noticeable that, compared with other regions, the posterior uncertainties are very low in the southern central GBR (Figure 3.9b). The reason for this is because greater southern central sediment loading consistently improves the data-model misfit, by up to ∼15%, and thus the southern central sediment loading converges to the higher end of the prior distribution. For the other three regions, because the overall misfits are sensitive to the southern-central load, they show a similar level of uncertainty.

3.4.2.3 SIA-induced RSL Change

Using the posterior model parameter distributions, we quantify the impact of SIA on the total GBR RSL calculation (Figure 3.6). Overall, including the SIA signal reduces the data-model misfit (J in equation 3.5) by ∼10% and broadens the acceptable

region of the Earth model parameter space (Figure S3.5). The largest SIA signal is on the outer shelf of the southern-central GBR where sediment loading contributes >1.1 m to RSL rise since MIS 2 (Figure 3.9c). For HYD, incorporating the SIA-induced RSL rise (0.97 m; 0.83-1.17 m) improves the model fit to the SLIPs from 0.48 to 0.41, especially for SLIPs with ages 12.5-10 and 21-18 ka BP where observations show remarkably lower RSL than predicted by the GIA-only model. For the inner shelf region of the southern-central GBR, the SIA signal is lower, with an expected value of only 0.42 m (0.31-0.64 m; similar magnitude for sites 4-6), due to the lack of carbonate sediment. Similar to HYD, the inclusion of the SIA signal significantly improves the average model misfit by 0.04 for Fantome Island. But for Magnetic Island and Cleveland Bay, there is no noticeable improvement. For these four RSL sites, since the majority of sediment loading takes place at the shelf edge and in the Holocene reef domains, i.e., during the early-mid Holocene, the SIA signal remains almost unchanged before 14 ka BP (Figure 3.6).

To the north, SIA effects in Missionary Bay and Noggin Pass are predicted to have a similar magnitude of ∼0.3 m, but with different temporal patterns (Figure 3.6). For Missionary Bay, the local load is minor (<10 Gt; Figure 3.9a) and the SIA signal is primarily impacted by the long wavelength sediment signal from the southern-central GBR, where 910.7 Gt of sediment was deposited during the Holocene. In contrast, the SIA signal for NOG shows a much more linear rate of prior to before the Holocene, which is caused by continuous siliciclastic sediment discharge to the shelf edge during early deglaciation. Lastly, for Yule Point the SIA signal is predicted to be small (0.24 m) due to the low local sediment loading and the fact that it is located >500 km from the sediment deposition centre in the southern central GBR. Since the SLIPs generally show higher-than-predicted RSL at sites 1-3, the inclusion of the SIA signal slightly increases the model misfit to observations. But since the SIA signals for these sites are relatively small, the overall increase in model misfit is negligible compared with the misfit reduction associated with including SIA in the southern central GBR.

3.5 Discussion

3.5.1 GBR RSL Spatial Variability

We first investigate the degree to which the SIA signal can explain the RSL difference between NOG and HYD. The Monte Carlo binning analysis (section 3.3.4.1) yields a temporally-increasing RSL difference between these two locations, with a temporally-averaged value of 4.0 m (3.4-4.5 m, Figure 3.10). The increasing RSL difference at NOG and HYD prior to the Holocene can be explained by different sediment deposition histories. Between MIS 2 and the Holocene a considerable amount of siliciclastic sediment was discharged to the shelf edge near NOG, which gradually increased local RSL (Figure 3.6). Comparatively, our model predicts much less siliciclastic discharge near HYD (this site is not located close to any modern river mouths, Figure 3.3), hence the SIA signal remains low prior to the Holocene. These results are consistent with conceptual sediment depositional models which suggest that, during MIS 2 and MIS 1, the regions surrounding NOG and HYD were dominated by large estuaries and extensive coastal barriers and lagoons (Hinestrosa et al., 2016). Near NOG, the estuaries were fed by east-west elongated channels crossing the narrow continental shelf (<50 km) which provided an efficient way to transport coarse grained sediment to the shelf edge and upper continental slope. This can be verified by the presence of thick siliciclastic sediment in various records from the shelf edge and continental slope (Dunbar and Dickens, 2003). In contrast, the northwest-southeast elongated coastal choked lagoons of the southern central GBR were not efficient for transporting sediment towards the continental slope. The wider and flatter continental shelf in this region nurtured complex drainage networks with long and sinuous channels redirecting the sediment to the southeast (see Figure 1 of Hinestrosa et al., 2016). In addition, the presence of blocking barriers along the shelf edge strongly reduced lagoon flushing. In summary, prior to coral reef initiation during the Holocene, NOG was substantially more impacted by siliciclastic sediment loading than HYD (Figure 3.6), which explains the greater RSL rise observed at NOG during this period.

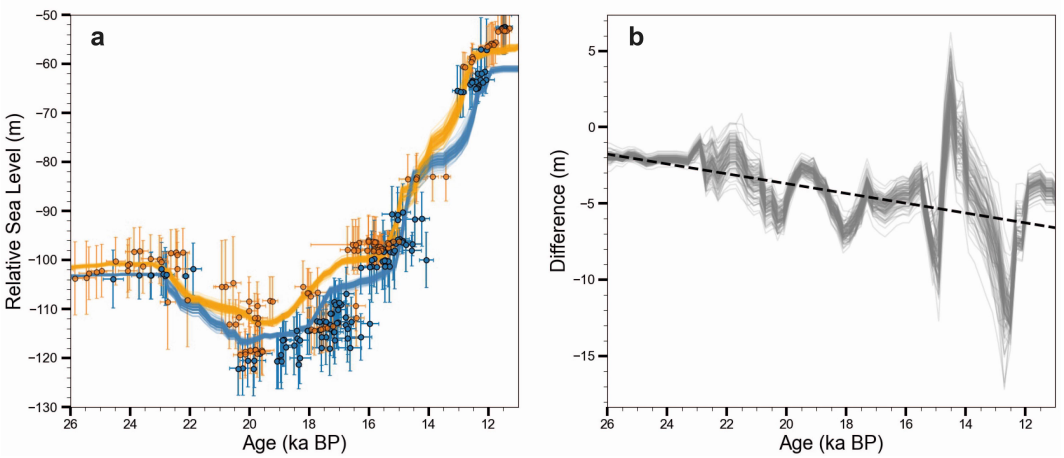

Figure 3.10: Monte Carlo binning analysis results. (a) Reconstructed time series of RSL variation at NOG (orange) and HYD (blue). The error bars indicate 2σ age and vertical data uncertainties. Each solid line represents one random realisation of the Monte Carlo binning analysis. (b) The time series of RSL difference between NOG and HYD, the dashed trendline indicates the temporally increasing RSL difference between these two sites from the LGM to the Holocene.

Subsequent to the initiation of reef development, HYD has experienced greater RSL rise than NOG, due to the development of extensive reefs in the southern central GBR. Specifically, our sediment model predicts the development of widespread, thick reefs across the shelf edge of the southern central, resulting in up to four times more sediment loading compared with the northern central GBR. This is consistent with seismic stratigraphy suggesting the extensive availability of low gradient substrate near HYD promoted the development of thick and wide fringing shelf edge reefs (Hinestrosa et al., 2016). In comparison, the lateral availability of substrate is very limited near NOG due to the narrow and steep physiography (Abbey et al., 2011). Additionally, our results show shelf edge reefs near HYD are thicker than those near NOG, consistent with the drill core observations shown in Figure 3.4. This may be due to the contrasting palaeo-environmental and physiographic conditions between NOG and HYD during the evolution of these reefs (e.g., different morphology and sediment and nutrient circulation; Hinestrosa et al., 2016). Similar to the shelf edge reef, a wide and flat physiography provides ample accommodation space for the Holocene reef to thrive in southern central GBR. Our interpolation results suggest the Holocene reef in this region is on average thicker than in the north (section S3.1) possibly due to the lower elevation prior to sea-level transgression (Salles et al., 2018;

Hopley et al., 2007). Overall, based on our expected sediment and Earth model parameters, we predict that sediment loading differences between NOG and HYD can explain 0.6 m (0.35-0.75 m) of the observed RSL difference.

Notably, our SIA model can only account for 15% of the mean RSL difference (4.0 m) between NOG and HYD. We propose three possible explanations for this. Firstly, as mentioned in section 3.4.1, our preferred Earth models are relatively strong (Table 3.2). These Earth models may be biased towards fitting LGM-age SLIPs from NOG and HYD, but it is important to note that these SLIPs have large chronological and indicative meaning uncertainties. Previous GIA analysis (e.g., Lambeck et al., 2002) and independent 3D mantle viscosity estimates suggest a thinner lithosphere and weaker mantle viscosity across the GBR, which would induce a larger SIA signal and explain more of the RSL difference between NOG and HYD. Therefore, we recalculate the SIA signal using an alternative Earth model with 46 km lithospheric thickness and 0.1×10^{21} Pa s upper mantle viscosity, which is supported by previous studies (Hoggard et al., 2021; Austermann et al., 2021) and is consistent with the Earth model determined by the Holocene SLIPs alone (Figure S3.4). The results show a larger SIA signal at NOG (0.59 m) and HYD (2.20 m), which accounts for almost half the observed RSL difference.

Secondly, differences in turbidity and nutrient level may impact the coral species' living depth and hence past RSL reconstructions (Hibbert et al., 2016). One important assumption when reconstructing past sea level is that each sea-level indicator of a given species should have an identical relationship to palaeo water depth, however, this is not robust. Indeed, there is no global relationship between coral species and bathymetry (Perrin et al., 1995), instead, it depends on local irradiance levels (affected by turbidity and nutrient levels), nutrient availability, temperature and hydrodynamic conditions (Hibbert et al., 2016). As mentioned above, NOG and HYD are dominated by estuarine and lagoonal environments, this difference may induce significantly different coral reef accretion environments, which could explain part of the observed RSL difference between NOG and HYD (Hinestrosa et al., 2016).

Thirdly, the simple sediment model adopted in this study may not adequately represent sediment evolution across the GBR, especially the terrigenous sediment

transport and depositional processes. Although the impact of shoreline migration is considered, we do not account for landscape and fluvial evolution driven by extrinsic forcings and sea-level variation or the sediment infill of some large palaeo river channels (Ryan et al., 2007), and instead we make the simple assumption that fluvial sediment is deposited (with an overall uniform rate) at the nearest concurrent shoreline position. These factors may misrepresent the spatio-temporal distribution of siliciclastic sediment. For example, our siliciclastic modelling results are similar to a classical reciprocal sedimentation concept, which may not fit well with the deglacial sediment accumulation rate inferred from sediment cores from Queensland Trough (Dunbar et al., 2000). Additionally, we do not consider the effect of wave processes on siliciclastic sedimentation, which can induce erosional and depositional phases near NOG and HYD (see Figure 4 of Salles et al., 2018).

Lastly, we note acknowledge that the relatively coarse resolution of the sediment SIA model used in this study may cannot be able to fully resolve coral reef structure (Figure 3.9), which is often characterised by narrow and isolated strips with <1 km coverage (Hinestrosa et al., 2016). This caveat and this may lead to structural bias in the resulting SIA signal. Rovere et al. (2022, preprint) provide a direct comparison of the SIA signals estimated by SIA models with 1 km and 40 km resolution (see their Figure 4b and 4f). Their results indicate although both SIA models produce a long wavelength SIA signal, the low-resolution SIA model would systematically underpredict SIA signal, especially in regions with noncontinuous sediment load. Therefore, this potential for our model to underestimate the local SIA signal may further explain some of the RSL difference between NOG and HYD. Considering all of the factors discussed here, we conclude that it is possible for the SIA process to partially explain the observed spatial variability in RSL between NOG and HYD. However, to better understand this RSL variability, further investigation is required of the missing processes mentioned above.

3.5.2 SIA Impact on Ice Volume Estimate

Using far-field sea-level data to constrain past grounded ice volume and infer past ice sheet dynamics is an important tool in palaeoclimate studies (e.g., Lambeck

et al., 2014). However, most studies do not consider the SIA signal, despite previous studies suggesting it can alter local RSL by >100 m since the Last Interglacial (Pico, 2020). Because SIA-induced RSL change is not associated with ice-water exchange, neglecting its effect will systematically bias inferences of global grounded ice volume. For the GBR, we find that SIA can cause up to 1.1 m RSL rise since MIS 2, which is equivalent to overestimating the volume of ice melt by $\sim 4.3 \times 10^5$ km^3 under the common assumption that ice-water exchange is the only cause of post-glacial sea-level change. This demonstrates that caution is needed when estimating global ice volume from SLIPs collected from margins characterised by high sediment input across large spatial areas (hundreds of kilometres, e.g., Argentine Shelf).

Based on the results of this study, we find that it is necessary to incorporate the SIA signal when determining global ice volume during the LGM, which is an outstanding problem in paleoclimate studies (Simms et al., 2019). Currently, there are five locations that have yielded RSL records for the LGM, specifically, NOG, HYD, Bonaparte Gulf, Sunda Shelf and Barbados. All of these locations are potentially impacted by sediment loading during the last deglaciation. In particular, cores from NOG, HYD and Barbados were collected from large coral reef frameworks near estuaries (Woodroffe and Webster, 2014) which are likely to have been affected by RSL rise due to reef and siliciclastic sediment loading. Although distant from large coral reef systems, Bonaparte Gulf and Sunda Shelf are located near major river mouths (Pico, 2020), and they may record some SIA signals caused by siliciclastic sediment deposition. In all cases, incorporating the SIA process will reduce the subsequent global grounded ice volume estimate, which will help to mitigate the current disagreement between the magnitude of post-LGM GMSL rise recorded by RSL indicators and the estimated amount of ice melt (Simms et al., 2019).

3.6 Conclusions

In this study, we develop a systematic RSL-driven framework to reconstruct a sediment deposition history for the world's largest carbonate-siliciclastic sediment system, the GBR. Using a Bayesian-style technique, we calibrate the sediment history

along with SIA- and GIA-induced RSL change using SLIPs from the GBR region. Based on our results, we highlight these key findings:

1. From MIS 2 to present, 1853.7 Gt (1613.1-2078.7 Gt) of sediment were deposited along the GBR consisting of 1319.7 Gt (1007.5-1563.8 Gt) of carbonate sediment, which mostly accreted between the late Pleistocene and mid Holocene, and 534.0 Gt (410.5-659.1 Gt) of terrigenous siliciclastic sediment.

2. There is a strong north-south gradient in the reconstructed sediment loading, with ∼75% of the sediment predicted to have been deposited in the southern-central and southern GBR. This latitudinal distinction is consistent with independent seismic stratigraphy analysis (Hinestrosa et al., 2014), continental shelf physiography (Hinestrosa et al., 2016) and sea-level observations (Yokoyama et al., 2018; Webster et al., 2018).

3. For the GBR, SIA can contribute up to 1.1 m of RSL rise during the last deglaciation. Neglecting its contribution to RSL will lead to an $\sim 4.3 \times 10^5$ km^3 overestimate of global grounded ice volume during the LGM. To accurately infer global ice volume from far-field SLIPs, we suggest a systematic assessment of the potential SIA signal is required, especially for SLIP locations near large sediment systems.

S3 Supplementary Information

S3.1 Holocene-Modern Reef Accretion Thickness

To capture the spatial variability of Holocene-modern reef accretion thickness, we use the ordinary kriging technique on a newly-compiled Holocene-modern reef accretion thickness database (Hinestrosa et al., 2022, n=52 , see Figure 3.5) . To implement ordinary kriging, one assumption that needs to be met is a constant mean and variance across the whole interpolated region (i.e., stationary, Wikle et al., 2019). This is achieved by de-trending the original accretion thickness data using a first-order multivariate least square method, which fits the sediment accretion thickness with each data point's longitude, latitude and elevation.

The least square residuals (i.e., observation minus least square prediction) are then assumed to be stationary and are used to build a linear empirical semivariogram. This semivariogram describes the spatial correlation that cannot be captured by the least square determined relationship. The final interpolated accretion thickness is then expressed as the summation of the least square and kriging solutions (Figure 3.5a), and the overall interpolation uncertainty is calculated as the quadrature summation of the uncertainty produced by both the least square and ordinary kriging processes (Figure 3.5b). This spatially variable uncertainty of accretion thickness is then propagated to the statistical calibration process.

S3.2 Calibration Processes

S3.2.1 Simulated Annealing

To perform simulated annealing on the model parameters, we start by selecting random model parameters from their prior distributions. Based on this initial parameterization, an initial RSL prediction and its posterior probability are calculated, which is marked as the last accepted model. A random perturbation is then applied to the last accepted model to generate a nearby newly proposed model. The perturbation is set to be uniformly distributed between $[-0.5, 0.5]$ for each model parameter space

at the start but will gradually decrease to $[-0.25, 0.25]$ by the end of the sampling procedure to produce a better convergence precision. We note that different model components make different contributions to the surface load history, so the calibration process may be over-sensitive to a few model components (e.g., Earth and ice models) leaving other components under-constrained. Hence, we apply a Gibbs sampling technique (Geman and Geman, 1984) to perturb each model component separately, this helps each model component to be better calibrated.

The simulated annealing algorithm accepts the proposed new model with probability (P):

$$P = (\frac{p_{prop}}{p_{last}})^{1/T} \tag{S1}$$

where p_{prop} and p_{last} indicate the posterior probability of the newly proposed model and the last accepted model. T is the so-called 'temperature' parameter, a term used to adjust the acceptance probability. When simulated annealing begins, the initial temperature is set to be relatively high, corresponding to a high acceptance probability of >80%, which helps the algorithm jump out from the local minima. As the simulated annealing algorithm continues to run, the temperature will gradually cool with an exponential decay rate of 0.98 (i.e., lowering the acceptance rate), ensuring the algorithm converges around the probability maxima. In total, one simulated annealing procedure generates 250,000 newly-proposed models with the last 30,000 accepted realisations being used to calculate the posterior probability distributions. To robustly sample the high dimensional parameter space (48 parameters in total) with acceptable computation time, we train a deep-learning-based statistical emulator to fast emulate the physical process of SIA (schematic framework in Figure 3.1 and details below). Using the calibrated posterior probability for each model parameter, we calculate the expected value, the value with maximum posterior probability, standard deviation, and confidence interval for model outputs based on the statistical definitions from Caron et al. (2017).

S3.2.2 Statistical Emulator

We use an iterative framework of emulation-based calibration process as described in Tarasov et al. (2012). Specifically, we first run two ice model scenarios, each

with 228 Earth models. These 456 RSL change predictions across the GBR are then used to force the sediment model with every sediment model parameter set to be the maximum, mean and minimum values from the prior distribution ranges (Figure 3.1). Additionally, for each Earth model we use a Latin Hypercube approach to randomly select three more realisations of the sediment model from the prior probability distributions (i.e., we refer to this as data augmentation). In total, we run an ensemble of 2736 forward models to produce our initial training database, which is used to train a perceptron neural network emulator with 10 hidden layers (details below). Using this emulator, we calibrate all model parameters using the simulated annealing algorithm described above. After the calibration, we select 12 more sediment model realisations - using the 2.5, 50 and 97.5 percentile values from the calibrated solution as well as nine randomly sampled sets of values - and combine these with 228 Earth models, which generates another 2736 forward modelling results. This new training database is then added to the existing training database to update the emulator from the last iteration (Figure 3.1). The *a posteriori* probability density distribution of model parameters is obtained by repeating this training and calibration procedure three times.

The statistical emulation of the sediment isostatic adjustment (SIA) process can be treated as a supervised learning problem where the inputs are the sediment loading history, spherical harmonic (SH) grid location and the adopted Earth model, and the output is the SIA history caused by the input parameters. The emulator we used is a 10-layer perceptron neural network (NN) regressor, with the first five hidden layers each consisting of 256 neurons and the second five hidden layers each consisting of 128 neurons. We use this NN to predict the SIA process for every SH grid cell across the Great Barrier Reef (GBR) from 28 ka to present with 400-year time intervals, which corresponds to 71 output values for each grid cell. Because the output SIA signal at each grid cell location not only depends on the local sediment load variation but also on the surrounding sediment loading history, we therefore provide both local and surrounding sediment loading histories (defined as total sediment load from locations $< 2.5°$ from the the local grid cell) to train the NN. Overall, each input sample contains 147 features, consisting of the local sediment history of one grid

cell (i.e., 71 features), the sum of surrounding sediment accretion thickness history (71 features), longitude, latitude, lithospheric thickness, upper mantle viscosity and lower mantle viscosity.

We first randomly divide the training database into a training set, containing 90% of the training database, and a test set, containing 10% of the database. We use the training set to train the emulator and use the test set as unseen cases to test the emulator's capability to emulate some unseen model samples. The activation function we use for this NN is the rectified linear unit function, and a L2 loss function is used to generate the loss gradient. The NN is trained by running the ADAM stochastic optimiser, with L2 regularisation of 10^{-5}, for 1500 iterations over the training set. Overall, our emulator shows 0.00006 mean square error for the training set and 0.00019 for the test set (Figure S3.1). By examining the model predictions that show larger than 3 sigma misfits, we find the majority of large misfits are produced while emulating the 46 km lithospheric thickness parameter. Because 46 km is similar to the spatial resolution of the 512-degree GIA model, adopting a lithosphere of this thickness will lead to a more localised SIA-induced RSL change signal in response to the spatially variable siliciclastic sediment load compared with models that use a thicker lithosphere of 71 or 96 km. Nevertheless, as the posterior Earth model parameter distributions largely reject a 46 km lithospheric thickness, hence, most of the large misfits produced by 46 km lithosphere can be avoided. Because the emulated SIA process is originally expressed in each SH grid cell, we further downscale the SIA predictions for each sea-level location using a radial basis function interpolation method, which shows $< 10^{-4}$ m interpolation error.

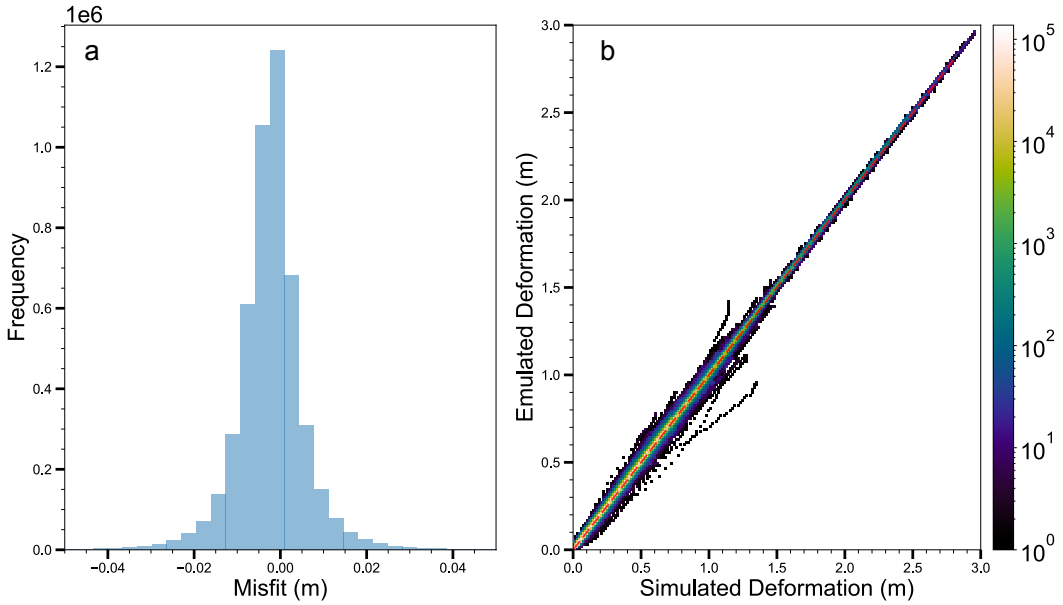

Figure S3.1: Emulator fit to the test set data. (a) Emulation residuals (emulated minus simulated results). (b) Emulator predictions versus simulations results.

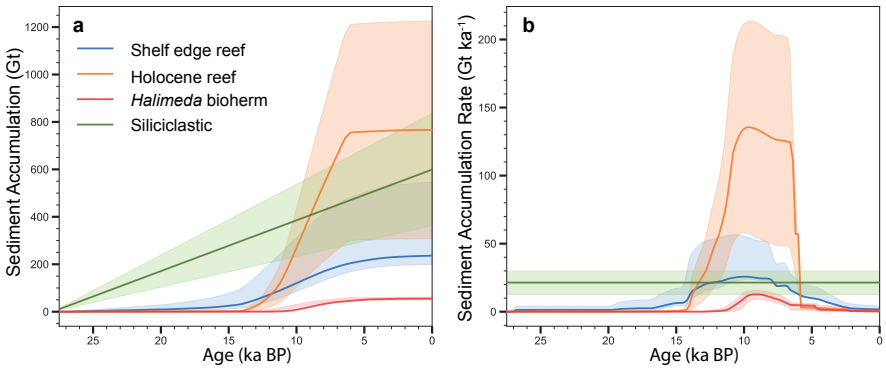

Figure S3.2: Prior sediment mass accumulation distribution. (a) Sediment mass accumulation. (b) Sediment mass accumulation rate. The solid lines indicate the mean value and uncertainty ranges denote the 95% confidence intervals. The upper range of uncertainty range for the shelf edge reef domain has been doubled to account for a potential inter-reef accumulation (see section 3.3.3).

Model Parameter	P_{max}	Expected Value	Standard Deviation	95% Confidence Interval
γ_{se}^{1}	0.15	0.19	0.11	0.055, 0.43
γ_{se}^{2}	0.20	0.12	0.08	0.055, 0.30
γ_{se}^{3}	0.45	0.44	0.01	0.42, 0.45
γ_{se}^{4}	0.42	0.34	0.11	0.12, 0.45
τ_{2}^{1}	8.1	7.6	1.5	5, 10
τ_{2}^{2}	9.4	7.7	1.6	5, 10
τ_{2}^{3}	5.0	8.3	3.3	5, 14.6
τ_{2}^{4}	8.7	9.9	3.3	5, 15
τ_{3a}^{1}	14.6	14.8	3.1	10, 20
τ_{3a}^{2}	14.8	14.7	3.3	10, 20
τ_{3a}^{3}	25.7	21.1	5.8	12.2, 30
τ_{3a}^{4}	21.6	21.8	5.9	12.3, 30
τ_{3b}^{1}	7.1	10.1	3.1	5, 15
τ_{3b}^{2}	15.0	10.3	3.1	5, 15
τ_{3b}^{3}	20.0	18.7	2.3	13, 20
τ_{3b}^{4}	13.1	14.2	3.3	10, 20
τ_{4}^{1}	5.0	8.8	3.2	5, 15
τ_{4}^{2}	7.9	8.6	3.4	5, 15
τ_{4}^{3}	20.0	19.9	0.4	19.2, 20
τ_{4}^{4}	14.7	16.1	3.2	10, 20
ι_{se}^{1}	0	0.13	0.2	0, 0.6
ι_{se}^{2}	0	0.11	0.18	0, 0.4
ι_{se}^{3}	1.0	0.59	0.38	0, 1
ι_{se}^{4}	0.2	0.13	0.2	0, 0.6
γ_{ho}^{1}	-3.46	-2.76	1.18	-3.46, -0.25
γ_{ho}^{2}	-3.46	-2.45	1.72	-3.46, 1.65
γ_{ho}^{3}	3.46	3.31	0.42	2.47, 3.46
γ_{ho}^{4}	3.46	2.11	1.69	-1.55, 3.46
ι_{ho}^{1}	0	0.14	0.20	0, 0.6
ι_{ho}^{2}	0.2	0.19	0.24	0, 0.6
ι_{ho}^{3}	1.0	0.67	0.38	0, 1
ι_{ho}^{4}	0.6	0.22	0.28	0, 0.8
ϕ_{ha}^{1}	0.45	0.44	0.02	0.38, 0.45
ϕ_{ha}^{2}	0.45	0.45	0.01	0.42, 0.45
ϕ_{ha}^{3}	0.26	0.30	0.05	0.25, 0.42
ϕ_{ha}^{4}	0.28	0.32	0.06	0.25, 0.43
ι_{ha}^{1}	0	0.12	0.23	0, 0.6
ι_{ha}^{2}	0	0.21	0.33	0, 1
ι_{ha}^{3}	0.4	0.30	0.31	0, 1
ι_{ha}^{4}	0	0.13	0.19	0, 0.6
β^{1}	0.62	0.68	0.13	0.60, 0.98
β^{2}	1.08	0.90	0.23	0.60, 1.35
β^{3}	1.40	1.18	0.21	0.77, 1.40
β^{4}	1.29	1.03	0.26	0.61, 1.40

Table S3.1: Table of inverted sediment model parameters. P_{max} indicates the inverted value with the maximum posterior probability (i.e., best-fit value). Subscripts and superscripts are as follows: se = shelf edge reef; ho = Holocene reef, ha = *Halimeda* bioherms, si = siliciclastic discharge, 1= northern GBR, 2 = northern central GBR, 3 = southern central GBR, 4 = southern GBR. Detailed descriptions of each parameter is given in Table 3.1.

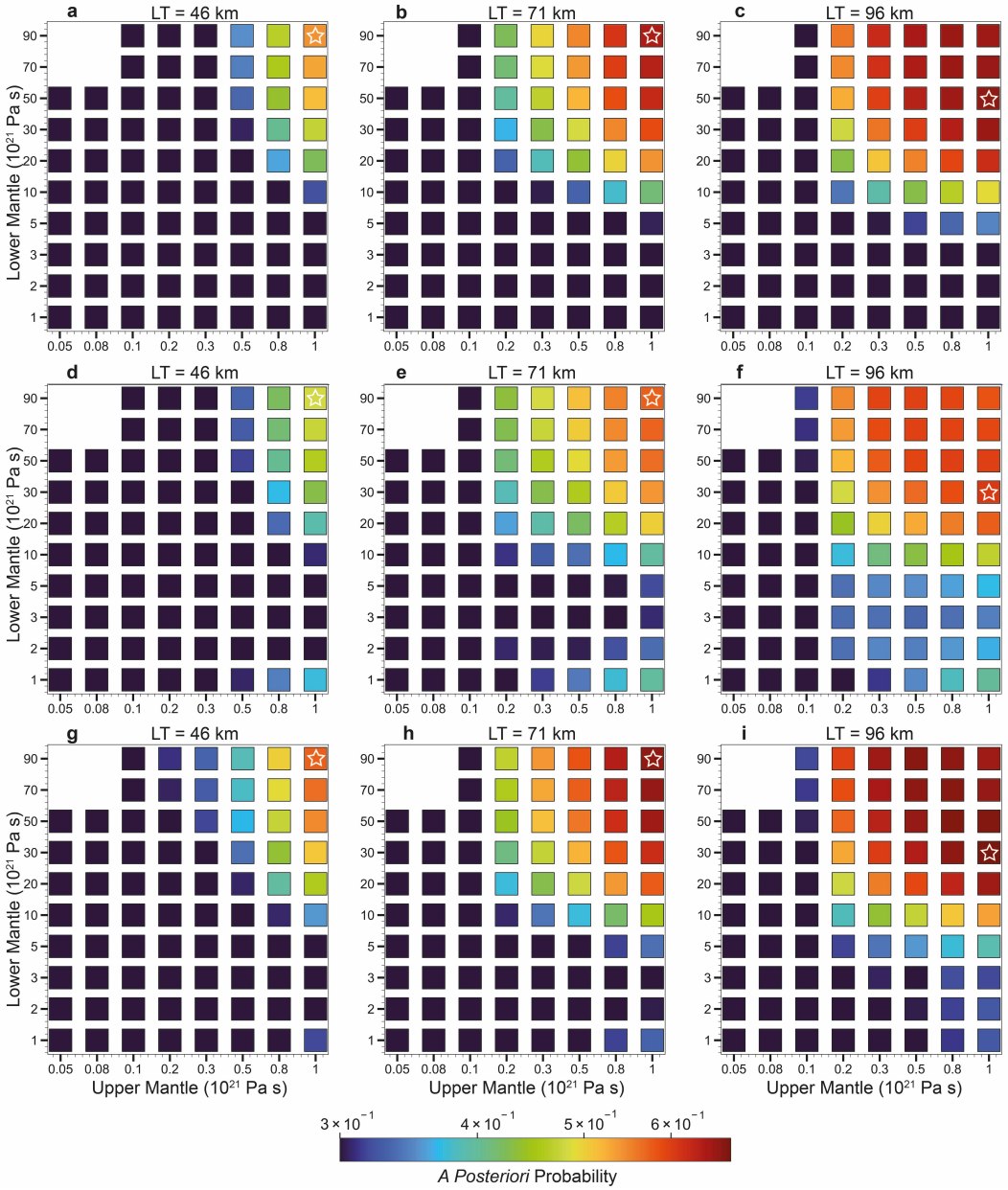

Figure S3.3: Model-data comparison given three Earth and ice model parameters. (a-c) *A posteriori* probability associated with GIA-induced RSL prediction, using the ice model scenario I, as a function of different upper and lower mantle given 46, 71 and 96 km lithospheric thickness. (d-f) Same as a-c but using the ice model scenario II (see section 3.3.2). (g-i) Same as a-c but additionally including the SIA-induced RSL prediction associated with each Earth model combination. The stars denote the best-fit model for each lithospheric thickness parameter. The sediment model adopted in g-i are the expected model obtained from *a posterior* probability distributions.

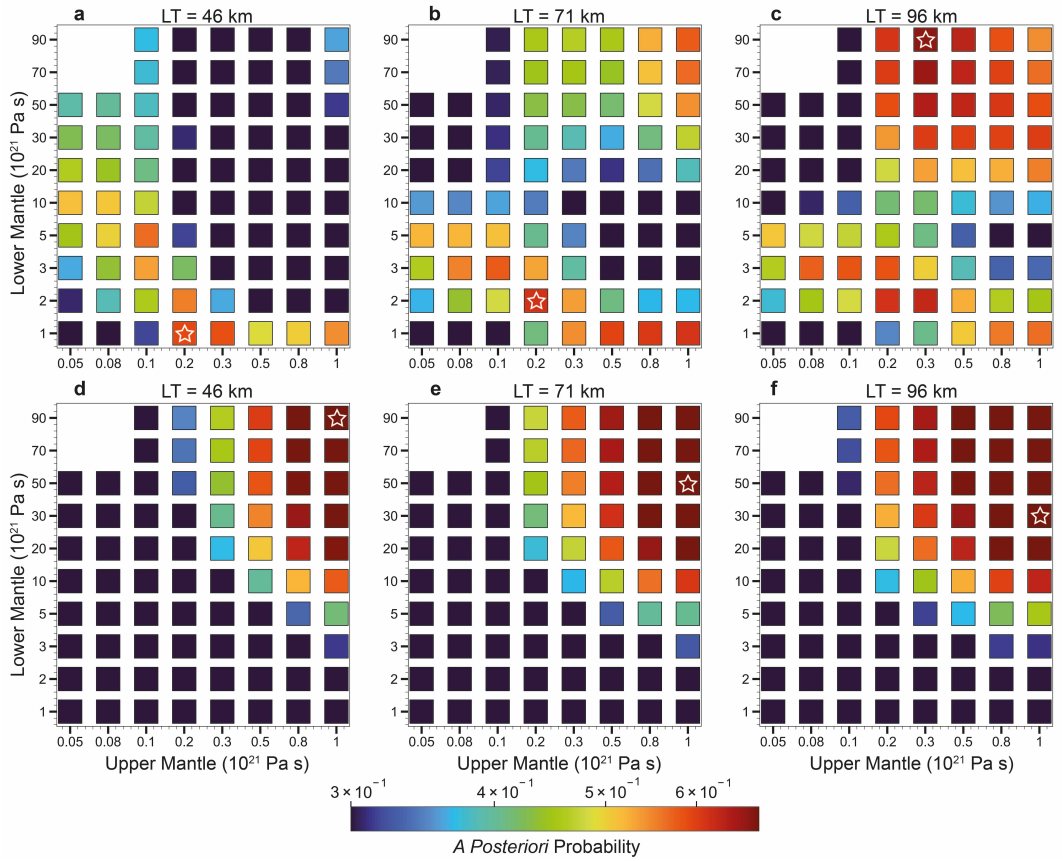

Figure S3.4: Model-data comparison given three Earth model parameters using Holocene and pre-Holocene sea-level data. (a-c) Holocene data based *A posteriori* probability as a function of different upper and lower mantle given 46, 71 and 96 km lithospheric thickness. (d-f) Same as a-c but using pre-Holocene SLIPs. Note the SIA process has not been included here. The stars denote the best-fit model for each lithospheric thickness parameter. The ice model adopted here are the expected model obtained from *a posterior* probability distributions (see section 3.3.4.1).

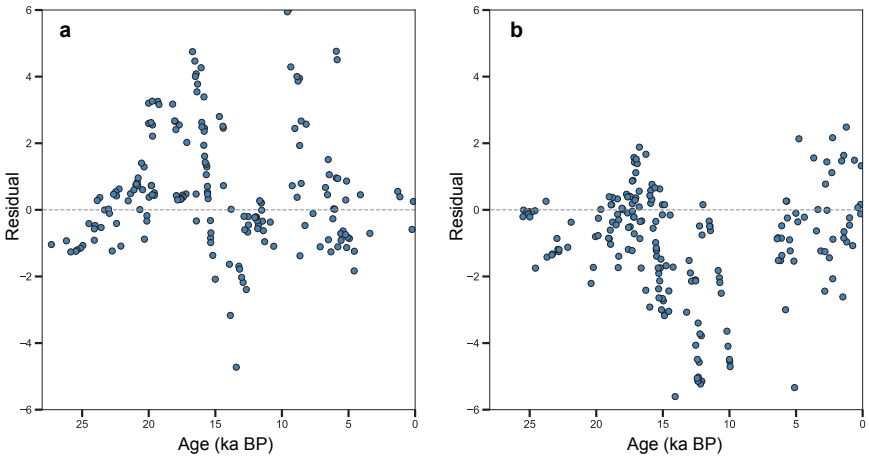

Figure S3.5: RSL prediction residual for SLIPs from the northern and northern central (a), and southern and southern central(b) GBR. The RSL residual shown here is calculated by subtract the expected RSL prediction from the SLIPs then divided by one sigma vertical uncertainty associated with RSL reconstruction. Therefore, a positive residual indicates the RSL observation is higher than the prediction and vice versa.

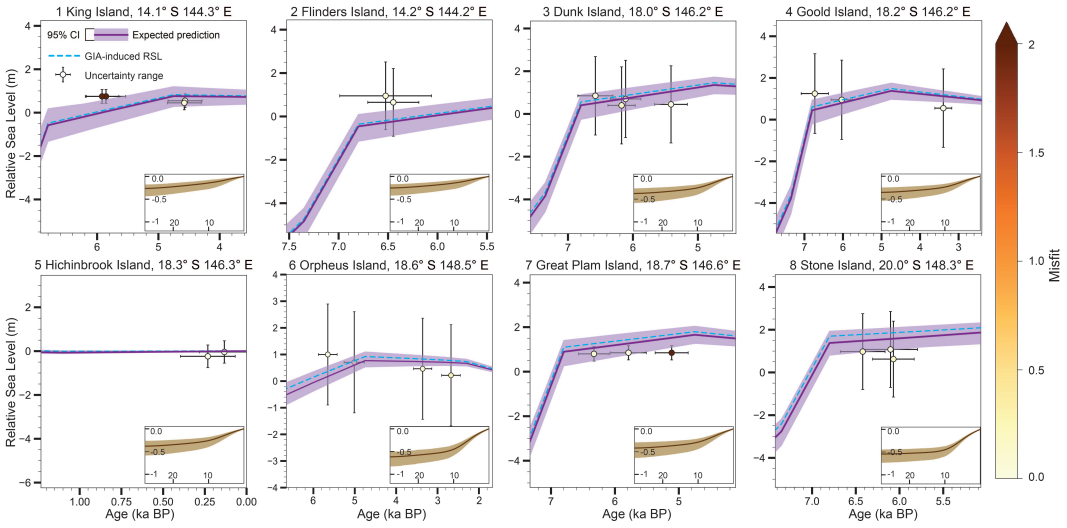

Figure S3.6: Relative sea level data-model comparison. Error bars show 2σ vertical and age uncertainties with the coloured dots indicate the data-model misfit (i.e., J in equation 3.5) of each SLIP. The RSL sites shown here are supplementary to Figure 3.6, which are listed from north to the south. Note the different axis.

S3.3 Monte Carlo Binning Analysis

To determine the temporally varying RSL difference between NOG and HYD, we first reconstruct the data-driven RSL time series for each of these two sites using the Monte Carlo binning analysis approach. We start by dividing the overall time interval (from 25 to 5 ka BP) into four 5-ka wide time windows. The vertical position (i.e. RSL height) of each time window is then determined by calculating the weighted average of all SLIPs whose median age lies within this time bin (the horizontal position is defined to be the middle of this time window). The weighting factor w of each SLIP is given by:

$$w = 1/\sqrt{\sigma_y^2 + (dy/dx)^2\sigma_x^2} \tag{S2}$$

where σ_y and σ_x are the standard deviations of each SLIP. dy/dx is the gradient of global mean sea-level change (obtained from Lambeck et al., 2014) at the time corresponding to the age of each sample; the gradient is used to convert the effective contribution of age uncertainty into depth uncertainty. We then repeat the calculation but shift all four time windows to be 0.2 ka younger (e.g., the first time bin is moved from 25-20 ka BP to 24.8-19.8 ka BP). In total, this slide-and-calculate process is repeated 25 times to recover the underlying RSL time series with 0.2 ka resolution. Furthermore, to assess the uncertainty caused by the noisy SLIPs, we apply a Monte Carlo style resampling approach. Specifically, for each binning analysis, we only use 90% of the randomly selected SLIPs. By repeating this stochastic process 100 times, we can calculate the ensemble mean and standard deviation of the underlying RSL signal at each time interval.

CHAPTER 4

GEORGIA: a Graph neural network based EmulatOR for Glacial Isostatic Adjustment

Lin, Y., Whitehouse, P.L., Valentine, A.P., and Woodroffe, S.A., 2023. GEORGIA: a Graph neural network based EmulatOR for Glacial Isostatic Adjustment. Geophysical Research Letters (under review in Geophysical Research Letters).

4.1 Abstract

Glacial isostatic adjustment (GIA) modelling is not only useful for understanding past relative sea-level (RSL) change but also for projecting future sea-level change due to ongoing land deformation. However, GIA model predictions are subject to parametric uncertainty of poorly-constrained global ice history. An effective way to reduce this uncertainty is to perform data-model comparisons over a large ensemble of possible ice histories. However, this is prohibited by the computation resources required by a GIA model. Here we address this problem by building a statistical GIA emulator that can mimic the behaviour of a physics-based GIA model while being computationally cheap to evaluate. Based on deep learning algorithms, our GIA emulator shows 0.54 m mean absolute error on 150 out-of-sample testing data with <0.5 seconds emulation time. Therefore, this emulator is a suitable tool to perform large ensemble of data-model comparisons to reduce the uncertainty related to ice histories.

4.2 Introduction

During glacial cycles, water-mass redistribution related to the wax and wane of continental ice sheets can alter global mean sea-level by over 100 m. Glacial isostatic adjustment (GIA) describes the spatially variable response of the solid Earth, oceans and global gravitational field to that change in water mass (Whitehouse, 2018; Horton et al., 2018). GIA models that describe GIA-induced relative sea-level (RSL; distance between the sea surface and the solid Earth) change have been widely used to investigate past (Lin et al., 2021; Lambeck et al., 2014), present (Frederikse et al., 2020; Hay et al., 2015) and future (Garner et al., 2018; Kopp et al., 2014) sea-level change problems. Within GIA modelling, a key parametric uncertainty relates to the poorly-constrained global ice history, which not only hinders our confidence in understanding past sea-level change but it also limits our ability to robustly project future sea-level variation due to the ongoing solid Earth deformation and geoid change associated with past glacial cycles.

A commonly-used approach to reduce ice history uncertainty involves performing data-model comparisons with geological data that directly relate to ice-sheet history, e.g. geomorphological evidence of past glaciation, or indirectly reflect ice-sheet variation, such as RSL records. Due to the sparse and noisy nature of geological records, a range of plausible ice-sheet histories may be compatible with the observations, and a robust study often requires testing a large number of these to explore what can be and cannot be constrained (Briggs et al., 2014; Tarasov et al., 2012). However, this is often prohibitive due to the computational cost of solving the complex physical equations required to perform data-model comparison. An effective way to mitigate this difficulty is to build a statistical model that mimics the behaviour of the physics-based simulator but is computationally cheap to run (Reichstein et al., 2019). Rather than solving the physical equations exactly, these 'statistical emulators' learn how the system behaves based on a (comparatively) small set of examples, and use this to predict what the simulation would output in other scenarios.

The concept of emulation (also known as 'surrogate modelling') is not particularly new (Sacks et al., 1989), but recent advances in machine learning have greatly expanded its scope and application (Reichstein et al., 2019). Recent studies have built statistical emulators to quantify the impact of basal melt on dynamic ice-sheet model behaviour (Berdahl et al., 2021), to investigate how different CO_2 emission scenarios affect ice-sheet model estimates for future sea-level rise (Edwards et al., 2021) and to probabilistically determine the contribution of a range of factors to future sea level (Fox-Kemper et al., 2021). For sea-level research, although Tarasov et al. (2012) created a neural-network-based emulator that can predict RSL chronologies based on a set of ice dynamic model parameters, there is currently no end-to-end GIA emulator that can predict global RSL variation history based on arbitrary ice models. In this study, we document a proof-of-concept attempt to build an end-to-end Graph neural network based EmulatOR for Glacial Isostatic Adjustment (GEORGIA) that can be used to rigorously explore global ice history uncertainty.

4.3 Methodology

Our goal is to build a statistical emulator that can predict global RSL variation based on a given global ice history from 25 ka BP to present. This can be treated as a supervised regression problem that maps the statistical relationship between input and output based on example input-output pairs generated by a physics-based GIA model. Below, we describe the example data generation, data pre-processing, and the methods used to build and validate our emulator.

4.3.1 Training Data

To provide example input-output pairs for training our emulator, we use a physics-based GIA model to calculate global RSL variation based on a collection of ice sheet reconstructions. The physical model we use is a gravitationally self-consistent GIA model that accounts for shoreline migration and Earth rotational feedback (Kendall et al., 2005; Mitrovica et al., 2005; Milne and Mitrovica, 1996). The solid Earth is represented by a spherically-symmetric Maxwell body consisting of an elastic lithosphere, and an upper and lower mantle extending to 670 km, and from 670 km to the core-mantle boundary, respectively. The GIA model calculates RSL change, caused by land deformation and the geoid response to ice-water mass redistribution, by solving the sea-level equation (Mitrovica et al., 2005) using a spherical harmonic truncation of degree and order 256. The elastic and density structure of the Earth model is derived from the Preliminary Reference Earth Model (Dziewonski and Anderson, 1981). Because the major focus of this study is to thoroughly sample ice history uncertainty, we do not incorporate Earth model parameter variation within the input data for our emulator. Instead, we adopt one specific Earth rheology that has a lithospheric thickness of 71 km and an upper and lower mantle viscosity of 0.3 and 70×10^{20} Pa s respectively (the 'low-viscosity' Earth model scenario from Lambeck et al., 2014).

One key task when building a GIA emulator is to generate a training database which evenly covers a wide range of possible deglaciation trajectories. We achieve this by collecting a wide range of ice history models for four different regions: North America

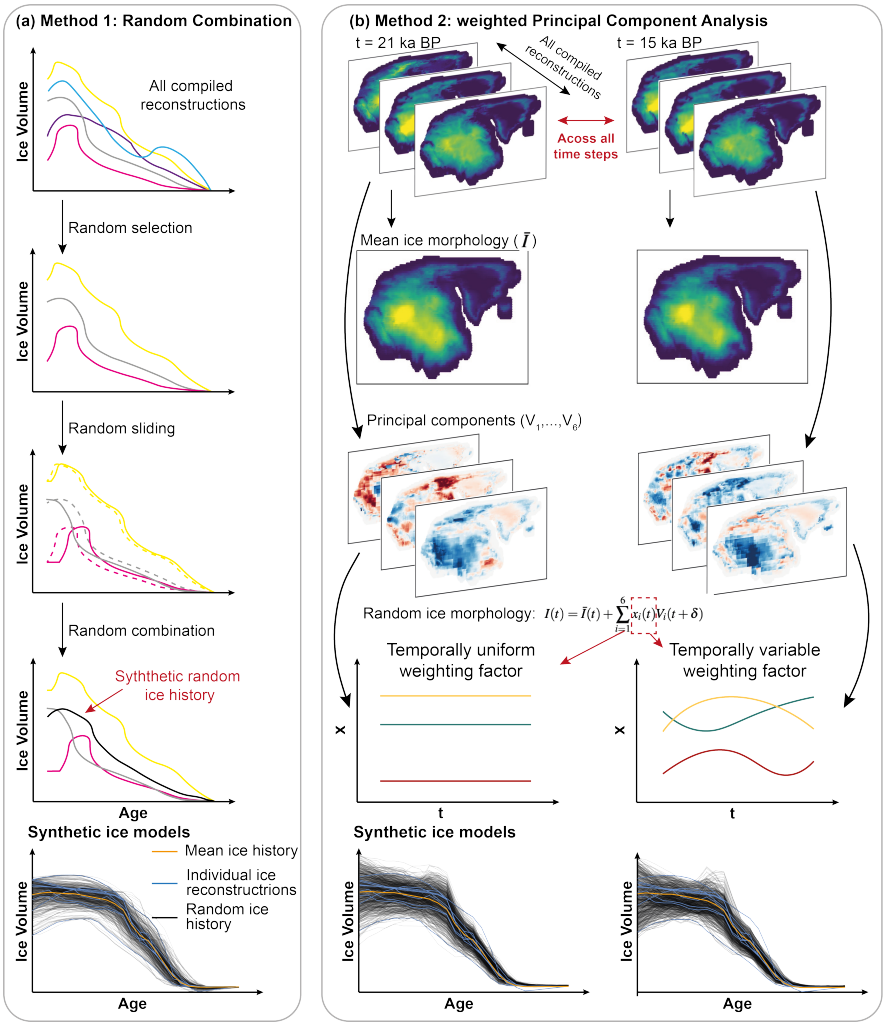

Figure 4.1: Illustration of the methods used to generate random synthetic ice histories from previous ice sheet reconstructions. (a) Random combination method, which consists of three randomised sampling procedures that reflect temporal (random selection and sliding) and spatial uncertainty (random selection and combination) in the underlying ice sheet reconstructions. (b) Weighted Principal Component Analysis method, which is implemented by calculating the mean ice sheet morphology and principal components of all time slices. From these, random ice sheet morphologies are generated via linear combination of the randomised principal components using two different temporal treatments of the random factor $x_i(t)$, which is illustrated by the equation with an asterisk. A detailed description of this equation can be found in section S4.2. The resulting synthetic random ice histories are shown in the bottom panel. All examples shown here are for the North American Ice Sheet, but the same approach was used to sample the Antarctic and Eurasian Ice Sheets, as well as mountain glaciers, to create a synthetic global ice history.

(including Greenland), Eurasia, Antarctica, and all other regions with mountain glaciers (including Patagonia), and sampling the spatio-temporal variability between

different reconstructions. In total, we use four global ice models that predict ice-sheet evolution in the four regions (Gowan et al., 2021; Peltier et al., 2015; Lambeck et al., 2014; Peltier, 2004), along with four North American (Roy and Peltier, 2018; Gowan et al., 2016a; Han et al., 2021; Tarasov et al., 2012; Tarasov and Peltier, 2003), four Eurasian (Clark et al., 2021; Han et al., 2021; Patton et al., 2017, 2016; Tarasov et al., 2014; Abe-Ouchi et al., 2013) and three Antarctic (Argus et al., 2014; Briggs et al., 2014; Whitehouse et al., 2012a,b) ice models. Because these ice models are reconstructed based on different principles (e.g., thermomechanical ice modelling, GIA modelling, and the interpolation of glacial geomorphological data), they provide good coverage of possible ice-sheet deglaciation uncertainty. Detailed information about each ice model is given in Table S4.1. We resample all the ice sheet reconstructions into a standardised format with 26 time slices (from 25 to 0 ka at 1 ka intervals) and spatial coverage corresponding to 256-degree spherical harmonic truncation, using linear interpolation as necessary. Because a GIA model is forced by ice thickness change rather than total ice thickness, we express all ice models in terms of ice thickness relative to present.

Using these standardised ice sheet reconstructions as building blocks, we generate a suite of randomised, synthetic ice histories that span the range of plausibility. We employ two main methods to systematically sample the spatio-temporal variability across different reconstructions– random combination and weighted principal component analysis (wPCA), the latter uses two approaches to account for temporal uncertainty. The random combination method samples the variability within the range bounded by previous reconstructions (Figure 4.1a), while the two wPCA approaches sample out-of-boundary variability, using two different approaches to account for long-term (e.g., grounded ice volume at the Last Glacial Maximum, Simms et al., 2019) and short-term (e.g., Meltwater Pulse 1A; Lin et al., 2021; Deschamps et al., 2012) temporal variability (Figure 4.1b). We provide a brief summary of these three approaches here, with a detailed description given in sections S4.1 and S4.2. The random combination method creates 500 synthetic ice histories by linearly combining different ice models into a new model. We randomly select 2-6 ice models for each region (i.e., random selection in Figure 4.1), and randomly translate each

in time (younger or older) in order to sample the temporal uncertainty. The new ice model is calculated to be the weighted average of the selected ice models, with the details determined using a set of random weighting factors. The second and third approaches use wPCA to extract important ice morphological patterns (i.e., principal components; PCs) from different ice models. A weighting scheme is applied to account for the spherical geometry of the Earth, which means that grid cells at different latitudes cover different areas. Using the extracted PCs, 1,000 synthetic ice histories (500 for each approach to temporal uncertainty) are generated by adding a random linear combination of the PCs to the mean ice history (Figure 4.1b; details in section S4.2).

After obtaining 1,500 synthetic ice histories for each region, we create global ice models by randomly sampling these regional ice model repositories and combining randomly selected regional ice models into a synthetic global model. This results in a global ice model that can contain regional ice histories generated by several different statistical methods. In total, we create 1,500 synthetic global ice histories, and for each we then simulate global RSL history from 25 ka to present, as described above. Because we express the input in terms of ice thickness relative to present, the modern ice thickness layer is a spatially uniform layer with all zero values, which contains no information. Therefore, we replace this layer with modern topography, which is important for calculating the continental levering and ocean siphoning processes (Mitrovica and Milne, 2002). Before being used to train a GIA emulator, we normalise all input and output data to ensure zero mean and unit standard deviation (more information in section S4.3). The 1,500 normalised input-output pairs are divided into training (80%), validation (10%) and testing (10%) sets.

4.3.2 Statistical Emulator

Using this training set, we now wish to build an emulator that can map ice history into RSL change. This is a typical machine learning problem, for which a convolutional neural network is commonly used. However, classical convolutional neural network algorithms are designed to perform convolution and pooling operations within Euclidean space, which is not appropriate when representing geographical

data such as ice or RSL history on a spherical Earth. Therefore, we use a graph-based spherical convolutional neural network (SCNN) algorithm that correctly implements convolution and pooling operations on data within a spherical manifold. We employ a Hierarchical Equal Area isoLatitude Pixelization (Healpix) scheme to build this spherical manifold, which produces a subdivision of a spherical surface where every pixel covers the same surface area (Gorski et al., 2005). This is an ideal property for emulating GIA processes because it ensures input ice thickness is proportional to the ice load applied to each grid cell. Furthermore, the SCNN algorithms used in this study use a graph filter that extracts information from nearby grid cells in a way that only depends on the distance between the grid centres, not on the direction. This ensures that information is rotationally equivariant. In other words, rotating the input ice history will result in an equivariant output RSL prediction. Rotational equivariance is desirable because it can significantly reduce the data sampling complexity. Underpinning these SCNN algorithms is a 3-layer U-Net (Ronneberger et al., 2015), a neural network architecture that is widely-used in regression and image segmentation problems (Lai et al., 2020; Yao et al., 2018) – see section S4.4 for more details. For this study, we adopt the SCNN algorithms from the *Deepshere* package (Defferrard et al., 2020, 2019), which has been successfully used in cosmological and weather prediction applications (Perraudin et al., 2019).

The emulator structure is governed by various hyperparameters, whose values influence the final emulation performance. Here we provide information on some key hyperparameters used in this study; a full list of the hyperparameters, along with definitions, is given in Table S4.2. A hyperparameter that should be noted is the Healpix sampling resolution. To achieve relatively fast emulation, we use a 16-degree Healpix sampling resolution ($n = 3072$), corresponding to $\sim$3.66 degree spatial coverage. All standardised input and output fields are interpolated onto 16-degree Healpix grids. Another essential hyperparameter for SCNNs is graph filter size, which determines the number of nearest-neighbourhoods included in each convolution process (i.e., spatial scale length). This is important for GIA problems because the solid Earth deformation signal tends to be long wavelength. For example, the peripheral bulge formed in response to loading of the North American Ice Sheet

can extend over 3,000 kilometres, to places like Barbados. In this study, we use a graph filter size of 60, corresponding to ∼1780 km radius.

We use a mean square error (MSE) loss function to quantify the misfit between emulator predictions and GIA modelling results and iteratively update model parameters by backpropagation (Goodfellow et al., 2016). Because the MSE loss function focuses on the misfit of each single grid point, we include two extra metrics to assess the overall quality of the emulation results: peak signal-to-noise ratio (PSNR, Korhonen and You, 2012) and structural similarity index measure (SSIM, Brunet et al., 2011). Both of these metrics are widely used to measure the quality of image and video compression (Wang and Bovik, 2009; Huynh-Thu and Ghanbari, 2008), with formal definitions given in section S4.5. A high PSNR value indicates low noise level, and vice versa, while the SSIM provides a similarity metric between 0 and 1 where a higher value indicates better emulation quality. Note that the SSIM is not directly correlated with either MSE or PSNR, and so can provide an independent assessment of output quality (Hore and Ziou, 2010). We also evaluate model performance by calculating the mean absolute error (MAE) because it provides a more indicative measurement of emulation error.

Finally, to assess the value of the SCNN model, and explore whether it is able to capture significant internal relationships between inputs and outputs, we also create a basic kernel model. When given previously-unseen inputs, this model simply finds the five most similar inputs from within the training set, and averages their known outputs. The misfit of this approach serves as a baseline for assessing the performance of the SCNN-based emulator.

4.4 Results and discussions

4.4.1 Emulator Performance

Using the trained SCNN-based emulator, which will be referred to as GEORGIA, we predict RSL variation results for 150 unseen testing examples. GEORGIA outperforms the kernel-based method on all evaluation metrics. Specifically, GEORGIA

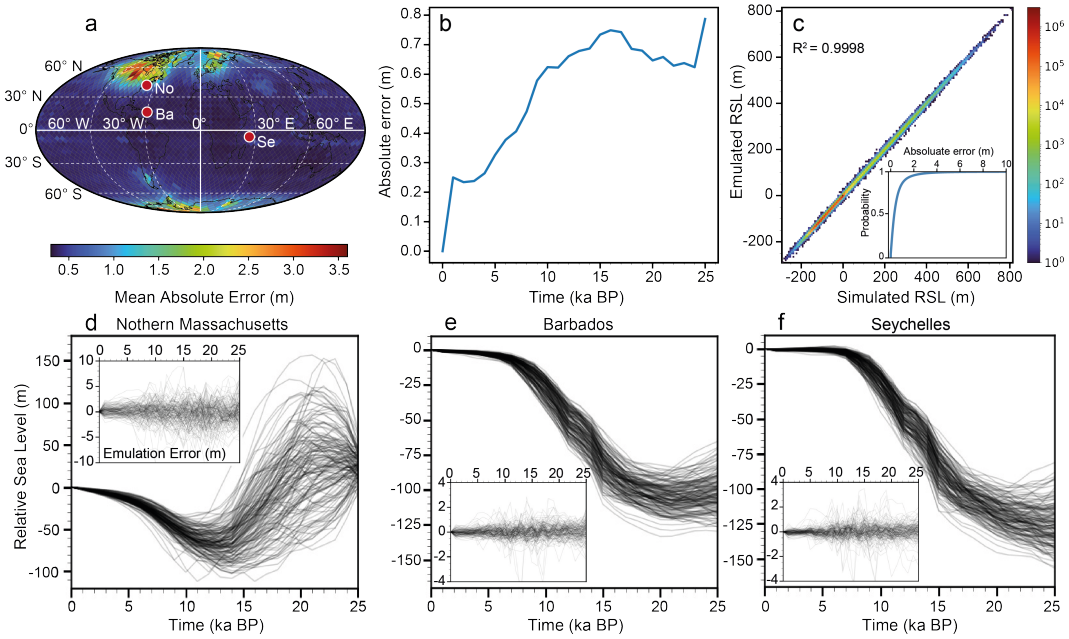

Figure 4.2: Emulator performance for the 150-member out-of-sample testing set. (a) Temporally-averaged spatial distribution of emulation error, locations here refer to typical near-, intermediate- and far-field sites: (No) Northern Massachusetts; (Ba) Barbados and (Se) Seychelles. (b) Spatially-averaged temporal variation of the emulation error. (c) 2-D histogram comparing the ground truth and emulator predictions. R^2 denotes the coefficient of determination. The subplot shows the cumulative probability of the absolute error. (d, e, f) RSL predictions generated using the physics-based GIA model for the 150-member test set, with emulation errors given in the subplots, at Northern Massachusetts, Barbados and Seychelles, respectively.

achieves an order of magnitude lower MSE (0.946 vs 29.53 m^2) and MAE (0.54 vs 5.84 m) along with distinctly higher PSNR (61.11 vs 46.18) and SSIM (0.9995 vs 0.9864) values. This indicates that the SCNN-based algorithm is able to capture the complex correlation between ice history and GIA-induced RSL history better than the baseline approach of finding similar training set pairs. The low MSE and MAE values, and the high PSNR and SSIM values, suggest a high-level of similarity between the RSL predictions generated by the emulator and the physical-based model. The 0.54 m MAE emulation error is also smaller than 87.8% of the 2σ RSL reconstruction uncertainties in a comprehensive sea-level database (Hibbert et al., 2018), suggesting a sufficient emulation accuracy.

The spatial and temporal distributions of emulation error between the physical and statistical models are show in Figure 4.2. The emulation MAE is strongly

heterogeneous in space (Figure 4.2a), with near-field regions showing large errors of up to 4 m, while errors in far-field regions (i.e., far from previous ice-sheet margins) are mostly below 0.5 m. This spatial heterogeneity reflects the spatial variability in the training set (Figure S4.1d), where near- and far-field RSL standard deviations can reach up to 500 m and 25 m, respectively, indicating that the average emulation error is 1-2% of the training variability. Considering the low emulation error, it is possible to use GEORGIA to perform large ensemble-based data-model comparison in order to refine ice history according to sea-level observations.

Temporally, emulation MAE peaks during the early stages of deglaciation (Figure 4.2b), when RSL is significantly different from present-day values (Figure 4.2b), and it decreases during the Holocene as global mean sea-level gradually approaches modern levels. Figures 4.2d,e,f show physics-based RSL predictions along with the emulation error at three typical near-, intermediate- and far-field sea-level sites. It is clear that although RSL predictions differ significantly between these sites, the temporal distributions of the emulation error follow an identical near-stationary trend, with larger emulation error occurring before the Holocene, similar to the global average pattern shown in Figure 4.2b. Considering this near-stationary and white-noise-like error distribution, we suggest that GEORGIA is able to capture the vast majority of correlation between ice history and the global RSL field.

Figure 4.2c provides an overall comparison between the physics- and statistical-based RSL predictions. It is clear that GEORGIA can well approximate the physics-based GIA model with a 0.9998 coefficient of determination (R^2) and no systematic error. 95.7% of the emulation results have a MAE of less than 2 m. In far-field regions, over 99% of the emulation results have a MAE of <2 m while 95% have a MAE of <1 m.

Although GEORGIA contains ∼33.8 million trainable parameters, it only takes 0.25 seconds to emulate RSL change through the last deglaciation on a Graphics Processing Unit (8GB NVIDIA GEFORCE RTX 3070 Ti). The computation time increases to 3.7 seconds when using a Central Processing Unit (Intel® CoreTM i9 14 Core Processor). This is 500 to 1000 times faster than the computation time of a physical forward GIA model. Considering the good emulation accuracy above, this emulator allows us to perform 500-1000 times more simulations within a

given computational budget – potentially making it feasible to employ a range of ensemble-based techniques for parameter estimation and uncertainty quantification.

4.4.2 GEORGIA Generalizability

A key question for any statistical emulator is generalizability: how does the emulator perform for arbitrary unseen inputs? For neural network based emulators, previous studies suggest that although they perform well in interpolation problems, they cannot meaningfully extrapolate non-linear functions (Xu et al., 2020; Goodfellow et al., 2016). In other words, while GEORGIA is effective for ice histories that are similar to those in our training set, GEORGIA may produce meaningless output if the input ice history comes from a significantly different distribution relative to the training set, such as putting an ice cap on Australia. This drawback means that in order to emulate a specific GIA problem, a well-designed training set is a prerequisite. Although our training set covers a wide range of possible ice histories by thoroughly sampling the spatio-temporal variability of previous ice-sheet reconstructions, this cross-reconstruction variability cannot describe the ice thickness uncertainty associated with poor knowledge of ice-sheet dynamical processes (e.g., large uncertainty in ice stream areas, Pittard et al., 2022; Albrecht et al., 2020; Tarasov et al., 2012) and ice margin chronology (Dalton et al., 2020). Therefore, incorporating more modelling results from physically-consistent ice sheet models that are constrained by empirical geomorphological evidence will be an important forward step to further improve the generalisation of GEORGIA.

4.4.3 Emulator Applications

Using GEORGIA, global RSL variation from 25 ka BP to present can be rapidly emulated using any ice history that is similar to our training set. Because our training set provides good coverage of possible deglaciation scenarios identified in previous studies, GEORGIA can predict RSL for most plausible ice models and therefore it can be used as a substitution for a physics-based GIA model in many applications. Additionally, benefitting from a modern machine learning framework, GEORGIA can

be used by other researchers with minimum requirements for programming experience or computational resources. Here, we provide two example GEORGIA applications, namely; (1) calculating the ice-sheet contribution to global barystatic sea level; and (2) mapping barystatic sea level in space and time.

4.4.3.1 Barystatic Sea Level Calculator

Barystatic sea level (BSL) describes the uniform shift of the global ocean surface due to ice-ocean mass exchange in the absence of gravitational effects and Earth deformation. It is a direct measure of global grounded ice volume change through time, and hence it is important for calibrating isotopic proxies and constraining ice-sheet variation history (Waelbroeck et al., 2002). However, for palaeo ice-sheet modelling studies, there is no straightforward way to calculate the ice-sheet contribution to global BSL without running a GIA model, due to the complexities associated with changes in global ocean area and topography (which impacts the grounded-floating ice transition). As a result, numerous studies (e.g., Gomez et al., 2020; Patton et al., 2017) only present their ice modelling results in terms of ice volume or an ice volume equivalent sea-level contribution (i.e., ice volume divided by modern ocean area). Based on our physics-based GIA modelling results, this latter approach overestimates the ice sheet contribution to global mean sea-level rise since 21 ka BP by 3.34 m (0.8-4.3 m depending on the adopted ice history), which is a non-negligible signal to consider.

Using GEORGIA, we provide a global BSL calculator that accounts for shoreline migration and the impact of solid Earth deformation on ice flotation (with detailed theory given in section S4.6). To test the accuracy of this GEORGIA-based BSL calculator, we compare its predictions to 150 examples of deglacial BSL history obtained using the physics-based model (i.e. those comprising the testing set). The results show emulation error (MAE) of 0.04 m. Thus, GEORGIA is a suitable tool to rapidly estimate the ice-sheet contribution to global BSL change, for example, as predicted by ice dynamic or general circulation models.

4.4.3.2 Barystatic Sea Level Map

A barystatic sea-level map identifies locations and times where local RSL approximates global BSL. Such sites are targeted by sea-level scientists to provide a close constraint on global ice volume. Because of spatially and temporally variable GIA-related perturbations to the gravity field and solid Earth surface (i.e., the non-barystatic signal), producing a BSL map requires robust estimates of the non-barystatic contributions to RSL. The detailed theory for calculating a BSL map was described in Milne and Mitrovica (2008) where they conclude that ideal locations to reconstruct palaeo BSL are where local RSL: (1) is relatively insensitive to plausible ranges in GIA model parameters (i.e., global ice history and solid Earth rheology); (2) closely approximates the barystatic value. Milne and Mitrovica (2008) provide a series of BSL maps at different time slices, based on GIA modelling results that use two ice histories (Bassett et al., 2005; Peltier, 2004), each paired with 162 plausible sets of Earth parameters. These maps have been used by the field community to target locations that approximate BSL during different parts of the deglacial period (e.g., Sefton, 2020; Woodroffe et al., 2015).

A major limitation of Milne and Mitrovica (2008) is that they only sample two ice models, and hence they are not able to thoroughly quantify the impact of ice history uncertainty on the resulting BSL estimates. Because GEORGIA has high computational efficiency while remaining sufficiently accurate for many applications (section 4.4.1), it is an ideal tool for testing the sensitivity of the BSL map to a large ensemble of ice histories. To produce a BSL map that represents ice history uncertainty, we emulate the global non-barystatic signal (i.e., RSL - BSL) for 10,000 randomly generated ice histories using the same methods introduced in section 4.3.1. Based on these emulation results, we calculate the probability that global RSL lies within 3 and 1 m of the barystatic value at 21 and 6 ka BP respectively (Figure 4.3).

Because uncertainty in the results of Milne and Mitrovica (2008, see their Figs. 6 and 7) largely reflects the uncertainty associated with radial mantle viscosity structure, combining their results with ours enables us to robustly identify regions where RSL approximates the global BSL value regardless of the choice of global ice history or

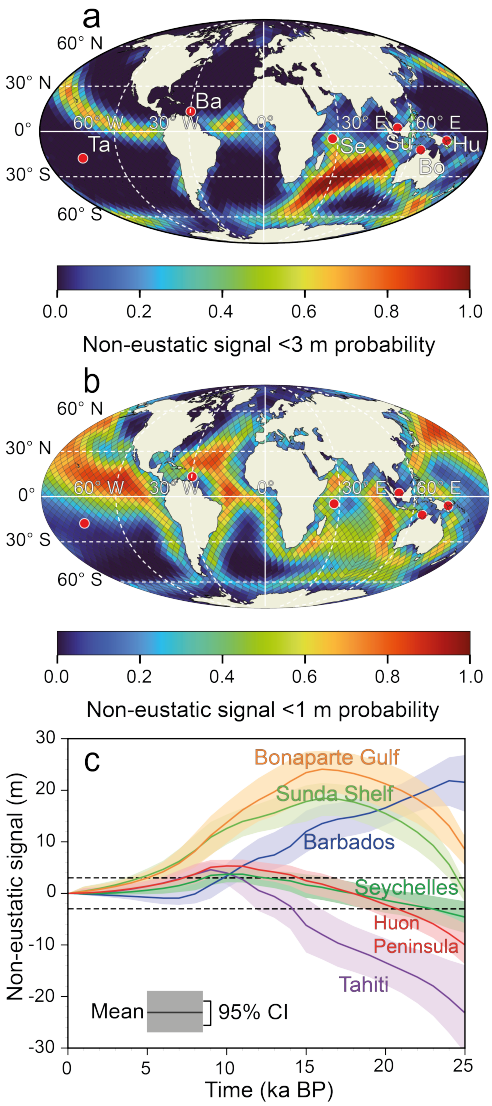

Figure 4.3: Barystatic sea-level maps based on 10,000 emulation results. (a) Probability that local RSL lies within 3 m of the barystatic value at 21 ka BP. (b) Probability that local RSL lies within 1 m of the barystatic value at 6 ka BP. (c) Temporal variation of the non-barystatic signal at six different sea-level sites. Note the confidence intervals shown here only reflect the uncertainty associated with combining 10,000 different ice histories with one Earth rheology. The area between the two black dashed lines represents the region where the non-barystatic signal is smaller than 3 m. Locations in (a) refer to (from west to east): Tahiti (Ta), Barbados (Ba), Seychelles (Se), Sunda Shelf (Su), Bonaparte Gulf (Bo) and Huon Peninsula (Hu).

radial mantle viscosity structure. We conclude that the southern Indian Ocean and southern Tasman Sea (close to south-western New Zealand) are ideal regions to reconstruct global BSL at 21 ka BP because it is highly likely that the non-barystatic signal here will be lower than 3 m, and predictions are insensitive to the Earth model

choice (Milne and Mitrovica, 2008). Although there is also a low non-barystatic signal shown in the mid-northern Pacific and mid Atlantic regions, these sites are not suitable for reconstructing global BSL because RSL is highly-sensitive to the choice of Earth rheology (Milne and Mitrovica, 2008). For the mid-Holocene, our map shows a broadly similar pattern to Milne and Mitrovica (2008), where optimal regions are the western and eastern Indian Ocean, the mid-northern Pacific Ocean and the mid-southern Atlantic Ocean. Meanwhile, agreeing with the results from Milne and Mitrovica (2008), the mid-southern Atlantic is not an ideal region for mapping mid-Holocene BSL.

In Figure 4.3c, we show the impact of ice history uncertainty on the temporal evolution of the non-barystatic signal at six locations that are commonly-used in sea-level studies (e.g., Lin et al., 2023; Webster et al., 2018; Woodroffe et al., 2015). Our results show that variations in the spatial and temporal distribution of the global ice sheets has a major effect on the magnitude of the non-barystatic signal, and a minor effect on the overall trend - the latter depends more on the Earth rheology, which we do not vary in this experiment. Regarding the six selected sea-level sites, as suggested in Milne and Mitrovica (2008), we confirm that Seychelles is a particularly good site to map global BSL history because it has a low uncertainty, minor non-barystatic signal throughout the last deglaciation (Figure 4.3c). Although Huon Peninsula is also predicted to have a small non-barystatic signal, and the uncertainty associated with ice history is small, this site is highly sensitive to the choice of Earth rheology (Milne and Mitrovica, 2008). In general, similar to the findings of Milne and Mitrovica (2008), who investigated the impact of the choice of Earth model on the non-barystatic signal, we find that uncertainty associated with poor knowledge of global ice history can reach up to 15/6 m at 21/6 ka BP, indicating that ice history uncertainty is an essential factor to consider when mapping global BSL history.

4.4.4 Future Development

In this study, we demonstrate that SCNNs can emulate RSL for a range of ice histories, assuming one specific Earth model. However, Earth rheology is a highly uncertain parameter that can result in hundreds of metres of RSL uncertainty in near-field

regions and tens of metres in far-field regions. Therefore, an ideal GIA emulator should be able to sample ice history and Earth rheological properties simultaneously. One way to achieve this would be to incorporate Earth rheological parameters into the input data. Taking a 1-D Earth model as an example, lithospheric thickness, upper and lower mantle viscosity can be represented by three spatially-uniform layers. This information could be embedded into the input data by stacking it with the ice history data, enabling mantle viscosity to be considered when performing the convolution operation. Another important aspect subject to future development is the spatial resolution of GEORGIA. The current version of GEORGIA only supports a 3.66 degree spatial resolution, which is insufficient to accurately reveal the ocean-continent transition zone, i.e., Figure 4.3 cannot resolve the coastal contour of global barystatic sea-level change. Although this problem could be solved directly by simply increasing the spatial resolution of GEORGIA, smart engineering is required to deal with the trade-off between emulation resolution and the computational demands of a specific modelling task. GEORGIA is an open source model and we hope that others will adapt it in the future to address a range of research questions.

4.5 Conclusions

Using a graph-based spherical convolutional neural network, we document the first attempt to build a statistical GIA emulator (GEORGIA) that can approximate global RSL variation history based on a given deglacial ice history. GEORGIA predicts RSL history 500-1000 times faster than a physics-based GIA model, with a mean absolute error of 0.54 m. Due to its low computation expense, it is a suitable tool for performing large-ensemble investigations of ice history uncertainty. By providing example applications of GEORGIA - calculating the ice-sheet contribution to global BSL change and creating a BSL change map - we demonstrate that GEORGIA will be a useful tool for improving our understanding of global ice and sea-level variation histories.

S4 Supplementary Information

S4.1 Random Combination of Ice Models

This section details the mathematical expressions used to generate a synthetic ice history based on a random combination of previous ice sheet reconstructions (Table S4.1). Starting from a set of regional ice histories with ice thickness $\mathbb{I}_i(t)$, we generate the synthetic ice model ($I(t)$) within a hierarchical framework:

$$I(t) = \sum_{i \in M} \sum_{j \in N} \mathbb{I}_i(t + \delta) W_j \tag{S4.1}$$

where M is an array containing randomly selected indices:

$$\begin{aligned} M &= (m_1, m_2, \cdots, m_n) \\ m &\sim [U(1, K)] \\ n &\sim [U(2, 6)] \end{aligned} \tag{S4.2}$$

U indicates a uniform distribution and [ ] means that all float numbers are rounded to their nearest integers. m and n control which original ice models are selected, and the number of random models being selected, respectively. K indicates the number of ice histories available for each regional ice sheet component.

δ in equation S4.1 is defined by:

$$\delta \sim [N(0, 2)] \tag{S4.3}$$

This is a Gaussian random noise model that moves the whole ice history younger or older. The selected ice history $\mathbb{I}_i(t + \delta)$ can be further expressed as:

$$\mathbb{I}_i(t + \delta) = \begin{cases} \mathbb{I}_i(25), & t + \delta > 25 \\ \mathbb{I}_i(t + \delta), & 0 \leq t + \delta \leq 25 \\ \mathbb{I}_i(0), & t + \delta < 0 \end{cases} \tag{S4.4}$$

where 25/0 is the first/last time step of ice history used in this study.

Lastly, W is an array containing random weighting factors for combining different ice models:

$$\begin{aligned} W &= (w_1, w_2, \cdots, w_K) \\ w_j &= \begin{cases} 0, & j \neq i \\ \sim Dir(\alpha), & j = i \end{cases} \\ \alpha &\sim U(0.2, 1) \end{aligned} \tag{S4.5}$$

Dir indicates a Dirichlet distribution, which is used to generate random weighting factors that fulfil the conditions $w_j \geq 0$ and $\sum(W) = 1$. The concentration parameter α describes how evenly information is drawn from the different ice models. A small α value will result in an uneven distribution of weighting factors (e.g., 0.80, 0.18, 0.01, 0.01), while a large alpha value will result in a more even distribution of weights (e.g., 0.23, 0.27, 0.24, 0.26), with information drawn more equally from the different ice models.

S4.2 Weighted Principal Component Analysis of Ice Models

This section details the mathematical expressions used to generate a synthetic ice history based on the weighted Principal Component Analysis (wPCA) approach. The wPCA approach is used to extract important ice morphological patterns from the initial set of reconstructions (Domingo et al., 2020). A weighting scheme is adopted to account for the spherical geometry of the Earth, which means that grid cells at different latitudes cover different areas. We apply a weighting factor to each grid cell that is proportional to its area. Using the wPCA approach, we calculate six principal components (PCs) for each ice-sheet region and time slice. This accounts for more than 99% of the variance, and hence captures most of the spatial variability. Synthetic regional ice morphology $I(t)$ at time t can then be generated by linearly combining different PCs:

$$I(t) = \bar{I}(t) + \sum_{i=1}^{6} x_i(t) V_i(t + \delta) \tag{S4.6}$$

$$\delta \sim [N(0, 2)] \tag{S4.7}$$

where $\bar{I}(t)$ represents the mean ice-sheet morphology at time t, x_i denotes the random weighting coefficient, and $V_i(t)$ is the i_{th} PC. To represent the temporal uncertainty within the ice sheet reconstruction, we applied a Gaussian random time shift δ (rounded to an integer, represented by square brackets) to each PC. This means that the final ice morphology can be influenced by temporally nearby PCs.

To further sample the variability of ice history, we use two methods to represent the random weighting coefficient x_i, with the first method using a temporally uniform coefficient and the second method using a temporally variable coefficient (see Figure 4.1). The first method is designed to represent general uncertainty associated with overall ice volume, and the second method is designed to reflect uncertainty associated with the short-term ice-sheet response to abrupt climate change (e.g., meltwater pulses). The temporally uniform coefficients are draw from a normal distribution with 0 mean and 1 standard deviation. The temporally variable coefficients are generated by creating a time series of random noise (0 mean and 3 standard deviation) and then applying a Gaussian filter (with 3 standard deviation) to smooth the temporal signal. The filtered signal is then standardised to maintain zero mean and unit standard deviation. Examples of the resulting random ice histories are given in Figure 4.1. We do not use the ice model from Han et al. (2021) when calculating PCs for the North American and Eurasian ice sheets because it has not been calibrated to fit any empirical constraints, and this may therefore lead to unrealistic variability.

S4.3 Data Normalisation

We normalised the input ice histories and output RSL variations using the expressions:

$$\tilde{I} = \frac{I - \mu_I}{\sigma_I} \tag{S4.8}$$

$$\tilde{RSL} = \frac{RSL - \mu_{RSL}}{\sigma_{RSL}} \tag{S4.9}$$

where I and RSL are 3-dimensional matrices, containing spatial and temporal information about ice thickness and RSL variation across 1,500 random examples. $\tilde{I}$ and $\tilde{RSL}$ are also 3-dimensional matrices representing normalised ice thickness and RSL variation values. μ_I/μ_{RSL} and σ_I/σ_{RSL} are 1-d arrays which contain spatial

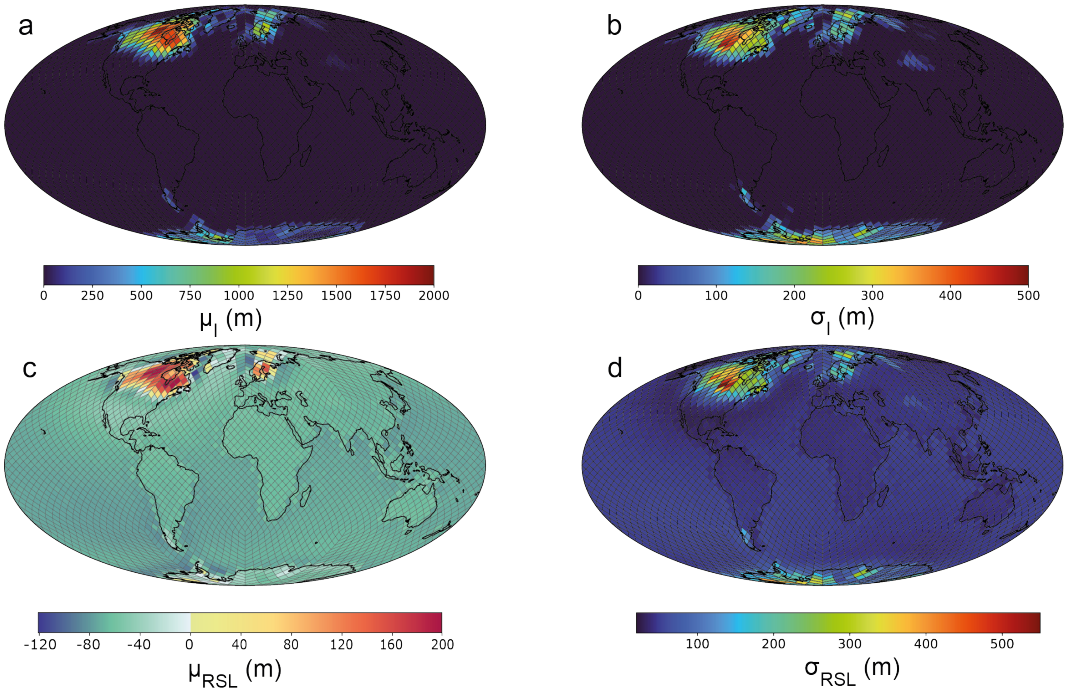

Figure S4.1: μ_I, μ_{RSL}, σ_I and σ_{RSL} mentioned in section S4.3. (a, b) Mean and standard deviation of ice thickness relative to present over all random ice histories and time slices. (c,d) Mean and standard deviation of relative sea-level variation induced by all random ice histories from 25 ka to present.

information about the mean and standard deviation of ice thickness/RSL across all time slices and random samples (see Figure S4.1).

S4.4 U-Net architecture

U-Net architecture (Ronneberger et al., 2015) is a widely-used convolutional neural network architecture that has been successfully applied to regression and image segmentation problems (Lai et al., 2020; Yao et al., 2018). This architecture consists of a contracting path and an expansive path (see architecture in Figure S4.2). The contracting path consists of three convolution blocks with two repeated convolution operations each followed by a rectified linear unit (ReLU) activation, followed by a max pooling operation. The expansive path then processes the feature information through a sequence of max unpooling, concatenation and convolution, to produce a high resolution prediction. The pooling and unpooling processes can be easily implemented within a Healpix sampling scheme, see Figure S4.3. The concatenation

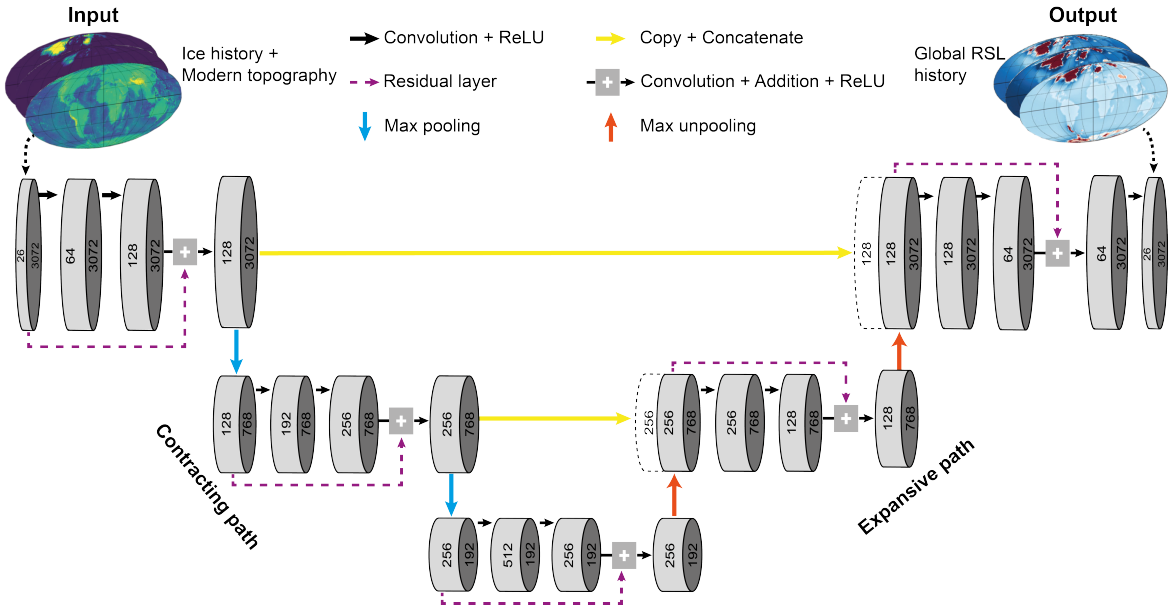

Figure S4.2: The spherical convolutional neural network U-Net architecture. U-Net consists of a contracting path and an expansive path, which gives it a U-shaped architecture. Arrows with different colours represent different operations within the network. For each step of operation, input and output data dimension is noted. ReLU = rectified linear unit activation.

operations pass the high resolution information from the contracting path to the expansive path which can effectively mitigate checkerboard artifacts in the outputs. Additionally, for each block in the contracting and expansive paths, we add a residual layer to create a shortcut for passing information from the start to the end before the ReLU activation function, which has been shown to mitigate the vanishing gradient problem for deep neural networks (Srivastava et al., 2015).

S4.5 Peak signal-to-noise ratio and structural similarity index measure

Peak signal-to-noise ratio (PSNR) and structural similarity index measure (SSIM) are two metrics that are widely used in measuring the quality of image and video compression (Wang and Bovik, 2009; Huynh-Thu and Ghanbari, 2008). Specifically, PSNR and SSIM can be expressed as:

$$PSNR = 10 \times \log_{10}(\frac{MAX^2}{MSE}) \tag{S4.10}$$

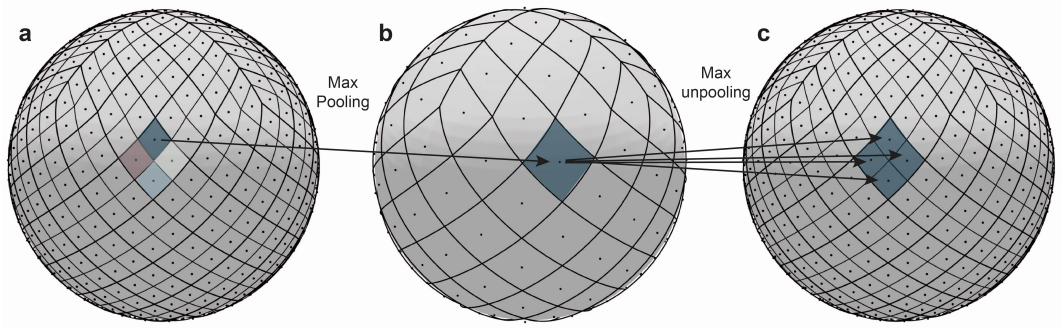

Figure S4.3: Pooling and unpooling within a Hierarchical Equal Area isoLatitude Pixelization (Healpix) sampling scheme. (a) Degree-8 Healpix of the sphere, $n = 768$. (b) Degree-4 Healpix of the sphere ($n = 192$), which can be seen as one level pooling from degree-8 Healpix. For max pooling, the maximum value within each 4-grid subdivision is assigned to the coarsened grid. (c) Same as (a) but illustrating the max unpooling process from degree-8 Healpix by copying the maximum value to the four grids within the original subdivision.

$$SSIM = \frac{1}{j^* \times T} \sum_{i=1}^{j^*} \sum_{t=1}^{T} \frac{(2\mu_{\hat{y}_{i,t}}^2 \mu_{y_{i,t}}^2 + c_1)(2\sigma_{\hat{y}_{i,t} y_{i,t}} + c_2)}{(\mu_{\hat{y}_{i,t}}^2 + \mu_{y_{i,t}}^2 + c_1)(\sigma_{\hat{y}_{i,t}}^2 + \sigma_{y_{i,t}}^2 + c_2)} \tag{S4.11}$$

where MAX is the absolute maximum value among all grids with MSE indicating mean squared error, and therefore a high PSNR value indicates low noise level. For SSIM, $\mu_{y_{i,t}}$ and $\sigma_{y_{i,t}}$ indicate the mean and standard deviation of $y_{i,t}$ (simulation result of a specific sample at a certain time interval) and $\sigma_{\hat{y}_{i,t}, y_{i,t}}$ is the covariance of a specific pair of emulation and simulation results. c_1, c_2 are trivial values for preventing a 0 denominator. SSIM provides a similarity metric between 0 and 1 where a higher SSIM value indicates better emulation quality.

Previous studies suggest that MSE and PSNR, which are based on point-by-point comparison, can perform well in assessing the quality of noisy images, but they cannot perform well when seeking to discriminate between the structural content of images because various types of degradations applied to the same image can yield the same value of MSE and PSNR (Hore and Ziou, 2010). Conversely, SSIM is correlated with the quality and perception of the human visual system, and it can therefore better discriminate structural content across different images. Note, SSIM is not directly correlated with either MSE or PSNR, and therefore they provide independent assessments of output quality.

S4.6 Barystatic sea-level calculation

In this study, we consider barystatic sea level as a direct indicator of global grounded ice volume through time ($BSL(t)$, Milne and Mitrovica, 2008), which can be expressed as:

$$BSL(t) = -\frac{\rho_{ice}}{\rho_{water}}\left[\frac{V_{ice}(t)}{A_{ocean}(t)} - \frac{V_{ice}(t_0)}{A_{ocean}(t_0)}\right] \tag{S4.12}$$

where ρ_{ice} and ρ_{water} denote ice and ocean water density; $V_{ice}(t)$ and $A_{ocean}(t)$ represents global grounded ice volume and global ocean surface area at time t, and t_0 represents the present day. To consider whether ice is grounded at each location (φ) and time (t), grounded ice volume ($v_{ice}(t,\varphi)$) can be defined as:

$$V_{ice}(t) = \int v_{ice}(t,\varphi)d\varphi \tag{S4.13}$$

$$v_{ice}(t,\varphi) = \begin{cases} 0, & i(t,\varphi) = 0 \vee i(t,\varphi) < \frac{\rho_{water}}{\rho_{ice}} b(t,\varphi) \\ v_{ice}(t,\varphi), & i(t,\varphi) \geq \frac{\rho_{water}}{\rho_{ice}} b(t,\varphi) \end{cases} \tag{S4.14}$$

where $i(t,\varphi)$ and $b(t,\varphi)$ denote ice thickness and bathymetry (positive value in ocean) at location φ and time t, and $b(t,\varphi)$ can be further expressed as:

$$b(t,\varphi) = b(t_0,\varphi) + RSL(t,\varphi) \tag{S4.15}$$

where $RSL(t,\varphi)$ indicates RSL prediction either by a physical simulator or the statistical emulator.

One important concept that should be noted is that the definition of BSL used here is a measure of global grounded ice volume, it does not reflect the magnitude of global mean sea-level rise that would occur if all grounded ice melts. This is due to the fact that some ice-sheets are marine-ground and hence the ice volume below flotation will not contribute to global mean sea-level rise. Based on our 1,500 forward modelling results, the difference between BSL and the magnitude of global mean sea-level rise since the Last Glacial Maximum can vary between 5 and 20 m.

Region	Model Name	Modelling Method	Reference
Global	PaleoMIST	Geomorphological evidence determined ice history assuming ice sheets are perfectly plastic and under equilibrium conditions	Gowan et al. (2021)
	ANU	Near- and far-field GIA modelling	Lambeck et al. (2017, 2014)
	ICE_6G	Near- and far-field GIA modelling	Peltier et al. (2015)
	ICE_5G	Near- and far-field GIA modelling	Peltier (2004)
North America	ICE-7G_NA	Near-field GIA modelling	Roy and Peltier (2018)
	NAICE	Near-field GIA modelling	Gowan et al. (2016a)
	Han_2021	Coupled ice-sheet and GIA modelling	Han et al. (2021)
	GLAC1-D-NA*	Glacial systems modelling with Bayesian style calibration	Tarasov et al. (2012); Tarasov and Peltier (2003)
Eurasia	BRITICE-CHRONO*	Geomorphological evidence determined ice history assuming ice sheets are perfectly plastic and under equilibrium conditions	Clark et al. (2021)
	Patton_2017	Thermomechanical ice modelling	Patton et al. (2017, 2016)
	Han_2021	Coupled ice-sheet and GIA modelling	Han et al. (2021)
	GLAC1-D-EUR	Glacial systems modelling with Bayesian style calibration	Tarasov et al. (2014); Abe-Ouchi et al. (2013)
Antarctica	W12	Ice sheet dynamic modelling	Whitehouse et al. (2012a,b)
	ICE6G_C	Near-field GIA modelling	Argus et al. (2014)
	GLAC1-D-ANT	Glacial systems modelling with Bayesian style calibration	Briggs et al. (2014)

Table S4.1: Ice sheet reconstructions used in this study. *For GLAC1-D-NA, we use two ice history scenarios for the North American Ice Sheet (nn9927 and nn9894), and for BRITICE-CHRONO, we use two scenarios for the Eurasian ice sheets (1C and 1D).

Model hyperparameter	Value	Parameter description
Graph kernel size	40, 60	A parameter that determines the number of nearest-neighbourhoods included in each convolution process
U-Net depth	3, 4	A parameter that describes the number of convolution convolution/deconvolution blocks contained within the contracting/expansive path of U-Net
Sampling scheme	Hierarchical Equal Area isoLatitude Pixelization	This defines how does a sphere being discretised.
Healpix sampling resolution	Hierarchical Equal Area isoLatitude Pixelization degree 16	This corresponds to a ∼3.66 degree resolution
Activation function	Rectified linear unit activation	A function that produces non-linearity after each node.
Optimizer	Adam	An algorithm that modifies the weights of the neural network based on loss gradient.
Learning rate	0.001 with a constant decay rate of 0.8 for each 100 epochs	A hyperparameter that controls how much to change the model in response to the estimated error each time the model weights are updated
Batch size	8	The number of sub samples given to the network after which parameter update happens.
Training epoch	1500-2500 depending on the model convergence situation	A parameters determines total number of iterations of all the training data in one cycle for training the machine learning model.

Table S4.2: Model hyperparameters used to build or train GEORGIA.

CHAPTER 5

Discussions

In this chapter, section 5.1 returns to the aim, research questions and objectives (Chapter 1, Section 1.2) of this thesis and provides a brief overview of each Chapter. Section 5.2 summarises the key scientific findings of this thesis in relation to the research questions outlined in Chapter 1, including their relation to the wider literature and recent research that has emerged since the publication of the findings presented in Chapters 2-4. Section 5.3 then discusses the implications of these findings for future sea-level research. Finally, Section 5.4 discusses limitations and prospective directions for future research that have emerged from this body of work.

5.1 Review of research aim, questions and objectives

The main aim of this research was to develop novel physical and statistical modelling approaches to improve understanding at process, data and parameter levels and therefore resolve outstanding postglacial sea-level change questions relating to MWP-1A sources, the missing ice problem, and the spatio-temporal evolution of barystatic sea-level. A series of research questions and objectives were outlined in Chapter 1 in order to address this aim. These were:

RQ1 How much did the North American, Scandinavian and Antarctic Ice Sheets contribute to Meltwater Pulse 1A?

RQ2 Can we mitigate the missing ice problem by incorporating another physical process (sediment isostatic adjustment) that has not been considered before?

RQ3 Where might we find sea-level records that closely approximate barystatic sea-level change regardless of the detailed geometry of past ice sheet change?

5.2 Summary of principal findings

This section revisits each of the research questions (RQs) presented in section 1.2 and outlines the key findings of this thesis. I will first focus on introducing the framework created in each project to better understand the process, data and parameter levels

of a specific question using a series of physical and statistical modelling approaches. Based on these novel frameworks, detailed findings regarding three outstanding questions in postglacial sea-level change will then be presented.

5.2.1 RQ 1: How much did the North American, Scandinavian and Antarctic Ice Sheets contribute to Meltwater Pulse 1A?

The contribution of the North American Ice Sheet (NAIS), the Scandinavian and Barents Sea Ice Sheet (SIS) and the Antarctic Ice Sheet (AIS) to Meltwater Pulse 1A (MWP-1A) was assessed in Chapter 2 of this thesis. Specifically, we combined a comprehensive statistical framework with a glacial isostatic adjustment (GIA) model to improve the understanding of MWP-1A sources at process, data and parameter levels. At the process level, Chapter 2 proposed a method that translates the non-linear local relative sea-level (RSL) change at each location during MWP-1A into a linear inversion problem of the meltwater contribution from the NAIS, SIS and AIS. At the data level, because the linear inversion problem can be solved efficiently through a least squares algorithm (which requires minor computational resources), it allows us to use a Monte Carlo based probabilistic approach to thoroughly sample the sophisticated age and depth uncertainty distributions associated with different types of sea-level indicator. We also tested two methods of representing the depth-habitat uncertainty for coral records, i.e. an empirical and uniform scenario, which therefore ensures a robust interpretation of coral records. Furthermore, we created a novel way to incorporate geological interpretations of isolation basin stratigraphic transitions as an extra constraint in the inversion algorithm, which significantly reduces the inversion uncertainty. All of these uncertainty sources have been taken into account in the final inversion results. Lastly, the parameter level is improved by performing a large ensemble of forward modelling with different combinations of uncertain physical parameters (e.g., Earth rheological parameters and global ice models) in order to test the inversion sensitivity.

Based on sea-level data from six geographically distributed sites, our inversion results suggest contributions from Antarctica, 1.3 m (0-5.9 m; 95% probability), Scandinavia, 4.6 m (3.2-6.4 m) and North America, 12.0 m (5.6-15.4 m), giving a global mean sea-

level rise of 17.9 m (15.7-20.2 m) in 500 years. Compared with the results of previous sea-level fingerprinting analyses, which are under-constrained and often non-unique due to the spatial and temporal scarcity of sea-level records across MWP-1A (Liu et al., 2016; Gomez et al., 2015; Bassett et al., 2005), the new inversion framework along with new sea-level data from Northwest Scotland and the Great Barrier Reef enable us to derive a unique solution of MWP-1A sources. An NAIS-dominant scenario with a substantial SIS and a minor AIS contribution to MWP-1A agree well with recent regional ice-sheet reconstructions (Tarasov et al., 2012; Peltier et al., 2015; Lambeck et al., 2017; Brendryen et al., 2020; Gomez et al., 2020; Albrecht et al., 2020).

Since the publication of the results presented in Chapter 2, there have been a series of discussions about regional RSL change during MWP-1A, MWP-1A sources, ice-sheet dynamics, meltwater injection impact on ocean circulation and global climate, and coastal, ecological evolution and human migration related to MWP-1A. Two independent sea-level reconstruction studies (Best et al., 2022; Dawson et al., 2022) further refine the RSL change history during MWP-1A across Scotland (specifically, data are from the islands of Skye, Jura and Islay) based on isolation basins and emerged palaeo shorelines, both of which suggest a steady local RSL fall during MWP-1A. This evidence agrees well with the Northwest Scottish sea-level data and the stratigraphic interpretation of the isolation basins presented in Chapter 2 and it further supports our interpretation that no sea-level oscillation occurred in Scotland during MWP-1A and an Antarctic-dominant scenario should be refuted.

Regarding regional ice-sheet dynamics, numerous studies published since our study provide additional field-based empirical evidence on the NAIS, SIS and AIS around MWP-1A. For the NAIS, several studies provide additional chronological control on the evolution of the Laurentide and Cordilleran Ice Sheets. Stoker et al. (2022) and Norris et al. (2022) present new cosmogenic ^{10}Be and ^{14}C exposure ages that suggest the splitting of the Laurentide and Cordilleran Ice Sheets initiated slightly before MWP-1A with a substantial ice-sheet saddle collapse observed in the north between 14.9 and 13.6 ka BP (Gregoire et al., 2012). For the southeastern Laurentide Ice Sheet, new cosmogenic exposure ages provide evidence for 1000 m of ice sheet

thinning between 15 and 13 ka BP, coinciding with MWP-1A (Halsted et al., 2022). While seismostratigraphic profiles from northern Baffin Bay (northeastern Laurentide Ice Sheet) show distinct ice stream acceleration during MWP-1A (Couette et al., 2022). Together, the evidence for ice sheet saddle collapse, fast ice sheet recession and accelerating ice streams are in general agreement with a dominant NAIS scenario, as deduced from our sea-level fingerprinting analysis.

Similarly, a new SIS ice sheet reconstruction derived by dynamic ice-sheet modelling and constrained by palaeoceanographic data (Sejrup et al., 2022) supports our suggestion that the separation of the Barents Sea Ice Sheet and the Fennoscandian Ice Sheet (Brendryen et al., 2020) can produce a substantial contribution to MWP-1A. Additional evidence for a substantial SIS contribution is provided by a sediment core from the upper continental slope of the western Barents Sea which shows rapid deposition of laminated sediments on top of an ice-rafted-debris layer dated to between 15.1 and 14.3 ka BP (Jessen et al., 2010). Conversely, for the AIS, despite the increasing number of studies employing cosmogenic nuclide exposure dating there is no evidence for rapid ice-sheet thinning coincident with MWP-1A across Antarctica, including in the Ellsworth Mountains (Bentley et al., 2010), the Prince Charles Mountains (White et al., 2011), the Transantarctic Mountains (Jones et al., 2015) and Dronning Maud Land (Suganuma et al., 2022). This field-based evidence points to a minor AIS contribution to MWP-1A, consistent with our results.

The above-mentioned community efforts of field-based ice-sheet reconstruction and sea-level-based analysis provide confidence that we now have a reconciled solution of MWP-1A sources. These better-constrained MWP-1A sources provide insight into the possible causes of the abrupt palaeoclimate changes that were concurrent with MWP-1A (Kapsch et al., 2022). Around the same time as the 15-20 m global mean sea-level (GMSL) rise that took place during MWP-1A (14.65-14.3 ka BP, Deschamps et al., 2012), Northern Hemispheric temperatures increased 4–5°C within just a few decades (Buizert et al., 2014; Lea et al., 2003) during BØlling–AllerØd warming (14.7-13.0 ka BP, Ivanovic et al., 2016). Interestingly, this Northern Hemisphere warming coincides with a gradual cooling (0-0.5 °C in 500 years, Shakun et al., 2012) in Antarctica (the Antarctic Cold Reversal, 14.7-13.0 ka BP; Pedro et al.,

2016). During MWP-1A, previous studies suggest fast meltwater influx into the Atlantic Ocean (Ivanovic et al., 2016; Lambeck et al., 2017; Tarasov et al., 2012), which is incompatible with a vigorous Atlantic Meridional Overturning Circulation (AMOC) (McManus et al., 2004) because most climate models predict AMOC to be strongly weakened under rapid freshwater influx (Ivanovic et al., 2017; Menviel et al., 2011; Liu et al., 2009). Since the oceanic response to meltwater influx is highly sensitive to the locations of freshwater discharge, combining the detailed probability density distributions of MWP-1A sources provided in our study with a high-resolution freshwater routing model (Love et al., 2021; Wickert et al., 2013) may better explain the observed inter-hemispheric temperature difference. The reason for this bipolar see-saw phenomenon is the formation of ocean bottom water in both poles take a long time to cause temperature change in the other hemisphere (e.g., several hundreds of years Barker et al., 2009). Future study should focus on bridging the knowledge from this study with different earth systems to better understand the sequencing of ice-ocean-climate interactions during this abrupt climate change event.

5.2.2 RQ 2: Can we mitigate the missing ice problem by incorporating another physical process (sediment isostatic adjustment) that has not been considered before?

As mentioned in Chapter 1, the missing ice problem refers to the distinctive imbalance between observed GMSL rise and the reconstructed amount of ice-sheet melt (Clark and Tarasov, 2014) since the Last Glacial Maximum (LGM). In Chapter 3, we focused on better describing the process level of estimating GMSL from sea-level records from the Great Barrier Reef (GBR), the world's largest mixed carbonate-siliciclastic passive margin. We investigated how sediment isostatic adjustment (SIA), a physical process that has not been considered in most sea-level studies, impacts on local relative sea-level (RSL) change. At the process level, we decomposed the RSL change into an ice-ocean mass exchange component and a sediment mass loading component, which are described by a GIA and a SIA model. A Bayesian framework was developed to simultaneously calibrate SIA and GIA model parameters (i.e., global ice history, sediment deposition history and Earth rheology; parameter level) using a sea-level

database with detailed treatment of uncertainties from different sources (data level). Because the adopted sediment deposition model consists of four different sub-models of different sediment components (containing >40 parameters to calibrate), we built a statistical emulator for the SIA process, which allows us to thoroughly sample the parameter space within an acceptable computation time.

Based on our results, 1853.7 Gt (1613.1-2078.7 Gt, 95% confidence interval) of sediment has been deposited across the GBR since 28 ka BP, causing spatially variable relative sea-level change with the highest magnitude (1.1 m) found on the outer shelf of the southern central GBR. Because SIA-induced RSL rise is unrelated to ice mass loss, failing to correct for this signal in the GBR will lead to systematic overestimation of grounded ice volume by up to $\sim 4.3 \times 10^5$ km^3 during the LGM. This demonstrates that caution is needed when estimating global ice volume from sea-level data collected from margins characterised by high sediment input across large spatial areas. This applies to all global locations that have yielded RSL records for the Last Glacial Maximum (LGM), namely, Noggin Pass (GBR), Hydrographer's Passage (GBR), Bonaparte Gulf (NW Australia), Sunda Shelf and Barbados (Ishiwa et al., 2019; Yokoyama et al., 2018; Webster et al., 2018; Hanebuth et al., 2009, 2000; Yokoyama et al., 2000; Fairbanks, 1989). In particular, sediment cores from NOG, HYD and Barbados were collected from large coral reef frameworks near large estuary systems (Woodroffe and Webster, 2014) which are likely to have been affected by RSL rise due to reef and siliciclastic sediment loading. Although distant from large coral reef systems, Bonaparte Gulf and Sunda Shelf are located near major river mouths (Pico, 2020), and they may record some SIA signals caused by siliciclastic sediment deposition. In all cases, incorporating the SIA process will reduce the global grounded ice volume estimate for the LGM, which will help to mitigate the current disagreement between the magnitude of post-LGM GMSL rise recorded by RSL indicators and the estimated amount of ice melt (Simms et al., 2019).

Another implication of this project is that, RSL data is not only useful for constraining global grounded ice volume but also for constraining other physical processes and their associated parameters. For example, based on RSL data across the GBR, this thesis reconstructs the spatio-temporal distribution of the SIA signal as well

as providing a complete reconstruction of the sediment accumulation history which shows good consistency with previous carbonate budget based reconstructions (e.g., Hinestrosa et al., 2022; McNeil et al., 2022; Rees, 2005). However, since a large part of the missing ice problem still cannot be explained even after incorporating the SIA signal, it is important to develop and calibrate models which represent other physical processes that may affect RSL change as in Chapter 3 (more details in section 5.3.1 below).

5.2.3 RQ3: Where might we find sea-level records that closely approximate barystatic sea-level change regardless of the detailed geometry of past ice sheet change?

A barystatic sea-level (BSL) map identifies locations and times where local RSL approximates global BSL. Such sites are targeted by sea-level scientists to provide a close constraint on global ice volume. Because of spatially and temporally variable GIA-related perturbations to the gravity field and solid Earth surface (i.e., the non-barystatic signal), producing a BSL map requires robust estimates of the non-barystatic contributions to RSL. Chapter 4 focused on producing a robust BSL map with minimum dependency on the assumed global ice history. In other words, we attempted to improve the parameter level of calculating a BSL map. In order to achieve this, we had to address two outstanding questions: (1) how can we create a series of plausible global deglaciation histories that well represent the ice model spatio-temporal uncertainty distribution? (2) how can we densely sample the ice model uncertainty distribution with limited computational resources?

Chapter 4 developed two statistical methods to randomly generate 1,500 synthetic ice histories based on previous reconstructions, which were then used as inputs for a GIA model to calculate global RSL and the non-barystatic signal. These 1,500 ice history-global RSL examples thoroughly sample the variability between published ice models based on several different reconstruction philosophies, hence, they represent up-to-date knowledge on the distribution of possible deglaciation trajectories. Using 1,200 of these examples as the training set, we built a GIA emulator that can accurately predict global RSL change based on a given ice model

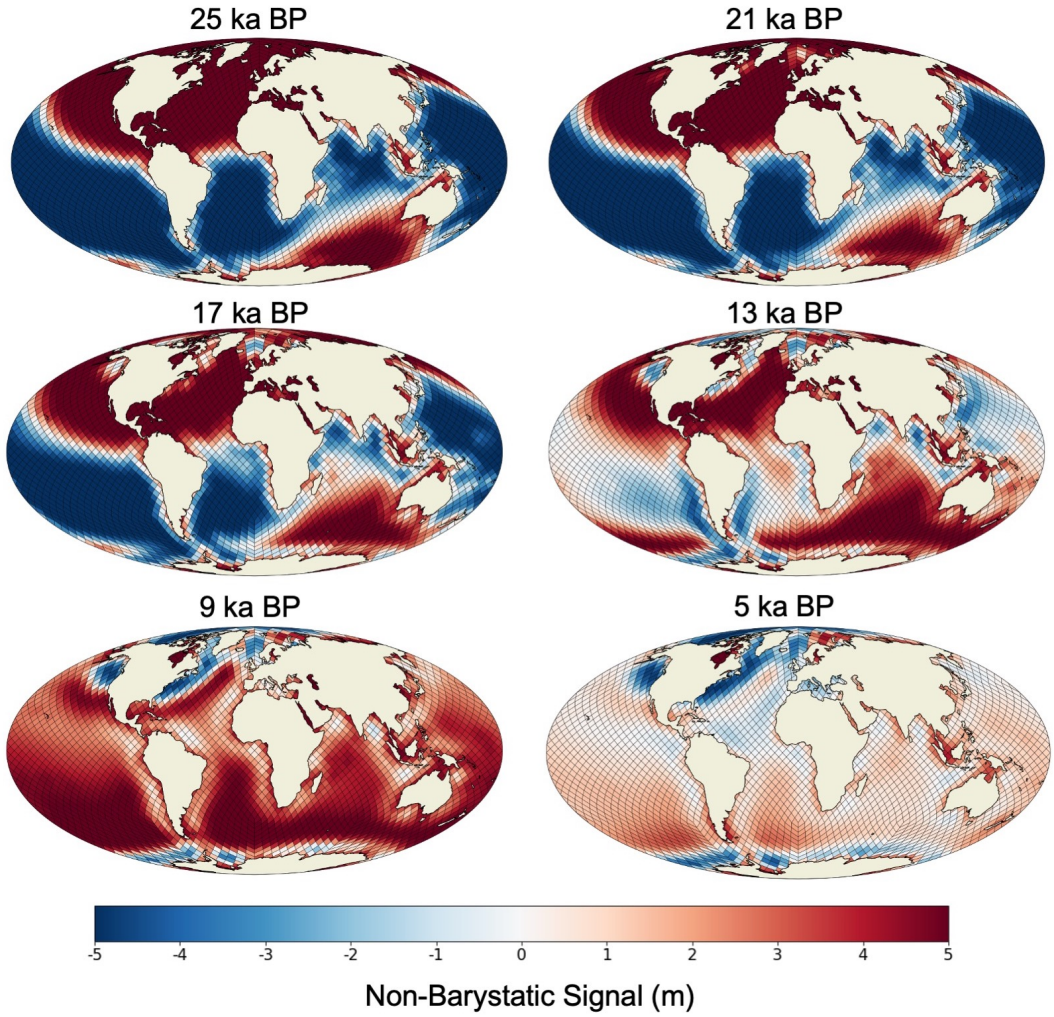

Figure 5.1: Ensemble mean global non-barystatic signal maps based on 10,000 emulation results. Note, the non-barystatic signal is the difference between local RSL and the global BSL value, where the blue/red colour indicates local RSL is lower/higher than global mean sea-level (or the barystatic signal).

and requires 500-1000 times smaller computational resources than a physics-based GIA model. Using this GIA emulator, we estimated global non-barystatic signals for 10,000 possible deglaciation histories (generated by the two statistical methods mentioned above). Using these ensemble-based results, we produced probabilistic BSL maps at 21 and 6 ka BP (Figure 4.3) along with a series of 10,000-member ensemble means of the non-barystatic signal at 25, 21, 17, 13, 9, and 5 ka BP (Figure 5.1).

Because the spatio-temporal histories of these 10,000 synthetic ice models vary

substantially from each other (see section 4.4), the resulting non-barystatic sea-level map indicates ideal locations to reconstruct the barystatic signal with minimum dependency on the assumed global ice history. It can be seen in Figure 5.1 that, during the LGM (25 and 17 ka BP), the large continental ice sheets are predicted to have produced strong perturbations to the solid Earth surface and the global gravitational and rotational fields, resulting in large non-barystatic signals in most locations. In particular, RSL in near- and intermediate-field regions was substantially higher than the global average (dark red areas) due to continental ice sheet-induced solid Earth subsidence and gravitational pull. In contrast, to compensate for high RSL in the near- and intermediate-field, far-field RSL was mostly lower than GMSL (dark blue areas) with only the southern Indian Ocean and part of the Southern Ocean showing higher than average RSL due to GIA-induced true polar wander (solid-body rotation of a planet with respect to its spin axis), which drives much of the azimuthal asymmetry in RSL predictions (Gomez et al., 2015; Mitrovica et al., 2011; Milne and Mitrovica, 1996). Between areas with a significant non-barystatic signal, regions with a minor non-barystatic signal can be found in the southern Indian Ocean, mid Pacific and Atlantic Oceans and the ocean-continent transition zones of South America, mid-southern Africa, southeastern Asia and Australia.

During a rapid GMSL rise period between 17 and 13 ka BP, regions with a minor non-barystatic signal slightly expanded, with part of the southeastern and north-western Pacific Ocean and southern Atlantic Ocean closely approximating the global BSL value. After 13 ka BP, as the ice sheets continued to melt, GMSL gradually approached its present-day level, indicating a near-zero global BSL signal. At 9 ka BP, due to the ocean syphoning mechanism (a process whereby peripheral bulge subsidence increases the capacity of the ocean and results in a fall in mean sea surface height; Mitrovica and Milne, 2002), RSL across most of the global ocean was higher than BSL, leaving only a minor part of the mid-northern Pacific area, along with the outer ocean-continent transition zone around South America, Africa and Eastern Asia, suitable for reconstructing the barystatic signal. With global ice melt gradually ceasing after 9 ka BP, the global non-barystatic signal steadily moved towards zero and more far-field regions became suitable for reconstructing the BSL signal.

It should be noted that ice history is only one of the two key inputs for a GIA model, and to estimate a robust BSL map, BSL sensitivity to another key parameter, Earth rheology, should also be tested. Milne and Mitrovica (2008) implemented a BSL sensitivity test with 162 Earth rheological models and provided a sensitivity map associated with Earth rheology at 21 and 6 ka BP (see their Figures 6 and 7). Based on their results, some locations should be excluded from BSL studies due to their high-sensitivity to uncertainty in Earth rheology. This includes the mid-Northern Pacific and Southern Ocean regions at 21 ka BP and the southern Pacific, southern Atlantic and southern Indian Oceans at 6 ka BP (Figure 5.1).

By providing the first proof-of-concept study to build an end-to-end GIA emulator, GEORGIA offers a new way to probabilistically quantify the uncertainties in GIA-induced RSL variation that are related to poorly-constrained global ice history. Compared with other components of Earth system, such as global mean surface temperature, global mean thermosteric sea level and ice sheet extent, whose epistemic and aleatory uncertainties have been efficiently quantified by statistical emulation and propagated into future sea-level projections within a consistent framework (Kopp et al., 2023; Fox-Kemper et al., 2021; Edwards et al., 2021; Nauels et al., 2019; Palmer et al., 2018; Nauels et al., 2017), GIA-induced uncertainties in RSL projections are often based on the variability between just a few ice models (e.g., Palmer et al., 2020). This can lead to a systematic underestimate of GIA-related uncertainty in future sea-level projection. Given the accuracy achieved by GEORGIA with relatively minor computational power, it may provide a novel way to sample GIA uncertainties.

5.3 Review of methodological advances

Compared with previous studies, the physical and statistical models developed in this thesis show the following advantages:

- Robust model uncertainty quantification: Reliable model uncertainty quantification is a prerequisite for drawing any rigorous conclusions. Unlike most GIA studies which typically use a small number of ice and Earth model combinations

(e.g., Gomez et al., 2015; Bassett et al., 2005), the results presented in this thesis are based on relatively large ensembles of forward modelling. In cases where solely relying on forward modelling would require overly large computational resources, multiple statistical emulators have been developed to mimic the behaviour of physical models thus reducing the computational burden by several orders of magnitude. All of these advances ensure the robust quantification of modelling uncertainties and the reliable interpretation of modelling results in this thesis.

- Better sea-level data representation: As mentioned in Chapter 1, although sea-level reconstructions are often accompanied by multiple sources of complicated uncertainties, most studies assume the uncertainties to be normally distributed (e.g., Khan et al., 2019). This simplification results in a loss of information when carrying out model calibration. This drawback is improved by the framework introduced in Chapter 2 which is able to propagate the full uncertainty probability distribution into the final inversion results.

- Alternative statistical inference methods: This thesis adopted both frequentist and bayesian methods to infer the answer to specific postglacial sea-level change questions. Chapter 2 used a frequentist method to sample the geophysical modelling and sea-level reconstruction uncertainties because the problem being investigated was not too complex and there was not enough knowledge to set informative priors. However, Chapter 3 developed a bayesian-style approach that allows informative priors, based on geomorphological and sedimentological evidence, to be set, and for these priors to provide a powerful constraint on the final inversion results.

5.4 Directions for future research

Understanding the mechanisms behind postglacial sea-level change and reconciling model predictions with observational data requires a holistic understanding of the impact of multiple physical processes on sea-level change at different spatio-temporal scales and their associated parametric uncertainties, along with careful consideration

of the underlying uncertainties inherited from various types of sea-level data. By developing better physical and statistical models to address three particular questions, the methodologies presented in this thesis should motivate further research into postglacial sea-level change at the process, data and parameter levels.

5.4.1 Process level

To further refine our process-based understanding of postglacial sea-level change, future research should focus on (i) developing next-generation physical models with better representations of the real-world; and (ii) incorporating more process-based physical models which have not been considered before. For the former, taking GIA modelling as an example, although a 1-D spherically symmetric solid Earth model with Maxwell rheology is still a widely-used technique because it is well-benchmarked and has decent computational efficiency (Martinec et al., 2018; Spada et al., 2011), there have been an increasing number of physical models developed during the past decade which better represent the solid Earth rheological properties observed in laboratories and seismological studies. This includes models with laterally heterogeneous lithospheric thickness and mantle viscosity (i.e., 3-D GIA models; Pan et al., 2022; Austermann et al., 2022; Powell et al., 2021; Li et al., 2020, 2018; Nield et al., 2018; Austermann et al., 2013), stress-dependent mantle viscosity or Non-Newtonian rheology (Kang et al., 2022; Blank et al., 2021; van der Wal et al., 2015) and transient rheology (Lau, 2023; Ivins et al., 2022; Caron et al., 2017). These models have already been shown to have a profound impact on the resulting RSL predictions (Kang et al., 2022; Simon et al., 2022), especially across near- and intermediate-field regions, which may yield novel insights into postglacial sea-level change and the corresponding global ice history. However, multiple challenges remain, including identifying whether incorporating such rheology can better reconcile model predictions with observations or the opposite (see an example in Peltier et al., 2022), and how to efficiently update ice models (which have traditionally been tuned assuming a 1D Earth model and hence might be biased Whitehouse et al., 2006) given that these more sophisticated physical models are computationally very expensive (running a 3-D GIA model usually takes more than 2 days).

In parallel with developing more sophisticated physical models, incorporating more physical processes within an integrated framework is also an essential step. As illustrated in Chapter 3, although considering SIA might reduce the magnitude of the missing ice problem, this problem remains largely unsolved. Consideration of additional process-based physical models is required to further reduce the observed imbalance. In light of the potential RSL change magnitude caused by each unconsidered physical process (see Figure 1.1), the spatio-temporal pattern of RSL change associated with steric effects, groundwater/postglacial lake variation and tidal range variation should be assessed with priority (Austermann et al., 2022; Callaghan et al., 2021). Based on the results from Simms et al. (2019) and Gebbie et al. (2019), both groundwater and steric effects are able to contribute sub-metre to multi-metre scale RSL contributions, but the detailed spatio-temporal evolution related to each of these remains unexplored. Similarly, despite Griffiths and Peltier (2009) showing that tidal ranges were significantly different during the LGM, which can systematically bias sea-level reconstruction results by up to 2 m, most sea-level reconstructions do not seek to account for this. Lastly, although the effects of mantle dynamic topography and tectonic movement on RSL are more prominent over longer timescales (de Gelder et al., 2022; Mitrovica et al., 2020; Austermann et al., 2017), it may be useful to evaluate whether they have the potential to introduce a signal that is detectable in LGM-age sea-level indicators.

It should be noted that this thesis only uses deterministic physical models to describe postglacial RSL change, not more statistically-based methods like spatio-temporal hierarchical Gaussian Process models that determine spatio-temporal RSL correlations purely based on the temporal and geographical proximity of sea-level data (Ashe et al., 2019; Khan et al., 2017). This is because such models cannot robustly capture the teleconnections revealed by physical models, such as sea-level fingerprints (Ashe et al., 2019), and most of the problems investigated in this thesis are at a global scale. Between purely physical- and statistical-based models, there are intermediate process level formulations that incorporate physical information into the construction of prior distributions for further statistical inference (e.g., Gaussian Processes, see (Creel et al., 2022; Ashe et al., 2019; Kopp et al., 2014, 2009)). These formulations

can also benefit from the better process-based physical models mentioned above.

5.4.2 Data level

As emphasised in this thesis, reconstructed palaeo sea-level has multiple uncertainty sources, including from coring, levelling, indicative meaning reconstruction, potential sediment compaction, potential tectonic movement, chronological measurement uncertainty and radiocarbon calibration uncertainty. To accurately reconstruct palaeo sea-level, each uncertainty source requires careful treatment and should be embedded into the final estimation of uncertainty. In addition, sea-level reconstructions from different studies should be standardised into a consistent format, such as Hibbert et al. (2018, 2016) used in this thesis and the HOLSEA format (Khan et al., 2019), to avoid structural bias due to inconsistent interpretations. Fundamental future work for better data level representation involves continuing to build community-based standardised sea-level databases with quality control and rigorous uncertainty quantification for each measurement.

Based on high-quality sea-level data, future modelling work should focus on building flexible hierarchical statistical frameworks to carefully incorporate multiple uncertainty sources. In particular, uncertainty sources with non-Gaussian errors (e.g. coral depth-habitat uncertainty, calibrated radiocarbon age uncertainty) should be propagated into results relating to the trend, rate and magnitude of sea-level change. Chapter 2 provided an opportunity to represent multiple uncertainty sources as data-specific empirical distributions, which could be thoroughly sampled by a Monte Carlo linear regression approach (i.e., assuming sea-level changes linearly) to quantify their impact on local sea-level rise estimation during MWP-1A. To infer sea-level time series with temporally-varying rates, Ashe et al. (2022) developed a statistical framework that is able to consider empirical uncertainty distributions on the vertical axis. There have been fewer attempts to calibrate physical model ensembles using empirically-derived data with complex vertical and age distributions. The only study to date is by Dyer et al. (2021) who measure the goodness of fit of a GIA model ensemble to coral-based sea-level data with an empirically-derived inverse-Gaussian distribution. Considering that the inverse-Gaussian distribution may not be suitable

for some coral species (e.g., Porites sp. which has a bimodal depth-habitat distribution) or radiocarbon ages, future work should aim to quantify the impact of such complex uncertainties on the inference of physical properties, such as ice history and Earth rheology.

5.4.3 Parameter level

Representing parametric uncertainty within postglacial sea-level change problems requires thorough sampling of possible parameter spaces. For the GIA modelling field, the major parameter spaces to sample are global ice history and solid Earth rheology. Chapters 2 and 3 provide examples of large-ensemble (each involving 400-800 forward GIA models) based approaches to sample Earth rheology parametric uncertainty using a 1-D GIA model, which is relatively computationally cheap to evaluate. Comparatively, ice history uncertainty is more difficult to sample due to its high-dimension along with the scarcity of empirical constraints, especially further back in time due to the erosive nature of glacial processes (Dalton et al., 2020). Therefore, thoroughly sampling ice history uncertainty often requires testing thousands to millions of possible ice models (see Tarasov et al. (2012)), which becomes computationally expensive even when using a 1-D GIA model. Chapter 4 revisits this problem by developing a GIA emulator. These approaches can be widely applied to 1-D GIA modelling problems for future research.

With more process-based physical models and more sophisticated physics involved, the demand for computational resources may increase dramatically and therefore prohibit large ensemble-based sampling approaches. To mitigate this problem, recent advances in Artificial Intelligence, especially in the field of machine learning for Earth system sciences, may provide directions for future development (Irrgang et al., 2021; Reichstein et al., 2019). For example, process-based GIA models could be accelerated by a machine learning based emulator. One problem with the GIA emulator developed in Chapter 4 is generalizability, which describes how well an emulator performs on arbitrary unseen inputs. To improve this problem, a promising direction for future research is to develop GIA-tailored neural network algorithms that can be informed by physics laws (i.e., a physics-informed neural network Raissi

et al., 2019). This approach has been suggested to achieve better performance and does not require a large or complete training data set (Arzani and Dawson, 2021).

For more sophisticated postglacial sea-level models, such as a 3-D GIA model, it is not realistic to generate several hundreds of training examples to build a statistical emulator. Therefore, future research should focus on developing novel approaches to accelerate the modelling process. Without this, sampling ice history uncertainty with a 3-D GIA model is not plausible. A possible way forward is to use tailored machine learning algorithms to learn the difference between 1D and 3D GIA modelling results. Once trained, these algorithms should be able to map RSL from 1D to 3D GIA predictions and hence enable large ensemble-based sampling of plausible ice histories by running a 1D GIA model instead.

CHAPTER 6

Conclusions

The main aim of this thesis was to improve our understanding of postglacial sea-level change problems by developing better physical and statistical models. To this end, novel modelling approaches have been developed to provide new insights into our understanding, at process, data, and parameter levels, of three outstanding postglacial sea-level change problems: meltwater pulse 1A sources, the missing ice problem and the barystatic sea-level map.

The potential sources of meltwater pulse 1A (MWP-1A) have been highly debated since the event was discovered in Barbados in 1989 (Fairbanks, 1989) due to the implications for understanding the cause of concurrent abrupt climate changes characterised by disruptions to oceanic and atmospheric circulation (Buizert et al., 2014; Fogwill et al., 2017). This thesis develops a framework to translate the MWP-1A source-detection problem into a series of linear inversion problems (process level) and simultaneously invert for the sources and magnitude of MWP-1A drawing on sophisticated treatment of uncertainties in sea-level data (data level) and geophysical models (parameter level). Importantly, this inversion includes the potential for a contribution from the Scandinavian Ice Sheet, which has not been considered in sea-level modelling

studies before. Our results suggest a dominant North American contribution, along with a substantial Scandinavian contribution and a minor Antarctic contribution, which shows good agreement with recent regional ice-sheet reconstructions (Tarasov et al., 2012; Peltier et al., 2015; Lambeck et al., 2017; Brendryen et al., 2020; Gomez et al., 2020; Albrecht et al., 2020), and therefore may lead to a reconciled solution of MWP-1A sources.

The missing ice problem, which refers to the large imbalance between observed global sea-level rise and the reconstructed amount of ice melt since the Last Glacial Maximum, is also a longstanding problem (Andrews, 1992) subject to great controversy (Yokoyama et al., 2022; Gowan et al., 2022, 2021; Simms et al., 2019; Clark and Tarasov, 2014). This thesis provides new insight into this problem by considering the sediment isostatic adjustment contribution to local sea-level rise (process level) in the Great Barrier Reef. Using a Bayesian-style approach, we calibrated a large ensemble of possible ice, sediment and Earth rheological models (parameter level) using sea-level observations and a detailed treatment of their vertical and age uncertainties (data level). Based on the calibrated results, sediment redistribution across the GBR contributed up to 1.1 m sea-level rise since Marine Isotope Stage 2. This result is of sufficient magnitude that this process should not be neglected when considering the missing ice problem. Because the consideration of sediment isostatic adjustment reduces the amount of sea-level rise that must be explained by melting ice, it goes some way towards resolving the missing ice problem. Most sea-level records that can extend back to the Last Glacial Maximum are located adjacent to large sediment systems. Future studies should aim to quantify the effect of sediment isostatic adjustment on global grounded ice volume estimation during the Last Glacial Maximum.

Producing a barystatic sea-level (BSL) map is a long-standing goal of the palaeo sea-level modelling community, as a way of guiding field scientists to collect data from the best possible locations for understanding palaeo ice volume variation. Although Milne and Mitrovica (2008) quantified the BSL map uncertainty associated with solid Earth rheology, the dependence of the results on global ice history, a key uncertainty that is more difficult to assess, has not been fully investigated.

Spatio-temporal global ice history is an extremely high-dimensional parameter to explore (parameter level), involving running up to millions of forward physical models, which is computationally prohibitive. Therefore, this thesis provides proof-of-concept development of a statistical emulator that mimics the behaviour of a forward physical model but which is 500-1000 times computationally cheaper to evaluate. We believe this is the first successful demonstration of an end-to-end (i.e., from ice model to global relative sea-level prediction) glacial isostatic adjustment emulator, and we have used it to provide insight into global BSL at different times since the LGM. This kind of emulator can be used in any sea-level related projects which require a prohibitive amount of computational load.

This thesis highlights the importance of developing novel statistical and physical approaches to understand the mechanisms of postglacial sea-level change and to help inform ongoing debates (such as the sources of MWP-1A and the missing ice problem). Based on novel modelling methods, the results presented in this thesis yield new insights on ice and ocean dynamic change during a period of abrupt climate change and the role of sediment isostatic adjustment along coastal margins. These advances can be used to inform future model development and calibration processes and hence improve future sea-level projections. Looking ahead, it is important to develop next-generation physical models, to better represent Earth systems (e.g., solid Earth rheology, tidal variation and dynamic sea-level change), and a statistical framework to calibrate these models using corresponding data, which may have complicated uncertainty distributions. This research and future progress in this area will further enhance understanding of long-term sea-level change and our ability to produce robust and accurate future sea-level change projections.

References

Abbey, E., Webster, J. M., and Beaman, R. J. (2011). Geomorphology of submerged reefs on the shelf edge of the Great Barrier Reef: the influence of oscillating Pleistocene sea-levels. *Marine Geology*, 288(1-4):61–78.

Abdul, N., Mortlock, R., Wright, J., and Fairbanks, R. (2016). Younger Dryas sea level and meltwater pulse 1B recorded in Barbados reef crest coral Acropora palmata. *Paleoceanography*, 31(2):330–344.

Abe-Ouchi, A., Saito, F., Kawamura, K., Raymo, M. E., Okuno, J., Takahashi, K., and Blatter, H. (2013). Insolation-driven 100,000-year glacial cycles and hysteresis of ice-sheet volume. *nature*, 500(7461):190–193.

Albrecht, T., Winkelmann, R., and Levermann, A. (2020). Glacial-cycle simulations of the Antarctic Ice Sheet with the Parallel Ice Sheet Model (PISM)–Part 2: Parameter ensemble analysis. *Cryosphere*, 14(2).

Anderson, J. B., Conway, H., Bart, P. J., Witus, A. E., Greenwood, S. L., McKay, R. M., Hall, B. L., Ackert, R. P., Licht, K., Jakobsson, M., et al. (2014). Ross Sea paleo-ice sheet drainage and deglacial history during and since the LGm. *Quaternary Science Reviews*, 100:31–54.

Andrews, J. T. (1992). A case of missing water. *Nature*, 358:281–281.

Argus, D. F., Peltier, W., Drummond, R., and Moore, A. W. (2014). The Antarctica component of postglacial rebound model ICE-6G_C (VM5a) based on GPS positioning, exposure age dating of ice thicknesses, and relative sea level histories. *Geophysical Journal International*, 198(1):537–563.

Arzani, A. and Dawson, S. T. (2021). Data-driven cardiovascular flow modelling: examples and opportunities. *Journal of the Royal Society Interface*, 18(175):20200802.

Ashe, E. L., Cahill, N., Hay, C., Khan, N. S., Kemp, A., Engelhart, S. E., Horton, B. P., Parnell, A. C., and Kopp, R. E. (2019). Statistical modeling of rates and trends in Holocene relative sea level. *Quaternary Science Reviews*, 204:58–77.

Ashe, E. L., Khan, N. S., Toth, L. T., Dutton, A., and Kopp, R. E. (2022). A statistical framework for integrating nonparametric proxy distributions into geological reconstructions of relative sea level. *Advances in Statistical Climatology, Meteorology and Oceanography*, 8(1):1–29.

Austermann, J., Hoggard, M. J., Latychev, K., Richards, F. D., and Mitrovica, J. X. (2021). The effect of lateral variations in Earth structure on Last Interglacial sea level. *Geophysical Journal International*, 227(3):1938–1960.

Austermann, J., Mitrovica, J. X., Huybers, P., and Rovere, A. (2017). Detection of a dynamic topography signal in last interglacial sea-level records. *Science Advances*, 3(7):e1700457.

Austermann, J., Mitrovica, J. X., Latychev, K., and Milne, G. A. (2013). Barbados-based estimate of ice volume at Last Glacial Maximum affected by subducted plate. *Nature Geoscience*, 6(7):553–557.

Austermann, J., Wickert, A., Pico, T., Kingslake, J., Callaghan, K., and Creel, R. (2022). Glacial isostatic adjustment shapes proglacial lakes over glacial cycles. *Geophysical Research Letters*, page e2022GL101191.

Bard, E., Hamelin, B., Arnold, M., Montaggioni, L., Cabioch, G., Faure, G., and Rougerie, F. (1996). Deglacial sea-level record from Tahiti corals and the timing of global meltwater discharge. *Nature*, 382(6588):241–244.

Bard, E., Hamelin, B., Deschamps, P., and Camoin, G. (2016). Comment on "Younger Dryas sea level and meltwater pulse 1B recorded in Barbados reefal crest coral Acropora palmata" by NA Abdul et al. *Paleoceanography*, 31(12):1603–1608.

Baril, A., Garrett, E., Milne, G., Gehrels, W., and Kelley, J. (2023). Postglacial relative sea-level changes in the Gulf of Maine, USA: Database compilation, assessment and modelling. *Quaternary Science Reviews*, 306:108027.

Barker, S., Diz, P., Vautravers, M. J., Pike, J., Knorr, G., Hall, I. R., and Broecker, W. S. (2009). Interhemispheric atlantic seesaw response during the last deglaciation. *Nature*, 457(7233):1097–1102.

Bassett, S. E., Milne, G. A., Mitrovica, J. X., and Clark, P. U. (2005). Ice sheet and solid earth influences on far-field sea-level histories. *Science*, 309(5736):925–928.

Beaman, R. (2010). 3DGBR: A high-resolution depth model for the Great Barrier Reef and Coral Sea. *Marine and Tropical Sciences Facility (MTSRF) Project*, 2:13.

Bentley, M. J., Fogwill, C. J., Le Brocq, A. M., Hubbard, A. L., Sugden, D. E., Dunai, T. J., and Freeman, S. P. (2010). Deglacial history of the West Antarctic Ice Sheet in the Weddell Sea embayment: Constraints on past ice volume change. *Geology*, 38(5):411–414.

Berdahl, M., Leguy, G., Lipscomb, W. H., and Urban, N. M. (2021). Statistical emulation of a perturbed basal melt ensemble of an ice sheet model to better quantify Antarctic sea level rise uncertainties. *The Cryosphere*, 15(6):2683–2699.

Best, L., Simms, A. R., Brader, M., Lloyd, J., Sefton, J., and Shennan, I. (2022). Local and regional constraints on relative sea-level changes in southern Isle of Skye, Scotland, since the Last Glacial Maximum. *Journal of Quaternary Science*, 37(1):59–70.

Blaauw, M. and Christen, J. A. (2011). Flexible paleoclimate age-depth models using an autoregressive gamma process.

Blank, B., Barletta, V., Hu, H., Pappa, F., and van der Wal, W. (2021). Effect of Lateral and Stress-Dependent Viscosity Variations on GIA Induced Uplift

Rates in the Amundsen Sea Embayment. *Geochemistry, Geophysics, Geosystems*, 22(9):e2021GC009807.

Bradley, S., Milne, G., Teferle, F. N., Bingley, R., and Orliac, E. (2009). Glacial isostatic adjustment of the British Isles: new constraints from GPS measurements of crustal motion. *Geophysical Journal International*, 178(1):14–22.

Bradley, S. L., Ely, J., Clark, C., Edwards, R., Shennan, I., and Hindmarsh, R. C. (2018). Glacial Isostatic Adjustment of the British Isles and North West Europe. In *EGU General Assembly Conference Abstracts*, volume 20, page 9701.

Bradley, S. L., Milne, G. A., Shennan, I., and Edwards, R. (2011). An improved glacial isostatic adjustment model for the British Isles. *Journal of Quaternary Science*, 26(5):541–552.

Brendryen, J., Haflidason, H., Yokoyama, Y., Haaga, K. A., and Hannisdal, B. (2020). Eurasian Ice Sheet collapse was a major source of Meltwater Pulse 1A 14,600 years ago. *Nature Geoscience*, pages 1–6.

Briggs, R. D., Pollard, D., and Tarasov, L. (2014). A data-constrained large ensemble analysis of Antarctic evolution since the Eemian. *Quaternary Science Reviews*, 103:91–115.

Brunet, D., Vrscay, E. R., and Wang, Z. (2011). On the mathematical properties of the structural similarity index. *IEEE Transactions on Image Processing*, 21(4):1488–1499.

Buizert, C., Gkinis, V., Severinghaus, J. P., He, F., Lecavalier, B. S., Kindler, P., Leuenberger, M., Carlson, A. E., Vinther, B., Masson-Delmotte, V., et al. (2014). Greenland temperature response to climate forcing during the last deglaciation. *Science*, 345(6201):1177–1180.

Cabioch, G., Montaggioni, L., Faure, G., and Ribaud-Laurenti, A. (1999). Reef coralgal assemblages as recorders of paleobathymetry and sea level changes in the Indo-Pacific province. *Quaternary Science Reviews*, 18(14):1681–1695.

Callaghan, K., Austermann, J., and Wickert, A. (2021). Quantifying changes in lakes, groundwater, and sea level over the deglaciation. In *AGU Fall Meeting Abstracts*, volume 2021, pages GC55K–0550.

Camoin, G. F., Iryu, Y., and McInroy, D. B. (2007). IODP Expedition 310 reconstructs sea level, climatic, and environmental changes in the South Pacific during the last deglaciation. *Scientific Drilling*, 5:4–12.

Camoin, G. F., Seard, C., Deschamps, P., Webster, J. M., Abbey, E., Braga, J. C., Iryu, Y., Durand, N., Bard, E., Hamelin, B., et al. (2012). Reef response to sea-level and environmental changes during the last deglaciation: Integrated Ocean Drilling Program Expedition 310, Tahiti Sea Level. *Geology*, 40(7):643–646.

Carlson, A. E. and Clark, P. U. (2012). Ice sheet sources of sea level rise and freshwater discharge during the last deglaciation. *Reviews of Geophysics*, 50(4).

Caron, L., Ivins, E., Larour, E., Adhikari, S., Nilsson, J., and Blewitt, G. (2018). GIA model statistics for GRACE hydrology, cryosphere, and ocean science. *Geophysical Research Letters*, 45(5):2203–2212.

Caron, L., Métivier, L., Greff-Lefftz, M., Fleitout, L., and Rouby, H. (2017). Inverting Glacial Isostatic Adjustment signal using Bayesian framework and two linearly relaxing rheologies. *Geophysical Journal International*, 209(2):1126–1147.

Chappell, J. (1980). Coral morphology, diversity and reef growth. *Nature*, 286(5770):249–252.

Cheng, H., Edwards, R. L., Shen, C.-C., Polyak, V. J., Asmerom, Y., Woodhead, J., Hellstrom, J., Wang, Y., Kong, X., Spötl, C., et al. (2013). Improvements in 230Th dating, 230Th and 234U half-life values, and U–Th isotopic measurements by multi-collector inductively coupled plasma mass spectrometry. *Earth and Planetary Science Letters*, 371:82–91.

Clark, C. D., Chiverrell, R. C., Fabel, D., Hindmarsh, R. C., Ó Cofaigh, C., and Scourse, J. D. (2021). Timing, pace and controls on ice sheet retreat: an introduction to the BRITICE-CHRONO transect reconstructions of the British–Irish Ice Sheet. *Journal of Quaternary Science*, 36(5):673–680.

Clark, C. D., Ely, J. C., Greenwood, S. L., Hughes, A. L., Meehan, R., Barr, I. D., Bateman, M. D., Bradwell, T., Doole, J., Evans, D. J., et al. (2018). BRITICE Glacial Map, version 2: a map and GIS database of glacial landforms of the last British–Irish Ice Sheet. *Boreas*, 47(1):11–27.

Clark, P. U., Dyke, A. S., Shakun, J. D., Carlson, A. E., Clark, J., Wohlfarth, B., Mitrovica, J. X., Hostetler, S. W., and McCabe, A. M. (2009). The last glacial maximum. *science*, 325(5941):710–714.

Clark, P. U., Mitrovica, J., Milne, G., and Tamisiea, M. (2002). Sea-level fingerprinting as a direct test for the source of global meltwater pulse IA. *Science*, 295(5564):2438–2441.

Clark, P. U., Shakun, J. D., Marcott, S. A., Mix, A. C., Eby, M., Kulp, S., Levermann, A., Milne, G. A., Pfister, P. L., Santer, B. D., et al. (2016). Consequences of twenty-first-century policy for multi-millennial climate and sea-level change. *Nature climate change*, 6(4):360–369.

Clark, P. U. and Tarasov, L. (2014). Closing the sea level budget at the Last Glacial Maximum. *Proceedings of the National Academy of Sciences*, 111(45):15861–15862.

Couette, P.-O., Lajeunesse, P., Ghienne, J.-F., Dorschel, B., Gebhardt, C., Hebbeln, D., and Brouard, E. (2022). Evidence for an extensive ice shelf in northern Baffin Bay during the Last Glacial Maximum. *Communications Earth & Environment*, 3(1):225.

Coulson, S., Dangendorf, S., Mitrovica, J. X., Tamisiea, M. E., Pan, L., and Sandwell, D. T. (2022). A detection of the sea level fingerprint of Greenland Ice Sheet melt. *Science*, 377(6614):1550–1554.

Creel, R. C., Austermann, J., Khan, N. S., D'Andrea, W. J., Balascio, N., Dyer, B., Ashe, E., and Menke, W. (2022). Postglacial relative sea level change in Norway. *Quaternary Science Reviews*, 282:107422.

Dalca, A., Ferrier, K., Mitrovica, J., Perron, J., Milne, G., and Creveling, J. (2013). On postglacial sea level—III. Incorporating sediment redistribution. *Geophysical Journal International*, 194(1):45–60.

Dalton, A. S., Margold, M., Stokes, C. R., Tarasov, L., Dyke, A. S., Adams, R. S., Allard, S., Arends, H. E., Atkinson, N., Attig, J. W., et al. (2020). An updated radiocarbon-based ice margin chronology for the last deglaciation of the North American Ice Sheet Complex. *Quaternary Science Reviews*, 234:106223.

Davies, B. J., Darvill, C. M., Lovell, H., Bendle, J. M., Dowdeswell, J. A., Fabel, D., García, J.-L., Geiger, A., Glasser, N. F., Gheorghiu, D. M., et al. (2020). The evolution of the Patagonian Ice Sheet from 35 ka to the present day (PATICE). *Earth-Science Reviews*, page 103152.

Davies, P. J. and Hopley, D. (1983). Growth facies and growth rates of Holocene reef in the Great Barrier Reef. *Bureau of Mineral Resources, Geology and Geophysics*, 8:237–251.

Dawson, A. G., Bishop, P., Hansom, J., and Fabel, D. (2022). 10Be exposure age dating of Late Quaternary relative sea level changes and deglaciation of W Jura and NE Islay, Scottish Inner Hebrides. *Earth and Environmental Science Transactions of the Royal Society of Edinburgh*, 113(3):253–266.

de Gelder, G., Husson, L., Pastier, A.-M., Fernández-Blanco, D., Pico, T., Chauveau, D., Authemayou, C., and Pedoja, K. (2022). High interstadial sea levels over the past 420ka from the Huon Peninsula, Papua New Guinea. *Communications Earth & Environment*, 3(1):256.

Dean, R. G. and Dalrymple, R. A. (2004). *Coastal processes with engineering applications*. Cambridge University Press.

DeConto, R. M., Pollard, D., Alley, R. B., Velicogna, I., Gasson, E., Gomez, N., Sadai, S., Condron, A., Gilford, D. M., Ashe, E. L., et al. (2021). The paris climate agreement and future sea-level rise from antarctica. *Nature*, 593(7857):83–89.

Defferrard, M., Milani, M., Gusset, F., and Perraudin, N. (2020). Deepsphere: a graph-based spherical cnn. *arXiv preprint arXiv:2012.15000*.

Defferrard, M., Perraudin, N., Kacprzak, T., and Sgier, R. (2019). Deepsphere: towards an equivariant graph-based spherical cnn. *arXiv preprint arXiv:1904.05146*.

Deschamps, P., Durand, N., Bard, E., Hamelin, B., Camoin, G., Thomas, A. L., Henderson, G. M., Okuno, J., and Yokoyama, Y. (2012). Ice-sheet collapse and sea-level rise at the Bølling warming 14,600 years ago. *Nature*, 483(7391):559–564.

Domingo, D., Malmierca-Vallet, I., Sime, L., Voss, J., and Capron, E. (2020). Using ice cores and Gaussian process emulation to recover changes in the Greenland ice sheet during the last interglacial. *Journal of Geophysical Research: Earth Surface*, 125(5):e2019JF005237.

Dunbar, G., Dickens, G., and Carter, R. (2000). Sediment flux across the Great Barrier Reef Shelf to the Queensland Trough over the last 300 ky. *Sedimentary Geology*, 133(1-2):49–92.

Dunbar, G. B. and Dickens, G. R. (2003). Massive siliciclastic discharge to slopes of the Great Barrier Reef Platform during sea-level transgression: constraints from sediment cores between 15 S and 16 S latitude and possible explanations. *Sedimentary Geology*, 162(1-2):141–158.

Dyer, B., Austermann, J., D'Andrea, W. J., Creel, R. C., Sandstrom, M. R., Cashman, M., Rovere, A., and Raymo, M. E. (2021). Sea-level trends across The Bahamas constrain peak last interglacial ice melt. *Proceedings of the National Academy of Sciences*, 118(33):e2026839118.

Dziewonski, A. M. and Anderson, D. L. (1981). Preliminary reference Earth model. *Physics of the earth and planetary interiors*, 25(4):297–356.

Edwards, T. L., Nowicki, S., Marzeion, B., Hock, R., Goelzer, H., Seroussi, H., Jourdain, N. C., Slater, D. A., Turner, F. E., Smith, C. J., et al. (2021). Projected land ice contributions to twenty-first-century sea level rise. *Nature*, 593(7857):74–82.

Fairbanks, R. G. (1989). A 17,000-year glacio-eustatic sea level record: influence of glacial melting rates on the Younger Dryas event and deep-ocean circulation. *Nature*, 342(6250):637–642.

Fairbanks, R. G., Mortlock, R. A., Chiu, T.-C., Cao, L., Kaplan, A., Guilderson, T. P., Fairbanks, T. W., Bloom, A. L., Grootes, P. M., and Nadeau, M.-J. (2005).

Radiocarbon calibration curve spanning 0 to 50,000 years BP based on paired 230Th/234U/238U and 14C dates on pristine corals. *Quaternary Science Reviews*, 24(16-17):1781–1796.

Farrell, W. and Clark, J. A. (1976). On postglacial sea level. *Geophysical Journal International*, 46(3):647–667.

Ferrier, K. L., Austermann, J., Mitrovica, J. X., and Pico, T. (2017). Incorporating sediment compaction into a gravitationally self-consistent model for ice age sea-level change. *Geophysical Journal International*, 211(1):663–672.

Ferrier, K. L., Li, Q., Pico, T., and Austermann, J. (2018). The Influence of Water Storage in Marine Sediment on Sea-Level Change. *Geophysical Research Letters*, 45(5):2444–2454.

Fischler, M. A. and Bolles, R. C. (1981). Random sample consensus: a paradigm for model fitting with applications to image analysis and automated cartography. *Communications of the ACM*, 24(6):381–395.

Fogwill, C., Turney, C., Golledge, N., Etheridge, D., Rubino, M., Thornton, D., Baker, A., Woodward, J., Winter, K., Van Ommen, T., et al. (2017). Antarctic ice sheet discharge driven by atmosphere-ocean feedbacks at the Last Glacial Termination. *Scientific reports*, 7(1):1–10.

Fox-Kemper, B., H.T., H., C., X., G., A., S.S., D., T.L., E., N.R., G., M., H., R.E., K., G., K., A., M., D., N., S., N., I.S., N., L., R., J.-B., S., A.B.A., S., and Y., Y. (2021). *Ocean, Cryosphere and Sea Level Change*. Ocean, Cryosphere and Sea Level Change. In Climate Change 2021: The Physical Science Basis. Contribution of Working Group I to the Sixth Assessment Report of the Intergovernmental Panel on Climate Change.

Frederikse, T., Landerer, F., Caron, L., Adhikari, S., Parkes, D., Humphrey, V. W., Dangendorf, S., Hogarth, P., Zanna, L., Cheng, L., et al. (2020). The causes of sea-level rise since 1900. *Nature*, 584(7821):393–397.

Garbe, J., Albrecht, T., Levermann, A., Donges, J. F., and Winkelmann, R. (2020). The hysteresis of the antarctic ice sheet. *Nature*, 585(7826):538–544.

Garner, A. J., Weiss, J. L., Parris, A., Kopp, R. E., Horton, R. M., Overpeck, J. T., and Horton, B. P. (2018). Evolution of 21st century sea level rise projections. *Earth's Future*, 6(11):1603–1615.

Gebbie, G., Simms, A. R., and Lisiecki, L. E. (2019). Why estimates of deglacial ice loss should be biased low. *Earth and Planetary Science Letters*, 515:112–124.

Geman, S. and Geman, D. (1984). Stochastic relaxation, Gibbs distributions, and the Bayesian restoration of images. *IEEE Transactions on pattern analysis and machine intelligence*, (6):721–741.

Golledge, N., Menviel, L., Carter, L., Fogwill, C., England, M., Cortese, G., and Levy, R. (2014). Antarctic contribution to meltwater pulse 1A from reduced Southern Ocean overturning. *Nature communications*, 5:5107.

Gomez, N., Gregoire, L., Mitrovica, J., and Payne, A. (2015). Laurentide-Cordilleran Ice Sheet saddle collapse as a contribution to meltwater pulse 1A. *Geophysical Research Letters*, 42(10):3954–3962.

Gomez, N., Latychev, K., and Pollard, D. (2018). A coupled ice sheet–sea level model incorporating 3D earth structure: Variations in Antarctica during the last deglacial retreat. *Journal of Climate*, 31(10):4041–4054.

Gomez, N., Weber, M. E., Clark, P. U., Mitrovica, J. X., and Han, H. K. (2020). Antarctic ice dynamics amplified by Northern Hemisphere sea-level forcing. *Nature*, 587(7835):600–604.

Goodfellow, I., Bengio, Y., and Courville, A. (2016). *Deep learning*. MIT press.

Gorski, K. M., Hivon, E., Banday, A. J., Wandelt, B. D., Hansen, F. K., Reinecke, M., and Bartelmann, M. (2005). HEALPix: A framework for high-resolution discretization and fast analysis of data distributed on the sphere. *The Astrophysical Journal*, 622(2):759.

Gowan, E. J., Tregoning, P., Purcell, A., Lea, J., Fransner, O. J., Noormets, R., and Dowdeswell, J. (2016a). ICESHEET 1.0: a program to produce paleo-ice

sheet reconstructions with minimal assumptions. *Geoscientific Model Development*, 9(5):1673–1682.

Gowan, E. J., Tregoning, P., Purcell, A., Montillet, J.-P., and McClusky, S. (2016b). A model of the western Laurentide Ice Sheet, using observations of glacial isostatic adjustment. *Quaternary Science Reviews*.

Gowan, E. J., Zhang, X., Khosravi, S., Rovere, A., Stocchi, P., Hughes, A. L., Gyllencreutz, R., Mangerud, J., Svendsen, J.-I., and Lohmann, G. (2021). A new global ice sheet reconstruction for the past 80 000 years. *Nature communications*, 12(1):1–9.

Gowan, E. J., Zhang, X., Khosravi, S., Rovere, A., Stocchi, P., Hughes, A. L., Gyllencreutz, R., Mangerud, J., Svendsen, J.-I., and Lohmann, G. (2022). Reply to: Towards solving the missing ice problem and the importance of rigorous model data comparisons. *Nature communications*, 13(1):6264.

Gregoire, L. J., Otto-Bliesner, B., Valdes, P. J., and Ivanovic, R. (2016). Abrupt Bølling warming and ice saddle collapse contributions to the Meltwater Pulse 1a rapid sea level rise. *Geophysical research letters*, 43(17):9130–9137.

Gregoire, L. J., Payne, A. J., and Valdes, P. J. (2012). Deglacial rapid sea level rises caused by ice-sheet saddle collapses. *Nature*, 487(7406):219–222.

Gregory, J. M., Griffies, S. M., Hughes, C. W., Lowe, J. A., Church, J. A., Fukimori, I., Gomez, N., Kopp, R. E., Landerer, F., Cozannet, G. L., et al. (2019). Concepts and terminology for sea level: Mean, variability and change, both local and global. *Surveys in Geophysics*, 40:1251–1289.

Griffiths, S. D. and Peltier, W. R. (2009). Modeling of polar ocean tides at the Last Glacial Maximum: Amplification, sensitivity, and climatological implications. *Journal of Climate*, 22(11):2905–2924.

Guilderson, T., Burckle, L., Hemming, S., and Peltier, W. (2000). Late Pleistocene sea level variations derived from the Argentine Shelf. *Geochemistry, Geophysics, Geosystems*, 1(12).

Halsted, C. T., Bierman, P. R., Shakun, J. D., Davis, P. T., Corbett, L. B., Caffee, M. W., Hodgdon, T. S., and Licciardi, J. M. (2022). Rapid southeastern Laurentide Ice Sheet thinning during the last deglaciation revealed by elevation profiles of in situ cosmogenic 10Be. *GSA Bulletin*.

Han, D. and Wahr, J. (1989). Post-glacial rebound analysis for a rotating earth. *Slow deformation and transmission of stress in the Earth*, 49:1–6.

Han, H. K., Gomez, N., Pollard, D., and DeConto, R. (2021). Modeling Northern Hemispheric ice sheet dynamics, sea level change, and solid Earth deformation through the last glacial cycle. *Journal of Geophysical Research: Earth Surface*, 126(4):e2020JF006040.

Hanebuth, T., Stattegger, K., and Grootes, P. M. (2000). Rapid flooding of the Sunda Shelf: a late-glacial sea-level record. *Science*, 288(5468):1033–1035.

Hanebuth, T. J., Stattegger, K., and Bojanowski, A. (2009). Termination of the Last Glacial Maximum sea-level lowstand: The Sunda-Shelf data revisited. *Global and Planetary Change*, 66(1-2):76–84.

Hay, C. C., Morrow, E., Kopp, R. E., and Mitrovica, J. X. (2015). Probabilistic reanalysis of twentieth-century sea-level rise. *Nature*, 517(7535):481–484.

Heaton, T. J., Köhler, P., Butzin, M., Bard, E., Reimer, R. W., Austin, W. E., Ramsey, C. B., Grootes, P. M., Hughen, K. A., Kromer, B., et al. (2020). Marine20—the marine radiocarbon age calibration curve (0–55,000 cal BP). *Radiocarbon*, 62(4):779–820.

Hibbert, F., Williams, F., Fallon, S., and Rohling, E. (2018). A database of biological and geomorphological sea-level markers from the Last Glacial Maximum to present. *Scientific data*, 5:180088.

Hibbert, F. D., Rohling, E. J., Dutton, A., Williams, F. H., Chutcharavan, P. M., Zhao, C., and Tamisiea, M. E. (2016). Coral indicators of past sea-level change: A global repository of U-series dated benchmarks. *Quaternary Science Reviews*, 145:1–56.

Hinestrosa, G., Webster, J. M., and Beaman, R. J. (2016). Postglacial sediment deposition along a mixed carbonate-siliciclastic margin: New constraints from the drowned shelf-edge reefs of the Great Barrier Reef, Australia. *Palaeogeography, Palaeoclimatology, Palaeoecology*, 446:168–185.

Hinestrosa, G., Webster, J. M., and Beaman, R. J. (2019). Spatio-temporal patterns in the postglacial flooding of the Great Barrier Reef shelf, Australia. *Continental Shelf Research*, 173:13–26.

Hinestrosa, G., Webster, J. M., and Beaman, R. J. (2022). New constraints on the postglacial shallow-water carbonate accumulation in the Great Barrier Reef. *Scientific Reports*, 12(1):1–18.

Hinestrosa, G., Webster, J. M., Beaman, R. J., and Anderson, L. M. (2014). Seismic stratigraphy and development of the shelf-edge reefs of the Great Barrier Reef, Australia. *Marine Geology*, 353:1–20.

Hogg, A. G., Heaton, T. J., Hua, Q., Palmer, J. G., Turney, C. S., Southon, J., Bayliss, A., Blackwell, P. G., Boswijk, G., Ramsey, C. B., et al. (2020). SHCal20 Southern Hemisphere calibration, 0–55,000 years cal Bp. *Radiocarbon*, 62(4):759–778.

Hoggard, M., Austermann, J., Randel, C., and Stephenson, S. (2021). Observational estimates of dynamic topography through space and time. *Mantle convection and surface expressions*, pages 371–411.

Hopley, D., Smithers, S. G., and Parnell, K. (2007). *The geomorphology of the Great Barrier Reef: development, diversity and change*. Cambridge University Press.

Hore, A. and Ziou, D. (2010). Image quality metrics: PSNR vs. SSIm. In *2010 20th international conference on pattern recognition*, pages 2366–2369. IEEE.

Horton, B. P., Kopp, R. E., Garner, A. J., Hay, C. C., Khan, N. S., Roy, K., and Shaw, T. A. (2018). Mapping sea-level change in time, space, and probability. *Annual Review of Environment and Resources*, 43:481–521.

Hughes, A. L., Gyllencreutz, R., Lohne, Ø. S., Mangerud, J., and Svendsen, J. I. (2016). The last Eurasian ice sheets–a chronological database and time-slice reconstruction, DATED-1. *Boreas*, 45(1):1–45.

Huynh-Thu, Q. and Ghanbari, M. (2008). Scope of validity of PSNR in image/video quality assessment. *Electronics letters*, 44(13):800–801.

Irrgang, C., Boers, N., Sonnewald, M., Barnes, E. A., Kadow, C., Staneva, J., and Saynisch-Wagner, J. (2021). Towards neural Earth system modelling by integrating artificial intelligence in Earth system science. *Nature Machine Intelligence*, 3(8):667–674.

Ishiwa, T., Yokoyama, Y., Okuno, J., Obrochta, S., Uehara, K., Ikehara, M., and Miyairi, Y. (2019). A sea-level plateau preceding the Marine Isotope Stage 2 minima revealed by Australian sediments. *Scientific reports*, 9(1):1–8.

Ivanovic, R., Gregoire, L., Wickert, A. D., and Burke, A. (2018). Climatic effect of Antarctic meltwater overwhelmed by concurrent Northern hemispheric melt. *Geophysical Research Letters*, 45(11):5681–5689.

Ivanovic, R. F., Gregoire, L. J., Kageyama, M., Roche, D. M., Valdes, P. J., Burke, A., Drummond, R., Peltier, W. R., and Tarasov, L. (2016). Transient climate simulations of the deglaciation 21–9 thousand years before present (version 1)–PMIP4 Core experiment design and boundary conditions. *Geoscientific Model Development*, 9(7):2563–2587.

Ivanovic, R. F., Gregoire, L. J., Wickert, A. D., Valdes, P. J., and Burke, A. (2017). Collapse of the North American ice saddle 14,500 years ago caused widespread cooling and reduced ocean overturning circulation. *Geophysical Research Letters*, 44(1):383–392.

Ivins, E. R., Caron, L., Adhikari, S., and Larour, E. (2022). Notes on a compressible extended Burgers model of rheology. *Geophysical Journal International*, 228(3):1975–1991.

Jessen, S. P., Rasmussen, T. L., Nielsen, T., and Solheim, A. (2010). A new Late Weichselian and Holocene marine chronology for the western Svalbard slope 30,000–0 cal years Bp. *Quaternary Science Reviews*, 29(9-10):1301–1312.

Ji, W., Robel, A., Tziperman, E., and Yang, J. (2021). Laurentide Ice Saddle Mergers Drive Rapid Sea Level Drops During Glaciations. *Geophysical Research Letters*, 48(14):e2021GL094263.

Johnston, P. (1993). The effect of spatially non-uniform water loads on prediction of sea-level change. *Geophysical Journal International*, 114(3):615–634.

Jones, R., Mackintosh, A. N., Norton, K. P., Golledge, N. R., Fogwill, C. J., Kubik, P. W., Christl, M., and Greenwood, S. L. (2015). Rapid Holocene thinning of an East Antarctic outlet glacier driven by marine ice sheet instability. *Nature Communications*, 6(1):8910.

Jungdal-Olesen, G., Pedersen, V., Andersen, J., Gomez, N., and Mitrovica, J. (2023). Sea level response to late pliocene-quaternary erosion and deposition in scandinavia. *Quaternary Science Reviews*, 301:107938.

Kang, K., Zhong, S., Geruo, A., and Mao, W. (2022). The effects of non-Newtonian rheology in the upper mantle on relative sea level change and geodetic observables induced by glacial isostatic adjustment process. *Geophysical Journal International*, 228(3):1887–1906.

Kapsch, M.-L., Mikolajewicz, U., Ziemen, F., and Schannwell, C. (2022). Ocean response in transient simulations of the last deglaciation dominated by underlying ice-sheet reconstruction and method of meltwater distribution. *Geophysical Research Letters*, 49(3):e2021GL096767.

Kemp, A. C. and Telford, R. J. (2015). Transfer functions. *Handbook of sea-level research*, pages 470–499.

Kendall, R. A., Mitrovica, J. X., and Milne, G. A. (2005). On post-glacial sea level–II. Numerical formulation and comparative results on spherically symmetric models. *Geophysical Journal International*, 161(3):679–706.

Khan, N. S., Ashe, E., Horton, B. P., Dutton, A., Kopp, R. E., Brocard, G., Engelhart, S. E., Hill, D. F., Peltier, W., Vane, C. H., et al. (2017). Drivers of Holocene sea-level change in the Caribbean. *Quaternary Science Reviews*, 155:13–36.

Khan, N. S., Horton, B. P., Engelhart, S., Rovere, A., Vacchi, M., Ashe, E. L., Törnqvist, T. E., Dutton, A., Hijma, M. P., and Shennan, I. (2019). Inception of a global atlas of sea levels since the Last Glacial Maximum. *Quaternary Science Reviews*, 220:359–371.

Kinsey, D. and Hopley, D. (1991). The significance of coral reefs as global carbon sinks—response to greenhouse. *Palaeogeography, Palaeoclimatology, Palaeoecology*, 89(4):363–377.

Kirkpatrick, S., Gelatt, C. D., and Vecchi, M. P. (1983). Optimization by simulated annealing. *science*, 220(4598):671–680.

Kopp, R. E., Garner, G. G., Hermans, T. H., Jha, S., Kumar, P., Slangen, A., Turilli, M., Edwards, T. L., Gregory, J. M., Koubbe, G., et al. (2023). The framework for assessing changes to sea-level (facts) v1. 0-rc: A platform for characterizing parametric and structural uncertainty in future global, relative, and extreme sea-level change. *EGUsphere*, pages 1–34.

Kopp, R. E., Gilmore, E. A., Little, C. M., Lorenzo-Trueba, J., Ramenzoni, V. C., and Sweet, W. V. (2019). Usable science for managing the risks of sea-level rise. *Earth's future*, 7(12):1235–1269.

Kopp, R. E., Horton, R. M., Little, C. M., Mitrovica, J. X., Oppenheimer, M., Rasmussen, D., Strauss, B. H., and Tebaldi, C. (2014). Probabilistic 21st and 22nd century sea-level projections at a global network of tide-gauge sites. *Earth's future*, 2(8):383–406.

Kopp, R. E., Kemp, A. C., Bittermann, K., Horton, B. P., Donnelly, J. P., Gehrels, W. R., Hay, C. C., Mitrovica, J. X., Morrow, E. D., and Rahmstorf, S. (2016). Temperature-driven global sea-level variability in the common era. *Proceedings of the National Academy of Sciences*, 113(11):E1434–E1441.

Kopp, R. E., Simons, F. J., Mitrovica, J. X., Maloof, A. C., and Oppenheimer, M. (2009). Probabilistic assessment of sea level during the last interglacial stage. *Nature*, 462(7275):863–867.

Korhonen, J. and You, J. (2012). Peak signal-to-noise ratio revisited: Is simple beautiful? In *2012 Fourth International Workshop on Quality of Multimedia Experience*, pages 37–38. IEEE.

Kuchar, J., Milne, G., Hubbard, A., Patton, H., Bradley, S., Shennan, I., and Edwards, R. (2012). Evaluation of a numerical model of the British–Irish ice sheet using relative sea-level data: implications for the interpretation of trimline observations. *Journal of Quaternary Science*, 27(6):597–605.

Lai, C.-Y., Kingslake, J., Wearing, M. G., Chen, P.-H. C., Gentine, P., Li, H., Spergel, J. J., and van Wessem, J. M. (2020). Vulnerability of Antarctica's ice shelves to meltwater-driven fracture. *Nature*, 584(7822):574–578.

Lambeck, K. (1993). Glacial rebound of the British Isles—II. A high-resolution, high-precision model. *Geophysical Journal International*, 115(3):960–990.

Lambeck, K. and Nakada, M. (1990). Late Pleistocene and Holocene sea-level change along the Australian coast. *Palaeogeography, Palaeoclimatology, Palaeoecology*, 89(1-2):143–176.

Lambeck, K., Purcell, A., Johnston, P., Nakada, M., and Yokoyama, Y. (2003). Water-load definition in the glacio-hydro-isostatic sea-level equation. *Quaternary Science Reviews*, 22(2-4):309–318.

Lambeck, K., Purcell, A., and Zhao, S. (2017). The North American Late Wisconsin ice sheet and mantle viscosity from glacial rebound analyses. *Quaternary Science Reviews*, 158:172–210.

Lambeck, K. and Purcell, A. P. (2001). Sea-level change in the Irish Sea since the Last Glacial Maximum: constraints from isostatic modelling. *Journal of Quaternary Science: Published for the Quaternary Research Association*, 16(5):497–506.

Lambeck, K., Rouby, H., Purcell, A., Sun, Y., and Sambridge, M. (2014). Sea level and global ice volumes from the Last Glacial Maximum to the Holocene. *Proceedings of the National Academy of Sciences*, 111(43):15296–15303.

Lambeck, K., Yokoyama, Y., and Purcell, T. (2002). Into and out of the Last Glacial Maximum: sea-level change during Oxygen Isotope Stages 3 and 2. *Quaternary Science Reviews*, 21(1-3):343–360.

Lau, H. C. (2023). Transient rheology in sea level change: Implications for Meltwater Pulse 1a. *Earth and Planetary Science Letters*, 609:118106.

Lawson, C. L. and Hanson, R. J. (1995). *Solving least squares problems*, volume 15. Siam.

Lea, D. W., Pak, D. K., Peterson, L. C., and Hughen, K. A. (2003). Synchroneity of tropical and high-latitude Atlantic temperatures over the last glacial termination. *Science*, 301(5638):1361–1364.

Lemieux-Dudon, B., Blayo, E., Petit, J.-R., Waelbroeck, C., Svensson, A., Ritz, C., Barnola, J.-M., Narcisi, B. M., and Parrenin, F. (2010). Consistent dating for Antarctic and Greenland ice cores. *Quaternary Science Reviews*, 29(1-2):8–20.

Li, T., Wu, P., Steffen, H., and Wang, H. (2018). In search of laterally heterogeneous viscosity models of glacial isostatic adjustment with the ICE-6G_C global ice history model. *Geophysical Journal International*, 214(2):1191–1205.

Li, T., Wu, P., Wang, H., Steffen, H., Khan, N. S., Engelhart, S. E., Vacchi, M., Shaw, T. A., Peltier, W. R., and Horton, B. P. (2020). Uncertainties of glacial isostatic adjustment model predictions in North America associated with 3D structure. *Geophysical Research Letters*, 47(10):e2020GL087944.

Lin, Y. (2019). Closing the Last Deglacial Global Sea Level Budget by Different Antarctic Deglaciation Models. Master thesis, The Australian National University.

Lin, Y., Hibbert, F. D., Whitehouse, P. L., Woodroffe, S. A., Purcell, A., Shennan, I., and Bradley, S. L. (2021). A reconciled solution of Meltwater Pulse 1A sources using sea-level fingerprinting. *Nature communications*, 12(1):1–11.

Lin, Y., Whitehouse, P. L., Hibbert, F. D., Woodroffe, S. A., Hinestrosa, G., and Webster, J. M. (2023). Relative sea level response to mixed carbonate-siliciclastic

sediment loading along the Great Barrier Reef margin. *Earth and Planetary Science Letters*, 607.

Liu, J. (2013). *Constraining the Source Distribution of Meltwater Pulse 1A Using Near-and Far-Field Sea-level Data*. PhD thesis, University of Ottawa.

Liu, J., Milne, G. A., Kopp, R. E., Clark, P. U., and Shennan, I. (2016). Sea-level constraints on the amplitude and source distribution of Meltwater Pulse 1A. *Nature Geoscience*, 9(2):130–134.

Liu, Z., Otto-Bliesner, B., He, F., Brady, E., Tomas, R., Clark, P., Carlson, A., Lynch-Stieglitz, J., Curry, W., Brook, E., et al. (2009). Transient simulation of last deglaciation with a new mechanism for Bølling-Allerød warming. *science*, 325(5938):310–314.

Love, R., Andres, H. J., Condron, A., and Tarasov, L. (2021). Freshwater routing in eddy-permitting simulations of the last deglacial: the impact of realistic freshwater discharge. *Climate of the Past*, 17(6):2327–2341.

Love, R., Milne, G. A., Tarasov, L., Engelhart, S. E., Hijma, M. P., Latychev, K., Horton, B. P., and Törnqvist, T. E. (2016). The contribution of glacial isostatic adjustment to projections of sea-level change along the Atlantic and Gulf coasts of North America. *Earth's Future*, 4(10):440–464.

Mackintosh, A. N., Verleyen, E., O'Brien, P. E., White, D. A., Jones, R. S., McKay, R., Dunbar, R., Gore, D. B., Fink, D., Post, A. L., et al. (2014). Retreat history of the East Antarctic Ice Sheet since the last glacial maximum. *Quaternary Science Reviews*, 100:10–30.

Martinec, Z., Klemann, V., van der Wal, W., Riva, R., Spada, G., Sun, Y., Melini, D., Kachuck, S., Barletta, V., Simon, K., et al. (2018). A benchmark study of numerical implementations of the sea level equation in GIA modelling. *Geophysical Journal International*, 215(1):389–414.

McManus, J. F., Francois, R., Gherardi, J.-M., Keigwin, L. D., and Brown-Leger, S. (2004). Collapse and rapid resumption of Atlantic meridional circulation linked to deglacial climate changes. *Nature*, 428(6985):834–837.

McNeil, M., Nothdurft, L. D., Hua, Q., Webster, J. M., and Moss, P. (2022). Evolution of the inter-reef Halimeda carbonate factory in response to Holocene sea-level and environmental change in the Great Barrier Reef. *Quaternary Science Reviews*, 277:107347.

McNeil, M. A., Nothdurft, L. D., Dyriw, N. J., Webster, J. M., and Beaman, R. J. (2020). Morphotype differentiation in the Great Barrier Reef Halimeda bioherm carbonate factory: Internal architecture and surface geomorphometrics. *The Depositional Record*.

McNeil, M. A., Webster, J. M., Beaman, R. J., and Graham, T. L. (2016). New constraints on the spatial distribution and morphology of the Halimeda bioherms of the Great Barrier Reef, Australia. *Coral Reefs*, 35(4):1343–1355.

Menviel, L., Timmermann, A., Timm, O. E., and Mouchet, A. (2011). Deconstructing the Last Glacial termination: the role of millennial and orbital-scale forcings. *Quaternary Science Reviews*, 30(9-10):1155–1172.

Mercer, J. H. (1978). West Antarctic ice sheet and CO2 greenhouse effect: a threat of disaster. *Nature*, 271(5643):321–325.

Milliman, J. D. and Farnsworth, K. L. (2013). *River discharge to the coastal ocean: a global synthesis*. Cambridge University Press.

Milne, G. A. and Mitrovica, J. X. (1996). Postglacial sea-level change on a rotating Earth: first results from a gravitationally self-consistent sea-level equation. *Geophysical Journal International*, 126(3):F13–F20.

Milne, G. A. and Mitrovica, J. X. (2008). Searching for eustasy in deglacial sea-level histories. *Quaternary Science Reviews*, 27(25-26):2292–2302.

Mitrovica, J., Austermann, J., Coulson, S., Creveling, J., Hoggard, M., Jarvis, G., and Richards, F. (2020). Dynamic topography and ice age paleoclimate. *Annual Review of Earth and Planetary Sciences*, 48:585–621.

Mitrovica, J., Gomez, N., Morrow, E., Hay, C., Latychev, K., and Tamisiea, M. (2011). On the robustness of predictions of sea level fingerprints. *Geophysical Journal International*, 187(2):729–742.

Mitrovica, J. and Milne, G. (2002). On the origin of late Holocene sea-level highstands within equatorial ocean basins. *Quaternary Science Reviews*, 21(20-22):2179–2190.

Mitrovica, J. X. and Milne, G. A. (1998). Glaciation-induced perturbations in the earth's rotation: A new appraisal. *Journal of Geophysical Research: Solid Earth*, 103(B1):985–1005.

Mitrovica, J. X., Tamisiea, M. E., Davis, J. L., and Milne, G. A. (2001). Recent mass balance of polar ice sheets inferred from patterns of global sea-level change. *Nature*, 409(6823):1026–1029.

Mitrovica, J. X. and Wahr, J. (2011). Ice age Earth rotation. *Annual Review of Earth and Planetary Sciences*, 39:577–616.

Mitrovica, J. X., Wahr, J., Matsuyama, I., and Paulson, A. (2005). The rotational stability of an ice-age earth. *Geophysical Journal International*, 161(2):491–506.

Nauels, A., Gütschow, J., Mengel, M., Meinshausen, M., Clark, P. U., and Schleussner, C.-F. (2019). Attributing long-term sea-level rise to paris agreement emission pledges. *Proceedings of the National Academy of Sciences*, 116(47):23487–23492.

Nauels, A., Meinshausen, M., Mengel, M., Lorbacher, K., and Wigley, T. M. (2017). Synthesizing long-term sea level rise projections–the magicc sea level model v2. 0. *Geoscientific Model Development*, 10(6):2495–2524.

Neumann, A. (1985). Reef response to sea-level rise: keep-up, catch-up, or give-up. In *Proceedings of the fifth international coral reef congress Tahiti, 27 May-1 June 1985 volume 3: Symposia and seminars (A)*, pages 105–110. Antenne Museum-EPHE.

Nield, G. A., Whitehouse, P. L., van der Wal, W., Blank, B., O'Donnell, J. P., and Stuart, G. W. (2018). The impact of lateral variations in lithospheric thickness on glacial isostatic adjustment in West Antarctica. *Geophysical Journal International*, 214(2):811–824.

Norris, S. L., Tarasov, L., Monteath, A. J., Gosse, J. C., Hidy, A. J., Margold, M., and Froese, D. G. (2022). Rapid retreat of the southwestern Laurentide Ice Sheet during the Bølling-Allerød interval. *Geology*, 50(4):417–421.

Obase, T. and Abe-Ouchi, A. (2019). Abrupt Bølling-Allerød warming simulated under gradual forcing of the last deglaciation. *Geophysical Research Letters*, 46(20):11397–11405.

Oppenheimer, M., Glavovic, B., Hinkel, J., van de Wal, R., Magnan, A. K., Abd-Elgawad, A., Cai, R., Cifuentes-Jara, M., Deconto, R. M., Ghosh, T., et al. (2019). Sea level rise and implications for low lying islands, coasts and communities. *The Intergovernmental Panel on Climate Change*.

Palmer, M., Gregory, J. M., Bagge, M., Calvert, D., Hagedoorn, J., Howard, T., Klemann, V., Lowe, J., Roberts, C., Slangen, A., et al. (2020). Exploring the drivers of global and local sea-level change over the 21st century and beyond. *Earth's Future*, 8(9):e2019EF001413.

Palmer, M. D., Harris, G. R., and Gregory, J. M. (2018). Extending cmip5 projections of global mean temperature change and sea level rise due to thermal expansion using a physically-based emulator. *Environmental Research Letters*, 13(8):084003.

Pan, L., Milne, G. A., Latychev, K., Goldberg, S. L., Austermann, J., Hoggard, M. J., and Mitrovica, J. X. (2022). The influence of lateral Earth structure on inferences of global ice volume during the Last Glacial Maximum. *Quaternary Science Reviews*, 290:107644.

Parrenin, F., Barnola, J.-M., Beer, J., Blunier, T., Castellano, E., Chappellaz, J., Dreyfus, G., Fischer, H., Fujita, S., Jouzel, J., et al. (2007). The EDC3 chronology for the EPICA Dome C ice core. *Climate of the Past*, 3:485–497.

Patton, H., Hubbard, A., Andreassen, K., Auriac, A., Whitehouse, P. L., Stroeven, A. P., Shackleton, C., Winsborrow, M., Heyman, J., and Hall, A. M. (2017). Deglaciation of the Eurasian ice sheet complex. *Quaternary Science Reviews*, 169:148–172.

Patton, H., Hubbard, A., Andreassen, K., Winsborrow, M., and Stroeven, A. P. (2016). The build-up, configuration, and dynamical sensitivity of the Eurasian ice-sheet complex to Late Weichselian climatic and oceanic forcing. *Quaternary Science Reviews*, 153:97–121.

Pedro, J. B., Bostock, H. C., Bitz, C. M., He, F., Vandergoes, M. J., Steig, E. J., Chase, B. M., Krause, C. E., Rasmussen, S. O., Markle, B. R., et al. (2016). The spatial extent and dynamics of the Antarctic Cold Reversal. *Nature Geoscience*, 9(1):51–55.

Peltier, W. (1974). The impulse response of a maxwell earth. *Reviews of Geophysics*, 12(4):649–669.

Peltier, W., Argus, D., and Drummond, R. (2015). Space geodesy constrains ice age terminal deglaciation: The global ICE-6G_C (VM5a) model. *Journal of Geophysical Research: Solid Earth*, 120(1):450–487.

Peltier, W. R. (2004). Global glacial isostasy and the surface of the ice-age Earth: the ICE-5G (VM2) model and GRACe. *Annu. Rev. Earth Planet. Sci.*, 32:111–149.

Peltier, W. R., Wu, P. P.-C., Argus, D. F., Li, T., and Velay-Vitow, J. (2022). Glacial isostatic adjustment: physical models and observational constraints. *Reports on Progress in Physics*, 85(9):096801.

Perraudin, N., Defferrard, M., Kacprzak, T., and Sgier, R. (2019). DeepSphere: Efficient spherical convolutional neural network with HEALPix sampling for cosmological applications. *Astronomy and Computing*, 27:130–146.

Perrin, C., Bosence, D., and Rosen, B. (1995). Quantitative approaches to palaeozonation and palaeobathymetry of corals and coralline algae in Cenozoic reefs. *Geological Society, London, Special Publications*, 83(1):181–229.

Pico, T. (2020). Towards assessing the influence of sediment loading on Last Interglacial sea level. *Geophysical Journal International*, 220(1):384–392.

Pico, T., Mitrovica, J., and Mix, A. (2020). Sea level fingerprinting of the Bering Strait flooding history detects the source of the Younger Dryas climate event. *Science advances*, 6(9):eaay2935.

Pittard, M. L., Whitehouse, P. L., Bentley, M. J., and Small, D. (2022). An ensemble of Antarctic deglacial simulations constrained by geological observations. *Quaternary Science Reviews*, 298:107800.

Pollard, D., DeConto, R. M., and Alley, R. B. (2015). Potential Antarctic Ice Sheet retreat driven by hydrofracturing and ice cliff failure. *Earth and Planetary Science Letters*, 412:112–121.

Powell, E. M., Pan, L., Hoggard, M. J., Latychev, K., Gomez, N., Austermann, J., and Mitrovica, J. X. (2021). The impact of 3-D Earth structure on far-field sea level following interglacial West Antarctic Ice Sheet collapse. *Quaternary Science Reviews*, 273:107256.

Purcell, A., Tregoning, P., and Dehecq, A. (2016). An assessment of the ICE6G_C (VM5a) glacial isostatic adjustment model. *Journal of Geophysical Research: Solid Earth*, 121(5):3939–3950.

Raissi, M., Perdikaris, P., and Karniadakis, G. E. (2019). Physics-informed neural networks: A deep learning framework for solving forward and inverse problems involving nonlinear partial differential equations. *Journal of Computational physics*, 378:686–707.

Ramsey, C. B. (2009). Bayesian analysis of radiocarbon dates. *Radiocarbon*, 51(1):337–360.

Rees, S. A. (2005). *Coral reefs of the Indo-Pacific and changes in global Holocene*. PhD thesis, University of Southampton.

Reichstein, M., Camps-Valls, G., Stevens, B., Jung, M., Denzler, J., Carvalhais, N., et al. (2019). Deep learning and process understanding for data-driven Earth system science. *Nature*, 566(7743):195–204.

Reimer, P. J., Austin, W. E., Bard, E., Bayliss, A., Blackwell, P. G., Ramsey, C. B., Butzin, M., Cheng, H., Edwards, R. L., Friedrich, M., et al. (2020). The IntCal20 Northern Hemisphere radiocarbon age calibration curve (0–55 cal kBP). *Radiocarbon*, 62(4):725–757.

Reimer, P. J., Bard, E., Bayliss, A., Beck, J. W., Blackwell, P. G., Ramsey, C. B., Buck, C. E., Cheng, H., Edwards, R. L., Friedrich, M., et al. (2013). IntCal13 and Marine13 radiocarbon age calibration curves 0–50,000 years cal BP. *Radiocarbon*, 55(4):1869–1887.

Ronneberger, O., Fischer, P., and Brox, T. (2015). U-net: Convolutional networks for biomedical image segmentation. In *International Conference on Medical image computing and computer-assisted intervention*, pages 234–241. Springer.

Rovere, A., Pico, T., Richards, F. D., O'Leary, M. J., Mitrovica, J. X., Goodwin, I. D., Austermann, J., and Latychev, K. (2022). The influence of reef isostasy, dynamic topography, and glacial isostatic adjustment on the Last Interglacial sea-level record of Northeastern Australia. https://doi.org/10.31223/X55S8X.

Roy, K. and Peltier, W. (2018). Relative sea level in the Western Mediterranean basin: A regional test of the ICE-7G_NA (VM7) model and a constraint on late Holocene Antarctic deglaciation. *Quaternary Science Reviews*, 183:76–87.

Ruetenik, G. A., Ferrier, K. L., Creveling, J. R., and Fox, M. (2020). Sea-level responses to rapid sediment erosion and deposition in Taiwan. *Earth and Planetary Science Letters*, 538:116198.

Ryan, D. A., Bostock, H. C., Brooke, B. P., and Marshall, J. F. (2007). Bathymetric expression of the Fitzroy River palaeochannel, northeast Australia: response of a major river to sea-level change on a semi-rimmed, mixed siliciclastic-carbonate shelf. *Sedimentary Geology*, 201(1-2):196–211.

Sacks, J., Welch, W. J., Mitchell, T. J., and Wynn, H. P. (1989). Design and analysis of computer experiments. *Statistical science*, 4(4):409–423.

Salles, T., Ding, X., Webster, J. M., Vila-Concejo, A., Brocard, G., and Pall, J. (2018). A unified framework for modelling sediment fate from source to sink and its interactions with reef systems over geological times. *Scientific reports*, 8(1):1–11.

Sanborn, K. L., Webster, J. M., Webb, G. E., Braga, J. C., Humblet, M., Nothdurft, L., Patterson, M. A., Dechnik, B., Warner, S., Graham, T., et al. (2020). A new model of Holocene reef initiation and growth in response to sea-level rise on the Southern Great Barrier Reef. *Sedimentary Geology*, 397:105556.

Sefton, J. (2020). *Evaluating mangrove proxies for quantitative relative sea-level reconstructions*. PhD thesis, Durham University.

Sejrup, H. P., Hjelstuen, B. O., Patton, H., Esteves, M., Winsborrow, M., Rasmussen, T. L., Andreassen, K., and Hubbard, A. (2022). The role of ocean and atmospheric dynamics in the marine-based collapse of the last Eurasian Ice Sheet. *Communications Earth & Environment*, 3(1):119.

Shakun, J. D., Clark, P. U., He, F., Marcott, S. A., Mix, A. C., Liu, Z., Otto-Bliesner, B., Schmittner, A., and Bard, E. (2012). Global warming preceded by increasing carbon dioxide concentrations during the last deglaciation. *Nature*, 484(7392):49–54.

Shennan, I. (1999). Global meltwater discharge and the deglacial sea-level record from northwest Scotland. *Journal of Quaternary Science*, 14(7):715–719.

Shennan, I., Bradley, S., Milne, G., Brooks, A., Bassett, S., and Hamilton, S. (2006). Relative sea-level changes, glacial isostatic modelling and ice-sheet reconstructions from the British Isles since the Last Glacial Maximum. *Journal of Quaternary Science: Published for the Quaternary Research Association*, 21(6):585–599.

Shennan, I., Bradley, S. L., and Edwards, R. (2018). Relative sea-level changes and crustal movements in Britain and Ireland since the Last Glacial Maximum. *Quaternary Science Reviews*, 188:143–159.

Shennan, I., Green, F., and Innes, J. (1997). Evaluation of rapid relative sea-level changes in north-west Scotland during the Last Glacial-Interglacial transition: evidence from Ardtoe and other isolation basins. *Oceanographic Literature Review*, 6(44):576.

Shennan, I., Innes, J. B., Long, A. J., and Zong, Y. (1993). Late Devensian and Holocene relative sea-level changes at Rumach, near Arisaig, northwest Scotland. *Norsk Geologisk Tidsskrift*, 73(3):161–174.

Shennan, I., Innes, J. B., Long, A. J., and Zong, Y. (1994). Late Devensian and Holocene relative sealevel changes at Loch nan Eala, near Arisaig, northwest Scotland. *Journal of Quaternary Science*, 9(3):261–283.

Shennan, I., Lambeck, K., Horton, B., Innes, J., Lloyd, J., McArthur, J., Purcell, T., and Rutherford, M. (2000). Late Devensian and Holocene records of relative sea-

level changes in northwest Scotland and their implications for glacio-hydro-isostatic modelling. *Quaternary Science Reviews*, 19(11):1103–1135.

Shennan, I., Rutherford, M. M., Innes, J. B., and Walker, K. J. (1996). Late glacial sea level and ocean margin environmental changes interpreted from biostratigraphic and lithostratigraphic studies of isolation basins in northwest Scotland. *Geological Society, London, Special Publications*, 111(1):229–244.

Simms, A. R., Lisiecki, L., Gebbie, G., Whitehouse, P. L., and Clark, J. F. (2019). Balancing the last glacial maximum (LGM) sea-level budget. *Quaternary Science Reviews*, 205:143–153.

Simon, K. M., Riva, R. E., and Broerse, T. (2022). Identifying geographical patterns of transient deformation in the geological sea level record. *Journal of Geophysical Research: Solid Earth*, 127(7):e2021JB023693.

Spada, G., Barletta, V. R., Klemann, V., Riva, R., Martinec, Z., Gasperini, P., Lund, B., Wolf, D., Vermeersen, L., and King, M. (2011). A benchmark study for glacial isostatic adjustment codes. *Geophysical Journal International*, 185(1):106–132.

Srivastava, R. K., Greff, K., and Schmidhuber, J. (2015). Training very deep networks. *Advances in neural information processing systems*, 28.

Steffen, H. and Wu, P. (2011). Glacial isostatic adjustment in Fennoscandia—a review of data and modeling. *Journal of geodynamics*, 52(3-4):169–204.

Stoker, B. J., Margold, M., Gosse, J. C., Hidy, A. J., Monteath, A. J., Young, J. M., Gandy, N., Gregoire, L. J., Norris, S. L., and Froese, D. (2022). The collapse of the Cordilleran–Laurentide ice saddle and early opening of the Mackenzie Valley, Northwest Territories, Canada, constrained by 10 Be exposure dating. *The Cryosphere*, 16(12):4865–4886.

Strauss, B. H., Orton, P. M., Bittermann, K., Buchanan, M. K., Gilford, D. M., Kopp, R. E., Kulp, S., Massey, C., Moel, H. d., and Vinogradov, S. (2021). Economic damages from hurricane sandy attributable to sea level rise caused by anthropogenic climate change. *Nature communications*, 12(1):2720.

Suganuma, Y., Kaneda, H., Mas e Braga, M., Ishiwa, T., Koyama, T., Newall, J. C., Okuno, J., Obase, T., Saito, F., Rogozhina, I., et al. (2022). Regional sea-level highstand triggered Holocene ice sheet thinning across coastal Dronning Maud Land, East Antarctica. *Communications Earth & Environment*, 3(1):273.

Swingedouw, D., Fichefet, T., Goosse, H., and Loutre, M.-F. (2009). Impact of transient freshwater releases in the Southern Ocean on the AMOC and climate. *Climate dynamics*, 33(2-3):365–381.

Tanabe, S., Tateishi, M., and Shibata, Y. (2009). The sea-level record of the last deglacial in the Shinano River incised-valley fill, Echigo Plain, central Japan. *Marine Geology*, 266(1-4):223–231.

Tarasov, L., Dyke, A. S., Neal, R. M., and Peltier, W. R. (2012). A data-calibrated distribution of deglacial chronologies for the North American ice complex from glaciological modeling. *Earth and Planetary Science Letters*, 315:30–40.

Tarasov, L., Hughes, A., Gyllencreutz, R., Lohne, O. S., Mangerud, J., and Svendsen, J.-I. (2014). The global GLAC-1c deglaciation chronology, melwater pulse 1-a, and a question of missing ice. In *IGS Symposium: Contribution of Glaciers and Ice Sheets to Sea-Level Change, Chamonix, France*, pages 26–30.

Tarasov, L. and Peltier, W. (2006). A calibrated deglacial drainage chronology for the North American continent: evidence of an Arctic trigger for the Younger Dryas. *Quaternary Science Reviews*, 25(7-8):659–688.

Tarasov, L. and Peltier, W. R. (2003). Greenland glacial history, borehole constraints, and Eemian extent. *Journal of Geophysical Research: Solid Earth*, 108(B3).

van der Wal, W., Whitehouse, P. L., and Schrama, E. J. (2015). Effect of GIA models with 3D composite mantle viscosity on GRACE mass balance estimates for Antarctica. *Earth and Planetary Science Letters*, 414:134–143.

Vasskog, K., Svendsen, J.-I., Mangerud, J., Agasøster Haaga, K., Svean, A., and Lunnan, E. M. (2019). Evidence of early deglaciation (18 000 cal a bp) and a postglacial relative sea-level curve from southern Karmøy, south-west Norway. *Journal of Quaternary Science*, 34(6):410–423.

Waelbroeck, C., Labeyrie, L., Michel, E., Duplessy, J.-C., Mcmanus, J. F., Lambeck, K., Balbon, E., and Labracherie, M. (2002). Sea-level and deep water temperature changes derived from benthic foraminifera isotopic records. *Quaternary science reviews*, 21(1-3):295–305.

Wang, Z. and Bovik, A. C. (2009). Mean squared error: Love it or leave it? A new look at signal fidelity measures. *IEEE signal processing magazine*, 26(1):98–117.

Weaver, A. J., Saenko, O. A., Clark, P. U., and Mitrovica, J. X. (2003). Meltwater pulse 1A from Antarctica as a trigger of the Bølling-Allerød warm interval. *Science*, 299(5613):1709–1713.

Webster, J. M., Braga, J. C., Humblet, M., Potts, D. C., Iryu, Y., Yokoyama, Y., Fujita, K., Bourillot, R., Esat, T. M., Fallon, S., et al. (2018). Response of the Great Barrier Reef to sea-level and environmental changes over the past 30,000 years. *Nature Geoscience*, 11(6):426.

White, D. A., Fink, D., and Gore, D. B. (2011). Cosmogenic nuclide evidence for enhanced sensitivity of an East Antarctic ice stream to change during the last deglaciation. *Geology*, 39(1):23–26.

Whitehouse, P., Latychev, K., Milne, G. A., Mitrovica, J. X., and Kendall, R. (2006). Impact of 3-D Earth structure on Fennoscandian glacial isostatic adjustment: Implications for space-geodetic estimates of present-day crustal deformations. *Geophysical Research Letters*, 33(13).

Whitehouse, P. L. (2018). Glacial isostatic adjustment modelling: historical perspectives, recent advances, and future directions. *Earth surface dynamics*, 6(2):401–429.

Whitehouse, P. L., Bentley, M. J., and Le Brocq, A. M. (2012a). A deglacial model for Antarctica: geological constraints and glaciological modelling as a basis for a new model of Antarctic glacial isostatic adjustment. *Quaternary Science Reviews*, 32:1–24.

Whitehouse, P. L., Bentley, M. J., Milne, G. A., King, M. A., and Thomas, I. D. (2012b). A new glacial isostatic adjustment model for Antarctica: calibrated and

tested using observations of relative sea-level change and present-day uplift rates. *Geophysical Journal International*, 190(3):1464–1482.

Whitehouse, P. L., Gomez, N., King, M. A., and Wiens, D. A. (2019). Solid Earth change and the evolution of the Antarctic Ice Sheet. *Nature communications*, 10(1):1–14.

Wickert, A. D., Mitrovica, J. X., Williams, C., and Anderson, R. S. (2013). Gradual demise of a thin southern Laurentide ice sheet recorded by Mississippi drainage. *Nature*, 502(7473):668–671.

Wikle, C. K., Zammit-Mangion, A., and Cressie, N. (2019). *Spatio-temporal Statistics with R*. Chapman and Hall/CRC.

Wolstencroft, M., Shen, Z., Törnqvist, T. E., Milne, G. A., and Kulp, M. (2014). Understanding subsidence in the Mississippi Delta region due to sediment, ice, and ocean loading: Insights from geophysical modeling. *Journal of Geophysical Research: Solid Earth*, 119(4):3838–3856.

Woodroffe, C. D. and Webster, J. M. (2014). Coral reefs and sea-level change. *Marine Geology*, 352:248–267.

Woodroffe, S. A., Long, A. J., Milne, G. A., Bryant, C. L., and Thomas, A. L. (2015). New constraints on late Holocene eustatic sea-level changes from Mahé, Seychelles. *Quaternary Science Reviews*, 115:1–16.

Wu, P. and Peltier, W. (1984). Pleistocene deglaciation and the earth's rotation: a new analysis. *Geophysical Journal International*, 76(3):753–791.

Xu, K., Zhang, M., Li, J., Du, S. S., Kawarabayashi, K.-i., and Jegelka, S. (2020). How neural networks extrapolate: From feedforward to graph neural networks. *arXiv preprint arXiv:2009.11848*.

Yao, W., Zeng, Z., Lian, C., and Tang, H. (2018). Pixel-wise regression using U-Net and its application on pansharpening. *Neurocomputing*, 312:364–371.

Yeung, N., Menviel, L., Meissner, K., and Sikes, E. (2020). Assessing the Spatial Origin of Meltwater Pulse 1A Using Oxygen-Isotope Fingerprinting. *Paleoceanography and Paleoclimatology*.

Yokoyama, Y., Esat, T. M., Thompson, W. G., Thomas, A. L., Webster, J. M., Miyairi, Y., Sawada, C., Aze, T., Matsuzaki, H., Okuno, J., et al. (2018). Rapid glaciation and a two-step sea level plunge into the Last Glacial Maximum. *Nature*, 559(7715):603–607.

Yokoyama, Y., Lambeck, K., De Deckker, P., Esat, T. M., Webster, J. M., and Nakada, M. (2022). Towards solving the missing ice problem and the importance of rigorous model data comparisons. *Nature Communications*, 13(1):6261.

Yokoyama, Y., Lambeck, K., De Deckker, P., Johnston, P., and Fifield, L. K. (2000). Timing of the Last Glacial Maximum from observed sea-level minima. *Nature*, 406(6797):713–716.

Yokoyama, Y. and Purcell, A. (2021). On the geophysical processes impacting palaeo-sea-level observations. *Geoscience Letters*, 8(1):1–19.

Yokoyama, Y., Purcell, A., Marshall, J. F., and Lambeck, K. (2006). Sea-level during the early deglaciation period in the Great Barrier Reef, Australia. *Global and Planetary Change*, 53(1-2):147–153.

Appendix A: A reconciled solution of Meltwater Pulse 1A sources using sea-level fingerprinting

nature COMMUNICATIONS

ARTICLE

https://doi.org/10.1038/s41467-021-21990-y OPEN

A reconciled solution of Meltwater Pulse 1A sources using sea-level fingerprinting

Yucheng Lin [1,2✉], Fiona D. Hibbert [2,4], Pippa L. Whitehouse [1], Sarah A. Woodroffe[1], Anthony Purcell [2], Ian Shennan [1] & Sarah L. Bradley [3]

The most rapid global sea-level rise event of the last deglaciation, Meltwater Pulse 1A (MWP-1A), occurred ~14,650 years ago. Considerable uncertainty regarding the sources of meltwater limits understanding of the relationship between MWP-1A and the concurrent fast-changing climate. Here we present a data-driven inversion approach, using a glacio-isostatic adjustment model to invert for the sources of MWP-1A via sea-level constraints from six geographically distributed sites. The results suggest contributions from Antarctica, 1.3 m (0–5.9 m; 95% probability), Scandinavia, 4.6 m (3.2–6.4 m) and North America, 12.0 m (5.6–15.4 m), giving a global mean sea-level rise of 17.9 m (15.7–20.2 m) in 500 years. Only a North American dominant scenario successfully predicts the observed sea-level change across our six sites and an Antarctic dominant scenario is firmly refuted by Scottish isolation basin records. Our sea-level based results therefore reconcile with field-based ice-sheet reconstructions.

[1] Department of Geography, Durham University, Durham, UK. [2] Research School of Earth Sciences, Australian National University, ACT, Canberra, Australia. [3] Department of Geography, The University of Sheffield, Sheffield, UK. [4] Present address: Department of Environment and Geography, University of York, York, UK. ✉email: yucheng.lin@durham.ac.uk

Meltwater Pulse 1A (MWP-1A) was the largest and most rapid global sea-level rise event of the last deglaciation, characterised by ~20 m global mean sea-level (GMSL) rise within 500 years[1,2]. It was driven by the collapse of vulnerable ice sheet sectors, and was concurrent with rapid Northern Hemispheric warming and disruptions in oceanic and atmospheric circulation[3,4]. The ice-ocean-climate feedbacks operating during this period are not well understood largely due to a lack of consensus on the sources of MWP-1A[5,6], which, in turn, were likely to be a key driver in stimulating rapid deglacial climate change[7–9].

Two major techniques have been used to constrain the sources of MWP-1A. The first uses physics-based models, constrained by field-based glacio-geological evidence, to simulate regional ice sheet change during the last deglaciation[10–12]. This approach is restricted by large uncertainties regarding palaeo ice-sheet boundary conditions, climatic conditions, and ice-sheet model parameters. Ice histories derived using this approach do not always match sea-level observations[11]. Conversely, the second method seeks to reconcile ice-sheet change with spatially variable records of sea-level change using a glacio-isostatic adjustment (GIA) model[1,13–15], an approach often termed sea-level fingerprinting[16,17]. The primary limitation of sea-level fingerprinting is the spatial and temporal scarcity of sea-level records across MWP-1A. Commonly, only three sites are used (Tahiti, Barbados and Sunda Shelf), resulting in an under-constrained problem and strongly non-unique solutions[15,17,18]. Other techniques, e.g., analysis of the oceanographic[8,19,20] or isotopic[21] effects of specific meltwater sources, add further constraints, but the primary source of MWP-1A remains controversial with three ice sheets proposed as the major contributor, namely, the North American Ice Sheet, including Greenland (NAIS)[2,10,22], the Antarctic Ice Sheet (AIS)[1,13] and the Scandinavian and the Barents Sea Ice Sheet (henceforth denoted together as SIS)[23].

In this work, we combine a data-driven inversion approach with sea-level fingerprinting to simultaneously determine probability distributions for the magnitude and sources of MWP-1A based on six sea-level sites spanning the far, intermediate and near field. The results indicate a 17.9 m (15.7–20.2 m; 95% probability) global mean sea-level rise during MWP-1A, which consists of a dominant NAIS contribution (accounting for 35–85% of total MWP-1A magnitude), a substantial SIS contribution (20-35%) and a minor AIS contribution (0–35%, with a strong preference for a <15% contribution). Unlike previous sea-level fingerprinting studies[1,13], our results show good agreement with most recent regional ice-sheet reconstructions[10,22–26], and may lead to a reconciled solution of MWP-1A sources.

Results

Sea-level fingerprinting approach. To robustly fingerprint the sources of MWP-1A, three main challenges need to be overcome. First, the above-mentioned non-uniqueness problem. Previously, only three sea-level sites showed sufficient temporal resolution for fingerprinting studies across MWP-1A[15,18], namely, coral reef records from Tahiti[1,27] and Barbados[28–30] and sedimentary indicators from Sunda Shelf[31]. The geographical distributions of these sites do not permit the separation of meltwater sources from the AIS and SIS (Fig. 1). Second, the relationship between coral living depth and environmental conditions, as well as the link between reef accretion and sea-level change[32], is not straightforward and may differ between different localities[33–35]. This can add considerable complexity when interpreting coral sea-level indicators. Third, most previous fingerprinting studies assumed a minor SIS contribution to MWP-1A (1–2.5 m)[1,13,15,18]. This is challenged by a recent chronological reinterpretation of the SIS ice history that proposes the SIS was a major MWP-1A contributor[23]. Such a large SIS contribution has not yet been tested using sea-level fingerprinting.

We address these challenges via three major methodological advances. First, we increase the number of sea-level sites, with data from extensive coral and coralline algae deposits on the Great Barrier Reef (GBR) at Hydrographer's Passage (HYD) and Noggin Pass (NOG)[36,37], and isolation basin stratigraphies from Northwest Scotland[38–40] (Fig. 1). Where necessary, a standardisation is applied to ensure that the sea-level index points (SLIPs) only reflect the sea-level fingerprint of MWP-1A (see Methods). Second, based on these standardised SLIPs, we estimate the local magnitude of relative sea-level (RSL) change across MWP-1A at each of our six sites using a Monte Carlo (MC) linear regression approach to capture the vertical and chronological uncertainties of the sea-level indicators. Third, these local MWP-1A magnitudes of RSL change are used to invert for the global magnitude, and regional partitioning of meltwater via fingerprinting of NAIS, AIS and SIS change.

Our approach relies on the assumption that SLIPs can be used to map out the fingerprint of ice-sheet change. A sea-level fingerprint reflects the global geoid variation and instantaneous elastic solid Earth response to ice mass change[16,17], also known as the elastic component of RSL change[18]. Assuming the NAIS, AIS and SIS were the only contributors to MWP-1A, the global pattern of RSL change caused by melt from these ice sheets can be identified as a linear combination of three spatially variable sea-level fingerprints (Fig. 1d–f), each scaled by the eustatic contribution from the related ice sheet[17]. Before using SLIPs to map out the fingerprint of MWP-1A, three issues must be addressed (i.e., our standardisation). The first only affects our Northwest Scotland data. RSL change here contains a large local GIA signal associated with changes to the British-Irish Ice Sheet (BIIS). We determine a local GIA correction for all these SLIPs to isolate the GIA signal associated with non-local ice sheet change[14,41] (see Methods, Fig. 2f). The second issue concerns the spatial gradient of the sea-level fingerprint between coring locations within one site (e.g., >10km wide)[15]. This affects the Sunda Shelf and Northwest Scotland data and is accounted for by subtracting the time-specific sea-level gradient between each SLIP and a reference location. The corrected SLIPs represent RSL at a single locality (red stars in Fig. 2c,f and Supplementary Fig. 2, see Methods). Lastly, for all SLIPs, we remove the age- and location-specific viscous component of RSL change. This correction accounts for the viscous solid Earth response to changes in surface loading and the accompanying change in geoid height caused by ice-sheet variation prior to and during MWP-1A (see Methods). We determine all three corrections using the mean of a GIA model ensemble that accounts for uncertainties associated with global ice history and mantle properties (see Methods). Because we focus on the centennial timescale of MWP-1A, our GIA corrections are not strongly sensitive to choice of mantle properties (see Supplementary Fig. 3), and hence neglect of heterogeneity (i.e., 3-D Earth structure)[42] should not bias our results.

Estimating local sea-level change across MWP-1A. The standardised SLIPs constrain local MWP-1A magnitude at each site. We use a conservative time window of 14.65-14.00 ka BP to select SLIPs at each site that clearly mark the initiation and termination of MWP-1A, enabling us to capture the full magnitude of MWP-1A sea-level rise. Ideally, only records with mean ages within this window will be selected, but for sites with insufficient temporal coverage we include records whose 2σ age error bars extend into it. We estimate local MWP-1A magnitude from the SLIPs using a

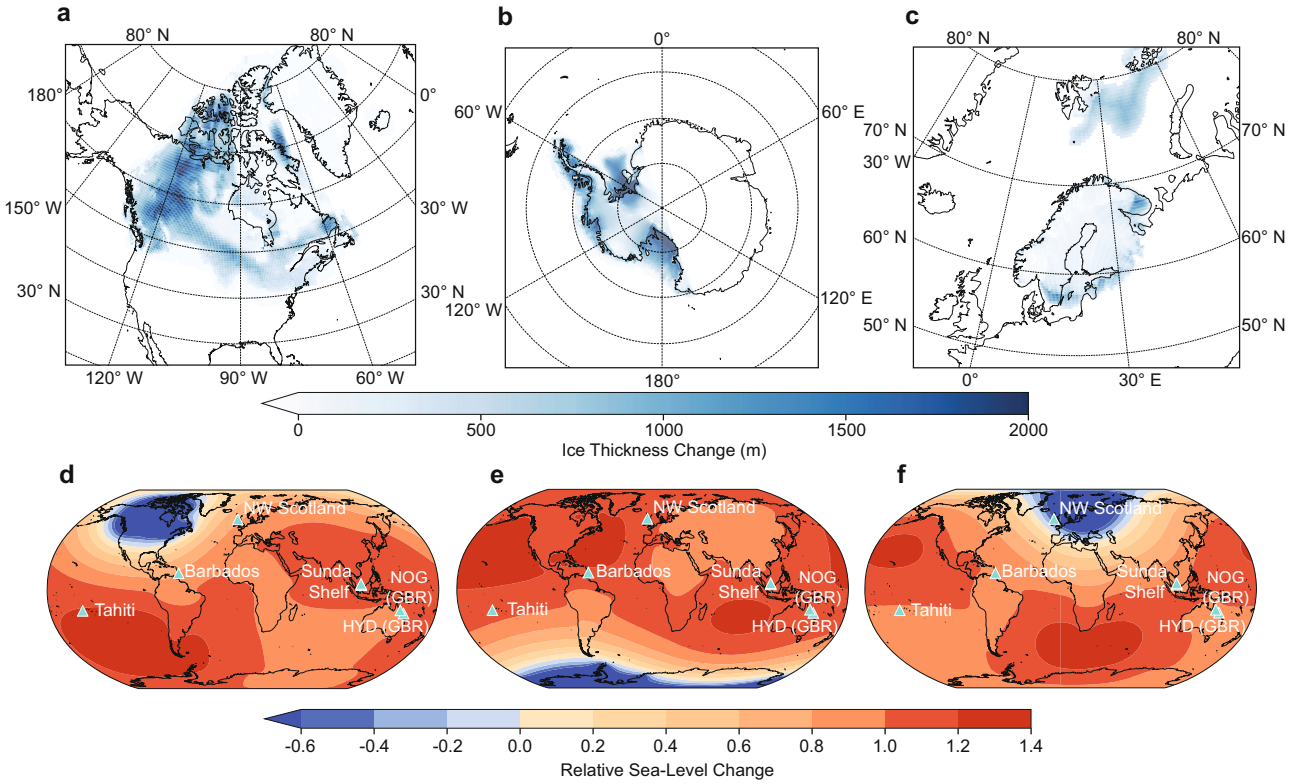

Fig. 1 Ice melt geometries and normalised sea-level fingerprints used in this study. a–c Ice mass loss pattern for the NAIS, AIS and SIS, which were used to generate sea-level fingerprints shown in (**d–f**) that represent elastic-induced global relative sea-level change corresponding to one unit of ice mass loss from each ice sheet. **a**, **c** The reconstructed MWP-1A ice melt geometries from Lambeck et al.[24] and BRITICE-CHRONO[52]. **b** The LGM-to-present West AIS melt geometry from Whitehouse et al.[54] (see Methods for details). The cyan triangles and text denote the location and name of each sea-level site. HYD = Hydrographer's Passage, NOG = Noggin Pass, GBR = Great Barrier Reef, NW Scotland = Northwest Scotland.

MC linear regression method, which captures any asymmetric depth and age uncertainties of different types of sea-level indicators by randomly sampling their uncertainty distributions. We use two approaches to represent indicative depth distributions of coral sea-level indicators; an empirically-derived distribution from modern coral analogues (the empirical scenario) and a uniform distribution, using palaeo-water depths from original publications (the uniform scenario)[35,43]. For non-coral SLIPs, both scenarios adopt a uniform indicative depth distribution based on original publications. The MC sampling process also accounts for the error propagation associated with any GIA correction applied and elevation measurement uncertainties (see Methods). We calculate chronological probability distributions following the methodology of Hibbert et al.[43], accounting for multimodal, asymmetric ^{14}C age distributions and age reliability screening (see Methods).

MC linear regression, using randomly selected data points and a weighted least square method, determines the local MWP–1A RSL rise rate at each site (see Methods). We convert this to local MWP-1A magnitude by multiplying by the assumed duration of MWP-1A (500 years in this study). We exclude, as implausible, regressions producing a reverse slope (i.e., a sea-level fall). Repeating this process 20,000 times (excluding the implausible iterations) produces distributions of local MWP-1A magnitude for each site (Figs. 2, 3a). Because our results are derived from the averaged sea-level rise rate throughout MWP-1A, they are linearly scalable to any assumed duration of MWP-1A.

The viscous component of RSL change has a significant effect on local sea-level change during MWP-1A. Far-field localities (Tahiti, Sunda Shelf, HYD and NOG) will have experienced local sea-level fall associated with the redistribution of water to regions experiencing peripheral bulge subsidence and due to the ocean load-induced continental levering effect (we refer to the combined effect as ocean siphoning[44]; Supplementary Fig. 3 and S4). Not considering this effect would lead to ~1 m underestimate of the local RSL magnitude. Conversely, Northwest Scotland will have experienced 0.8 m local RSL rise during MWP-1A due to subsidence of the SIS peripheral bulge. Being an intermediate-field site, Barbados experienced both ocean siphoning and peripheral bulge subsidence during MWP-1A. The effects of these two signals roughly balance each other (Supplementary Fig. 3 and S4). It should be noted that given the exponential-like form of postglacial decay, the non-linear viscous signal associated with ice melt during MWP-1A is approximately double the linear pre-MWP-1A viscous signal (see Methods), a point largely unconsidered in previous work[15]. We recommend both viscous signals be considered in future meltwater source inversion studies.

At Tahiti, our inversion is tightly constrained by samples containing vermetid gastropods (yellow error bars in Fig. 2a) that indicate very shallow environments (<5–6 m[1,45,46]). Most of the other Tahiti coral samples were identified as *Porites* sp.[1]. Modern analogues (the empirical scenario) suggest a bimodal depth-habitat distribution concentrated at 0–15 m and 40–50 m[43]. This bimodal empirical distribution was generated from a global compilation, and given insufficient modern observations at Tahiti, we consider it a maximum vertical depth range for this species. Comparatively, the palaeo-water depths derived from coral-algal assemblages (our uniform scenario) suggest depths of 0–10 m or even 0–20 m[46,47]. Therefore our empirical scenario yields a larger uncertainty range for the MWP-1A magnitude (13.6–30.9 m for a 500-year duration; 95% confidence interval;

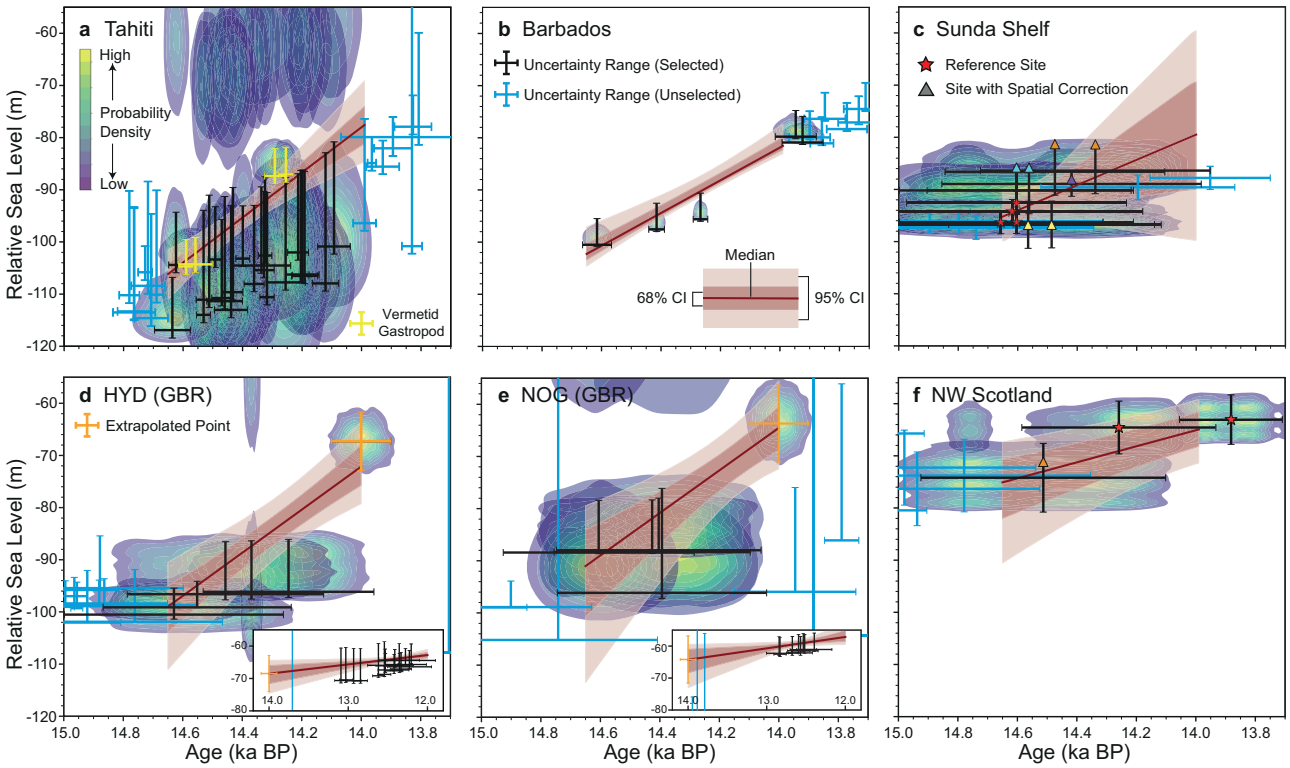

Fig. 2 Estimated local MWP-1A sea-level rise trend at six selected sites using our empirical scenario. Blue-green-yellow shading indicates the data-point-specific probability density accounting for age and depth uncertainties. The depth uncertainty for coral-based SLIPs (**a**, **b**, **d**, **e**) was determined using modern ecological data (the empirical scenario), some of which present a bimodal habitat depth, resulting in complex data clouds. For the uniform scenario, see Supplementary Fig. 6. The median and 95/68% confidence interval (CI) were determined by 20,000 MC simulations (see main text). Black/blue error bars reflect uncertainty ranges associated with viscous and spatial signal corrections applied to SLIPs that were selected/unselected to train the MC model. Vertical and horizontal bars indicate combined depth uncertainty and 2σ age error. **a** The selected coral samples containing vermetid gastropods are highlighted in yellow. **c**, **f** A spatial sea-level gradient correction was applied to ensure all SLIPs represent sea level at a single locality (reference site, denoted by red stars) in Sunda Shelf and Northwest Scotland. Triangles with different colours correspond to different localities, their vertical position indicates the original elevation prior to spatial gradient correction. **d**, **e** Orange error bars indicate the extrapolated point, the extrapolation process is shown in the subplot. **f** SLIPs have been corrected for the local GIA signal using the BRITICE-CHRONO ice model with 120 Earth models. GIA modelling uncertainty is incorporated into the error bars and data clouds.

CI) than the uniform scenario (15.5–26.6 m, see uniform scenario results in Supplementary Fig. 6). Under a 340-year duration, our result suggests a 14.5 m sea-level rise (18.7 m if only using the vermetid gastropods records), similar to a previous estimate of 12–22 m[1].

Because the two Great Barrier Reef sites experienced reef demise and landward migration across MWP-1A, SLIPs from HYD and NOG only show a rapid ~10 m sea-level rise ~14.6–14.4 ka BP with no clear post-MWP-1A marker until the initiation of new coral reefs at ~13.0 ka BP (Fig. 2d,e)[36,37]. To estimate the MWP-1A magnitude at these sites, we determined RSL at 14.0 ka BP by extrapolating back from the large number of SLIPs between ~13.0 and 12.0 ka BP (see Methods and Supplementary Fig. 5). Based on the extrapolated points, our bimodal empirical distribution yields larger MWP-1A uncertainty ranges of 12.0–32.7 m and 7.3–37.7 m for HYD and NOG (95% CI; 500 years) than the counterpart generated by the uniform scenario (9.3–31.9 m and 11.5–28.2 m, Fig. 3a), with both showing good agreement with Tahiti.

At Sunda Shelf, temporally clustered SLIPs with ~0.4 ka age uncertainties (2σ; Fig. 2c) provide a poor constraint on RSL rise, with ~35% of MC simulations producing a reverse slope. We therefore only use weighted least square (without MC simulation) to calculate the local MWP-1A RSL magnitude, fitting to the mean of the age/depth distribution of each SLIP, which was assumed to be normally distributed. We exclude one data point, from site 18302 (blue error bars in Fig. 2c), because it is inconsistent with other SLIPs from this region (dated ~14.2 ka BP but suggests 5 m lower RSL than SLIPs at 14.4 ka BP) and would strongly bias the local MWP-1A magnitude estimation. These modified regression conditions, combined with the 2-5 m between-site sea-level gradient corrections (Supplementary Fig. 2), produce a large uncertainty range for the MWP-1A magnitude, 0–35.7 m (95% CI, median 15.5 m). Compared with MWP-1A magnitude estimates for other far-field sites, this median value is slightly lower (Fig. 3a), likely due to SLIPs from site 18301 (yellow triangles in Fig. 2c) indicating 10-15 m lower RSL than other SLIPs of a similar age. The RANSAC outlier detection algorithm[48] suggests, with >90% probability, that these index points are outliers, and excluding them yields a ~21.7 m MWP-1A magnitude. However, we choose to retain them for our analysis, and the large uncertainty range, because the MWP-1A partitioning results do not strongly depend on the local MWP-1A magnitude at Sunda Shelf (see Supplementary Note 2).

At Barbados, a recent coral-based sea-level reconstruction[30] significantly improved the temporal control on local RSL at the termination of MWP-1A; two samples at ~14.0 ka BP in Fig. 2b were not available to former studies[1,15]. Constrained by these new SLIPs, both empirical and uniform scenarios yield a tight 95% confidence range of 12.1–20.0 m and 12.8–18.2 m with a common

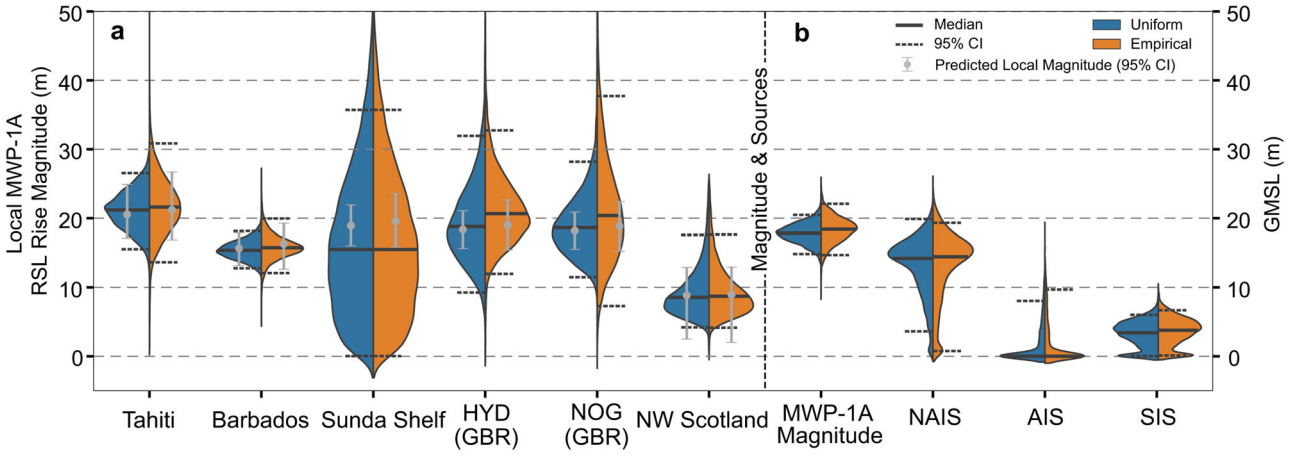

Fig. 3 Inversion results of local MWP-1A RSL rise magnitude and MWP-1A sources. Probability distributions of (**a**) local MWP-1A RSL rise magnitudes, (**b**) total MWP-1A magnitude and contribution from each ice sheet assuming a 500-year duration are shown as a violin plot. The two sides of each violin plot correspond to the empirical (orange) and uniform (blue) scenarios used to represent coral living depths. For non-coral SLIPs (Sunda Shelf and Northwest Scotland), both scenarios adopt a uniform distribution, small differences between the two sides are associated with different viscous signal corrections. Grey error bars in (**a**) represent the predicted local MWP-1A magnitude (95% probability) calculated using the inverted MWP-1A sources in (**b**). All probability density functions are derived by Gaussian kernel density estimation, and all inversion results are exclusively non-negative.

median of ~15.5 m (500-year MWP-1A duration; Fig. 3a). Linearly scaling to 340 years yields a median of 10.7 m, which is lower than previous estimates of ~15 m[1] or 9.7–33.6 m[15], and lower than our estimated MWP-1A magnitudes at other far-field sites.

A low MWP-1A magnitude is also observed in Northwest Scotland. After correcting for the local GIA signal and the spatial sea-level gradient, we identify an 8.6 m MWP-1A magnitude (500-year duration) within a 95% confidence range of 3.9–17.3 m (Fig. 3a). The majority of this uncertainty is associated with the three ice models used to determine the local GIA signal, ANU[2,49], PATTON2017[50,51] and BRITICE-CHRONO (S. Bradley, personal communication 2020)[52], with only minor uncertainty associated with Earth parameters (see Methods and Supplementary Fig. 7). Although the three BIIS models yield relatively large differences regarding the magnitude of the local GIA signal, they provide good consensus on the local elastic-induced MWP-1A sea-level rise magnitude: 9.0 m for ANU, 8.9 m for PATTON2017 and 7.7 m for BRITICE-CHRONO (see Supplementary Note 1). The low MWP-1A magnitude observed in Barbados and Northwest Scotland indicates a dominant contribution to MWP-1A from their nearby ice sheets (i.e., the SIS and NAIS, see Fig. 1).

MWP-1A source inversion. For each of our 20,000 MC simulations of local MWP-1A magnitude, we adopted a non-negative weighted least square algorithm[53] to optimise the contribution of the NAIS, AIS and SIS to MWP-1A based on sea-level fingerprints generated using realistic deglaciation geometries[24,52,54,55] (Fig. 1a–c; see Methods). We also tested alternative sea-level fingerprints based on MWP-1A ice melt geometries from ICE6G_C[22], GLAC-1D[10] and G12[11,18] for the NAIS and PATTON2017[50,51] for the SIS, which results in a negligible difference to our results (Supplementary Table 3). The optimisation process was repeated six times, each time removing one site from the six-site database to quantify the bias associated with data over-dependency and assess the consistency of the overall results (i.e., jackknife resampling). We achieve a bias-corrected inversion of MWP-1A magnitude and sources by subtracting the bias (i.e., the difference between overall jackknife ensemble mean and original results) from the original inversion result (Fig. 3b). The averaged 95% CI of the empirical and uniform scenarios gives GMSL rise during MWP-1A between 15.6 and 20.3 m (mean 17.9 m, Fig. 3b). The SLIPs prefer a dominant NAIS contribution to MWP-1A of 13.1 m (6.0–18.3 m), a substantial contribution from the SIS of 3.3 m (0.5–6.0 m) and a small contribution from the AIS of 1.5 m (0–6.9 m). The jackknifing results (i.e., inversion results when each site is excluded in turn) are generally in agreement (Supplementary Fig. 8), pointing to a dominant NAIS contribution and a minor AIS contribution, but they highlight the non-uniqueness of the solution when near-field sites are excluded (Supplementary Note 2).

Our GMSL rise magnitude is primarily constrained by data from Tahiti, Sunda Shelf, HYD and NOG because they are relatively insensitive to the origins of the meltwater (Fig. 1), in contrast to Barbados and Northwest Scotland. For Barbados, melt from the NAIS is the only scenario that produces a considerably reduced local sea-level rise (20% less than the global mean, Fig. 1d). A dominant NAIS contribution is therefore required to produce ~15.5 m sea-level rise at Barbados under a 17.9 m GMSL rise scenario. NAIS melting also results in reduced RSL rise in Northwest Scotland (25% less than the global mean), but to match the observed 8.6 m sea-level rise at this site (<50% of the GMSL magnitude) requires a significant MWP-1A contribution from the SIS. Our inversion approach for the partitioning of melt between the NAIS, AIS, and SIS, successfully reproduces the local MWP-1A magnitude at our six sites (Fig. 3a, grey error bars).

Our inversion results are used to predict deglacial RSL change at our six sites by incorporating our MWP-1A ice history into the ANU ice model (denoted the ANU_MWP model, Fig. 4h; see Methods). The RSL predictions (Fig. 4a–f) show good fit to the data at all six sites. In particular, predictions at four sites across Northwest Scotland show monotonic sea-level fall during MWP-1A (Fig. 4g), which is supported by the stratigraphic interpretation of isolation basins that were isolated shortly before or during MWP-1A, and where no RSL oscillation is recorded (Supplementary Note 3)[38–40,56]. This condition of no RSL oscillation during MWP-1A can only be achieved if the rate of RSL rise due to far-field melt did not outpace land uplift due to local GIA (detailed interpretation in Supplementary Note 3). Modelling of the local GIA signal suggests the largest plausible rate of land uplift at Arisaig (one of the sites in Northwest Scotland) is 9.8 m in 500 years (Supplementary Note 3). After accounting for 0.8 m sea-level rise caused by subsidence of the SIS peripheral bulge, to avoid a local sea-level oscillation, the RSL fingerprint of MWP-1A

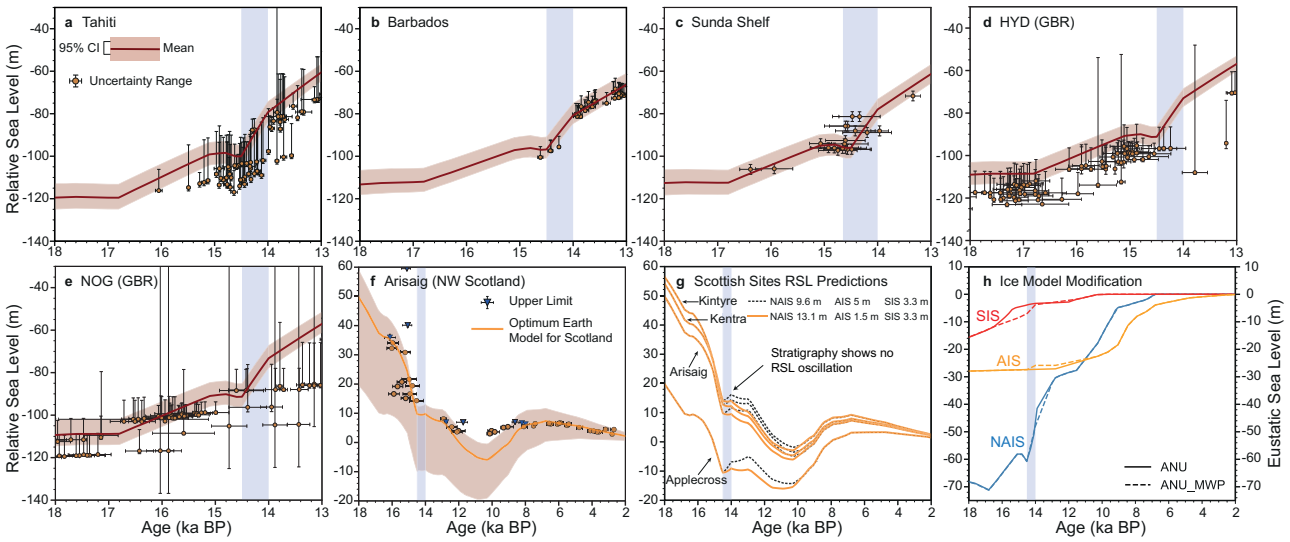

Fig. 4 RSL predictions using the modified ANU model (ANU_MWP). Error bars show depth range and 2σ age uncertainties provided by original studies. The blue vertical band indicates the duration of MWP-1A assumed in the ANU ice model (14.5–14.0 ka BP). **f** Orange solid line indicates the RSL prediction generated using the optimum Earth model (65 km lithospheric thickness, 4/200 × 10^{20} Pa s upper/lower mantle viscosity) instead of the ensemble mean as in (**a**–**e**). By combining our MWP-1A solution with this optimum Earth model in Scotland, we achieve a good fit to RSL data and meanwhile avoid a local RSL oscillation. **g** RSL predictions for four Northwest Scotland sites generated using the optimum Earth model in combination with two MWP-1A scenarios: one that uses the ensemble mean inversion result of this study (orange solid lines) and one where the AIS contributes 5 m to MWP-1A (black dashed lines). The isolation basin stratigraphies indicate no RSL oscillation in Northwest Scotland during MWP-1A. **h** Ice history modifications, solid and dashed lines represent the ANU and ANU_MWP model, respectively. Note the different axis.

cannot exceed ~9 m within 500 years. We refer to this as the sea-level oscillation limit. Under the scenario of 17.9 m GMSL rise, this 9 m limit is exceeded for any substantial AIS contribution because sea-level rise due to melt from the AIS is amplified by 10% across Scotland (Fig. 1e). We assessed the potential consequence of a 5 m AIS contribution to MWP-1A (with the NAIS contribution equivalently reduced, see Methods). This produces a distinct 2,000-year RSL oscillation following the start of MWP-1A (black dashed lines in Fig. 4g). The stratigraphic evidence firmly refutes such an oscillation[56]. In summary, the isolation basin evidence supports a minor AIS, a substantial SIS and a dominant NAIS contribution scenario.

We recalculate uncertainty ranges for our inversion results by imposing a 9 m upper limit on the local MWP-1A magnitude in Northwest Scotland to avoid a local sea-level oscillation. The resulting 95% probability range of the averaged empirical and uniform scenarios suggests a total GMSL rise of 17.9 m (15.7–20.2 m), which consists of a dominant NAIS contribution of 5.6–15.4 m (accounting for 35-85% of total MWP-1A magnitude), a substantial SIS contribution of 3.2–6.4 m (20–35%) and a minor AIS contribution of 0–5.9 m (0–35%) with median values of 12.0, 4.6 and 1.3 m, respectively (Fig. 5).

Discussion

Our estimates show good agreement with recent field-based ice-sheet reconstructions for the NAIS and AIS (Supplementary Table 2). Conversely, most SIS regional reconstructions propose a 1–2.5 m contribution[2,51,55], considerably lower than our estimate. A possible reason for this discrepancy is previous studies are commonly based on radiocarbon chronology that assumes a temporally constant Scandinavian marine radiocarbon reservoir age, which suggests the southern Barents Sea sector collapsed well before MWP-1A (see Fig. 4h). A recent study adopts a temporally varying Scandinavian marine radiocarbon reservoir age to reinterpret the chronology of SIS retreat and suggests that the southern Barents Sea sector may have collapsed during MWP-1A, accompanied by marginal retreat of the Scandinavian Ice Sheet, contributing 4.0–7.4 m to GMSL rise (we calculate the eustatic contribution by subtracting the volume of ice below flotation, as defined in the PATTON2017 ice model[51], from the total ice volume change[23]), similar to our estimate. We suggest a substantial SIS contribution is essential to reconcile the gap between regional ice-sheet reconstructions and global sea-level fingerprinting (see Supplementary Table 2), and thus close the MWP-1A global sea-level budget. Such a substantial freshwater input to the Nordic Sea (~0.12 sverdrup), combined with NAIS freshwater routed along the Mackenzie River into the Arctic, may have contributed to a weakening of this limb of the Atlantic Meridional Overturning Circulation[57], potentially helping to explain the termination of Bølling warming and the initiation of the Older Dryas stadial[8,19,58].

Based on our inversion results, we hypothesise that MWP-1A was triggered by rapid disintegration of Northern Hemispheric ice sheets, which account for at least 65% (95% probability) of GMSL rise during this period. Rapid disintegration of the NAIS and SIS has been proposed to be consistent with the operation of ice-sheet saddle collapse[11,59] and unstable grounding line retreat[60,61] forced by abrupt Northern Hemispheric atmospheric and oceanic warming[3,57]. However, the detailed ice dynamic behaviour of these two ice sheets remains elusive. Although most recent studies suggest that saddle collapse between the Western Laurentide and Cordilleran Ice Sheets was a major contributor to MWP-1A[10,11,18,22,24], a recent study based on the Bering Strait flooding history suggests this saddle collapse did not operate until the Younger Dryas and the NAIS contribution to MWP-1A solely originated from the Eastern Laurentide Ice Sheet[62]. Similarly, for the SIS, the new southern Barents Sea sector collapse chronology proposed by Brendryen et al.[23] is yet to be validated.

To test the sensitivity of our inversion results to alternative ice melt configurations, we separated the NAIS into the Western and Eastern NAIS (separated by 110°W, as defined in Pico et al.[62]) and generated two sea-level fingerprints using the ICE6G_C model[22]. We solve for the contribution of these two NAIS sectors to MWP-1A separately along with the AIS and SIS. The results

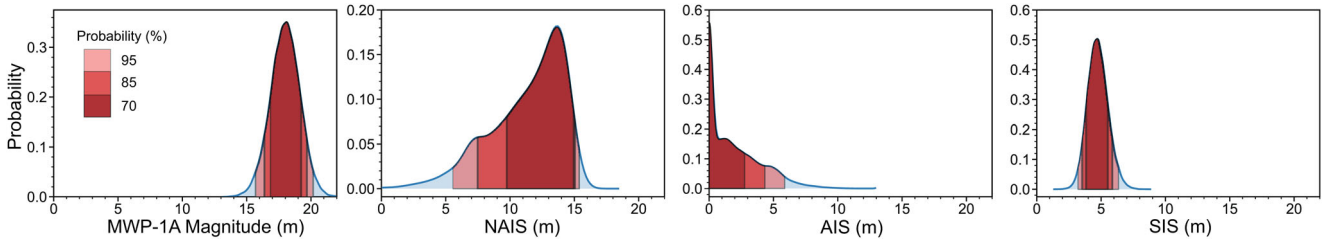

Fig. 5 Sea-level oscillation limit constrained inversion results. Each panel shows a probability density function of the averaged inversion result of the empirical and uniform scenarios associated with total MWP-1A magnitude or the contribution from each ice sheet. Shaded areas indicate 95/85/70% probability range.

yield 4.4 m (0–12.5 m; 95% CI) and 8.7 m (0–16.8 m) contributions from the Western and Eastern NAIS, respectively, with little change to the AIS and SIS contributions (Supplementary Table 3). The total NAIS contribution is similar to our original inversion and this NAIS partitioning is consistent with recent NAIS reconstruction studies[10,22,24,63], but due to the limited sea-level sites available, we cannot robustly determine the relative contribution from these two NAIS sectors. For the SIS, we replace the adopted SIS sea-level fingerprint (Fig. 1f, reflecting ice melt from northern Barents Sea and eastern Fennoscandia) with a fingerprint generated using an ice melt geometry that is predominantly sourced from the southern Barents Sea (from the PATTON2017 model[51]). The impact on the inferred MWP-1A contribution from each ice sheet is <0.3 m (Supplementary Table 3). Therefore, our results are not strongly sensitive to the assumed ice melt geometry.

Our results suggest the AIS was relatively stable during the concurrent Antarctic Cold Reversal[64], which is consistent with recent AIS modelling studies[25,26,65]. Based on our melt geometries, MWP-1A induced 15–18 m local RSL rise around Antarctica. This may have started to destabilise the AIS[25,65,66], eventually leading to substantial AIS retreat from 13 ka BP[67].

Our inversion, which includes sophisticated treatment of uncertainties associated with sea-level data and geophysical modelling processes, provides calibrated MWP-1A contributions from the NAIS, AIS and SIS that are consistent with both sea-level constraints and regional ice-sheet reconstructions. In particular, our MWP-1A partitioning is supported by Scottish isolation basin stratigraphies, which can only be fit by a minor Antarctic contribution. Use of our results to prescribe the global pattern of meltwater discharge during MWP-1A[68] may yield novel insights into the sequencing of ice-ocean-climate interactions during this recent abrupt climate change event.

Methods

Inversion strategy. We solve for the meltwater contributions from the NAIS, AIS, and SIS that bestfit observations of RSL change across MWP-1A (ΔRSL_{Obs}). RSL change takes place due to changes in the shape of the solid Earth and the sea surface, with the latter being defined by the shape of Earth's gravity field. Because the solid Earth behaves viscoelastically over the timescale of interest, RSL change at location φ can be divided into a component that reflects the instantaneous response of the solid Earth and sea surface to an influx of meltwater ($\Delta RSL_{Elastic}$) and a component that reflects ongoing perturbations to these surfaces due to past surface load change ($\Delta RSL_{Viscous}$):

$$\Delta RSL_{Obs}(\varphi) = \Delta RSL_{Viscous}(\varphi) + \Delta RSL_{Elastic}(\varphi) \quad (1)$$

The elastic term can be further decomposed into:

$$\Delta REL_{Elastic}(\varphi) = ESL_{NAIS} \times F_{NAIS}(\varphi) + ESL_{AIS} \times F_{AIS}(\varphi) + ESL_{SIS} \times F_{SIS}(\varphi) \quad (2)$$

where the three ESL terms represent eustatic sea-level (ESL) contributions from the NAIS, AIS, and SIS ice sheets and the $F(\varphi)$ terms denote ice-sheet-specific, site-specific sea-level fingerprint values. The term sea-level fingerprint describes the normalised elastic component of RSL change triggered by a given pattern of ice loss[16,17]. $F_i(\varphi)$ is insensitive to the value of ESL_i and the choice of Earth rheology[17,69]. Therefore, it can be calculated using existing ice sheet reconstructions and treated as a known parameter (see Sea-level fingerprint). The three ESL terms are the unknown parameters in our inversion. We assume that the NAIS, AIS, and SIS are the only contributors to MWP-1A, where any Greenland contribution is included in the NAIS.

The viscous component of RSL change can also be decomposed into two terms:

$$\Delta RSL_{Viscous}(\varphi) = \Delta RSL_{PreViscous}(\varphi) + \Delta RSL_{DurViscous}(\varphi) \quad (3)$$

where $\Delta RSL_{PreViscous}(\varphi)$ and $\Delta RSL_{DurViscous}(\varphi)$ are the changes associated with the viscous effects of ice melt prior to and during MWP-1A respectively (see Viscous component of sea-level change).

Substituting Eq. 3 into Eq. 1 yields an expression for the elastic component of RSL change at each field site:

$$\begin{aligned}\Delta RSL_{Elastic}(\varphi) &= \Delta RSL_{Obs}(\varphi) - \Delta RSL_{PreViscous}(\varphi) - \Delta RSL_{DurViscous}(\varphi) \\ &= ESL_{NAIS} \times F_{NAIS}(\varphi) + ESL_{AIS} \times F_{AIS}(\varphi) \\ &\quad + ESL_{SIS} \times F_{SIS}(\varphi)\end{aligned} \quad (4)$$

By deriving estimates of $\Delta RSL_{Elastic}$ at our six field sites we create a set of equations that can be inverted to yield the ESL contribution to MWP-1A from each of the three ice sheets considered here (see Inversion for MWP-1A sources).

Monte Carlo linear regression is used to estimate probability distribution of the $\Delta RSL_{Elastic}$ at each site by computing the fit to probability distributions of all viscous-corrected sea-level index points (SLIPs) at that site that lie within MWP-1A (see Monte Carlo linear regression). Prior to carrying out the linear regression, the SLIPs are also corrected for any local GIA effects (see Local GIA signal in Northwest Scotland) and any spatial gradient of RSL that exists between sites that are combined to estimate sea-level change at a single location (see Spatial sea-level gradient). We assume the thermosteric contribution to RSL change during MWP-1A is negligible.

Because $\Delta RSL_{PreViscous}(\varphi)$ is controlled by ice melt prior to MWP-1A it can be calculated using an existing global ice model (see below). In contrast, $\Delta RSL_{DurViscous}(\varphi)$ depends on the unknown ESL parameters, which makes Eq. 4 an implicit equation that must be solved iteratively. We employ the following approach (see Supplementary Fig. 1): (i) Calculate the first approximation of $\Delta RSL_{Elastic}(\varphi)$ at six sea-level sites (see main text) using a Monte Carlo linear regression method that assumes $\Delta RSL_{DurViscous}(\varphi)$ is zero. (ii) Invert for the three ESL values using the $\Delta RSL_{Elastic}(\varphi)$ values calculated in step i (for the first iteration) or step v (for all other iterations). (iii) Correct the bias within the inversion results using jackknife resampling (see details below). (iv) Calculate $\Delta RSL_{DurViscous}(\varphi)$ using the bias-corrected ESL inversion from step iii (see details below). (v) Computing $\Delta RSL_{Elastic}(\varphi)$ using the $\Delta RSL_{DurViscous}(\varphi)$ values obtained in step iv. (vi) Repeat step ii-v until convergence of ESL values has been achieved.

GIA modelling. Sea-level change and the solid Earth response to changes in surface loading are computed using the CALSEA software package[70,71], which uses a gravitationally self-consistent theory that accounts for migrating shorelines and Earth rotational feedback[72–75]. The Earth is represented by a spherically symmetric, radially stratified (i.e., 1-D), self-gravitating Maxwell body comprising an elastic lithosphere, and an upper and lower mantle extending to 670 km and from 670 km to the core-mantle boundary, respectively. The elastic and density structure of the Earth is derived from the preliminary reference Earth model[76]. GIA modelling is used to calculate sea-level fingerprints, the local GIA signal in Northwest Scotland, spatial sea-level gradients, and the viscous component of sea-level change.

Sea-level fingerprint. The sea-level fingerprint for each ice sheet is obtained by calculating the normalised global pattern of RSL change associated with melt from a specific ice sheet over a finite time interval. Because sea-level fingerprints are sensitive to the geometry of ice melt[69], we use realistic melt geometries across MWP-1A from two recent regional ice-sheet reconstructions of Lambeck et al.[24] and the BRITICE-CHRONO project (with SCEAN1D scenario; S. Bradley, personal communication 2020) for the NAIS and SIS, respectively (Fig. 1a, c). The latter is constrained using geomorphological data compiled in Hughes et al.[55] and Clark et al.[52], and reconstructed using a plastic ice-sheet model[77]. We also used

some alternative NAIS and SIS melt geometries from ICE6G_C[22], GLAC-1D[10] and G12[11] for the NAIS and PATTON2017[50,51] for the SIS to test the dependence of the inversion results on the assumed ice melt geometries. This leads to essentially unchanged inversion results (see Supplementary Table 3). For the AIS, due to the lack of geological constraints, the melt geometry across MWP-1A remains largely unknown. Since East Antarctica is estimated to have contributed only ~1 m to post-Last Glacial Maximum ESL rise, with this melt most likely to have occurred after MWP-1A[78], any Antarctic contribution to MWP-1A is likely to have come from the West AIS. We therefore generate the AIS sea-level fingerprint using the Last Glacial Maximum-to-present pattern of ice loss across West Antarctica adopted by the W12 ice model[54] (Fig. 1b). Because all our six sea-level sites are far away from the AIS, their AIS sea-level fingerprint values are not sensitive to the assumed West AIS melt geometry.

Local GIA signal in Northwest Scotland. As demonstrated in previous studies[14,41,56], RSL change across Northwest Scotland can be described in terms of a local GIA signal caused by the growth and decay of the BIIS and a non-local GIA signal associated with the growth and decay of other ice sheets around the world. During MWP-1A, if the local GIA signal can be estimated and removed from the SLIPs, the remaining signal will be the non-local GIA signal associated with changes to the NAIS, AIS, and SIS.

Ice history and Earth rheology are not perfectly known for the British Isles. Therefore, we test 360 parameter sets when computing the local GIA signal. Specifically, we use three different BIIS models: BRITICE-CHRONO[52], PATTON2017[50,51] and ANU[2,49,79], and combine each with 120 Earth models. Because these BIIS models were constructed based on different principles (geomorphological reconstruction guided by GIA modelling for BRITICE-CHRONO, thermomechanical ice modelling for PATTON2017 and GIA modelling for ANU) they provide conservative estimates on ice history uncertainties. These ice models were combined with Earth parameters that reflect the rheological properties beneath the British Isles (denoted as near-field rheology). Specifically, we use elastic lithospheric thicknesses of 65, 72 and 80 km, upper mantle viscosities of 4, 4.5, 5, 5.5 and 6×10^{20} Pa s and lower mantle viscosities of 1, 1.5, 2, 3, 4, 5, 7 and 10×10^{22} Pa s. These ranges are constrained by previous GPS analysis and are largely independent of the assumed ice history[80]. We calculate the age-specific local GIA signal for each SLIP and subtract this from the original RSL reconstruction to give the non-BIIS GIA signal. The uncertainty for this procedure is considered within the inversion strategy by sampling the 360 local GIA correction values (each applied to 20,000 Monte Carlo simulations, see details below) and adding the standard deviation of the corrections to the original depth uncertainty in quadrature. After removing the local GIA signal, there is a distinct RSL jump recorded between 14.5 and 14.2 ka BP, which is consistent with the MWP-1A signal observed in far-field sea-level records (Supplementary Fig. 7).

Spatial sea-level gradient. Due to the large geographical spread of the SLIPs from Sunda Shelf and Northwest Scotland, there will be a non-negligible time-dependent difference in the RSL recorded at the different localities (i.e., a spatial sea-level gradient[15]). We apply a correction for this spatial gradient that enables us to determine the RSL change across MWP-1A at a single locality for each region. We quantify this gradient by testing 240 parameter combinations to incorporate uncertainties associated with ice history and Earth rheology. Specifically, we combine the two global ice models ICE6G_C[22] and ANU[2] with 120 different Earth models. The Earth models each have an elastic lithospheric thickness of 60, 72 or 90 km, an upper mantle viscosity of 1, 3, 5, 6 or 7×10^{20} Pa s, and a lower mantle viscosity of 0.1, 0.2, 0.3, 0.5, 0.6, 0.7, 0.9 or 1×10^{22} Pa s for ICE6G_C, or 0.7, 0.9, 1, 1.5, 3, 4, 5 or 7×10^{22} Pa s for the ANU model (we made different choices for lower mantle viscosity because the two ice models have different preference ranges). Because the local GIA signal in Northwest Scotland is removed separately we do not include the BIIS component of ICE6G_C and ANU when calculating the spatial gradient for Northwest Scotland to avoid a double correction. The ensemble mean of the 240 parameter combinations is used to determine the time-dependent data-specific spatial sea-level gradient (Supplementary Fig. 2). Site 18300 and Applecross are defined as reference sites for Sunda Shelf and Northwest Scotland respectively (red stars in Fig. 2 and Supplementary Fig. 2), to which all other sites are corrected. As for the local GIA signal correction, the uncertainty in this procedure is added to the original depth uncertainty in quadrature.

Viscous component of sea-level change. To correct for the viscous signal across MWP-1A, we estimate the viscous contribution of RSL change to each SLIP, accounting for their specific age and location. Given that the viscous response to ice melt prior to MWP-1A ($\Delta RSL_{PreViscous}$) will be approximately linear over MWP-1A[15,18], we quantify this linear rate by considering the viscous response to ice sheet change between the end of the last interglacial and the start of MWP-1A (14.65 ka BP). We assume no melting after 14.65 ka BP and calculate the linear rate of RSL change during the following 1,000 years (Supplementary Fig. 3). This linear rate is used to determine the $\Delta RSL_{PreViscous}(\varphi)$ signal that is specific to the age and location of each SLIP, assuming the viscous contribution is 0 at the initiation of MWP-1A (14.65 ka BP). For all sites except Northwest Scotland we use the mean value derived from a 240-member GIA model ensemble, as described in the previous section. For Northwest Scotland, since the dominant viscous signal here relates to SIS-induced peripheral bulge subsidence (roughly 90% of the signal), which primarily depends on the local rheology of the British Isles, we use the near-field Earth parameters described in the section on Northwest Scotland. Again, to avoid a double correction, we did not include the BIIS in the global ice model when calculating $\Delta RSL_{PreViscous}(\varphi)$ for Northwest Scotland.

Because the $\Delta RSL_{DurViscous}(\varphi)$ terms depend on the ESL values in Eq. 4, which are unknown during the first iteration, we neglect this component of RSL change during the first iteration. Since these terms are relatively small compared to $\Delta RSL_{Elastic}(\varphi)$ (less than 10%), neglecting them will not significantly alter the inversion result during the first iteration. Beginning from the second iteration, we scale the ice melt geometries that are used to generate the sea-level fingerprints (main text Fig. 1) according to the bias-corrected ESL values determined in the previous iteration (details below). The pattern of $\Delta RSL_{DurViscous}(\varphi)$ is then calculated assuming a linear rate of ice melt throughout MWP-1A. A range of Earth models are used, as for $\Delta RSL_{PreViscous}(\varphi)$ above, and the ensemble mean of each set is used to determine the $\Delta RSL_{DurViscous}(\varphi)$ terms, accounting for the age and location of each SLIP (see Supplementary Fig. 4).

Monte Carlo linear regression. To quantify the elastic-induced local MWP-1A magnitude at each site ($\Delta RSL_{Elastic}(\varphi)$ in Eq. 4), we use a Monte Carlo (MC) linear regression technique to estimate the distribution of local sea-level rise rates recorded by selected SLIPs at that site. The MC simulation approach is used to capture the potentially asymmetric age and depth uncertainties of different types of sea-level indicators by randomly sampling each sea-level index point's depth and chronological distributions. These distributions are calculated following the methodology of Hibbert et al.[35,43].

For the coral sea-level indicators, we test two methods for representing their indicative depth distributions. First, we use an empirically-derived taxon-specific depth-habitat distribution for each coral-based sea-level indicator[43], which is obtained using the modern coral analogue from the Ocean Biogeographical Information System (www.iobis.org). Where possible, we use a spatially variable local coral depth-habitat distribution instead of a global compilation for each coral species. This method is denoted as the empirical scenario. Alternatively, we use the coral palaeo-water depth determinations (i.e., upper/lower limit of living range) from the original publications for different coral species. For this method, we assume a uniform distribution, in that the indicator may occur equally anywhere within the given range[43]. We denote this method as the uniform scenario. For non-coral SLIPs (including coral samples additionally constrained by vermetid gastropods in Tahiti), we use the indicative range or facies formation range as determined by the original authors, which is also assumed to be uniformly distributed. Furthermore, when sampling the depth distributions of all SLIPs, we considered the error distribution associated with each of the GIA corrections described above and elevation measurement uncertainties due to coring, levelling and tectonic correction if necessary. We exclude any data explicitly stated as not in situ by the original authors.

The chronological probability distributions depend on the method used to date each SLIP. For samples that are radiocarbon dated, we use OxCal version 4.4[81] to obtain the calibrated age probability distribution by recalibrating the conventional radiocarbon age and uncertainty using the latest calibration curves: IntCal20[82] for Northern Hemisphere terrestrial samples; SHCal20[83] for Southern Hemisphere terrestrial samples and Marine20[84] for all marine samples. For marine samples, we apply appropriate, updated (i.e., calculated using Marine20) local marine reservoir corrections (ΔR; http://calib.org/marine). For all other samples, U-series ages have been recalculated where necessary, assuming a closed system with the latest decay constants[85]. Only U-series ages passing the following age reliability screening criteria (calcite < 2%, $[^{232}Th] \leq 2$ ppb, $\delta^{234}U_{initial} = 147 \pm 5$ ‰) are considered. A normal distribution is adopted for U-series ages, whereas our radiocarbon ages use the full age probability distribution[43]. For any replicated ages, we use the inverse weighted mean value/distribution of each replicate group.

For each of our six sites, we use MC simulation to randomly sample the age and depth distributions of each selected SLIP, and for each MC sampling, we use a weighted least square method to compute an optimum straight line to fit the randomly sampled points. The slope of this line is the averaged RSL rate across MWP-1A (units m/ka), which is assumed to be temporally linear throughout MWP-1A. Note that, since the lack of temporal resolution and uneven temporal distribution of sea-level data prohibit our ability to capture the maximum rates of sea-level rise at each site, our results should be interpreted as the averaged rate of RSL change at each site across our MWP-1A time window (14.65–14.0 ka BP). Within each weighted least square calculation, the weighting factor w for each SLIP is calculated by

$$w = /\sqrt{\sigma_y^2 + (dy/dx)^2 \sigma_x^2} \quad (5)$$

where σ_y and σ_x are standard deviations estimated from the depth and age distributions, respectively, and dy/dx is the gradient of global sea-level change at the sampled age obtained from Lambeck et al.[2]. The last term is used to convert the effective contribution of age uncertainty into depth uncertainty. Regressions that

produce a reverse slope (i.e., a sea-level fall) are excluded as implausible. The process is repeated 20,000 times (excluding the implausible iterations) to produce a distribution of local MWP-1A sea-level rise rates for each site. Lastly, the local MWP-1A magnitude is obtained by scaling this linear rate to the MWP-1A duration. We use a 500-year MWP-1A duration in this study since it leads to more comparable results with the MWP-1A magnitude from regional ice-sheet reconstructions, but our inversion results can be linearly scaled to any assumed MWP-1A duration for comparison.

Data extrapolation. For HYD and NOG, the SLIPs only show a rapid ~10 m sea-level rise between 14.6 and 14.4 ka BP with no clear post-MWP-1A SLIP until the initiation of new coral reefs at ~13.0 ka BP, showing another 20–25 m sea-level rise. This sequence is identified as "rapid growth then drowning and further landward migration" (Webster et al. p. 420[36]; see their Fig. 4a). In order to constrain RSL at the end of MWP–1A, we adopt a data extrapolation approach that uses the large number of SLIPs between ~13.0 and 12.0 ka BP at the two sites to extrapolate RSL backwards in time. To ensure the accuracy of the data extrapolation we only use SLIPs that pertain to a shallow, high-energy/exposed reef edge environment (the cA coral-algal assemblage[36]), i.e. SLIPs which have a relatively small depth uncertainty. The data extrapolation was implemented using the same MC linear regression method as above, in combination with the uniform scenario (Supplementary Fig. 5) as the empirical depth distribution for some SLIPs contains a bimodal habitat depth, resulting in over-large extrapolation uncertainty. The depth uncertainty of the extrapolated data point is defined by the extrapolation process, and it was assigned an age uncertainty of 0.1 ka assuming a normal distribution.

Inversion for MWP-1A sources. Based on the site-specific elastic-induced local MWP-1A magnitude distributions ($\Delta RSL_{Elastic}(\varphi)$) estimated above, the inversion for MWP-1A sources can be made by identifying the optimum ESL parameters in Eq. 4 for each of the 20,000 MC iterations. This is achieved using a weighted non-negative least square method using the Lawson−Hanson algorithm[53] since we assume that ice sheet growth during MWP-1A would be implausible. The weighting factor for each site is given by $w(\varphi) = 1/\sigma(\varphi)2$ where $\sigma(\varphi)$ is the standard deviation estimated from the local MWP-1A magnitude distributions.

Jackknife resampling. After each iteration of our method (i.e., each time we invert for the sources of MWP-1A, see Supplementary Fig. 1), we adopt a jackknife resampling technique to correct for any bias associated with data over-dependency. Specifically, we invert for the sources of MWP-1A six times, each time removing one site from the six-site database. The difference between the mean jackknife inversion result and the original inversion result is defined as the bias contained in the original inversion result. Subtracting this bias from the original result yields a bias-corrected inversion of MWP-1A sources.

RSL prediction. We modified the deglaciation history during MWP-1A in the ANU ice model[2] and used this revised model to predict RSL variation at the six sea-level sites used in this study. This revised model (denoted as the ANU_MWP model) was created by leaving the ice history prior to MWP-1A unchanged, but assuming that ice loss during MWP-1A followed the magnitude and spatial pattern of ice loss represented by the mean of our inversion result: 13.1 m NAIS, 3.3 m SIS, and 1.5 m AIS. The rate of ice melt during MWP-1A was assumed to be linear. In the original ANU model, there is not enough ice for the SIS to melt 3.3 m during MWP-1A. We therefore decrease the rate of ice melt between 16.5 and 14.5 ka BP (the latter is the time of MWP-1A initiation in the ANU model) to ensure there is enough ice to provide 3.3 m ESL melt during MWP-1A (Fig. 4h). The synthetic test of a larger AIS contribution to MWP-1A adopted the same pre-MWP-1A ice geometries as in the ANU_MWP model but used different MWP-1A sources: 9.6 m NAIS, 3.3 m SIS and 5 m AIS. The modified ice models were combined with the 120 ANU-specific Earth models to produce RSL curves from the last interglacial to present.

Data availability

All sea-level data used for this study are publicly available and can be accessed from cited original publications. The datasets generated for this publication are available in the Zenodo database (https://zenodo.org/record/4459366#.YCbVyRP7TzU) with the identifier https://doi.org/10.5281/zenodo.4459366[86].

Code availability

The code for generating the depth uncertainty distribution for each type of sea-level indicator can be accessed via https://figshare.com/articles/Matlab_Code_-_calculation_of_sea_level/5890579. The codes used to invert MWP-1A magnitude and sources are available at https://github.com/yc-lin-geo/lin_MWP1A_sources.

Received: 2 October 2020; Accepted: 17 February 2021;
Published online: 01 April 2021

References

1. Deschamps, P. et al. Ice-sheet collapse and sea-level rise at the Bølling warming 14,600 years ago. *Nature* **483**, 559–564 (2012).
2. Lambeck, K., Rouby, H., Purcell, A., Sun, Y. & Sambridge, M. Sea level and global ice volumes from the Last Glacial Maximum to the Holocene. *Proc. Natl Acad. Sci. USA* **111**, 15296–15303 (2014).
3. Buizert, C. et al. Greenland temperature response to climate forcing during the last deglaciation. *Science* **345**, 1177–1180 (2014).
4. Fogwill, C. et al. Antarctic ice sheet discharge driven by atmosphere-ocean feedbacks at the Last Glacial Termination. *Sci. Rep.* **7**, 1–10 (2017).
5. Menviel, L., Timmermann, A., Timm, O. E. & Mouchet, A. Deconstructing the Last Glacial termination: the role of millennial and orbital-scale forcings. *Quat. Sci. Rev.* **30**, 1155–1172 (2011).
6. Ivanovic, R., Gregoire, L., Wickert, A. D. & Burke, A. Climatic effect of Antarctic meltwater overwhelmed by concurrent Northern hemispheric melt. *Geophys. Res. Lett.* **45**, 5681–5689 (2018).
7. Liu, Z. et al. Transient simulation of last deglaciation with a new mechanism for Bølling-Allerød warming. *science* **325**, 310–314 (2009).
8. Ivanovic, R. F., Gregoire, L. J., Wickert, A. D., Valdes, P. J. & Burke, A. Collapse of the North American ice saddle 14,500 years ago caused widespread cooling and reduced ocean overturning circulation. *Geophys. Res. Lett.* **44**, 383–392 (2017).
9. Obase, T. & Abe-Ouchi, A. Abrupt Bølling-Allerød warming simulated under gradual forcing of the last deglaciation. *Geophys. Res. Lett.* **46**, 11397–11405 (2019).
10. Tarasov, L., Dyke, A. S., Neal, R. M. & Peltier, W. R. A data-calibrated distribution of deglacial chronologies for the North American ice complex from glaciological modeling. *Earth Planet. Sci. Lett.* **315**, 30–40 (2012).
11. Gregoire, L. J., Payne, A. J. & Valdes, P. J. Deglacial rapid sea level rises caused by ice-sheet saddle collapses. *Nature* **487**, 219–222 (2012).
12. Golledge, N. et al. Antarctic contribution to meltwater pulse 1A from reduced Southern Ocean overturning. *Nat. Commun.* **5**, 5107 (2014).
13. Bassett, S. E., Milne, G. A., Mitrovica, J. X. & Clark, P. U. Ice sheet and solid earth influences on far-field sea-level histories. *Science* **309**, 925–928 (2005).
14. Liu, J. *Constraining the Source Distribution of Meltwater Pulse 1A Using Near- and Far-Field Sea-level Data*. MA thesis, University of Ottawa (2013).
15. Liu, J., Milne, G. A., Kopp, R. E., Clark, P. U. & Shennan, I. Sea-level constraints on the amplitude and source distribution of Meltwater Pulse 1A. *Nat. Geosci.* **9**, 130–134 (2016).
16. Mitrovica, J. X., Tamisiea, M. E., Davis, J. L. & Milne, G. A. Recent mass balance of polar ice sheets inferred from patterns of global sea-level change. *Nature* **409**, 1026–1029 (2001).
17. Clark, P. U., Mitrovica, J., Milne, G. & Tamisiea, M. Sea-level fingerprinting as a direct test for the source of global meltwater pulse IA. *Science* **295**, 2438–2441 (2002).
18. Gomez, N., Gregoire, L., Mitrovica, J. & Payne, A. Laurentide-Cordilleran Ice Sheet saddle collapse as a contribution to meltwater pulse 1A. *Geophys. Res. Lett.* **42**, 3954–3962 (2015).
19. Weaver, A. J., Saenko, O. A., Clark, P. U. & Mitrovica, J. X. Meltwater pulse 1A from Antarctica as a trigger of the Bølling-Allerød warm interval. *Science* **299**, 1709–1713 (2003).
20. Yeung, N., Menviel, L., Meissner, K. & Sikes, E. Assessing the spatial origin of meltwater pulse 1A using oxygen-isotope fingerprinting. *Paleoceanogr. Paleoclimatol.* **34**, 2031–2046 (2019).
21. Wickert, A. D., Mitrovica, J. X., Williams, C. & Anderson, R. S. Gradual demise of a thin southern Laurentide ice sheet recorded by Mississippi drainage. *Nature* **502**, 668–671 (2013).
22. Peltier, W., Argus, D. & Drummond, R. Space geodesy constrains ice age terminal deglaciation: the global ICE6G_C (VM5a) model. *J. Geophys. Res.: Solid Earth* **120**, 450–487 (2015).
23. Brendryen, J., Haflidason, H., Yokoyama, Y., Haaga, K. A. & Hannisdal, B. Eurasian Ice Sheet collapse was a major source of Meltwater Pulse 1A 14,600 years ago. *Nat. Geosci.* **13**, 363–368 (2020).
24. Lambeck, K., Purcell, A. & Zhao, S. The North American Late Wisconsin ice sheet and mantle viscosity from glacial rebound analyses. *Quat. Sci. Rev.* **158**, 172–210 (2017).
25. Gomez, N., Weber, M. E., Clark, P. U., Mitrovica, J. X. & Han, H. K. Antarctic ice dynamics amplified by Northern Hemisphere sea-level forcing. *Nature* **587**, 600–604 (2020).
26. Albrecht, T., Winkelmann, R. & Levermann, A. Glacialcycle simulations of the Antarctic Ice Sheet with the Parallel Ice Sheet Model (PISM)–Part 2: Parameter ensemble analysis. Cryosphere 14,633–656 (2020).
27. Bard, E. et al. Deglacial sea-level record from Tahiti corals and the timing of global meltwater discharge. *Nature* **382**, 241–244 (1996).
28. Fairbanks, R. G. A 17,000-year glacio-eustatic sea level record: influence of glacial melting rates on the Younger Dryas event and deep-ocean circulation. *Nature* **342**, 637–642 (1989).

29. Fairbanks, R. G. et al. Radiocarbon calibration curve spanning 0 to 50,000 years BP based on paired 230Th/234U/238U and 14C dates on pristine corals. *Quat. Sci. Rev.* **24**, 1781–1796 (2005).
30. Abdul, N., Mortlock, R., Wright, J. & Fairbanks, R. Younger Dryas sea level and meltwater pulse 1B recorded in Barbados reef crest coral Acropora palmata. *Paleoceanography* **31**, 330–344 (2016).
31. Hanebuth, T., Stattegger, K. & Grootes, P. M. Rapid flooding of the Sunda Shelf: a late-glacial sea-level record. *Science* **288**, 1033–1035 (2000).
32. Woodroffe, C. D. & Webster, J. M. Coral reefs and sea-level change. *Mar. Geol.* **352**, 248–267 (2014).
33. Chappell, J. Coral morphology, diversity and reef growth. *Nature* **286**, 249–252 (1980).
34. Bard, E., Hamelin, B., Deschamps, P. & Camoin, G. Comment on "Younger Dryas sea level and meltwater pulse 1B recorded in Barbados reefal crest coral Acropora palmata" by NA Abdul et al. *Paleoceanography* **31**, 1603–1608 (2016).
35. Hibbert, F. D. et al. Coral indicators of past sea-level change: a global repository of U-series dated benchmarks. *Quat. Sci. Rev.* **145**, 1–56 (2016).
36. Webster, J. M. et al. Response of the Great Barrier Reef to sea-level and environmental changes over the past 30,000 years. *Nat. Geosci.* **11**, 426 (2018).
37. Yokoyama, Y. et al. Rapid glaciation and a two-step sea level plunge into the Last Glacial Maximum. *Nature* **559**, 603–607 (2018).
38. Shennan, I., Rutherford, M. M., Innes, J. B. & Walker, K. J. Late glacial sea level and ocean margin environmental changes interpreted from biostratigraphic and lithostratigraphic studies of isolation basins in northwest Scotland. *Geol. Soc., Lond., Spec. Publ.* **111**, 229–244 (1996).
39. Shennan, I., Innes, J. B., Long, A. J. & Zong, Y. Late Devensian and Holocene relative sea-level changes at Loch nan Eala, near Arisaig, northwest Scotland. *J. Quat. Sci.* **9**, 261–283 (1994).
40. Shennan, I. et al. Late Devensian and Holocene records of relative sea-level changes in northwest Scotland and their implications for glacio-hydro-isostatic modelling. *Quat. Sci. Rev.* **19**, 1103–1135 (2000).
41. Bradley, S. L., Milne, G. A., Shennan, I. & Edwards, R. An improved glacial isostatic adjustment model for the British Isles. *J. Quat. Sci.* **26**, 541–552 (2011).
42. Austermann, J., Mitrovica, J. X., Latychev, K. & Milne, G. A. Barbados-based estimate of ice volume at Last Glacial Maximum affected by subducted plate. *Nat. Geosci.* **6**, 553–557 (2013).
43. Hibbert, F., Williams, F., Fallon, S. & Rohling, E. A database of biological and geomorphological sea-level markers from the Last Glacial Maximum to present. *Sci. data* **5**, 180088 (2018).
44. Mitrovica, J. & Milne, G. On the origin of late Holocene sea-level highstands within equatorial ocean basins. *Quat. Sci. Rev.* **21**, 2179–2190 (2002).
45. Cabioch, G., Montaggioni, L., Faure, G. & RibaudLaurenti, A. Reef coralgal assemblages as recorders of paleobathymetry and sea level changes in the Indo-Pacific province. *Quat. Sci. Rev.* **18**, 1681–1695 (1999).
46. Camoin, G. F. et al. Reef response to sea-level and environmental changes during the last deglaciation: Integrated Ocean Drilling Program Expedition 310, Tahiti Sea Level. *Geology* **40**, 643–646 (2012).
47. Camoin, G. F., Iryu, Y. & McInroy, D. B. IODP Expedition 310 reconstructs sea level, climatic, and environmental changes in the South Pacific during the last deglaciation. Scientific. *Drilling* **5**, 4–12 (2007).
48. Fischler, M. A. & Bolles, R. C. Random sample consensus: a paradigm for model fitting with applications to image analysis and automated cartography. *Commun. ACM* **24**, 381–395 (1981).
49. Lambeck, K. & Purcell, A. P. Sea-level change in the Irish Sea since the Last Glacial Maximum: constraints from isostatic modelling. *J. Quat. Sci.: Published Quat. Res. Assoc.* **16**, 497–506 (2001).
50. Patton, H., Hubbard, A., Andreassen, K., Winsborrow, M. & Stroeven, A. P. The build-up, configuration, and dynamical sensitivity of the Eurasian ice-sheet complex to Late Weichselian climatic and oceanic forcing. *Quat. Sci. Rev.* **153**, 97–121 (2016).
51. Patton, H. et al. Deglaciation of the Eurasian ice sheet complex. *Quat. Sci. Rev.* **169**, 148–172 (2017).
52. Clark, C. D. et al. BRITICE Glacial Map, version 2: a map and GIS database of glacial landforms of the last British–Irish Ice Sheet. *Boreas* **47**, 11–27 (2018).
53. Lawson, C. L. & Hanson, R. J. *Solving Least Squares Problems* (SIAM, 1995).
54. Whitehouse, P. L., Bentley, M. J. & Le Brocq, A. M. A deglacial model for Antarctica: geological constraints and glaciological modelling as a basis for a new model of Antarctic glacial isostatic adjustment. *Quat. Sci. Rev.* **32**, 1–24 (2012).
55. Hughes, A. L., Gyllencreutz, R., Lohne, Ø. S., Mangerud, J. & Svendsen, J. I. The last Eurasian ice sheets–a chronological database and time-slice reconstruction, DATED-1. *Boreas* **45**, 1–45 (2016).
56. Shennan, I., Bradley, S. L. & Edwards, R. Relative sea-level changes and crustal movements in Britain and Ireland since the Last Glacial Maximum. *Quat. Sci. Rev.* **188**, 143–159 (2018).
57. McManus, J. F., Francois, R., Gherardi, J.-M., Keigwin, L. D. & Brown-Leger, S. Collapse and rapid resumption of Atlantic meridional circulation linked to deglacial climate changes. *Nature* **428**, 834–837 (2004).
58. Swingedouw, D., Fichefet, T., Goosse, H. & Loutre, M.-F. Impact of transient freshwater releases in the Southern Ocean on the AMOC and climate. *Clim. Dyn.* **33**, 365–381 (2009).
59. Gregoire, L. J., Otto-Bliesner, B., Valdes, P. J. & Ivanovic, R. Abrupt Bølling warming and ice saddle collapse contributions to the Meltwater Pulse 1a rapid sea level rise. *Geophys. Res. Lett.* **43**, 9130–9137 (2016).
60. Mercer, J. H. West Antarctic ice sheet and CO2 greenhouse effect: a threat of disaster. *Nature* **271**, 321–325 (1978).
61. Pollard, D., DeConto, R. M. & Alley, R. B. Potential Antarctic Ice Sheet retreat driven by hydrofracturing and ice cliff failure. *Earth Planet. Sci. Lett.* **412**, 112–121 (2015).
62. Pico, T., Mitrovica, J. & Mix, A. Sea level fingerprinting of the Bering Strait flooding history detects the source of the Younger Dryas climate event. *Sci. Adv.* **6**, eaay2935 (2020).
63. Gowan, E. J., Tregoning, P., Purcell, A., Montillet, J.-P. & McClusky, S. A model of the western Laurentide Ice Sheet, using observations of glacial isostatic adjustment. *Quat. Sci. Rev.* **139**, 1–16 (2016).
64. Parrenin, F. et al. The EDC3 chronology for the EPICA Dome C ice core. *Climate* **3**, 485–497 (2007).
65. Gomez, N., Latychev, K. & Pollard, D. A coupled ice sheet–sea level model incorporating 3D earth structure: Variations in Antarctica during the last deglacial retreat. *J. Clim.* **31**, 4041–4054 (2018).
66. Whitehouse, P. L., Gomez, N., King, M. A. & Wiens, D. A. Solid Earth change and the evolution of the Antarctic Ice Sheet. *Nat. Commun.* **10**, 1–14 (2019).
67. Anderson, J. B. et al. Ross Sea paleo-ice sheet drainage and deglacial history during and since the LGM. *Quat. Sci. Rev.* **100**, 31–54 (2014).
68. Ivanovic, R. et al. Transient climate simulations of the deglaciation 21-9 thousand years before present (version 1)-PMIP4 Core experiment design and boundary conditions. Geoscientific Model. *Development* **9**, 2563–2587 (2016).
69. Mitrovica, J. et al. On the robustness of predictions of sea level fingerprints. *Geophys. J. Int.* **187**, 729–742 (2011).
70. Lambeck, K., Purcell, A., Johnston, P., Nakada, M. & Yokoyama, Y. Water-load definition in the glacio-hydroisostatic sea-level equation. *Quat. Sci. Rev.* **22**, 309–318 (2003).
71. Purcell, A., Tregoning, P. & Dehecq, A. An assessment of the ICE6G_C (VM5a) glacial isostatic adjustment model. *J. Geophys. Res.: Solid Earth* **121**, 3939–3950 (2016).
72. Milne, G. A. & Mitrovica, J. X. Postglacial sea-level change on a rotating Earth: first results from a gravitationally self-consistent sea-level equation. *Geophys. J. Int.* **126**, F13–F20 (1996).
73. Kendall, R. A., Mitrovica, J. X. & Milne, G. A. On postglacial sea level–II. Numerical formulation and comparative results on spherically symmetric models. *Geophys. J. Int.* **161**, 679–706 (2005).
74. Mitrovica, J. X., Wahr, J., Matsuyama, I. & Paulson, A. The rotational stability of an ice-age earth. *Geophys. J. Int.* **161**, 491–506 (2005).
75. Mitrovica, J. X. & Wahr, J. Ice age Earth rotation. *Annu. Rev. Earth Planet. Sci.* **39**, 577–616 (2011).
76. Dziewonski, A. M. & Anderson, D. L. Preliminary reference Earth model. *Phys. Earth Planet. Inter.* **25**, 297–356 (1981).
77. Gowan, E. et al. ICESHEET 1.0: a program to produce paleo-ice sheet reconstructions with minimal assumptions. *Geoscientific Model Dev.* **9**, 1673–1682 (2016).
78. Mackintosh, A. N. et al. Retreat history of the East Competing interests Antarctic Ice Sheet since the last glacial maximum. *Quat. Sci. Rev.* **100**, 10–30 (2014).
79. Lambeck, K. Glacial rebound of the British Isles—II. A high-resolution, high-precision model. *Geophys. J. Int.* **115**, 960–990 (1993).
80. Bradley, S., Milne, G., Teferle, F. N., Bingley, R. & Orliac, E. Glacial isostatic adjustment of the British Isles: new constraints from GPS measurements of crustal motion. *Geophys. J. Int.* **178**, 14–22 (2009).
81. Ramsey, C. B. Bayesian analysis of radiocarbon dates. *Radiocarbon* **51**, 337–360 (2009).
82. Reimer, P. J. et al. The IntCal20 Northern Hemisphere radiocarbon age calibration curve (0–55 cal kBP). *Radiocarbon* **62**, 725–757 (2020).
83. Hogg, A. G. et al. SHCal20 Southern Hemisphere calibration, 0–55,000 years cal BP. *Radiocarbon* **62**, 759–778 (2020).
84. Heaton, T. J. et al. Marine20—the marine radiocarbon age calibration curve (0–55,000 cal BP). *Radiocarbon* **62**, 779–820 (2020).
85. Cheng, H. et al. Improvements in 230Th dating, 230Th and 234U half-life values, and U–Th isotopic measurements by multi-collector inductively coupled plasma mass spectrometry. *Earth Planet. Sci. Lett.* **371**, 82–91 (2013).
86. Lin, Y. et al. A reconciled solution of Meltwater Pulse 1A sources using sea-level fingerprinting. *Zenodo.* https://doi.org/10.5281/zenodo.4459366 (2021).

Acknowledgements

The authors thank Chris D. Clark, Jeremy C. Ely and Henry Patton for providing their ice models, and W.R Peltier and Lev Tarasov for making their ice models publicly available. Y.L. was supported by China Scholarship Council—Durham University joint scholarship. F.D.H. received funding from the European Union's Horizon 2020 research and innovation programme under the Marie Skłodowska-Curie grant agreement (No. 838841—ExTaSea). S.L.B. was supported by the Natural Environment Research Council consortium grant BRITICE-CHRONO NE/J009768/1 and has benefited from the PalGlac team of researchers and received funding from the European Research Council (ERC) to Chris Clark under the European Union's Horizon 2020 research and innovation programme (Grant agreement No. 787263). The collection of the Scottish isolation basin data was supported by NERC Grants GST/02/0760 and GST/02/0761. The authors acknowledge PALSEA, a working group of the International Union for Quaternary Sciences (INQUA) and Past Global Changes (PAGES), which in turn received support from the Swiss Academy of Sciences and the Chinese Academy of Sciences. GIA calculations in this study were performed on the Terrawulf cluster, a computational facility supported through the AuScope Australian Geophysical Observing System (AGOS) and the Australian National Collaborative Research Infrastructure Strategy (NCRIS).

Author contributions

Y.L. led the research; Y.L, F.D.H., P.L.W. and S.A.W conceived the scope and design of the research. Y.L., P.L.W., S.A.W and F.D.H. led the writing of the manuscript. P.L.W., A.P. and S.L.B. advised Y.L. in performing GIA modelling. F.D.H., S.A.W and I.S. advised Y.L. in sea-level and field data analysis. All authors contributed ideas and to the writing of the manuscript.

Competing interests

The authors declare no competing interests.

Additional information

Supplementary information The online version contains supplementary material available at https://doi.org/10.1038/s41467-021-21990-y.

Correspondence and requests for materials should be addressed to Y.L.

Peer review information *Nature Communications* thanks the anonymous reviewers for their contribution to the peer review of this work. Peer Review Reports are available.

Reprints and permission information is available at http://www.nature.com/reprints

Publisher's note Springer Nature remains neutral with regard to jurisdictional claims in published maps and institutional affiliations.

Appendix B: Relative sea level response to mixed carbonate-siliciclastic sediment loading along the Great Barrier Reef margin

Earth and Planetary Science Letters 607 (2023) 118066

Contents lists available at ScienceDirect

Earth and Planetary Science Letters

journal homepage: www.elsevier.com/locate/epsl

Relative sea level response to mixed carbonate-siliciclastic sediment loading along the Great Barrier Reef margin

Yucheng Lin [a,*], Pippa L. Whitehouse [a], Fiona D. Hibbert [b], Sarah A. Woodroffe [a], Gustavo Hinestrosa [c], Jody M. Webster [c]

[a] Department of Geography, Durham University, Durham, DH1 3LE, UK
[b] Department of Environment and Geography, University of York, York, YO10 5NG, UK
[c] Geocoastal Research Group, School of Geosciences, The University of Sydney, NSW 2006, Australia

ARTICLE INFO

Article history:
Received 1 July 2022
Received in revised form 10 February 2023
Accepted 15 February 2023
Available online 1 March 2023
Editor: Y. Asmerom

Keywords:
the Great Barrier Reef
sediment isostatic adjustment
glacial isostatic adjustment
sea-level change
sediment evolution
statistical inversion

ABSTRACT

The continental shelf along northeastern Australia is the world's largest mixed carbonate-siliciclastic passive margin and the location of the Great Barrier Reef (GBR). Following sea-level transgression during the last deglaciation, extensive sediment was deposited along the GBR due to neritic carbonate deposition (including shelf edge reefs, Holocene reefs and *Halimeda* bioherms) and fluvial discharge of terrigenous siliciclastic sediments. Such sediment loading can alter local relative sea level (RSL) by several metres through the sediment isostatic adjustment (SIA) process, a signal that is poorly constrained at the GBR. In this study, we used a glacial isostatic adjustment (GIA) model to develop an ensemble-based sediment loading history for the GBR since Marine Isotope Stage 2 (MIS 2). A Bayesian style framework is adopted to calibrate the sediment history ensemble and GIA model parameters using a sea-level database. According to our results, 1853.7 Gt (1613.1-2078.7 Gt, 95% confidence interval) of sediment have been deposited across the GBR since MIS 2 (28 ka BP), causing spatially variable relative sea-level change with the highest magnitude (0.9-1.1 m) found in the outer shelf of the southern central GBR (18.4-21.6° S). Because the SIA-induced RSL rise is unrelated to ice mass loss, failing to correct for this signal will lead to systematic overestimation of grounded ice volume by up to $\sim 4.3 \times 10^5$ km^3 during the Last Glacial Maximum. Additionally, we found that spatial variation in sediment loading and coastal environment may explain the different RSL history documented by published fossil coral reef records from Noggin Pass and Hydrographer's Passage. These results highlight the importance of considering SIA for any postglacial sea-level studies adjacent to large sediment systems. Lastly, by quantifying both the GIA and SIA signals, we provide a spatially and temporally complete RSL reconstruction that is well-suited to be used as a boundary condition to study the evolution of the GBR shelf and slope sedimentary system.

1. Introduction

Located on the world's largest mixed carbonate-siliciclastic passive margin in northeastern Australia, the Great Barrier Reef (GBR) is an ideal place to study coral reef framework development and terrigenous sediment transportation in response to sea-level variation during glacial cycles (Webster et al., 2018). To accurately understand and model the physical and ecological mechanisms behind the spatio-temporal evolution of this complex sediment system, a key boundary condition is the relative sea-level (RSL) change history, which is by far the most important driver on millennial timescales (Hopley et al., 2007; Woodroffe and Webster, 2014). Previous work suggests strong spatial variability in past RSL along this >2000 km coastline (Lambeck et al., 2002), prompting the need for a comprehensive understanding of the processes controlling sea-level change in this region. Currently, the most commonly-used physical model to explain this variability is a glacial isostatic adjustment (GIA) model, which describes the solid Earth and ocean surface response to changes in surface loading due to ice-ocean mass redistribution. Based on GIA theory, RSL recorded at the far-field location (i.e., far from previous ice sheet margins) of the GBR is primarily a function of solid Earth rheology, the change in global ice volume through time and local shelf morphology (Lambeck et al., 2014), with these factors

* Corresponding author.
E-mail address: yucheng.lin@durham.ac.uk (Y. Lin).

https://doi.org/10.1016/j.epsl.2023.118066

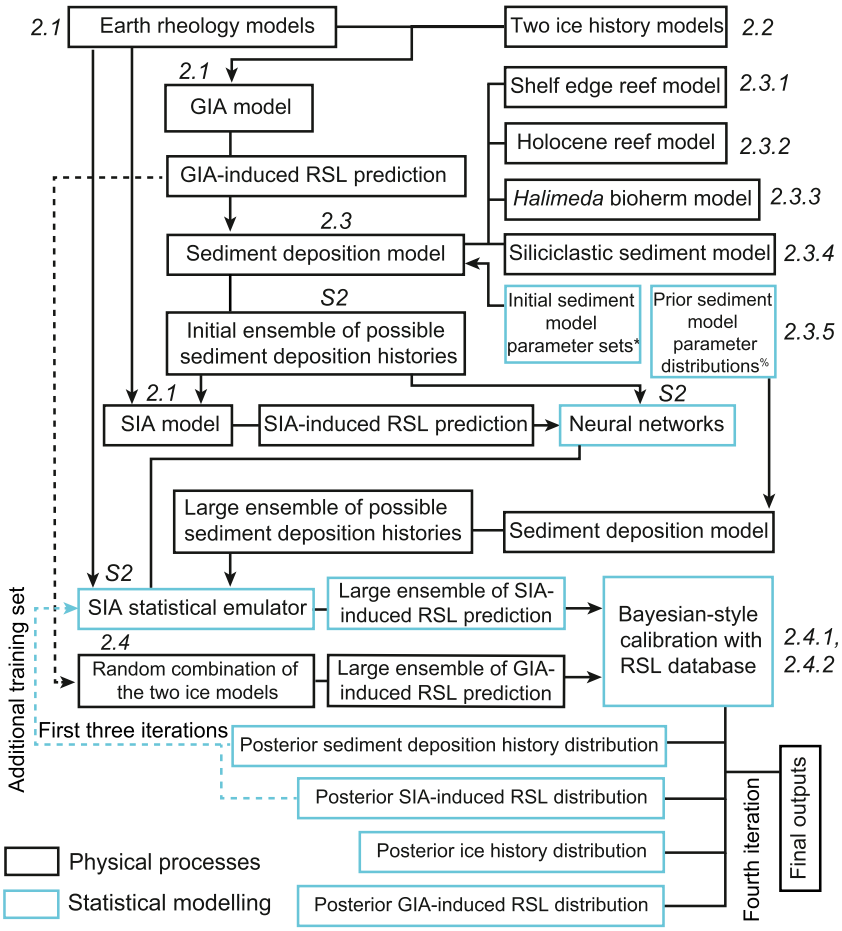

Fig. 1. Schematic overview of the inversion procedure adopted in this study. The black and blue boxes represent the physical processes and statistical modelling processes and results, respectively. Each arrow indicates that a previous model output acts as the input for the next model. *Initial sediment model parameter sets denote six sediment parameter combinations used to generate sediment models to train a SIA statistical emulator (details in Supplementary section 2). %Prior sediment model parameter distributions are given in Table 1, which can be used to create a large ensemble of random sediment models. Note the sediment deposition model appears in multiple places. The annotated italic number beside each box indicates the section that provides detailed descriptions of each modelling procedure, S2 indicates Supplementary section 2.

having previously been invoked to explain different magnitudes of postglacial RSL rise (Yokoyama et al., 2006) and mid-Holocene highstand (Lambeck et al., 2002) along the GBR coastline.

However, recent coral reef records from Noggin Pass (NOG) and Hydrographer's Passage (HYD), two shelf edge sites with similar shelf morphology located 500 km apart from each other, show a consistent RSL offset (reconstructed RSL at NOG is several metres higher at HYD) during the last deglaciation (Yokoyama et al., 2018; Webster et al., 2018) which cannot be explained by a GIA model. To understand this discrepancy, an additional physical process that is able to generate metre scale regional RSL variation within a 10^3-10^5 year timescale is required. For coral reef records from a passive margin, minimally impacted by sediment compaction, the most obvious possibility is RSL change caused by sediment loading (Horton et al., 2018). Similar to ice loading, sediment loading can lead to isostatic adjustment that changes the local geoid and deforms the land surface depending on the regional load magnitude and Earth rheology (i.e., sediment isostatic adjustment, SIA; Dalca et al., 2013). Previous studies suggest there have been more than 1000 gigaton (Gt) of neritic carbonate sediment (Hinestrosa et al., 2022; Rees, 2005) accumulated across the GBR since the Last Glacial Maximum (LGM) along with a considerable amount of fluvial discharge of terrigenous siliciclastic sediment (Salles et al., 2018). Such sediment loading could be large enough to drive localised RSL variations.

In this study, we aim to simultaneously quantify the ice, ocean and sediment loading impact on RSL variation across the GBR from Marine Isotope Stage (MIS) 2 to present. To quantify the SIA signal, we develop a GIA-model-enabled ensemble-based sediment accretion model, which allows us to reconstruct the spatio-temporal evolution of sediment deposition across the GBR. We then use a Bayesian formalism to calibrate the net RSL history predicted by the GIA and SIA models using a sea-level database. The outputs of our study are a set of high-quality predictions of RSL change and sediment deposition history, with quantified uncertainty (Fig. 1).

2. Methodology

The methodology for reconstructing RSL change across the GBR is comprised of three major components: GIA/SIA modelling, sediment deposition history reconstruction and statistical calibration of the first two components using a GBR sea-level database (Fig. 1).

2.1. Glacial/sediment isostatic adjustment modelling

In this study, we describe RSL variation as a combined signal caused by GIA and SIA (Wolstencroft et al., 2014). We compute GIA-induced RSL change using a gravitationally self-consistent theory that accounts for migrating shorelines and Earth rotational feedback (Kendall et al., 2005; Mitrovica et al., 2005). For SIA,

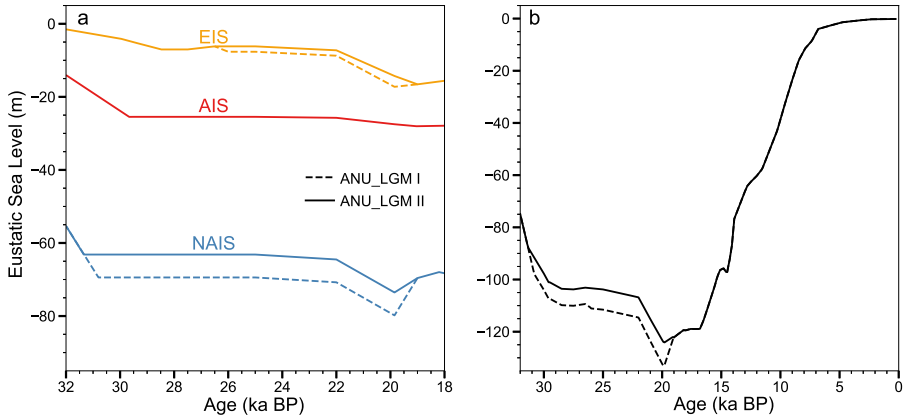

Fig. 2. Ice history modifications. (a) Pre-LGM ice history modifications for three ice sheets. (b) Modified global ice histories. The dashed and solid lines indicate the scenarios I and II we tested in this study. Note we use the same Antarctic model for both ice loading scenarios. NAIS = North American Ice Sheet; AIS = Antarctic Ice Sheet; EIS = Eurasian Ice Sheet.

we use the methodology of Wolstencroft et al. (2014) which considers the RSL change caused by sediment-driven Earth deformation without considering the sediment impact on geoid variation, shoreline migration and Earth rotation as they are minor signals (generally accounting for less than 5% of the total SIA caused RSL signal; Ferrier et al., 2018). Although a self-consistent GIA and SIA model has recently been developed (Ferrier et al., 2017), we do not adopt this model here because we wish to rigorously sample the GBR deposition sediment history uncertainty range independently, and solving for the gravitationally self-consistent response to both ice and sediment loading would significantly increase the required computational power.

The Earth model used in this study is represented by a spherically symmetric Maxwell body consisting of an elastic lithosphere, and an upper and lower mantle extending to 670 km and from 670 km to the core-mantle boundary, respectively. The elastic and density structure of the Earth model is derived from the preliminary reference Earth model (Dziewonski and Anderson, 1981). To sample the uncertainty range associated with the rheological properties of the Earth we test lithospheric thickness values of 46, 71 and 96 km and upper and lower mantle viscosity values ranging between 0.05-1 and 1-90 $\times$ 10^{21} Pa s, respectively. The relatively thin lithosphere and weak upper mantle viscosity values that we explore reflect the values constrained by previous GIA studies of the GBR region (Ishiwa et al., 2019; Lambeck et al., 2002) and are supported by a recent global 3D mantle viscosity reconstruction (Austermann et al., 2021). In total, we test 228 Earth model combinations. We use the same Earth model for calculating GIA and SIA in order to produce internally consistent RSL predictions. We perform all calculations using a spherical harmonic truncation of degree and order 512 ($\sim$40 km), which is suitable for calculating long-wavelength SIA and GIA signals in regions where lithospheric thickness is $\sim$50 km or greater, such as the GBR.

2.2. Ice model

We use a version of the ANU ice model (denoted as ANU_LGM; Lin, 2019) that has been updated to reflect the early rapid global mean sea-level (GMSL) fall to the LGM lowstand, as revealed by sea-level index points (SLIPs) from NOG and HYD (Yokoyama et al., 2018; Webster et al., 2018). We assume that the majority (90%) of this GMSL fall was caused by rapid growth of the North American and Eurasian Ice Sheets (Fig. 2), possibly due to the saddle merger mechanism (Ji et al., 2021). Because GMSL prior to the LGM is poorly-constrained, we test two possible ice loading scenarios, corresponding to a 134 m (scenario I; Lambeck et al., 2014) and a 125 m (scenario II; Yokoyama et al., 2018) GMSL lowstand, which can considered as two end-member scenarios of the LGM GMSL lowstand.

2.3. Sediment model

To reconstruct a complete sediment history for the GBR, we divide its sediment system into four domains: shelf edge reef, Holocene reef, *Halimeda* bioherms (the first three are carbonate sediment) and siliciclastic sediment (Fig. 3). We then use 456 GIA-induced RSL histories (produced by combining 2 ice models with 228 Earth models) to force simple linear accretion models and reconstruct the sediment history for each domain as an ensemble (Fig. 1). Sediment accretion is first reconstructed at high spatial resolution by combining the RSL predictions with a 100 m resolution modern GBR digital elevation model (DEM, Beaman, 2010) to create a series of palaeo-DEMs, and hence determine the detailed spatial evolution of inundation and sediment accretion. For the purposes of calculating the SIA response, net sediment load in each $\sim$40 km grid cell of our study region is then summed to produce a loading time series. We do not consider the influence of hydrodynamic effects on sediment distribution because short-wavelength variations in surface load will have a relatively minor effect on the SIA signal, which is long-wavelength and is spatially and temporally smooth.

2.3.1. Shelf edge reef

The shelf edge is defined as the region between the modern outer barrier reef front and the 130 m isobath (Fig. 3, Beaman, 2010; Abbey et al., 2011). Based on the evidence derived from drill cores at NOG and HYD, the shelf edge reef growth structure can be described by four reef formation-demise sequences: reef 2 (27-22 ka BP; initiation and demise time), reef 3a (22-17 ka BP), reef 3b (17-14 ka BP) and reef 4 (14-10 ka BP; modified from Webster et al., 2018).

To reconstruct the spatio-temporal reef development, we adopt a linear accretion model from Hinestrosa et al. (2022). For this model, the averaged vertical accretion rate (ν_{se}) and maximum accretion thickness (τ_{se}) are defined for each reef sequence based on the dating of drill core material from HYD and NOG (Supplementary Figure 1). We assume each reef sequence initiates after local inundation, with a time lag (ι_{se}) of between 0 and 1 ka, and that it accumulates uniformly following the rate of ν_{se} until reaching thickness τ_{se}. The 0-1 ka lag between local inundation and reef initiation is defined based on observational evidence from Sanborn et al. (2020). Each reef within the shelf edge polygon (i.e., each DEM

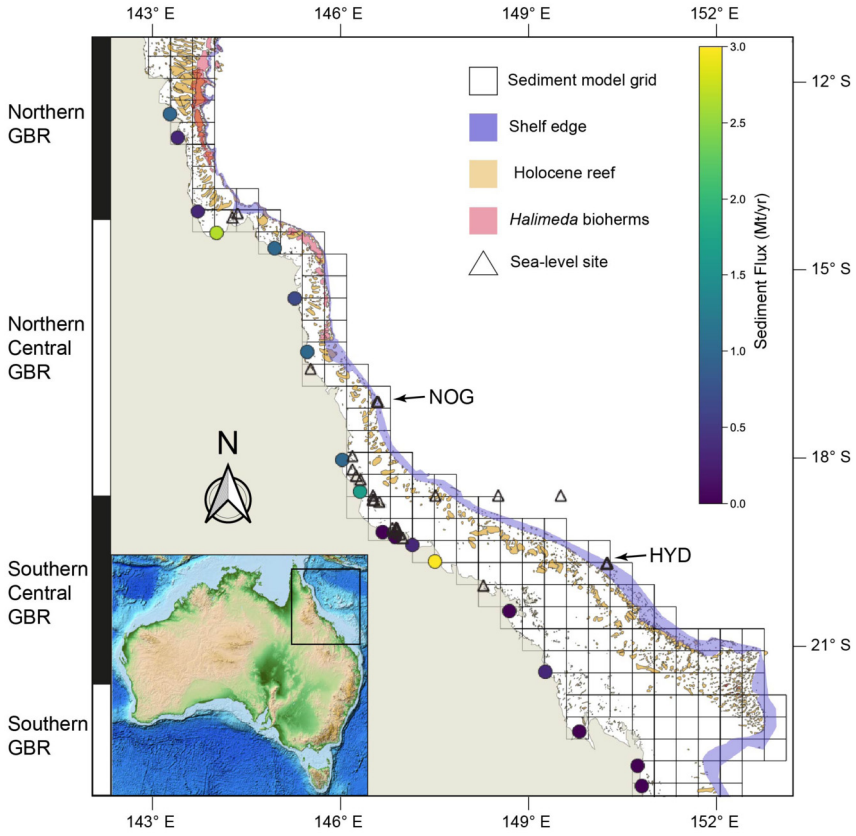

Fig. 3. Overview of four sediment domains. The orange polygons indicate the locations where Holocene reefs accumulate. The purple polygons outline the domains where shelf edge reefs are likely to have accumulated (shelf edge reefs have not yet been fully mapped along the GBR margin). In the northern GBR, pink polygons show the locations of *Halimeda* bioherms. Coloured dots along the modern coastline indicate the rate of present-day fluvial sediment discharge (Milliman and Farnsworth, 2013). The black triangles are the RSL site locations used to calibrate the sediment loading history. The zebra boxes on the left indicate the four latitudinal GBR regions defined in 2.3.5. The sediment loading grid is indicated by the black squares.

grid cell) is classified to one of the four reef sequences (Webster et al., 2018) based on its initiation time, which in turn determines its ν_{se} and τ_{se}. Because constraints on ν_{se} and τ_{se} are currently only available for HYD and NOG, we assume the information derived from them is representative of the southern and northern GBR, respectively.

2.3.2. Holocene reef

The spatial distribution of the Holocene reef has been mapped by modern bathymetric and remote sensing surveys (http://www.gbrmpa.gov.au/). The only variable to estimate is the spatially-variable Holocene reef accretion thickness, which will vary according to local environmental conditions (Hinestrosa et al., 2022; Hopley et al., 2007). To account for this heterogeneity, we use a kriging method (details in supplementary section 1) to interpolate the spatial pattern of reef accretion thickness based on a Holocene reef accretion thickness database (Hinestrosa et al., 2022, Supplementary Figure 2). One advantage of this method is that the uncertainty estimation is included in its conceptualisation, hence the interpolation uncertainty can be easily propagated.

Next, to accurately determine the time when the local pre-Holocene substrate was flooded, we create a pre-Holocene GBR DEM by subtracting the interpolated accretion thickness from the modern DEM. We carry out calculations based on this pre-Holocene DEM. We then combine our 456 GIA-induced RSL predictions with this pre-Holocene DEM to create a series of palaeo-DEMs that can be used to determine the timing of local inundation and hence the temporal development of the Holocene reefs. Using interpolated reef accretion thickness estimates as a boundary condition, each Holocene reef is assumed to begin accumulating following local sea-level transgression, with a time lag (ι_{ho}) of between 0 and 1 ka (same as shelf edge reef), and stop accumulating when local RSL is 30 m higher than the modern reef surface (i.e., when the coral reef surface becomes too deep for significant shallow water reef growth). Where the modern water depth is less than 30 m, we assume the reef stops accumulating when local RSL first reaches its maximum value (mid-Holocene highstand or present). Between the defined starting and terminating time, reefs are assumed to grow at a linear rate depending on the interpolated accretion thickness.

2.3.3. Halimeda bioherms

Halimeda bioherms are a dominant source of inter-reef carbonate deposits for the northern GBR and have been extensively mapped (Fig. 3, McNeil et al., 2016). McNeil et al. (2020) provide an overall estimate of 55.12 Gt of accumulation, corresponding to a 7.63 m sediment layer across all mapped regions of *Halimeda* bioherms (assumes aragonite density of 2.94 g/m^2 with 0.58 porosity (McNeil et al., 2020)). As for the Holocene reef sediment model, we build a pre-Holocene DEM for the *Halimeda* bioherms domain by subtracting 7.63 m from the original GBR DEM within the accumulation region (i.e., pink polygons in Fig. 3). The temporal evolution of the *Halimida* bioherms is then calculated using the same method as for the Holocene reef model, using a lag parameter ι_{ha}. Although previous studies suggest that other sources of carbonate sediment accumulate across inter-reef regions, such as benthic foraminifera and coralline algae (Hopley et al., 2007), at present there is no comprehensive database which documents the inter-reef carbonate thickness or mass accumulation since MIS 2. We

therefore do not consider this possible source of carbonate sediment in our reconstruction.

2.3.4. Siliciclastic sediment

To quantify siliciclastic load, we use a modern global database of fluvial sediment flux measurements (Fig. 3, Milliman and Farnsworth, 2013) and assume the averaged discharge rate for the whole of the deglacial period is proportional to the modern measurement, with absolute values controlled by a scaling parameter (β) that increases/decreases the modern sediment flux by up to 40%. For each model run, the sediment discharge rate is assumed to be temporally constant. The spatial distribution of siliciclastic sediment deposition will have varied through time due to shoreline migration during postglacial sea-level change. This palaeo shoreline migration is reconstructed by combining a modern DEM with GIA-induced RSL predictions. For each model time step, sediment load is discharged to the nearest palaeo shoreline location relative to the modern river mouth position (Fig. 3). To conserve mass, we uniformly remove a layer of sediment from the North East Coast drainage basin with a mass equivalent to the siliciclastic sediment deposition in the ocean.

2.3.5. Sediment model parameters

We use two types of parameter (pattern and magnitude) to represent uncertainties in the sediment history reconstructions. For all sediment domains, Earth and ice model parameters are the primary pattern parameters because they determine the spatio-temporal pattern of RSL variation, and in turn the sediment accumulation pattern. Additionally, the lag parameters mentioned above (ι_{se}, ι_{ho}, ι_{ha}) allow a delay to the initiation of carbonate sediment accumulation of between 0 and 1 ka after local transgression, which provides additional control on the temporal evolution of the three carbonate sediment domains.

The magnitude parameters control the magnitude of sediment accumulation for each domain. When determining the sediment accretion thickness of the shelf edge reef, we limit the maximum reef accretion thickness for the four reef sequences using the parameters $\tau_{2,3a,3b,4}$ (Table 1, values are empirically derived from Hinestrosa et al., 2022). For the Holocene reef, the accretion thickness is subject to spatially variable uncertainty produced by the kriging interpolation, which is described by $\alpha_{ho}(\varphi)$, and varies from -3σ to 3σ. Lastly, the magnitude of the siliciclastic sediment load is controlled by a scaling parameter β (section 2.3.4).

The reconstructed sediment accumulation thickness $H(\varphi, t)$ at location φ and time t is converted to a sediment load, $M(\varphi, t)$, by:

$$M_{se}(\varphi, t) = H_{se}(\varphi, t)A(\varphi)\rho_a(1 - \phi_{se})\epsilon_{se} \quad (1)$$

$$M_{ho}(\varphi, t) = H_{ho}(\varphi, t)A(\varphi)\rho_a(1 - \phi_{ho})\alpha_{ho}(\varphi) \quad (2)$$

$$M_{hb}(\varphi, t) = H_{hb}(\varphi, t)A(\varphi)\rho_a(1 - \phi_{hb}) \quad (3)$$

where fixed parameters $A(\varphi)$ and ρ_a indicate bathymetric grid cell area and the density of aragonite (2.94 g/cm^3). ϕ is the averaged sediment porosity for the shelf edge (se), Holocene (ho) and *Halimeda* bioherms (hb) domains; it is allowed to vary from 25% to 45% to represent uncertainty of the overall accumulation magnitude. For the shelf edge reef, one important uncertainty is that only a minor part of our defined shelf edge area (Fig. 3) is covered by reefal deposit, i.e., significantly thicker sediment than the surrounding area. Therefore, we assign a reefal area percentage parameter (ϵ_{se}), varying between 10-30% (derived from seismic mapping of shelf edge reef structure, Hinestrosa et al., 2016), to describe this uncertainty. Although the non-reefal area shows substantially lower sediment thickness (generally <10 m, Hinestrosa et al., 2016), it covers a much larger proportion of the shelf edge area, meaning it can potentially contribute as much sediment loading as the reefal area. Therefore, the upper limit of ϵ_{se} is doubled (to 60%) to account for this condition. To reduce computation time, we combine $1 - \phi_{se}$ and ϵ_{se} in the shelf edge reef model (as γ_{se}), and $1 - \phi_{ho}$ and $\alpha_{ho}(\varphi)$ in the Holocene reef model (as γ_{ho}) together, as they are all scaling parameters.

Due to different climate, local antecedent substrate and shelf physiography, previous studies suggest a contrasting sediment deposition system between the northern and southern GBR (Hinestrosa et al., 2016). Considering this difference, we separate the whole GBR region into northern (10-14.2° S, Fig. 3), northern-central (14.2-18.4° S), southern-central (18.4-21.6° S) and southern GBR (21.6-26.2° S) sectors based on the definition from Hinestrosa et al. (2019). All sediment parameters are allowed to vary between sectors (Table 1), which is indicated by the superscripts 1 (northern), 2 (northern central), 3 (southern central) and 4 (southern). We use the same prior distributions for sediment model parameters across all four regions, except the thickness parameters $\tau_{2,3a,3b,4}$; our compiled database generally shows thicker sediment in the southern GBR (HYD) compared to the north (NOG, Supplementary Figure 1) so we use different prior distributions for these parameters in each region. The prior distributions for all sediment domain parameters are given in Table 1 and the resulting sediment loading history prior distributions are given in Supplementary Figure 4.

2.4. Statistical calibration

During the calibration process, to consider uncertainty associated with the poorly-constrained pre-LGM ice history, we allow the ice model to vary between scenarios I and II using a weighting parameter ω. The final RSL predictions are calculated using a weighted combination of the two ice history scenarios. ω therefore indicates the data preference for the assumed pre-LGM ice history. The data used for calibration are sea-level index points (SLIPs). Each SLIP provides information about the age and height of past RSL at a single location, which is assumed to represent the combined signal of GIA and SIA processes. Based on SLIP databases, we use a Bayesian framework to sample the posterior probability density distribution for each model parameter (Table 1) conditioned on sea-level data (Fig. 1).

2.4.1. Calibration data

We compile a GBR RSL database following the methodology of Hibbert et al. (2018, 2016). For radiocarbon dated SLIPs we recalibrate the conventional radiocarbon age using the SHCal20 calibration curve (Hogg et al., 2020) for terrestrial samples, and Marine20 (Heaton et al., 2020) with appropriate and up-to-date local marine reservoir corrections (ΔR; http://calib.org/marine) for marine samples. For Uranium-Thorium dated coral samples we recalculate the U-series ages where necessary, assuming a closed system with the latest decay constant (Cheng et al., 2013). We only include the U-series ages that pass the age reliability screening criteria of [^{232}Th] $\leq$ 2 ppb and $\delta^{234}U_{initial}$ = 147 $\pm$ 5‰. We exclude any SLIPs that are explicitly stated as not being *in situ* by the original paper.

For SLIP depth uncertainty we use local palaeo-water depth determination for each record taken from original publications, assuming that the indicator may occur equally anywhere within the given upper and lower limit (i.e., the uniform distribution scenario, Hibbert et al., 2016, 2018; Lin et al., 2021). Additionally, we consider the elevation measurement uncertainty caused by coring, levelling and tectonic correction when necessary. Overall, our study uses 375 SLIPs (supplementary database). To systematically quantify the RSL difference between NOG and HYD, we use a Monte Carlo binning analysis approach to reconstruct the underlying RSL signal at these two sites. The details of this approach are given in Supplementary section 3.

Table 1
Table of prior sediment model parameters. We assume a uniform prior distribution for all parameters within the defined parameter space. The uniform distributions with parentheses indicate a continuous uniform distribution, those with square brackets indicate a discrete uniform distribution comprising the listed parameters. Superscripts 1 to 4 represent spatially different parameters for the northern, northern central, southern central and southern GBR.

Model Component	Parameters and Prior Distribution(s)	Parameter Description
Earth model	LT $\sim U$[46,71,96]	Effective lithospheric thickness with unit kilometre
	μ_{up} $\sim U$[0.05,0.08,0.1,0.2,0.3,0.5,0.8,1]	Upper mantle viscosity with unit 10^{21} Pa s
	μ_{lo} $\sim U$[1,2,3,5,8,10,20,30,50,70,90]	Lower mantle viscosity with unit 10^{21} Pa s
Ice model	ω $\sim U$(0,1)	Relative weighting associated with ice loading scenario II
Shelf edge reef	γ_{se}^{1-4} $\sim U$(0.055,0.45)	A combined parameter that describes the uncertainty associated with shelf edge reef formation porosity and reefal area percentage
	τ_2^{1-4} $\sim U$(5,10), U(5,10),U(5,15),U(5,15)	Maximum accretion thickness for shelf edge reef stage 2 with unit metre (same for all maximum accretion thickness parameters below)
	τ_{3a}^{1-4} $\sim U$(10,20),U(10, 20),U(15,30),U(15,30)	Maximum accretion thickness for shelf edge reef stage 3a
	τ_{3b}^{1-4} $\sim U$(5, 15),U(5,15),U(10,20),U(10,20)	Maximum accretion thickness for shelf edge reef stage 3b
	τ_4^{1-4} $\sim U$(5, 15),U(5,15),U(10,20),U(10,20)	Maximum accretion thickness for shelf edge reef stage 4
	ι_{se}^{1-4} $\sim U$[0,0.2,0.4,0.6,0.8,1]	Lag between local inundation and shelf edge reef initiation with unit ka (same for all lag parameters below)
Holocene reef	γ_{ho}^{1-4} $\sim U$(-3σ,3σ)	A combined parameter that describes the uncertainty associated with reef formation porosity and kriging determined reef depth uncertainty (defined by σ).
	ι_{ho}^{1-4} $\sim U$[0,0.2,0.4,0.6,0.8,1]	Lag between local inundation and Holocene reef initiation
Halimeda bioherms	ϕ_{ha}^{1-4} $\sim U$(0.25,0.45)	*Halimeda* bioherms formation porosity
	ι_{ha}^{1-4} $\sim U$[0,0.2,0.4,0.6,0.8,1]	Lag between local inundation and *Halimeda* bioherms initiation
Siliciclastic sediment	β^{1-4} $\sim U$(0.6,1.4)	Averaged siliciclastic discharge rate relative to present day

2.4.2. Calibration procedure

The posterior probability distributions are calculated using a simulated annealing algorithm (Kirkpatrick et al., 1983), a probability-based technique which shows good capacity to converge to the global minimum solution. Within a Bayesian framework, a likelihood function describes the joint probability of the observed data as a function of the model parameters. We assume a uniform prior distribution for all model parameters (Table 1), meaning the posterior probability is equivalent to the likelihood. In this study we express the likelihood as:

$$p(y|x) = exp(-\frac{1}{N}\sum_{n=1}^{N} w_n J_n) \tag{4}$$

$$J_n = \sqrt{\frac{(RSL_n^y - RSL_n^m)^2}{\sigma_{RSL,n}^2} + \frac{(t_n^y - t_n^m)^2}{\sigma_{t,n}^2}} \tag{5}$$

where x is the vector of all model parameters, y is the SLIP data set consisting of n samples, each containing information about palaeo RSL height (RSL_n^y) and age (t_n^y) with 1 sigma uncertainties of $\sigma_{RSL,n}$ and $\sigma_{t,n}$, respectively. w_n is a weighting parameter to offset calibration bias due to variable temporal data density using the definition from Tarasov et al. (2012). For each set of model parameters, and for each SLIP location, a RSL curve is produced and we calculate the minimum distance (J_n) between the SLIP and the RSL curve, where RSL_n^m and t_n^m represent the RSL and age of the closest point on the modelled curve (adapted from Love et al., 2016). The minimum distance data-model comparison metric J provides a unitless measurement of model misfit for both chronological and vertical uncertainties. Because we assume past sea level may occur equally anywhere between the upper and lower limit of each SLIP, we assume no vertical misfit if the model predictions are within the 2 sigma uncertainty range of the observations. Therefore, we express RSL_n^y as:

$$RSL_n^y = \begin{cases} RSL_n^y + 2\sigma_{RSL,n}, & RSL_n^m \geq RSL_n^y + 2\sigma_{RSL,n} \\ RSL_n^m, & RSL_n^y - 2\sigma_{RSL,n} < RSL_n^m < RSL_n^y + 2\sigma_{RSL,n} \\ RSL_n^y - 2\sigma_{RSL,n}, & RSL_n^m \leq RSL_n^y - 2\sigma_{RSL,n} \end{cases} \tag{6}$$

Based on this likelihood formulization, we calculate the posterior probability distributions for each model parameter, and to speed up the calibration process, we use a statistical emulator to emulate the SIA process. Details on the implementation of this approach are provided in Supplementary section 2.

3. Results

Based on the posterior probability distributions of the model parameters drawn from the simulated annealing (Supplementary Table 1), we calculate the spatio-temporal field of sediment accumulation and RSL variation for the GBR. We start by presenting the results of the Earth and ice model parameter inversion and describe the resulting GIA-induced RSL predictions. Using these GIA predictions, we illustrate the palaeo GBR shoreline reconstructions and quantify how they affect the sediment accumulation history. Lastly, we present the sediment loading induced RSL change and RSL model-data comparison.

3.1. Earth and ice model parameters

The inversion results are given in Table 2. For a far-field region like the GBR, post-glacial sea-level change was predominantly driven by ice-ocean mass exchange (causing >100 m RSL change compared to ~1 m by SIA). Hence, although the Earth model parameters impact the prediction of both GIA- and SIA-induced RSL

Table 2
Inversion results. P_{max} indicates the value with the maximum posterior probability (i.e., best-fit value). The load values represent the total sediment load deposited during the last 28 ka BP, subscripts and superscripts are as follows: se = shelf edge reef; ho = Holocene reef, ha = *Halimeda* bioherms, si = siliciclastic discharge, 1= northern GBR, 2 = northern central GBR, 3 = southern central GBR, 4 = southern GBR.

	P_{max}	Expected Value	Standard Deviation	95% Confidence Interval
LT (km)	96	89.3	11.2	71-96
μ_{up} (10^{21} Pa s)	1	0.93	0.15	0.5-1
μ_{lo} (10^{21} Pa s)	30	38.3	11.3	20-50
ω	1	0.98	0.06	0.9-1
$Load_{total}$ (Gt)	1939.6	1853.7	112.4	1613.1-2078.7
$Load_{se}$ (Gt)	559.1	478.8	68.9	330.8-566.3
$Load_{ho}$ (Gt)	797.6	794.2	59.3	630.0-943.4
$Load_{ha}$ (Gt)	47.0	46.7	3.8	46.7-54.1
$Load_{si}$ (Gt)	536.3	534.0	61.3	410.5-659.1
$Load^1$ (Gt)	138.1	167.8	53.1	137.1-271.9
$Load^2$ (Gt)	183.1	229.8	59.3	169.3-361.0
$Load^3$ (Gt)	1007.2	994.6	45.7	905.0-1042.2
$Load^4$ (Gt)	611.3	461.5	98.9	296.2-617.5

change, the Earth model parameter distributions are primarily calibrated to replicate the GIA process. The maximum probability fit to the SLIPs is achieved using an Earth model combination of 96 km (71-96 km; 95% confidence interval, CI) lithospheric thickness, and 1 (0.5-1) and 30 (20-70) $\times$ 10^{21} Pa s upper and lower mantle viscosity. These inverted Earth parameters are generally consistent with recent global 3D viscosity field reconstructions (Austermann et al., 2021) but reflect a substantially stronger upper mantle compared with previous estimates based on GIA analysis of Holocene sea-level data from east Australia (0.15-0.3 $\times$ 10^{21} Pa s Lambeck et al., 2002). The main reason for this difference is our inclusion of pre-Holocene coral reef records, which prefer a stronger upper mantle viscosity (details in Supplementary Figure 6).

The ice model weighting parameter predominantly converges to scenario II (Fig. 2), indicating that a smaller pre-LGM grounded ice volume is preferred by the SLIPs. The blue dashed lines in Fig. 4 are the expected GIA-induced RSL change for RSL sites with at least five SLIPs; results for other RSL sites are shown in Supplementary Figure 8. It is clear that SLIPs with ages between 19.5 and 21.5 ka BP at NOG represent substantially higher RSL than the prediction produced by the preferred ice loading scenario II. Using scenario I, which has a larger LGM global ice volume, would result in an even lower RSL prediction during this period, therefore further enlarging the data-model misfit, leading to the rejection of this scenario in the inversion.

3.2. Sediment deposition history

3.2.1. Temporal distribution

Using the posterior Earth and ice model parameters, we show detailed palaeo shoreline positions (note that the SIA impact on shoreline migration is minor and is not considered here) for eight key time frames (Fig. 5). Comparing to the commonly used approach that assumes sea-level rise uniformly follows the GMSL curve (e.g., Hinestrosa et al., 2019), our calculation shows local RSL can significantly depart from GMSL by >10 m depending on local morphology. During early MIS 2 (28-22 ka BP; Fig. 2), RSL was 90-105 m below present with only part of the shelf edge submerged near the south-eastern Capricorn Channel. The growth of reef stage 2 here (Supplementary Figure 1; Webster et al., 2018) contributed 10% to overall sediment accumulation for this period (Fig. 6). Comparatively, 19.1 Gt/ka (14.7-23.5 Gt/ka) of siliciclastic sediment was deposited at the continental slope and shelf edge during this period, which dominated the sediment budget (contributing ~90% of total loading). This siliciclastic proportion became even greater when GMSL dropped to LGM conditions between 22-19.9 ka BP.

After the LGM, local sea level rose gradually prior to 16.5 ka BP and accelerated between 16.5 and 14.65 ka BP, which induced the coastline near the Capricorn Channel to migrate slightly onshore. As a result of the initiation of reef 3b and the continuous growth of reefs 3a and 2 (Supplementary Figure 1), shelf edge reef accumulation increased from 1.6 Gt/ka to 11.1 Gt/ka (Fig. 7b). Following the start of Meltwater Pulse 1A at 14.5 ka BP, the rate of local sea-level rise exceeded 40 m/ka, which further inundated the Capricorn Channel by hundreds of kilometres and caused the shelf edge accumulation rate to increase to ~20 Gt/ka. Although the RSL rise rate decreased to ~15 m/ka after 14.0 ka BP, the coastline continued to retreat significantly in the southern central GBR and less so in the northern central GBR until 13.2 ka BP. Due to the flat morphology of the southern central GBR shelf, a large area of middle shelf near Mackay was flooded at this time, initiating the growth of the Holocene reef. The rest of the outer-middle shelf within the southern central GBR was submerged following ~6.5 m RSL rise leading up to 12.6 ka BP. Meanwhile, north of the southern central GBR, most of the middle shelf and even parts of the shelf edge were still sub-aerially exposed, indicating the strong temporal variability in transgression time. The accretion rate of the shelf edge reef along the whole GBR continued to rise until 10 ka BP, when most of the shelf edge had been inundated with its contribution to the sediment budget peaking at 32.3% (Fig. 7c). Similarly, as the coastline moved across the middle shelf (except in the northern GBR), this accelerated the growth of the Holocene reef and initiated *Halimeda* bioherm growth at 11 ka BP. This timing agrees well with a recent radiocarbon analysis of inter-reef sediment cores, which suggests *Halimeda* bioherm initiation occurred around 11.1 ka BP in the northern GBR (McNeil et al., 2022).

Between 10-8 ka BP, the shoreline migrated to a geometry similar to present day and the growth rate of the Holocene reef and *Halimeda* bioherms domains reached their maximum values of 130.5 and 11.2 Gt/ka at 8.2 and 8.8 ka BP, respectively (Fig. 7b). Concurrently, much of the shelf edge reef had attained its maximum thickness and stopped accreting, therefore, its contribution to the sediment budget was gradually surpassed by the Holocene reef (Fig. 7c). RSL continued to rise until 4.8 ka BP with the maximum magnitude of the Mid-Holocene highstand (3.2 m) being predicted near Rockhampton and Mackay (Fig. 5) where the shoreline is estimated to have been up to tens of kilometres inland of its modern position, with the subsequent re-advance being due to the impact of water loading on the adjacent wide continental shelf. The growth rate of carbonate sediment decreased in the late Holocene, with the largest reduction seen in the Holocene

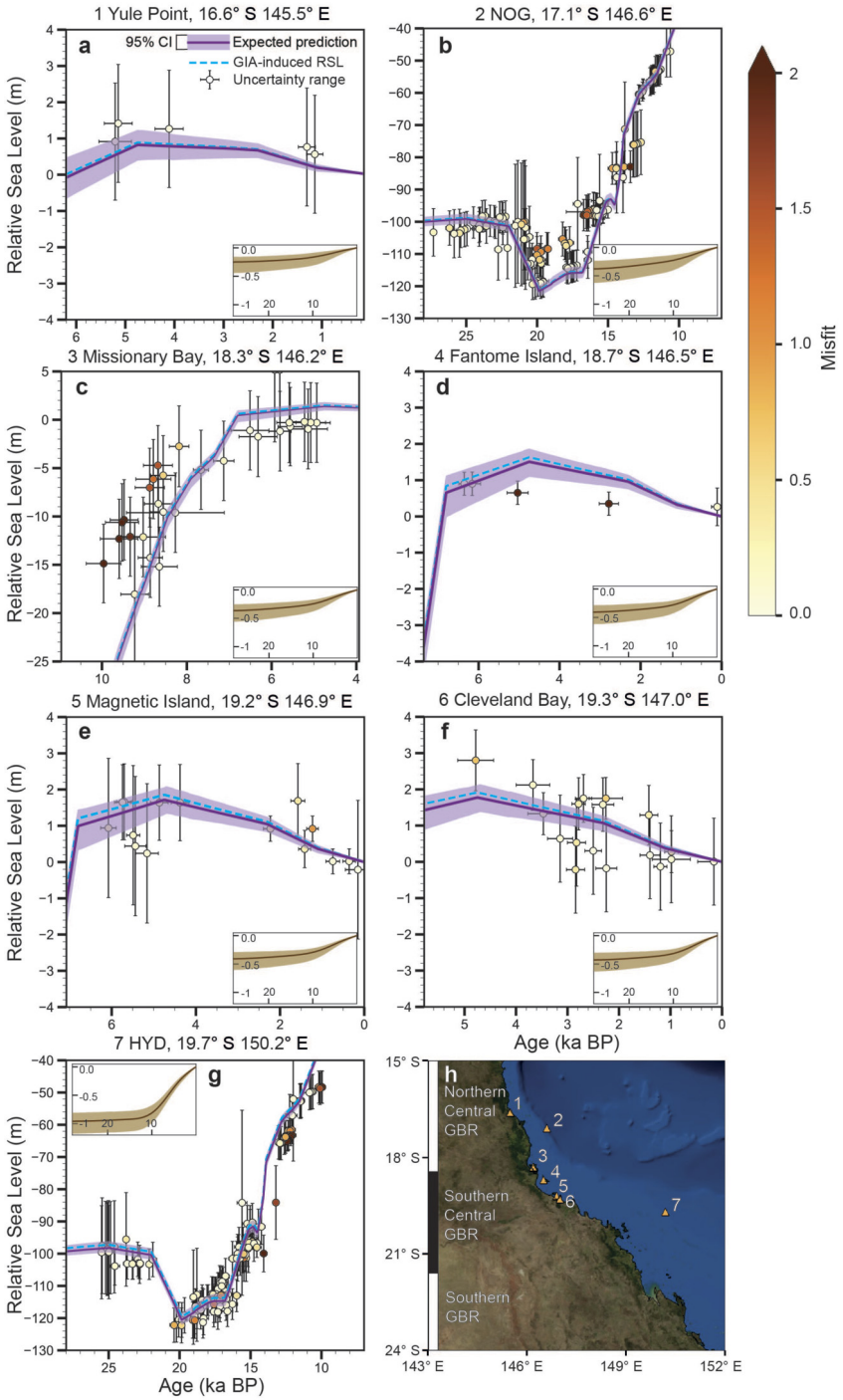

Fig. 4. Relative sea level data-model comparison. Each error bar shows 2σ vertical and age uncertainties with the coloured dots indicating the unitless data-model misfit (i.e., J in equation (5)). Note we plot the 2σ vertical uncertainty range of the reconstructed RSL instead of showing the original recorded elevation. The RSL sites are listed from north to south with the site's number, name and coordinates given as the subtitle. The expected SIA-induced RSL change and its associated 95% CI are shown in the subplot within each frame. The last frame shows the RSL site locations and corresponding site numbers. Note the different axes used in each plot.

reef domain due to the reef surface leaving the photic zone or the cessation of growth following the highstand (section 2.3.2). Overall, reconstructed Holocene growth rates for carbonate sediment domains agree well with the theoretical bell-shaped curve (Davies and Hopley, 1983), which suggests a slow growth during reef initiation followed by accelerated growth when the reef is "keeping-up" or "catching-up" to sea level. The final maturation phase exhibits a slow accretion rate mostly due to lack of accommodation space.

Our inversion results indicate the GBR experienced 1853.7 Gt (1613.1-2078.7 Gt) of sediment loading from MIS 2 to present (Fig. 7a). Three carbonate domains produced 1319.7 Gt (1007.5-1563.8 Gt) of sediment, comparable with previous estimates of 939 Gt (622-1398 Gt Hinestrosa et al., 2022) and 1709.4 Gt (Rees, 2005). The timing of increased carbonate deposition identified in our study correlates with a period of minor decrease in atmospheric CO_2 (14.3-12.7 ka BP), which is consistent with the idea that coral reef growth played a significant role in the postglacial

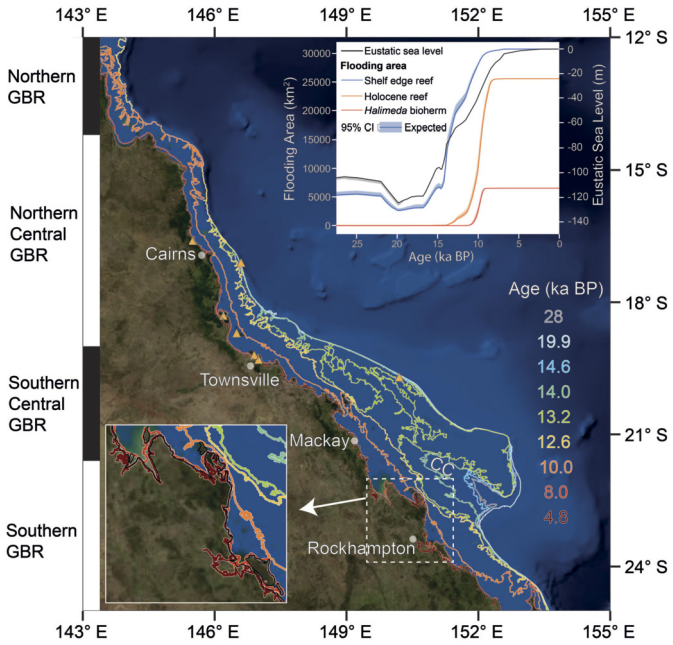

Fig. 5. Expected GBR postglacial flooding pattern. The eight coloured shoreline reconstructions correspond to the eight time intervals shown on the right. Time series of posterior flooding area for each sediment domain and eustatic sea-level are shown in the subplot in the top-right corner. The subplot in the bottom-left corner shows an enlarged version of the shoreline reconstruction results near Rockhampton. The orange triangles indicate site locations for the sea-level data shown in Fig. 4. Some key locations are labelled, CC = Capricorn Channel.

carbon cycle (Lemieux-Dudon et al., 2010; Kinsey and Hopley, 1991).

3.2.2. Spatial distribution

Fig. 7 shows the sediment spatial distribution conditioned on the SLIP database. There is a distinct north-south gradient with more sediment accumulated in the southern (central) GBR. This gradient reflects the different physiography of the northern and southern GBR, with the southern GBR having a wider and flatter shelf morphology. This provides ample accommodation space for carbonate material to grow (Fig. 3). The SLIPs support this gradient and mostly show higher-than-predicted RSL in the northern (central) GBR and, conversely, lower-than-predicted RSL in the southern central GBR. During sea-level transgression, the GBR sediment system is mostly in a depositional phase, therefore the effect of SIA is to increase the magnitude of post-depositional RSL rise, which results in lower-than-predicted RSL (Fig. 4). To minimise the misfit to SLIPs, model parameters associated with sediment domains in the northern (central) GBR gradually converged to the lower end of the prior distribution, producing 167.8 Gt and 229.8 Gt of sediment. In contrast, the southern central GBR sediment mass distributions strongly skew to the higher end, producing 994.6 Gt of sediment. Although there are no SLIPs in the southern GBR sector, the larger-than-prior sediment loading results (461.5 Gt) reflect the fact that sediment loading in the southern sector has a long-wavelength impact on RSL change in the southern central GBR.

This north-south distinction is supported by recent seismic mapping of shelf edge reef structures (Hinestrosa et al., 2016, 2014) and a modelling study of the GBR carbonate-siliciclastic systems (Salles et al., 2018), both of which show substantially thicker shelf edge sediment in the southern (central) GBR. The good agreement between RSL observations and these independent studies suggests it is possible to use SLIPs to constrain sediment deposition history. It is noticeable that, compared with other regions, the posterior uncertainties are very low in the southern central GBR (Fig. 7b). The reason for this is because greater southern central sediment loading consistently improves the data-model misfit, by up to ∼15%, and thus the southern central sediment loading converges to the higher end of the prior distribution. For the other three regions, because the overall misfits are sensitive to the southern-central load, they show a similar level of uncertainty.

3.2.3. SIA-induced RSL change

Using the posterior model parameter distributions, we quantify the impact of SIA on the total GBR RSL calculation (Fig. 4). Overall, including the SIA signal reduces the data-model misfit (J in equation (4)) by ∼10% and broadens the acceptable region of the Earth model parameter space (Supplementary Figure 7). The largest SIA signal is on the outer shelf of the southern-central GBR where sediment loading contributes >1.1 m to RSL rise since MIS 2 (Fig. 7c). For HYD, incorporating the SIA-induced RSL rise (0.97 m; 0.83-1.17 m) improves the model fit to the SLIPs from 0.48 to 0.41, especially for SLIPs with ages 12.5-10 and 21-18 ka BP where observations show remarkably lower RSL than predicted by the GIA-only model. For the inner shelf region of the southern-central GBR, the SIA signal is lower, with an expected value of only 0.42 m (0.31-0.64 m; similar magnitude for sites 4-6), due to the lack of carbonate sediment. Similar to HYD, the inclusion of the SIA signal significantly improves the average model misfit by 0.04 for Fantome Island. But for Magnetic Island and Cleveland Bay, there is no noticeable improvement. For these four RSL sites, since the majority of sediment loading takes place at the shelf edge and in the Holocene reef domains, i.e., during the early-mid Holocene, the SIA signal remains almost unchanged before 14 ka BP (Fig. 4).

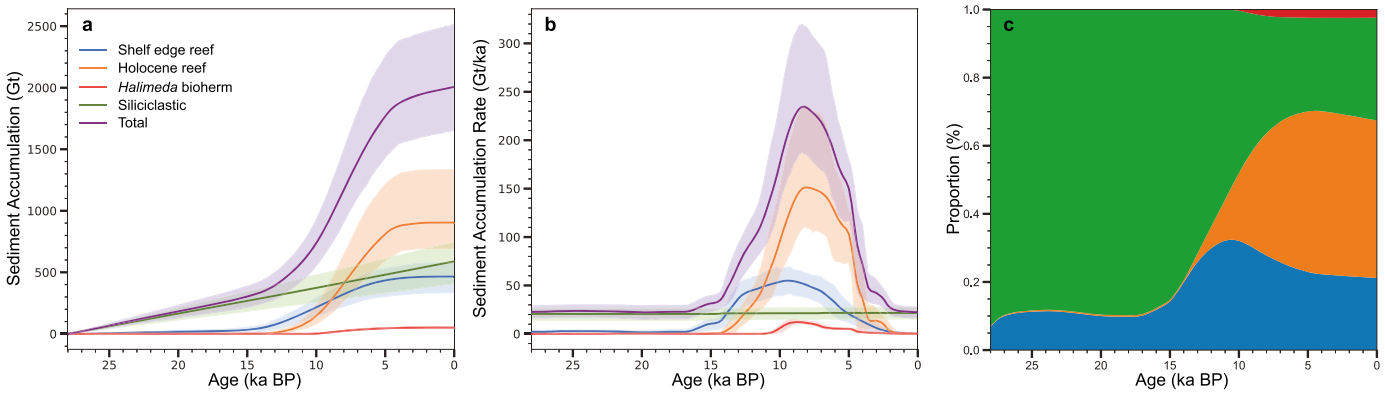

Fig. 6. GBR posterior sediment mass accumulation history. (a) Total sediment mass accumulation and sediment accumulation associated with each sediment domain. (b) As in (a), but showing the rate of sediment accumulation. The solid lines indicate the expected sediment models and uncertainty ranges denote the 95% confidence intervals. (c) The proportional contribution of each sediment domain to total mass accumulation through time.

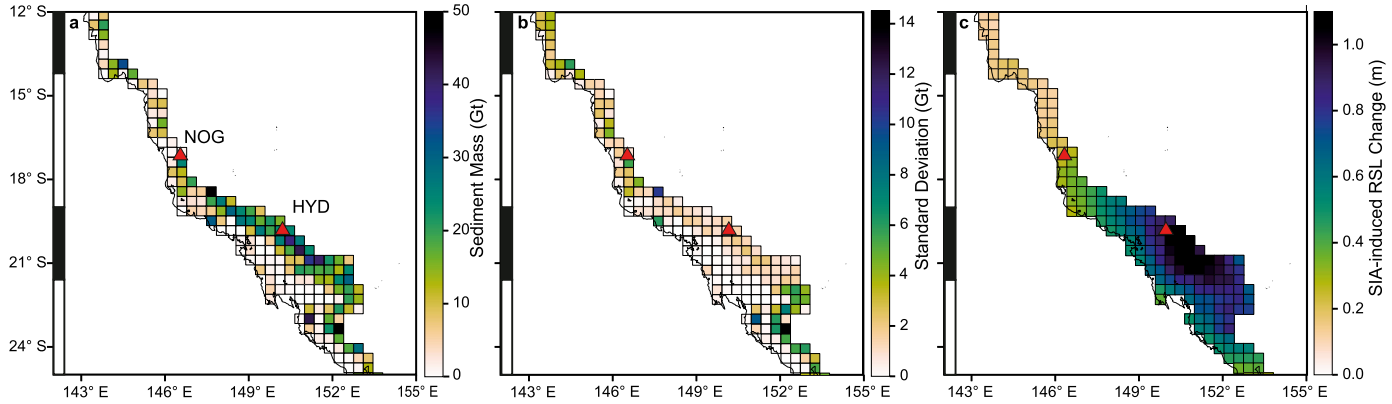

Fig. 7. Reconstructed spatial distribution of sediment mass accumulated from MIS 2 to present. (a) Expected sediment accumulation mass distribution. (b) One sigma standard deviation of sediment accumulation mass. (c) Expected RSL change due to SIA. The black and white bands on the left define the four GBR latitudinal sectors as in Fig. 5. The red triangles indicate the locations of NOG and HYD.

To the north, SIA effects in Missionary Bay and Noggin Pass are predicted to have a similar magnitude of ∼0.3 m, but with different temporal patterns (Fig. 4). For Missionary Bay, the local load is minor (<10 Gt; Fig. 7a) and the SIA signal is primarily impacted by the long wavelength sediment signal from the southern-central GBR, where 910.7 Gt of sediment was deposited during the Holocene. In contrast, the SIA signal for NOG shows a much more linear rate of prior to before the Holocene, which is caused by continuous siliciclastic sediment discharge to the shelf edge during early deglaciation. Lastly, for Yule Point the SIA signal is predicted to be small (0.24 m) due to the low local sediment loading and the fact that it is located >500 km from the sediment deposition centre in the southern central GBR. Since the SLIPs generally show higher-than-predicted RSL at sites 1-3, the inclusion of the SIA signal slightly increases the model misfit to observations. But since the SIA signals for these sites are relatively small, the overall increase in model misfit is negligible compared with the misfit reduction associated with including SIA in the southern central GBR.

4. Discussion

4.1. GBR RSL spatial variability

We first investigate the degree to which the SIA signal can explain the RSL difference between NOG and HYD. The Monte Carlo binning analysis (section 2.4.1) yields a temporally-increasing RSL difference between these two locations, with a temporally-averaged value of 4.0 m (3.4-4.5 m, Fig. 8). The increasing RSL difference at NOG and HYD prior to the Holocene can be explained by different sediment deposition histories. Between MIS 2 and the Holocene a considerable amount of siliciclastic sediment was discharged to the shelf edge near NOG, which gradually increased local RSL (Fig. 4). Comparatively, our model predicts much less siliciclastic discharge near HYD (this site is not located close to any modern river mouths, Fig. 3), hence the SIA signal remains low prior to the Holocene. These results are consistent with conceptual sediment depositional models which suggest that, during MIS 2 and MIS 1, the regions surrounding NOG and HYD were dominated by large estuaries and extensive coastal barriers and lagoons (Hinestrosa et al., 2016). Near NOG, the estuaries were fed by east-west elongated channels crossing the narrow continental shelf (<50 km) which provided an efficient way to transport coarse grained sediment to the shelf edge and upper continental slope. This can be verified by the presence of thick siliciclastic sediment in various records from the shelf edge and continental slope (Dunbar and Dickens, 2003). In contrast, the northwest-southeast elongated coastal choked lagoons of the southern central GBR were not efficient for transporting sediment towards the continental slope. The wider and flatter continental shelf in this region nurtured complex drainage networks with long and sinuous channels redirecting the sediment to the southeast (see Figure 1 of Hinestrosa et al., 2016). In addition, the presence of blocking barriers along the shelf edge strongly reduced lagoon flushing. In summary, prior to coral reef initiation during the Holocene, NOG was substantially more impacted by siliciclastic sediment loading than HYD (Fig. 4), which explains the greater RSL rise observed at NOG during this period.

Subsequent to the initiation of reef development, HYD has experienced greater RSL rise than NOG, due to the development of extensive reefs in the southern central GBR. Specifically, our sediment model predicts the development of widespread, thick reefs across the shelf edge of the southern central, resulting in up to four times more sediment loading compared with the northern central GBR. This is consistent with seismic stratigraphy suggesting the extensive availability of low gradient substrate near HYD promoted the development of thick and wide fringing shelf edge reefs (Hinestrosa et al., 2016). In comparison, the lateral availability of substrate is very limited near NOG due to the narrow and steep physiography (Abbey et al., 2011). Additionally, our results show shelf edge reefs near HYD are thicker than those near NOG, consistent with the drill core observations shown in Supplementary Figure 1. This may be due to the contrasting palaeo-environmental and physiographic conditions between NOG and HYD during the evolution of these reefs (e.g., different morphology and sediment and nutrient circulation; Hinestrosa et al., 2016). Similar to the shelf edge reef, a wide and flat physiography provides ample accommodation space for the Holocene reef to thrive in southern central GBR. Our interpolation results suggest the Holocene reef in this region is on average thicker than in the north (Supplementary section 1) possibly due to the lower elevation prior to sea-level transgression (Salles et al., 2018; Hopley et al., 2007). Overall, based on our expected sediment and Earth model parameters, we predict that sediment loading differences between NOG and HYD can explain 0.6 m (0.35-0.75 m) of the observed RSL difference.

Notably, our SIA model can only account for 15% of the mean RSL difference (4.0 m) between NOG and HYD. We propose three possible explanations for this. Firstly, as mentioned in section 3.1, our preferred Earth models are relatively strong (Table 2). These Earth models may be biased towards fitting LGM-age SLIPs from NOG and HYD, but it is important to note that these SLIPs have large chronological and indicative meaning uncertainties. Previous GIA analysis (e.g., Lambeck et al., 2002) and independent 3D mantle viscosity estimates suggest a thinner lithosphere and weaker

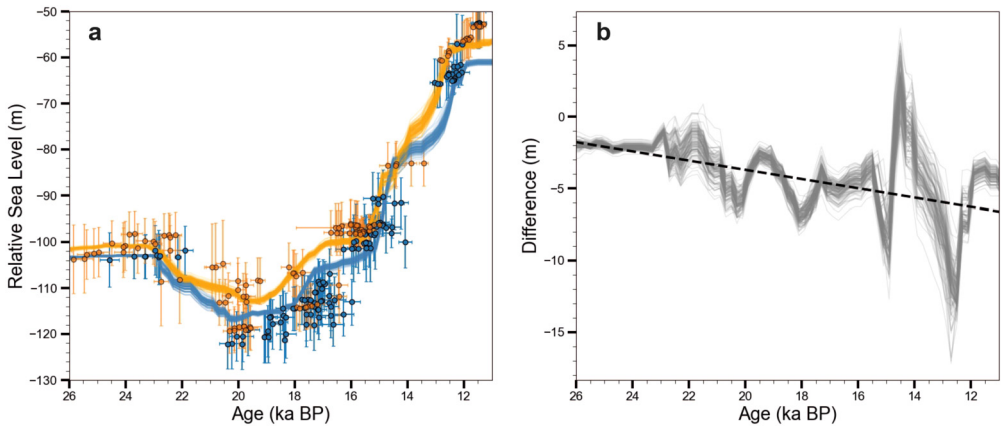

Fig. 8. Monte Carlo binning analysis results. (a) Reconstructed time series of RSL variation at NOG (orange) and HYD (blue). The error bars indicate 2σ age and vertical data uncertainties. Each solid line represents one random realisation of the Monte Carlo binning analysis. (b) The time series of RSL difference between NOG and HYD, the dashed trendline indicates the temporally increasing RSL difference between these two sites from the LGM to the Holocene.

mantle viscosity across the GBR, which would induce a larger SIA signal and explain more of the RSL difference between NOG and HYD. Therefore, we recalculate the SIA signal using an alternative Earth model with 46 km lithospheric thickness and 0.1×10^{21} Pa s upper mantle viscosity, which is supported by previous studies (Hoggard et al., 2021; Austermann et al., 2021) and is consistent with the Earth model determined by the Holocene SLIPs alone (Supplementary Figure 6). The results show a larger SIA signal at NOG (0.59 m) and HYD (2.20 m), which accounts for almost half the observed RSL difference.

Secondly, differences in turbidity and nutrient level may impact the coral species' living depth and hence past RSL reconstructions (Hibbert et al., 2016). One important assumption when reconstructing past sea level is that each sea-level indicator of a given species should have an identical relationship to palaeo water depth, however, this is not robust. Indeed, there is no global relationship between coral species and bathymetry (Perrin et al., 1995), instead, it depends on local irradiance levels (affected by turbidity and nutrient levels), nutrient availability, temperature and hydrodynamic conditions (Hibbert et al., 2016). As mentioned above, NOG and HYD are dominated by estuarine and lagoonal environments, this difference may induce significantly different coral reef accretion environments, which could explain part of the observed RSL difference between NOG and HYD (Hinestrosa et al., 2016).

Thirdly, the simple sediment model adopted in this study may not adequately represent sediment evolution across the GBR, especially the terrigenous sediment transport and depositional processes. Although the impact of shoreline migration is considered, we do not account for landscape and fluvial evolution driven by extrinsic forcings and sea-level variation or the sediment infill of some large palaeo river channels (Ryan et al., 2007), and instead we make the simple assumption that fluvial sediment is deposited (with an overall uniform rate) at the nearest concurrent shoreline position. These factors may misrepresent the spatio-temporal distribution of siliciclastic sediment. For example, our siliciclastic modelling results are similar to a classical reciprocal sedimentation concept, which may not fit well with the deglacial sediment accumulation rate inferred from sediment cores from Queensland Trough (Dunbar et al., 2000). Additionally, we do not consider the effect of wave processes on siliciclastic sedimentation, which can induce erosional and depositional phases near NOG and HYD (see Figure 4 of Salles et al., 2018).

Lastly, we note acknowledge that the relatively coarse resolution of the sediment SIA model used in this study may cannot be able to fully resolve coral reef structure (Fig. 7), which is often characterised by narrow and isolated strips with <1 km coverage (Hinestrosa et al., 2016). This caveat and this may lead to structural bias in the resulting SIA signal. Rovere et al. (2022, preprint) provide a direct comparison of the SIA signals estimated by SIA models with 1 km and 40 km resolution (see their Figure 4b and 4f). Their results indicate although both SIA models produce a long wavelength SIA signal, the low-resolution SIA model would systematically underpredict SIA signal, especially in regions with non-continuous sediment load. Therefore, this potential for our model to underestimate the local SIA signal may further explain some of the RSL difference between NOG and HYD. Considering all of the factors discussed here, we conclude that it is possible for the SIA process to partially explain the observed spatial variability in RSL between NOG and HYD. However, to better understand this RSL variability, further investigation is required of the missing processes mentioned above.

4.2. SIA impact on ice volume estimate

Using far-field sea-level data to constrain past grounded ice volume and infer past ice sheet dynamics is an important tool in palaeoclimate studies (e.g., Lambeck et al., 2014). However, most studies do not consider the SIA signal, despite previous studies suggesting it can alter local RSL by >100 m since the Last Interglacial (Pico, 2020). Because SIA-induced RSL change is not associated with ice-water exchange, neglecting its effect will systematically bias inferences of global grounded ice volume. For the GBR, we find that SIA can cause up to 1.1 m RSL rise since MIS 2, which is equivalent to overestimating the volume of ice melt by $\sim 4.3 \times 10^5$ km^3 under the common assumption that ice-water exchange is the only cause of post-glacial sea-level change. This demonstrates that caution is needed when estimating global ice volume from SLIPs collected from margins characterised by high sediment input across large spatial areas (hundreds of kilometres, e.g., Argentine Shelf).

Based on the results of this study, we find that it is necessary to incorporate the SIA signal when determining global ice volume during the LGM, which is an outstanding problem in paleoclimate studies (Simms et al., 2019). Currently, there are five locations that have yielded RSL records for the LGM, specifically, NOG, HYD, Bonaparte Gulf, Sunda Shelf and Barbados. All of these locations are potentially impacted by sediment loading during the last deglaciation. In particular, cores from NOG, HYD and Barbados were collected from large coral reef frameworks near estuaries (Woodroffe and Webster, 2014) which are likely to have been affected by RSL rise due to reef and siliciclastic sediment loading. Although distant from large coral reef systems, Bonaparte Gulf and Sunda Shelf are located near major river mouths (Pico, 2020), and

they may record some SIA signals caused by siliciclastic sediment deposition. In all cases, incorporating the SIA process will reduce the subsequent global grounded ice volume estimate, which will help to mitigate the current disagreement between the magnitude of post-LGM GMSL rise recorded by RSL indicators and the estimated amount of ice melt (Simms et al., 2019).

5. Conclusions

In this study, we develop a systematic RSL-driven framework to reconstruct a sediment deposition history for the world's largest carbonate-siliciclastic sediment system, the GBR. Using a Bayesian-style technique, we calibrate the sediment history along with SIA- and GIA-induced RSL change using SLIPs from the GBR region. Based on our results, we highlight these key findings:

1. From MIS 2 to present, 1853.7 Gt (1613.1-2078.7 Gt) of sediment were deposited along the GBR consisting of 1319.7 Gt (1007.5-1563.8 Gt) of carbonate sediment, which mostly accreted between the late Pleistocene and mid Holocene, and 534.0 Gt (410.5-659.1 Gt) of terrigenous siliciclastic sediment.
2. There is a strong north-south gradient in the reconstructed sediment loading, with ∼75% of the sediment predicted to have been deposited in the southern-central and southern GBR. This latitudinal distinction is consistent with independent seismic stratigraphy analysis (Hinestrosa et al., 2014), continental shelf physiography (Hinestrosa et al., 2016) and sea-level observations (Yokoyama et al., 2018; Webster et al., 2018).
3. For the GBR, SIA can contribute up to 1.1 m of RSL rise during the last deglaciation. Neglecting its contribution to RSL will lead to an $\sim 4.3 \times 10^5$ km^3 overestimate of global grounded ice volume during the LGM. To accurately infer global ice volume from far-field SLIPs, we suggest a systematic assessment of the potential SIA signal is required, especially for SLIP locations near large sediment systems.

CRediT authorship contribution statement

Y.L. led the research; Y.L., P.L.W., F.D.H. and S.A.W. conceived the scope and design of the research. Y.L., P.L.W., F.D.H. and S.A.W. led the writing of the manuscript. G.H. and J.M.W. guided Y.L. in building the sediment model. P.L.W. advised Y.L. in performing GIA and SIA modelling. F.D.H., S.A.W., G.H. and J.M.W. advised Y.L. in sediment data analysis. All authors contributed ideas and to the writing of the manuscript.

Declaration of competing interest

The authors declare that they have no known competing financial interests or personal relationships that could have appeared to influence the work reported in this paper.

Data availability

The relative sea-level data used for this study along with the reconstructed sediment deposition, and relative sea-level change history and shoreline migration patterns across the Great Barrier Reef, and the SIA emulator are available at https://github.com/yc-lin-geo/GBR-Sediment. The code for generating the depth uncertainty distribution for each type of sea-level indicator can be accessed from Hibbert et al. (2018), via https://figshare.com/articles/dataset/Matlab_Code_-_calculation_of_sea_level/5890579.

Acknowledgements

The authors thank two anonymous reviewers for their constructive comments, and Glenn A. Milne for providing the code used to perform the GIA modelling. Y.L. was supported by a China Scholarship Council - Durham University joint scholarship (No. 201908190020). F.D.H. received funding from the European Union's Horizon 2020 research and innovation programme under the Marie Skłodowska-Curie grant agreement (No. 838841 – ExTaSea). J.M.W. received funding from the Australian Research Council (DP1094001). The authors acknowledge the collaborative research oppurtunities created by PALSEA, a working group of the International Union for Quaternary Sciences (INQUA) and Past Global Changes (PAGES), which in turn received support from the Swiss Academy of Sciences and the Chinese Academy of Sciences.

Appendix A. Supplementary material

Supplementary material related to this article can be found online at https://doi.org/10.1016/j.epsl.2023.118066.

References

Abbey, Elizabeth, Webster, Jody M., Beaman, Robin J., 2011. Geomorphology of submerged reefs on the shelf edge of the Great Barrier Reef: the influence of oscillating Pleistocene sea-levels. Mar. Geol. 288 (1–4), 61–78.

Austermann, Jacqueline, Hoggard, Mark J., Latychev, Konstantin, Richards, Fred D., Mitrovica, Jerry X., 2021. The effect of lateral variations in Earth structure on Last Interglacial sea level. Geophys. J. Int. 227 (3), 1938–1960.

Beaman, R.J., 2010. 3DGBR: a high-resolution depth model for the Great Barrier Reef and Coral Sea. In: Marine and Tropical Sciences Facility (MTSRF) Project, 2, p. 13.

Cheng, Hai, Edwards, R. Lawrence, Shen, Chuan-Chou, Polyak, Victor J., Asmerom, Yemane, Woodhead, Jon, Hellstrom, John, Wang, Yongjin, Kong, Xinggong, Spötl, Christoph, et al., 2013. Improvements in 230Th dating, 230Th and 234U half-life values, and U–Th isotopic measurements by multi-collector inductively coupled plasma mass spectrometry. Earth Planet. Sci. Lett. 371, 82–91.

Dalca, A.V., Ferrier, K.L., Mitrovica, J.X., Perron, J.T., Milne, G.A., Creveling, J.R., 2013. On postglacial sea level—III. Incorporating sediment redistribution. Geophys. J. Int. 194 (1), 45–60.

Davies, Peter J., Hopley, David, 1983. Growth fabrics and growth rates of Holocene reefs in the Great Barrier Reef. BMR J. Aust. Geol. Geophys. 8, 237–251.

Dunbar, Gavin B., Dickens, Gerald R., 2003. Massive siliciclastic discharge to slopes of the Great Barrier Reef Platform during sea-level transgression: constraints from sediment cores between 15 S and 16 S latitude and possible explanations. Sediment. Geol. 162 (1–2), 141–158.

Dunbar, G.B., Dickens, G.R., Carter, R.M., 2000. Sediment flux across the Great Barrier Reef Shelf to the Queensland Trough over the last 300 ky. Sediment. Geol. 133 (1–2), 49–92.

Dziewonski, Adam M., Anderson, Don L., 1981. Preliminary reference Earth model. Phys. Earth Planet. Inter. 25 (4), 297–356.

Ferrier, Ken L., Austermann, Jacqueline, Mitrovica, Jerry X., Pico, Tamara, 2017. Incorporating sediment compaction into a gravitationally self-consistent model for ice age sea-level change. Geophys. J. Int. 211 (1), 663–672.

Ferrier, Ken L., Li, Qi, Pico, Tamara, Austermann, Jacqueline, 2018. The influence of water storage in marine sediment on sea-level change. Geophys. Res. Lett. 45 (5), 2444–2454.

Heaton, Timothy J., Köhler, Peter, Butzin, Martin, Bard, Edouard, Reimer, Ron W., Austin, William E.N., Bronk Ramsey, Christopher, Grootes, Pieter M., Hughen, Konrad A., Kromer, Bernd, et al., 2020. Marine20—the marine radiocarbon age calibration curve (0–55, 000 cal BP). Radiocarbon 62 (4), 779–820.

Hibbert, Fiona D., Rohling, Eelco J., Dutton, Andrea, Williams, Felicity H., Chutcharavan, Peter M., Zhao, Cheng, Tamisiea, Mark E., 2016. Coral indicators of past sea-level change: a global repository of U-series dated benchmarks. Quat. Sci. Rev. 145, 1–56.

Hibbert, F.D., Williams, F.H., Fallon, S.J., Rohling, E.J., 2018. A database of biological and geomorphological sea-level markers from the Last Glacial Maximum to present. Sci. Data 5, 180088.

Hinestrosa, Gustavo, Webster, Jody M., Beaman, Robin J., Anderson, Louise M., 2014. Seismic stratigraphy and development of the shelf-edge reefs of the Great Barrier Reef, Australia. Mar. Geol. 353, 1–20.

Hinestrosa, Gustavo, Webster, Jody M., Beaman, Robin J., 2016. Postglacial sediment deposition along a mixed carbonate-siliciclastic margin: new constraints from the drowned shelf-edge reefs of the Great Barrier Reef, Australia. Palaeogeogr. Palaeoclimatol. Palaeoecol. 446, 168–185.

Hinestrosa, Gustavo, Webster, Jody M., Beaman, Robin J., 2019. Spatio-temporal patterns in the postglacial flooding of the Great Barrier Reef shelf, Australia. Cont. Shelf Res. 173, 13–26.

Hinestrosa, Gustavo, Webster, Jody M., Beaman, Robin J., 2022. New constraints on the postglacial shallow-water carbonate accumulation in the Great Barrier Reef. Sci. Rep. 12 (1), 1–18.

Hogg, Alan G., Heaton, Timothy J., Hua, Quan, Palmer, Jonathan G., Turney, Chris S.M., Southon, John, Bayliss, Alex, Blackwell, Paul G., Boswijk, Gretel, Bronk Ramsey, Christopher, et al., 2020. SHCal20 Southern Hemisphere calibration, 0–55,000 years cal Bp. Radiocarbon 62 (4), 759–778.

Hoggard, Mark, Austermann, Jacqueline, Randel, Cody, Stephenson, Simon, 2021. Observational estimates of dynamic topography through space and time. Mantle Convect. Surf. Expr., 371–411.

Hopley, David, Smithers, Scott G., Parnell, Kevin, 2007. The Geomorphology of the Great Barrier Reef: Development, Diversity and Change. Cambridge University Press.

Horton, Benjamin P., Kopp, Robert E., Garner, Andra J., Hay, Carling C., Khan, Nicole S., Roy, Keven, Shaw, Timothy A., 2018. Mapping sea-level change in time, space, and probability. Annu. Rev. Environ. Resour. 43, 481–521.

Ishiwa, Takeshige, Yokoyama, Yusuke, Okuno, Jun'ichi, Obrochta, Stephen, Uehara, Katsuto, Ikehara, Minoru, Miyairi, Yosuke, 2019. A sea-level plateau preceding the Marine Isotope Stage 2 minima revealed by Australian sediments. Sci. Rep. 9 (1), 1–8.

Ji, Weiwen, Robel, Alexander, Tziperman, Eli, Yang, Jun, 2021. Laurentide ice saddle mergers drive rapid sea level drops during glaciations. Geophys. Res. Lett. 48 (14), e2021GL094263.

Kendall, Roblyn A., Mitrovica, Jerry X., Milne, Glenn A., 2005. On post-glacial sea level–II. Numerical formulation and comparative results on spherically symmetric models. Geophys. J. Int. 161 (3), 679–706.

Kinsey, D.W., Hopley, D., 1991. The significance of coral reefs as global carbon sinks—response to greenhouse. Palaeogeogr. Palaeoclimatol. Palaeoecol. 89 (4), 363–377.

Kirkpatrick, Scott, Gelatt, C. Daniel, Vecchi, Mario P., 1983. Optimization by simulated annealing. Science 220 (4598), 671–680.

Lambeck, Kurt, Yokoyama, Yusuke, Purcell, Tony, 2002. Into and out of the Last Glacial Maximum: sea-level change during Oxygen Isotope Stages 3 and 2. Quat. Sci. Rev. 21 (1–3), 343–360.

Lambeck, Kurt, Rouby, Hélène, Purcell, Anthony, Sun, Yiying, Sambridge, Malcolm, 2014. Sea level and global ice volumes from the Last Glacial Maximum to the Holocene. Proc. Natl. Acad. Sci. 111 (43), 15296–15303.

Lemieux-Dudon, Bénédicte, Blayo, Eric, Petit, Jean-Robert, Waelbroeck, Claire, Svensson, Anders, Ritz, Catherine, Barnola, Jean-Marc, Narcisi, Bianca Maria, Parrenin, Frédéric, 2010. Consistent dating for Antarctic and Greenland ice cores. Quat. Sci. Rev. 29 (1–2), 8–20.

Lin, Yucheng, 2019. Closing the Last Deglacial Global Sea Level Budget by Different Antarctic Deglaciation Models. Masters dissertation. The Australian National University, Canberra.

Lin, Yucheng, Hibbert, Fiona D., Whitehouse, Pippa L., Woodroffe, Sarah A., Purcell, Anthony, Shennan, Ian, Bradley, Sarah L., 2021. A reconciled solution of Meltwater Pulse 1A sources using sea-level fingerprinting. Nat. Commun. 12 (1), 1–11.

Love, Ryan, Milne, Glenn A., Tarasov, Lev, Engelhart, Simon E., Hijma, Marc P., Latychev, Konstantin, Horton, Benjamin P., Törnqvist, Torbjörn E., 2016. The contribution of glacial isostatic adjustment to projections of sea-level change along the Atlantic and Gulf coasts of North America. Earth's Future 4 (10), 440–464.

McNeil, Mardi A., Webster, Jody M., Beaman, Robin J., Graham, Trevor L., 2016. New constraints on the spatial distribution and morphology of the Halimeda bioherms of the Great Barrier Reef, Australia. Coral Reefs 35 (4), 1343–1355.

McNeil, Mardi A., Nothdurft, Luke D., Dyriw, Nicholas J., Webster, Jody M., Beaman, Robin J., 2020. Morphotype differentiation in the Great Barrier Reef Halimeda bioherm carbonate factory: internal architecture and surface geomorphometrics. Depositional Rec. 7 (2), 176–199.

McNeil, Mardi, Nothdurft, Luke D., Hua, Quan, Webster, Jody M., Moss, Patrick, 2022. Evolution of the inter-reef Halimeda carbonate factory in response to Holocene sea-level and environmental change in the Great Barrier Reef. Quat. Sci. Rev. 277, 107347.

Milliman, John D., Farnsworth, Katherine L., 2013. River Discharge to the Coastal Ocean: A Global Synthesis. Cambridge University Press.

Mitrovica, Jerry X., Wahr, John, Matsuyama, Isamu, Paulson, Archie, 2005. The rotational stability of an ice-age Earth. Geophys. J. Int. 161 (2), 491–506.

Perrin, Christine, Bosence, Dan, Rosen, Brian, 1995. Quantitative approaches to palaeozonation and palaeobathymetry of corals and coralline algae in Cenozoic reefs. Geol. Soc. (Lond.) Spec. Publ. 83 (1), 181–229.

Pico, T., 2020. Towards assessing the influence of sediment loading on Last Interglacial sea level. Geophys. J. Int. 220 (1), 384–392.

Rees, Siwan Angharad, 2005. Coral reefs of the Indo-Pacific and changes in global Holocene. PhD thesis. University of Southampton.

Rovere, Alessio, Pico, Tamara, Richards, Fred D., O'Leary, Michael J., Mitrovica, Jerry X., Goodwin, Ian D., Austermann, Jacqueline, Latychev, Konstantin, 2022. The influence of reef isostasy, dynamic topography, and glacial isostatic adjustment on the Last Interglacial sea-level record of Northeastern Australia. https://doi.org/10.31223/X55S8X.

Ryan, David A., Bostock, Helen C., Brooke, Brendan P., Marshall, John F., 2007. Bathymetric expression of the Fitzroy River palaeochannel, northeast Australia: response of a major river to sea-level change on a semi-rimmed, mixed siliciclastic-carbonate shelf. Sediment. Geol. 201 (1–2), 196–211.

Salles, Tristan, Ding, Xuesong, Webster, Jody M., Vila-Concejo, Ana, Brocard, Gilles, Pall, Jodie, 2018. A unified framework for modelling sediment fate from source to sink and its interactions with reef systems over geological times. Sci. Rep. 8 (1), 1–11.

Sanborn, Kelsey L., Webster, Jody M., Webb, Gregory E., Carlos Braga, Juan, Humblet, Marc, Nothdurft, Luke, Patterson, Madhavi A., Dechnik, Belinda, Warner, Susan, Graham, Trevor, et al., 2020. A new model of Holocene reef initiation and growth in response to sea-level rise on the Southern Great Barrier Reef. Sediment. Geol. 397, 105556.

Simms, Alexander R., Lisiecki, Lorraine, Gebbie, Geoffrey, Whitehouse, Pippa L., Clark, Jordan F., 2019. Balancing the last glacial maximum (LGM) sea-level budget. Quat. Sci. Rev. 205, 143–153.

Tarasov, Lev, Dyke, Arthur S., Neal, Radford M., Peltier, W. Richard, 2012. A data-calibrated distribution of deglacial chronologies for the North American ice complex from glaciological modeling. Earth Planet. Sci. Lett. 315, 30–40.

Webster, Jody M., Carlos Braga, Juan, Humblet, Marc, Potts, Donald C., Iryu, Yasufumi, Yokoyama, Yusuke, Fujita, Kazuhiko, Bourillot, Raphael, Esat, Tezer M., Fallon, Stewart, et al., 2018. Response of the Great Barrier Reef to sea-level and environmental changes over the past 30,000 years. Nat. Geosci. 11 (6), 426.

Wolstencroft, Martin, Shen, Zhixiong, Törnqvist, Torbjörn E., Milne, Glenn A., Kulp, Mark, 2014. Understanding subsidence in the Mississippi Delta region due to sediment, ice, and ocean loading: insights from geophysical modeling. J. Geophys. Res., Solid Earth 119 (4), 3838–3856.

Woodroffe, Colin D., Webster, Jody M., 2014. Coral reefs and sea-level change. Mar. Geol. 352, 248–267.

Yokoyama, Yusuke, Purcell, Anthony, Marshall, John F., Lambeck, Kurt, 2006. Sea-level during the early deglaciation period in the Great Barrier Reef, Australia. Glob. Planet. Change 53 (1–2), 147–153.

Yokoyama, Yusuke, Esat, Tezer M., Thompson, William G., Thomas, Alexander L., Webster, Jody M., Miyairi, Yosuke, Sawada, Chikako, Aze, Takahiro, Matsuzaki, Hiroyuki, Okuno, Jun'ichi, et al., 2018. Rapid glaciation and a two-step sea level plunge into the Last Glacial Maximum. Nature 559 (7715), 603–607.

Appendix C: GEORGIA: a Graph neural network based EmulatOR for Glacial Isostatic Adjustment

Geophysical Research Letters

RESEARCH LETTER
10.1029/2023GL103672

GEORGIA: A Graph Neural Network Based EmulatOR for Glacial Isostatic Adjustment

Yucheng Lin[1], Pippa L. Whitehouse[1], Andrew P. Valentine[2,3], and Sarah A. Woodroffe[1]

[1]Department of Geography, Durham University, Durham, UK, [2]Department of Earth Sciences, Durham University, Durham, UK, [3]Research School of Earth Sciences, The Australian National University, Acton, ACT, Australia

Key Points:

- The first attempt to build a deep-learning based Glacial isostatic adjustment (GIA) emulator that can accurately predict global sea-level change based on a given ice model
- This emulator (GEORGIA) can predict global sea-level change history within 0.5 s with minor emulation error
- This GIA emulator along with two illustrative applications are available for use by the wider sea-level community

Supporting Information:

Supporting Information may be found in the online version of this article.

Correspondence to:

Y. Lin,
yucheng.lin@durham.ac.uk

Citation:

Lin, Y., Whitehouse, P. L., Valentine, A. P., & Woodroffe, S. A. (2023). GEORGIA: A graph neural network based EmulatOR for glacial isostatic adjustment. *Geophysical Research Letters*, *50*, e2023GL103672. https://doi.org/10.1029/2023GL103672

Received 13 MAR 2023
Accepted 9 AUG 2023

Author Contributions:

Conceptualization: Yucheng Lin, Pippa L. Whitehouse, Andrew P. Valentine
Data curation: Yucheng Lin
Formal analysis: Yucheng Lin
Investigation: Yucheng Lin, Pippa L. Whitehouse, Andrew P. Valentine
Methodology: Yucheng Lin, Pippa L. Whitehouse, Andrew P. Valentine, Sarah A. Woodroffe
Supervision: Pippa L. Whitehouse, Andrew P. Valentine, Sarah A. Woodroffe

Abstract Glacial isostatic adjustment (GIA) modeling is not only useful for understanding past relative sea-level change but also for projecting future sea-level change due to ongoing land deformation. However, GIA model predictions are subject to a range of uncertainties, most notably due to uncertainty in the input ice history. An effective way to reduce this uncertainty is to perform data-model comparisons over a large ensemble of possible ice histories, but this is often impossible due to computational limitations. Here we address this problem by building a deep-learning-based GIA emulator that can mimic the behavior of a physics-based GIA model while being computationally cheap to evaluate. Assuming a single 1-D Earth rheology, our emulator shows 0.54 m mean absolute error on 150 out-of-sample testing data with <0.5 s emulation time. Using this emulator, two illustrative applications related to the calculation of barystatic sea level are provided for use by the sea-level community.

Plain Language Summary Piecing together the history of ice sheet change during past glacial cycles is not only important for understanding past sea-level change but also for predicting how ongoing glacial rebound contributes to future sea-level change. Traditionally, a physics-based "sea-level model" is used to predict the sea-level change associated with a particular reconstruction of past ice sheet change and compare the results with geological records of past sea level. However, a fundamental limitation of this approach is the need to compute sea-level change for a large number of plausible ice histories, which is often prohibited by the computational resources required to repeatedly solve the complex physical equations. In this paper, we describe a machine-learning-based statistical model that can mimic the behavior of a physics-based sea-level model. This statistical model is computationally cheap and we demonstrate that it is able to accurately predict global sea-level change for a suite of 150 "unseen" ice histories. Our statistical model predicts sea-level change 100–1,000 times faster than a physics-based model, making it an ideal tool for investigating and improving our understanding of global ice sheet change.

1. Introduction

During Quaternary glacial cycles, water-mass redistribution related to the waxing and waning of ice sheets altered global mean sea-level by as much as ∼130 m. The spatially variable response of the solid Earth, oceans and global gravitational field to that change in water mass is known as glacial isostatic adjustment (GIA), a process which causes local relative sea level (RSL; distance between the sea surface and the solid Earth) to differ substantially from global mean sea level. GIA models that describe RSL change (Farrell & Clark, 1976; Whitehouse, 2018) have been widely used to investigate past (Lambeck et al., 2014; Lin et al., 2021), present (Frederikse et al., 2020; Hay et al., 2015) and future (Caron et al., 2018; Love et al., 2016) sea-level change problems. Within GIA modeling, a key parametric uncertainty relates to poorly constrained ice histories, which not only reduces our confidence in understanding past sea-level change but also limits our ability to robustly project future sea-level variation due to the ongoing GIA effects associated with past glacial cycles.

A commonly used approach to reduce ice history uncertainty involves performing data-model comparisons with geological data that relate to ice-sheet history: either directly for example, geomorphological evidence of past glaciation, or indirectly such as RSL records. Due to the sparse and noisy nature of geological records, a range of plausible ice-sheet histories may be compatible with the observations, and a robust study often requires testing a large number of these to explore what can be and cannot be constrained (Briggs et al., 2014; Tarasov et al., 2012). However, it is computationally expensive to solve the complex physical equations required to perform data-model comparison. An effective way to mitigate this difficulty is to build a statistical model that mimics the behavior of

Visualization: Yucheng Lin
Writing – original draft: Yucheng Lin
Writing – review & editing: Pippa L. Whitehouse, Andrew P. Valentine, Sarah A. Woodroffe

the physics-based simulator but is computationally cheap to run (Reichstein et al., 2019). Rather than solving the physical equations exactly, these "statistical emulators" learn how the system behaves based on a (comparatively) small set of examples, and use this to predict what the simulation would output in other scenarios.

The concept of emulation (also known as "surrogate modeling") is not particularly new (Sacks et al., 1989), but recent advances in machine learning have greatly expanded its scope and application (Reichstein et al., 2019). Recent studies have built statistical emulators to quantify the impact of basal melt on dynamic ice-sheet model behavior (Berdahl et al., 2021) and to investigate how different CO_2 emission scenarios affect ice-sheet model estimates for future sea-level rise (Edwards et al., 2021). For sea-level research, although Tarasov and Peltier (2005) and Tarasov et al. (2012) created a neural-network-based emulator that can predict RSL chronologies based on a set of glacial systems model parameters, there is currently no end-to-end GIA emulator that can predict global RSL variation history based on arbitrary ice models. In this study, we document a proof-of-concept attempt to build an end-to-end Graph neural network based EmulatOR for GIA (GEORGIA) that can be used to rigorously explore global ice history uncertainty.

2. Methodology

Our goal is to build a statistical emulator that can predict global RSL variation based on a given global ice history from 25 ka BP to present. This can be treated as a supervised regression problem that maps the statistical relationship between input and output based on example input-output pairs generated by a physics-based GIA model. Below, we describe the example data generation, data pre-processing, and the methods used to build and validate our emulator.

2.1. Training Data

To provide example input-output pairs for training our emulator, we use a physics-based GIA model to calculate global RSL variation based on a collection of ice sheet reconstructions. The physical model we use is a gravitationally self-consistent GIA model that accounts for shoreline migration and Earth rotational feedback (Kendall et al., 2005; Milne & Mitrovica, 1996; Mitrovica et al., 2005). The solid Earth is represented by a spherically symmetric Maxwell body consisting of an elastic lithosphere, and an upper and lower mantle extending to 670 km, and from 670 km to the core-mantle boundary, respectively. The GIA model calculates RSL change, caused by land deformation and the geoid response to ice-water mass redistribution, by solving the sea-level equation (Mitrovica et al., 2005) using a spherical harmonic truncation of degree and order 256. The elastic and density structure of the Earth model is derived from the preliminary reference Earth model (Dziewonski & Anderson, 1981). Because the major focus of this study is to thoroughly sample ice history uncertainty, we do not incorporate Earth model parameter variation within the input data for our emulator. Instead, we adopt one specific Earth rheology that has a lithospheric thickness of 71 km and an upper and lower mantle viscosity of 0.3 and 70×10^{20} Pa s respectively (the "low-viscosity" Earth model scenario from Lambeck et al. (2014)).

One key task when building a GIA emulator is to generate a training database which evenly covers a wide range of possible deglaciation trajectories. We achieve this by collecting a wide range of ice history models for four different regions: North America (including Greenland), Eurasia, Antarctica, and all other regions with mountain glaciers (including Patagonia), and sampling the spatio-temporal variability between different reconstructions. In total, we use four global ice models that predict ice-sheet evolution in the four regions (Gowan et al., 2021; Lambeck et al., 2014; Peltier, 2004; Peltier et al., 2015), along with four North American (Gowan et al., 2016; Han et al., 2021; Roy & Peltier, 2018; Tarasov & Peltier, 2003; Tarasov et al., 2012), four Eurasian (Abe-Ouchi et al., 2013; Clark et al., 2021; Han et al., 2021; Patton et al., 2016, 2017; Tarasov et al., 2014) and three Antarctic (Argus et al., 2014; Briggs et al., 2014; Whitehouse, Bentley, & Le Brocq, 2012; Whitehouse, Bentley, Milne, et al., 2012) ice models. Because these ice models are reconstructed based on different principles (e.g., thermo-mechanical ice modeling, GIA modeling, and the interpolation of glacial geomorphological data), they provide good coverage of possible ice-sheet deglaciation uncertainty. Detailed information about each ice model is given in Table S1 of the Supporting Information S1. We resample all the ice sheet reconstructions into a standardized format with 26 time slices (from 25 to 0 ka at 1 ka intervals) and spatial coverage corresponding to 256° spherical harmonic truncation, using linear interpolation as necessary. Because a GIA model is forced by ice thickness change rather than total ice thickness, we express all ice models in terms of ice thickness relative to present.

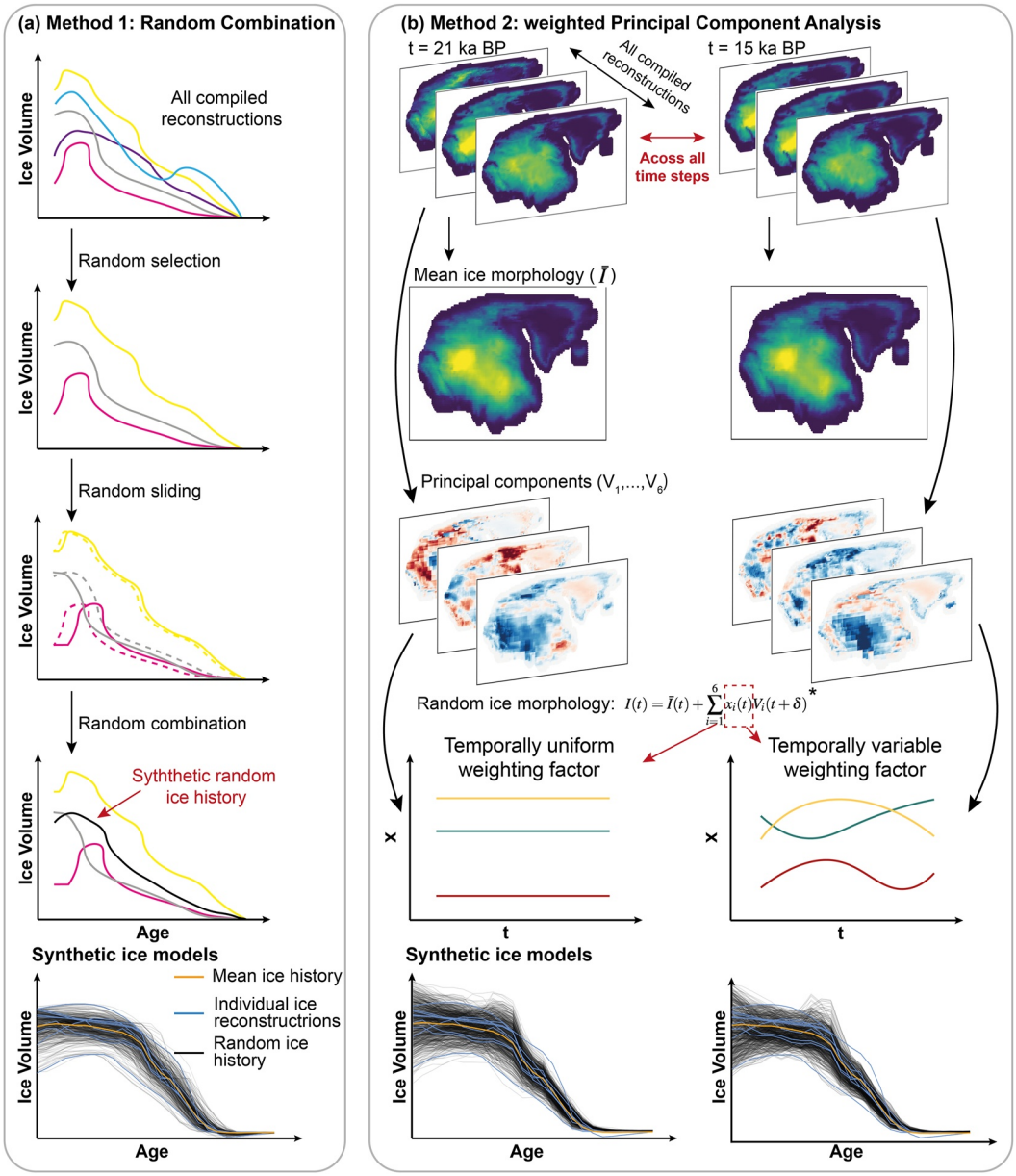

Figure 1. Illustration of the methods used to generate random synthetic ice histories from previous ice sheet reconstructions. (a) Random combination method, which consists of three randomized sampling procedures that reflect temporal (random selection and sliding) and spatial uncertainty (random selection and combination) in the underlying ice sheet reconstructions. (b) Weighted Principal Component Analysis method, which is implemented by calculating the mean ice sheet morphology and principal components of all time slices. From these, random ice sheet morphologies are generated via linear combination of the randomized principal components using two different temporal treatments of the random factor $x_i(t)$, which is illustrated by the equation with an asterisk. A detailed description of this equation can be found in Text S2 of the Supporting Information S1. The resulting synthetic random ice histories are shown in the bottom panel. All examples shown here are for the North American Ice Sheet, but the same approach was used to sample the Antarctic and Eurasian Ice Sheets, as well as mountain glaciers, to create a synthetic global ice history.

Using these standardized ice sheet reconstructions as building blocks, we generate a suite of randomized, synthetic ice histories that span the range of plausibility. We employ two main methods to systematically sample the spatio-temporal variability across different reconstructions: random combination and weighted principal component analysis (wPCA). The random combination method samples the variability within the range bounded by previous reconstructions (Figure 1a), while the wPCA approach samples out-of-boundary variability, with two

different strategies employed to account for long-term (e.g., grounded ice volume at the Last Glacial Maximum, Simms et al., 2019) and short-term (e.g., Meltwater Pulse 1A; Deschamps et al., 2012; Lin et al., 2021) temporal variability (Figure 1b). We provide a brief summary of these approaches here, with a detailed description given in Texts S1 and S2 of the Supporting Information S1. The random combination method creates 500 synthetic ice histories by linearly combining different ice models into a new model. We randomly select 2–6 ice models for each region (i.e., random selection in Figure 1), and randomly translate each in time (younger or older) in order to sample the temporal uncertainty. The new ice model is calculated to be the weighted average of the selected ice models, with the details determined using a set of random weighting factors. The second approach uses wPCA to extract important ice morphological patterns (i.e., principal components; PCs) from different ice models. A weighting scheme is applied to account for the spherical geometry of the Earth, which means that grid cells at different latitudes cover different areas. Using the extracted PCs, 1,000 synthetic ice histories (500 for each strategy to temporal uncertainty) are generated by adding a random linear combination of the PCs to the mean ice history (Figure 1b; details in Text S2 of the Supporting Information S1).

After obtaining 1,500 synthetic ice histories for each region, we create global ice models by randomly selecting ice models for each region, with the result that one global ice model may contain regional ice histories generated by several different statistical methods. In total, we create 1,500 synthetic global ice histories. For each we then simulate global RSL history from 25 ka to present, as described above. Because we express the input in terms of ice thickness relative to present, the modern ice thickness layer is a spatially uniform layer with all zero values, which contains no information. Therefore, we replace this layer with modern topography, which is important for calculating the continental levering and ocean siphoning processes (Mitrovica & Milne, 2002). Before being used to train a GIA emulator, we normalize all input and output data to ensure zero mean and unit standard deviation (more information in Text S3 of the Supporting Information S1). The 1,500 normalized input-output pairs are divided into training (80%), validation (10%) and testing (10%) sets.

2.2. Statistical Emulator

Using this training set, we now wish to build an emulator that can map ice history into RSL change. This is a typical machine learning problem, for which a convolutional neural network is commonly used. However, classical convolutional neural network algorithms are designed to perform convolution and pooling operations within Euclidean space, which is not appropriate when representing geographical data such as ice or RSL history on a spherical Earth. Therefore, we use a graph-based spherical convolutional neural network (SCNN) algorithm that correctly implements convolution and pooling operations on data within a spherical manifold. We employ a Hierarchical Equal Area isoLatitude Pixelization (Healpix) scheme to build this spherical manifold, which produces a subdivision of a spherical surface where every pixel covers the same surface area (Gorski et al., 2005). This is an ideal property for emulating GIA processes because it ensures that input ice thickness is proportional to the ice load applied to each grid cell. Furthermore, the SCNN algorithms used in this study use a graph filter that extracts information from nearby grid cells in a way that only depends on the distance between the grid centers, not on the direction. This ensures that information is rotationally equivariant. In other words, rotating the input ice history will result in an equivariant output RSL prediction. Rotational equivariance is desirable because it can significantly reduce the data sampling complexity. Underpinning these SCNN algorithms is a 3-layer U-Net (Ronneberger et al., 2015), a neural network architecture that is widely used in regression and image segmentation problems (Lai et al., 2020; Yao et al., 2018)—see Text S4 in Supporting Information S1 for more details. For this study, we adopt the SCNN algorithms from the *DeepSphere* package (Defferrard et al., 2019, 2020), which has been successfully used in cosmological and weather prediction applications (Perraudin et al., 2019).

The emulator structure is governed by various hyperparameters, whose values influence the final emulation performance. Here we provide information on some key hyperparameters used in this study; a full list of the hyperparameters along with selection criteria are given in Text S5 of the Supporting Information S1. A hyperparameter that should be noted is the Healpix sampling resolution. To achieve relatively fast emulation, we use a 16° Healpix sampling resolution ($n = 3{,}072$), corresponding to ~3.66° spatial coverage. All standardized input and output fields are interpolated onto 16° Healpix grids. Another essential hyperparameter for SCNNs is graph filter size, which determines the number of nearest-neighborhoods included in each convolution process (i.e., spatial scale length). This is important for GIA problems because the solid Earth deformation signal tends to be long wavelength. For example, the peripheral bulge formed in response to loading of the North American Ice Sheet

can extend over 3,000 km, to places like Barbados. In this study, we use a graph filter size of 60, corresponding to ~1,780 km radius.

We use a mean square error (MSE) loss function to quantify the misfit between predictions and observations and iteratively update model parameters by backpropagation (Goodfellow et al., 2016). Because the MSE loss function focuses on the misfit of each single grid point, we include two extra metrics to assess the overall quality of the emulation results: peak signal-to-noise ratio (PSNR, Korhonen & You, 2012) and structural similarity index measure (SSIM, Brunet et al., 2011). Both of these metrics are widely used to measure the quality of image and video compression (Huynh-Thu & Ghanbari, 2008; Wang & Bovik, 2009), with formal definitions given in Text S6 of the Supporting Information S1. A high PSNR value indicates low noise level, and vice versa, while the SSIM provides a similarity metric between 0 and 1 where a higher value indicates better emulation quality. Note that the SSIM is not directly correlated with either MSE or PSNR, and so can provide an independent assessment of output quality (Hore & Ziou, 2010). We also evaluate model performance by calculating the mean absolute error (MAE). This metric is arguably more directly interpretable than the root-mean-square error, which was used during emulator training for its mathematical convenience. To produce predictive uncertainty estimates, we adopt an ensemble learning approach, which is proved to be an efficient tool for estimating neural network based emulator uncertainty (Lakshminarayanan et al., 2017). The approach involves training an ensemble of 30 alternative SCNNs. The SCNNs all have the same model structure but they are initialized using different model weights and they use different training examples. The 1,200 training examples are constructed by randomly sampling our training and validation sets (the testing set remains unseen for all SCNNs). The variance between the 30 SCNNs represents GEORGIA's predictive uncertainty.

Finally, to assess the value of the SCNN model, and explore whether it is able to capture significant internal relationships between inputs and outputs, we also create a basic kernel model. When given previously unseen inputs, this model simply finds the five most similar inputs from within the training set, and averages their known outputs. The misfit of this approach serves as a baseline for assessing the performance of the SCNN-based emulator.

3. Results and Discussions

3.1. Emulator Performance

Using the trained SCNN-based emulator, which will be referred to as GEORGIA, we predict RSL variation results for 150 unseen testing examples. GEORGIA out-performs the kernel-based method on all evaluation metrics. Specifically, GEORGIA achieves an order of magnitude lower MSE (0.946 vs. 29.53 m^2) and MAE (0.54 vs. 5.84 m) along with distinctly higher PSNR (61.11 vs. 46.18) and SSIM (0.9995 vs. 0.9864) values. This indicates that the SCNN-based algorithm is able to capture the complex correlation between ice history and GIA-induced RSL history better than the baseline approach of finding similar training set pairs. The low MSE and MAE values, and the high PSNR and SSIM values, suggest a high-level of similarity between the RSL predictions generated by the emulator and the physical-based model. The 0.54 m MAE emulation error is also smaller than 87.8% of the 2σ RSL reconstruction uncertainties in a comprehensive sea-level database (Hibbert et al., 2018), suggesting a sufficient emulation accuracy.

The spatial and temporal distributions of emulation error between the physical and statistical models are show in Figure 2. The emulation MAE is strongly heterogeneous in space (Figure 2a), with near-field regions showing large errors of up to 4 m, while errors in far-field regions (i.e., far from previous ice-sheet margins) are mostly below 0.5 m. This spatial heterogeneity reflects the spatial variability in the training set (Figure S1d in Supporting Information S1), where near- and far-field RSL standard deviations can reach up to 500 and 25 m, respectively, indicating that the average emulation error is 1%–2% of the training variability.

Temporally, emulation MAE is generally higher during the early stages of deglaciation (Figure 2b), when RSL is significantly different from present-day values (Figure 2b). Emulation MAE peaks between 20 and 10 ka BP due to the rapid unloading of the major ice sheets, and it decreases during the Holocene as global mean sea-level gradually approaches modern levels. Figures 2d–2f show physics-based RSL predictions along with the emulation error at three typical near-, intermediate- and far-field sea-level sites. It is clear that although RSL predictions differ significantly between these sites, the temporal distributions of the emulation error follow an identical near-stationary trend, with larger emulation error occurring before the Holocene, similar to the global average

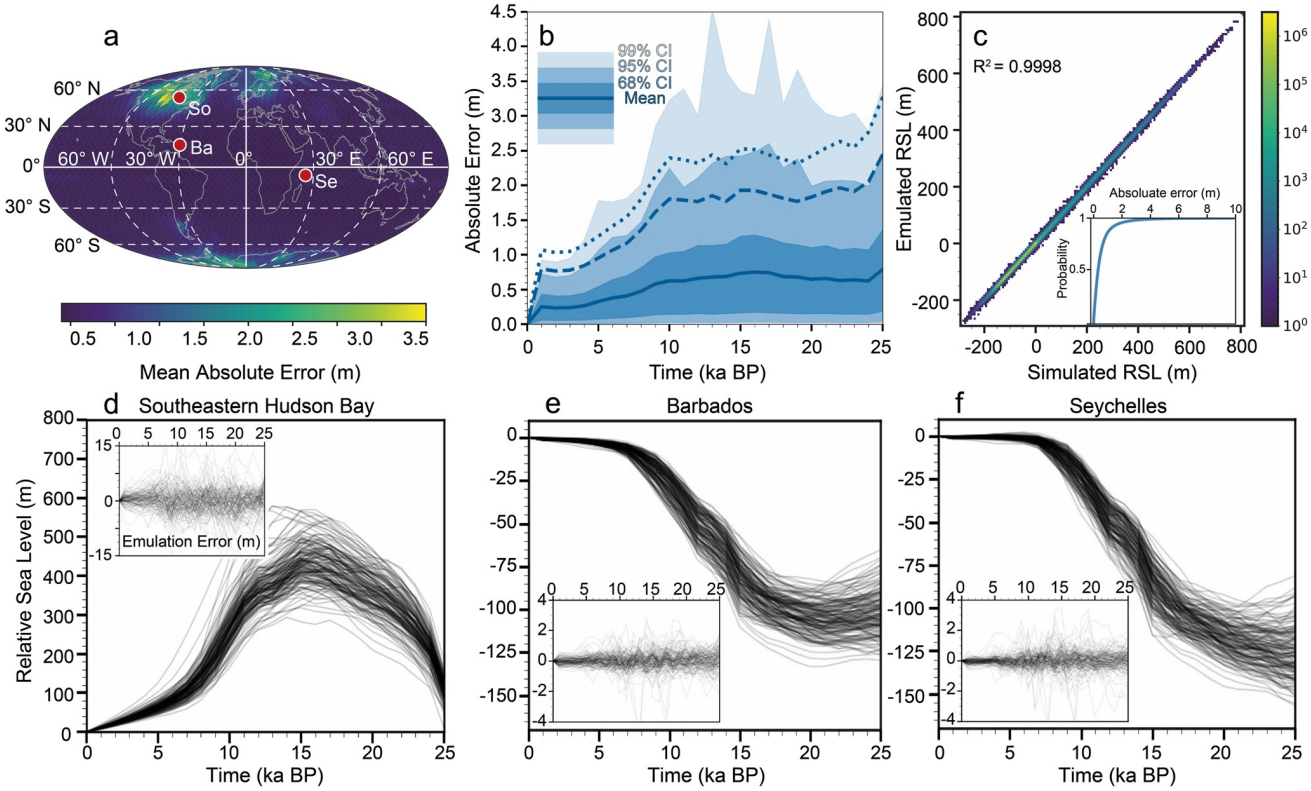

Figure 2. Emulator performance for the 150-member out-of-sample testing set. (a) Temporally averaged spatial distribution of emulation error, locations here refer to typical near-, intermediate- and far-field sites: (So) Southeastern Hudson Bay; (Ba) Barbados and (Se) Seychelles. (b) Mean and confidence intervals of spatially averaged temporal variation of the emulation error and predictive uncertainty, where colored areas indicate the emulation error confidence interval and dashed/dotted lines denote the upper range of 95/99% confidence interval of predictive uncertainty produced by GEORGIA; CI = confidence interval. (c) 2-D histogram comparing the ground truth and emulator predictions. R^2 denotes the coefficient of determination. The subplot shows the cumulative probability of the absolute error. (d–f) RSL predictions generated using the physics-based Glacial isostatic adjustment model for the 150-member test set, with emulation errors and time shown on the *y* and *x* axes in the subplots, at Southeastern Hudson Bay, Barbados and Seychelles, respectively.

pattern shown in Figure 2b. Considering this near-stationary and white-noise-like error distribution, we suggest that GEORGIA is able to capture the vast majority of correlation between ice history and the global RSL field.

Figure 2c provides an overall comparison between the physics- and statistical-based RSL predictions. It is clear that GEORGIA can well approximate the physics-based GIA model with a 0.9998 coefficient of determination (R^2) and no systematic error. 95.7% of the emulation results have a MAE of less than 2 m. In far-field regions, over 99% of the emulation results have a MAE of <2 m while 95% have a MAE of <1 m.

To assess the performance of GEORGIA's predictive uncertainty estimates, we compare them with emulation errors on unseen testing examples (Figure S4 in Supporting Information S1). The 3σ predictive uncertainties are mostly larger than the emulation errors with 99% of emulation predictive intervals (i.e., $\pm 3\sigma$) being able to encompass 94.5% of ground truth values. GEORGIA's predictive uncertainties also agree well with the temporal trend of emulation errors (Figure 2b). These observations suggest our uncertainty estimates are robust. However, for some extreme cases (e.g., the 97.5%–99.5% percentile of the emulation error in Figure 2b), GEORGIA's predictive uncertainties may slightly underestimate the emulation errors. Therefore, we show the 97.5% percentile of the emulation errors across the 150-member testing set at 9 different time steps (Figure S5 in Supporting Information S1) as a conservative estimate on emulation uncertainty, which can reach up to 14/3.5 m in the near/far field, corresponding to 5%–8% of the training variability.

Although GEORGIA contains ~33.8 million trainable parameters, it only takes 3.7 s to emulate RSL change through the last deglaciation on a Central Processing Unit (Intel® CoreTM i9 14 Core Processor). The computation time decreases to 0.25 s when using a Graphics Processing Unit (8GB NVIDIA GEFORCE RTX 3070 Ti). This is 100–1,000 times faster than the computation time of our physical forward GIA model (see Section 2.1),

which takes 6 min to run three iterations (necessary to initialize palaeo topography), and where each iteration comprises 26 time steps at 256° spherical harmonic resolution. Considering the good emulation accuracy above, this emulator allows us to perform 100–1,000 times more simulations within a given computational budget—potentially making it feasible to employ a range of ensemble-based techniques for parameter estimation and uncertainty quantification.

3.2. GEORGIA Generalizability

A key question for any statistical emulator is generalizability: how does the emulator perform for arbitrary unseen inputs? For neural network based emulators, previous studies suggest that although they perform well in interpolation problems (GEORGIA performs well for unseen ice histories that are taken from a similar distribution to our training set, see Section 3.1 and further examples in Text S7 of the Supporting Information S1), they cannot meaningfully extrapolate non-linear functions (Goodfellow et al., 2016; Xu et al., 2020). In other words, while GEORGIA is effective for ice histories that are similar to those in our training set, GEORGIA may produce meaningless output if an ice sheet reconstruction has been generated using an approach or philosophy that is very different to the approach used to generate the ice history models included in our training set. This drawback means that in order to emulate a specific GIA problem, a well-designed training set is a prerequisite. Although our training set covers a wide range of possible ice histories by thoroughly sampling the spatio-temporal variability of previous ice-sheet reconstructions, this cross-reconstruction variability cannot describe the ice thickness uncertainty associated with poor knowledge of ice-sheet dynamical processes (e.g., large uncertainty in ice stream areas, Albrecht et al., 2020; Pittard et al., 2022; Tarasov et al., 2012) and ice margin chronology (Dalton et al., 2020). Therefore, incorporating more modeling results from physically consistent ice sheet models that are constrained by empirical geomorphological evidence will be an important forward step to further improve the generalization of GEORGIA.

3.3. Emulator Applications

Using GEORGIA, global RSL variation from 25 ka BP to present can be rapidly emulated using any ice history that is similar to our training set. Because our training set provides good coverage of possible deglaciation scenarios identified in previous studies, GEORGIA can be used as a substitute for a physics-based GIA model in many applications. Additionally, benefitting from a modern machine learning framework, GEORGIA can be used by other researchers with minimum requirements for programming experience or computational resources. Here, we provide two example GEORGIA applications, namely; (a) calculating the ice-sheet contribution to global Barystatic sea level (BSL); and (b) mapping BSL in space and time.

3.3.1. Barystatic Sea Level Calculator

BSL describes the uniform shift of the global ocean surface due to ice-ocean mass exchange in the absence of gravitational effects and Earth deformation. It is a direct measure of global grounded ice volume change through time, and hence it is important for calibrating isotopic proxies and constraining ice-sheet variation history (Waelbroeck et al., 2002). However, for palaeo ice-sheet modeling studies, there is no straightforward way to calculate the ice-sheet contribution to global BSL without running a GIA model, due to the complexities associated with changes in global ocean area and topography (which impacts the grounded-floating ice transition). As a result, numerous studies (e.g., Gomez et al., 2020; Patton et al., 2017) only present their ice modeling results in terms of ice volume or an ice volume equivalent sea-level contribution (i.e., ice volume divided by modern ocean area). Based on our physics-based GIA modeling results, this latter approach overestimates the ice sheet contribution to barystatic sea-level at 21 ka BP by 3.34 m (0.8–4.3 m depending on the adopted ice history), which is a non-negligible signal to consider.

Using GEORGIA, we provide a global BSL calculator that accounts for shoreline migration and the impact of solid Earth deformation on ice flotation (with detailed theory given in Text S8 of the Supporting Information S1). To test the accuracy of this GEORGIA-based BSL calculator, we compare its predictions to 150 examples of deglacial BSL history obtained using the physics-based model (i.e., those comprising the testing set). The results show emulation error (MAE) of 0.04 m. Thus, GEORGIA is a suitable tool to rapidly estimate the ice-sheet contribution to global BSL change, for example, as predicted by ice dynamic or general circulation models.

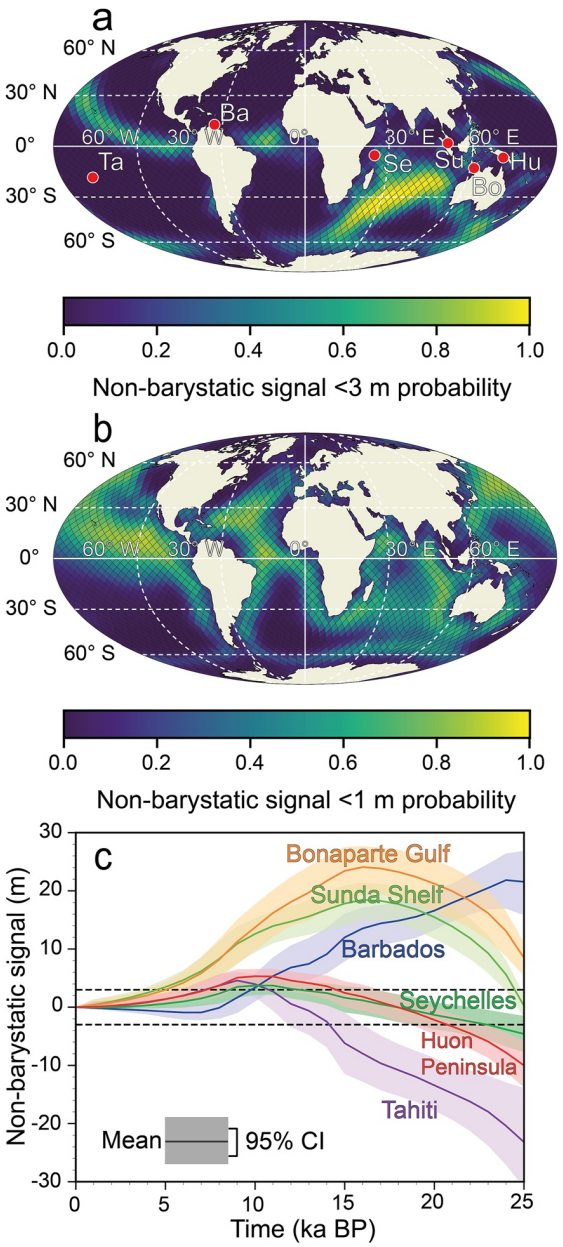

Figure 3. Barystatic sea-level maps based on 10,000 emulation results. (a) Probability that local RSL lies within 3 m of the barystatic value at 21 ka BP. (b) Probability that local RSL lies within 1 m of the barystatic value at 6 ka BP. (c) Temporal variation of the non-barystatic signal at six different sea-level sites. Note the confidence intervals shown here only reflect the uncertainty associated with combining 10,000 different ice histories with one Earth rheology. The non-barystatic signal indicates the difference between GIA-induced RSL change and Barystatic sea level without considering any sterodynamic effects. The area between the two black dashed lines represents the region where the non-barystatic signal is smaller than 3 m. Locations in (a) refer to (from west to east): Tahiti (Ta), Barbados (Ba), Seychelles (Se), Sunda Shelf (Su), Bonaparte Gulf (Bo) and Huon Peninsula (Hu).

3.3.2. Barystatic Sea Level Map

A barystatic sea-level map identifies locations and times where local RSL approximates global BSL. Such sites are targeted by sea-level scientists to provide a close constraint on global ice volume. Because of spatially and temporally variable GIA-related perturbations to the gravity field and solid Earth surface (i.e., the non-barystatic signal), producing a BSL map requires robust estimates of the non-barystatic contributions to RSL. The detailed theory for calculating a BSL map was described in Milne and Mitrovica (2008) where they conclude that ideal locations to reconstruct palaeo BSL are where local RSL: (a) is relatively insensitive to plausible ranges in GIA model parameters (i.e., global ice history and solid Earth rheology); (b) closely approximates the barystatic value. Milne and Mitrovica (2008) provide a series of BSL maps at different time slices, based on GIA modeling results that use two ice histories (Bassett et al., 2005; Peltier, 2004), each paired with 162 plausible sets of Earth parameters. These maps have been used by the field community to target locations that approximate BSL during different parts of the deglacial period (e.g., Sefton, 2020; Woodroffe et al., 2015).

A major limitation of Milne and Mitrovica (2008) is that they only sample two ice models, and hence they are not able to thoroughly quantify the impact of ice history uncertainty on the resulting BSL estimates. Because GEORGIA has high computational efficiency while remaining sufficiently accurate for many applications (Section 3.1), it is an ideal tool for testing the sensitivity of the BSL map to a large ensemble of ice histories. To produce a BSL map that represents ice history uncertainty, we emulate the global non-barystatic signal (i.e., RSL—BSL, neglecting any sterodynamic effects) for 10,000 randomly generated ice histories using the same methods introduced in Section 2.1. Based on these emulation results, we calculate the probability that global RSL lies within 3 and 1 m of the barystatic value at 21 and 6 ka BP respectively (Figure 3).

Because uncertainty in the results of Milne and Mitrovica (2008, see their Figures 6 and 7) largely reflects the uncertainty associated with radial mantle viscosity structure, combining their results with ours enables us to identify regions where, although RSL approximates the global BSL value with minimal sensitivity to the choice of radially varying Earth model, it is sensitive to the choice of ice history (e.g., offshore regions near eastern Australian at 21 ka BP). After excluding such regions, we conclude that the southern Indian Ocean and southern Tasman Sea (close to south-western New Zealand) are ideal regions to reconstruct global BSL at 21 ka BP because it is highly likely that the non-barystatic signal here will be lower than 3 m, and predictions are insensitive to the Earth model choice (Milne & Mitrovica, 2008). Although there is also a low non-barystatic signal shown in the mid-northern Pacific and mid Atlantic regions, these sites are not suitable for reconstructing global BSL because RSL is highly sensitive to the choice of Earth rheology (Milne & Mitrovica, 2008). For the mid-Holocene, our map shows a broadly similar pattern to Milne and Mitrovica (2008), where optimal regions are the western and eastern Indian Ocean, the mid-northern Pacific Ocean and the mid-southern Atlantic Ocean. Meanwhile, agreeing with the results from Milne and Mitrovica (2008), the mid-southern Atlantic is not an ideal region for mapping mid-Holocene BSL.

In Figure 3c, we show the impact of ice history uncertainty on the temporal evolution of the non-barystatic signal at six locations that are commonly used in sea-level studies (e.g., Lin et al., 2023; Webster et al., 2018; Woodroffe et al., 2015). Our results show that variations in the spatial and temporal distribution of the global ice sheets have a major effect on the magnitude of the non-barystatic signal, and a minor effect on the overall trend—the latter depends more on the Earth rheology, which we do not vary in this experiment. Regarding the six selected sea-level sites, as suggested in Milne and Mitrovica (2008), we confirm that the Seychelles is a particularly good site to map global BSL history because it has a low uncertainty, minor non-barystatic signal throughout the last deglaciation (Figure 3c). Although the Huon Peninsula is also predicted to have a small non-barystatic signal, and the uncertainty associated with ice history is small, this site is highly sensitive to the choice of Earth rheology (Milne & Mitrovica, 2008). In general, similar to the findings of Milne and Mitrovica (2008), who investigated the impact of the choice of Earth model on the non-barystatic signal, we find that uncertainty associated with poor knowledge of global ice history can reach up to 15/6 m at 21/6 ka BP, indicating that ice history uncertainty is an essential factor to consider when mapping global BSL history.

3.4. Future Development

In this study, we demonstrate that SCNNs can emulate RSL for a range of ice histories, assuming one specific Earth model. However, Earth rheology is a highly uncertain parameter that can result in hundreds of meters of RSL uncertainty in near-field regions and tens of meters in far-field regions. Therefore, an ideal GIA emulator should be able to sample ice history and Earth rheological properties simultaneously. One way to achieve this would be to incorporate Earth rheological parameters into the input data or a particular layer of the neural network. This would enable solid Earth rheology information to be considered when performing the convolution operations. While this is conceptually straightforward, it significantly complicates the computational task of constructing an emulator: considerably more training data would be required to fully sample the range of possibilities, and the relationship between model inputs and outputs would increase in complexity. Further investigation is required to develop an efficient and effective implementation of this concept, but as GEORGIA is an open-sourced model built upon a popular machine learning framework (PyTorch, Paszke et al., 2017), it is easily scalable for any further developments.

4. Conclusions

Using a graph-based SCNN, we document the first attempt to build a statistical GIA emulator (GEORGIA) that can approximate global RSL variation history based on a given deglacial ice history. GEORGIA predicts RSL history 100–1,000 times faster than a physics-based GIA model, with a MAE of 0.54 m. Due to its low computation expense, it is a suitable tool for performing large-ensemble investigations of ice history uncertainty. By providing example applications of GEORGIA—calculating the ice-sheet contribution to global BSL change and creating a BSL change map—we demonstrate that GEORGIA will be a useful tool for improving our understanding of global ice and sea-level variation histories.

Conflict of Interest

The authors declare no conflicts of interest relevant to this study.

Data Availability Statement

The spherical neural networks used in this study were built by the *DeepSphere* package which can be found at https://github.com/deepsphere/deepsphere-pytorch. GEORGIA, GEORGIA ensemble, along with the codes for creating example applications and visualization, are available at https://github.com/yc-lin-geo/Georgia_GIA, and Zenodo database with identifier https://zenodo.org/record/8216017.

Acknowledgments
We thank Roger Creel and Lev Tarasov for their constructive reviews, which helped to significantly improve this paper. The authors thank Glenn A. Milne for providing the code used to perform the GIA modeling, Parviz Ajourlou and Ryan Love for useful discussion, Kurt Lambeck and Anthony Purcell for sharing the ANU ice model. Y.L. was supported by a China Scholarship Council—Durham University joint scholarship. A.P.V acknowledges support from the Australian Research Council under Grant DP200100053. This work made use of the facilities of the N8 Centre of Excellence in Computationally Intensive Research (N8 CIR) provided and funded by the N8 research partnership and EPSRC (Grant EP/T022167/1). The Centre is co-ordinated by the Universities of Durham, Manchester and York. The authors acknowledge the collaborative research opportunities created by PALSEA, a working group of the International Union for Quaternary Sciences (INQUA) and Past Global Changes (PAGES), which in turn received support from the Swiss Academy of Sciences and the Chinese Academy of Sciences.

References

Abe-Ouchi, A., Saito, F., Kawamura, K., Raymo, M. E., Okuno, J., Takahashi, K., & Blatter, H. (2013). Insolation-driven 100,000-year glacial cycles and hysteresis of ice-sheet volume. *Nature*, *500*(7461), 190–193. https://doi.org/10.1038/nature12374

Albrecht, T., Winkelmann, R., & Levermann, A. (2020). Glacial-cycle simulations of the Antarctic Ice Sheet with the Parallel Ice Sheet Model (PISM)–Part 2: Parameter ensemble analysis. *The Cryosphere*, *14*(2), 633–656. https://doi.org/10.5194/tc-14-633-2020

Argus, D. F., Peltier, W., Drummond, R., & Moore, A. W. (2014). The Antarctica component of postglacial rebound model ICE-6G_C (VM5a) based on GPS positioning, exposure age dating of ice thicknesses, and relative sea level histories. *Geophysical Journal International*, *198*(1), 537–563. https://doi.org/10.1093/gji/ggu140

Bassett, S. E., Milne, G. A., Mitrovica, J. X., & Clark, P. U. (2005). Ice sheet and solid earth influences on far-field sea-level histories. *Science*, *309*(5736), 925–928. https://doi.org/10.1126/science.1111575

Berdahl, M., Leguy, G., Lipscomb, W. H., & Urban, N. M. (2021). Statistical emulation of a perturbed basal melt ensemble of an ice sheet model to better quantify Antarctic sea level rise uncertainties. *The Cryosphere*, *15*(6), 2683–2699. https://doi.org/10.5194/tc-15-2683-2021

Briggs, R. D., Pollard, D., & Tarasov, L. (2014). A data-constrained large ensemble analysis of Antarctic evolution since the Eemian. *Quaternary Science Reviews*, *103*, 91–115. https://doi.org/10.1016/j.quascirev.2014.09.003

Brunet, D., Vrscay, E. R., & Wang, Z. (2011). On the mathematical properties of the structural similarity index. *IEEE Transactions on Image Processing*, *21*(4), 1488–1499. https://doi.org/10.1109/tip.2011.2173206

Caron, L., Ivins, E., Larour, E., Adhikari, S., Nilsson, J., & Blewitt, G. (2018). GIA model statistics for GRACE hydrology, cryosphere, and ocean science. *Geophysical Research Letters*, *45*(5), 2203–2212. https://doi.org/10.1002/2017gl076644

Clark, C. D., Chiverrell, R. C., Fabel, D., Hindmarsh, R. C., Ó Cofaigh, C., & Scourse, J. D. (2021). Timing, pace and controls on ice sheet retreat: An introduction to the BRITICE-CHRONO transect reconstructions of the British–Irish Ice Sheet. *Journal of Quaternary Science*, *36*(5), 673–680. https://doi.org/10.1002/jqs.3326

Dalton, A. S., Margold, M., Stokes, C. R., Tarasov, L., Dyke, A. S., Adams, R. S., et al. (2020). An updated radiocarbon-based ice margin chronology for the last deglaciation of the North American ice sheet complex. *Quaternary Science Reviews*, *234*, 106223. https://doi.org/10.1016/j.quascirev.2020.106223

Defferrard, M., Milani, M., Gusset, F., & Perraudin, N. (2020). DeepSphere: A graph-based spherical CNN. arXiv preprint arXiv:2012.15000.

Defferrard, M., Perraudin, N., Kacprzak, T., & Sgier, R. (2019). DeepSphere: Towards an equivariant graph-based spherical CNN. arXiv preprint arXiv:1904.05146.

Deschamps, P., Durand, N., Bard, E., Hamelin, B., Camoin, G., Thomas, A. L., et al. (2012). Ice-sheet collapse and sea-level rise at the Bølling warming 14,600 years ago. *Nature*, *483*(7391), 559–564. https://doi.org/10.1038/nature10902

Dziewonski, A. M., & Anderson, D. L. (1981). Preliminary reference Earth model. *Physics of the Earth and Planetary Interiors*, *25*(4), 297–356. https://doi.org/10.1016/0031-9201(81)90046-7

Edwards, T. L., Nowicki, S., Marzeion, B., Hock, R., Goelzer, H., Seroussi, H., et al. (2021). Projected land ice contributions to twenty-first-century sea level rise. *Nature*, *593*(7857), 74–82. https://doi.org/10.1038/s41586-021-03302-y

Farrell, W., & Clark, J. A. (1976). On postglacial sea level. *Geophysical Journal International*, *46*(3), 647–667. https://doi.org/10.1111/j.1365-246x.1976.tb01252.x

Frederikse, T., Landerer, F., Caron, L., Adhikari, S., Parkes, D., Humphrey, V. W., et al. (2020). The causes of sea-level rise since 1900. *Nature*, *584*(7821), 393–397. https://doi.org/10.1038/s41586-020-2591-3

Gomez, N., Weber, M. E., Clark, P. U., Mitrovica, J. X., & Han, H. K. (2020). Antarctic ice dynamics amplified by Northern Hemisphere sea-level forcing. *Nature*, *587*(7835), 600–604. https://doi.org/10.1038/s41586-020-2916-2

Goodfellow, I., Bengio, Y., & Courville, A. (2016). *Deep learning*. MIT Press.

Gorski, K. M., Hivon, E., Banday, A. J., Wandelt, B. D., Hansen, F. K., Reinecke, M., & Bartelmann, M. (2005). Healpix: A framework for high-resolution discretization and fast analysis of data distributed on the sphere. *The Astrophysical Journal*, *622*(2), 759–771. https://doi.org/10.1086/427976

Gowan, E., Tregoning, P., Purcell, A., Lea, J., Fransner, O. J., Noormets, R., et al. (2016). ICESHEET 1.0: A program to produce paleo-ice sheet reconstructions with minimal assumptions.

Gowan, E. J., Zhang, X., Khosravi, S., Rovere, A., Stocchi, P., Hughes, A. L., et al. (2021). A new global ice sheet reconstruction for the past 80 000 years. *Nature Communications*, *12*(1), 1–9. https://doi.org/10.1038/s41467-021-21469-w

Han, H. K., Gomez, N., Pollard, D., & DeConto, R. (2021). Modeling northern hemispheric ice sheet dynamics, sea level change, and solid earth deformation through the last glacial cycle. *Journal of Geophysical Research: Earth Surface*, *126*(4), e2020JF006040. https://doi.org/10.1029/2020jf006040

Hay, C. C., Morrow, E., Kopp, R. E., & Mitrovica, J. X. (2015). Probabilistic reanalysis of twentieth-century sea-level rise. *Nature*, *517*(7535), 481–484. https://doi.org/10.1038/nature14093

Hibbert, F., Williams, F., Fallon, S., & Rohling, E. (2018). A database of biological and geomorphological sea-level markers from the Last Glacial Maximum to present. *Scientific Data*, *5*(1), 180088. https://doi.org/10.1038/sdata.2018.88

Hore, A., & Ziou, D. (2010). Image quality metrics: PSNR vs. SSIM. In *2010 20th international conference on pattern recognition* (pp. 2366–2369). IEEE.

Huynh-Thu, Q., & Ghanbari, M. (2008). Scope of validity of PSNR in image/video quality assessment. *Electronics Letters*, *44*(13), 800–801. https://doi.org/10.1049/el:20080522

Kendall, R. A., Mitrovica, J. X., & Milne, G. A. (2005). On post-glacial sea level–II. Numerical formulation and comparative results on spherically symmetric models. *Geophysical Journal International*, *161*(3), 679–706. https://doi.org/10.1111/j.1365-246x.2005.02553.x

Korhonen, J., & You, J. (2012). Peak signal-to-noise ratio revisited: Is simple beautiful? In *2012 fourth international workshop on quality of multimedia experience* (pp. 37–38). IEEE.

Lai, C.-Y., Kingslake, J., Wearing, M. G., Chen, P.-H. C., Gentine, P., Li, H., et al. (2020). Vulnerability of Antarctica's ice shelves to meltwater-driven fracture. *Nature*, *584*(7822), 574–578. https://doi.org/10.1038/s41586-020-2627-8

Lakshminarayanan, B., Pritzel, A., & Blundell, C. (2017). Simple and scalable predictive uncertainty estimation using deep ensembles. *Advances in Neural Information Processing Systems*, *30*.

Lambeck, K., Rouby, H., Purcell, A., Sun, Y., & Sambridge, M. (2014). Sea level and global ice volumes from the Last Glacial Maximum to the Holocene. *Proceedings of the National Academy of Sciences of the United States of America*, *111*(43), 15296–15303. https://doi.org/10.1073/pnas.1411762111

Lin, Y., Hibbert, F. D., Whitehouse, P. L., Woodroffe, S. A., Purcell, A., Shennan, I., & Bradley, S. L. (2021). A reconciled solution of Meltwater Pulse 1A sources using sea-level fingerprinting. *Nature Communications*, *12*(1), 1–11. https://doi.org/10.1038/s41467-021-21990-y

Lin, Y., Whitehouse, P. L., Hibbert, F. D., Woodroffe, S. A., Hinestrosa, G., & Webster, J. M. (2023). Relative sea level response to mixed carbonate-siliciclastic sediment loading along the Great Barrier Reef margin. *Earth and Planetary Science Letters*, *607*, 118066. https://doi.org/10.1016/j.epsl.2023.118066

Love, R., Milne, G. A., Tarasov, L., Engelhart, S. E., Hijma, M. P., Latychev, K., et al. (2016). The contribution of glacial isostatic adjustment to projections of sea-level change along the Atlantic and gulf coasts of North America. *Earth's Future*, *4*(10), 440–464. https://doi.org/10.1002/2016ef000363

Milne, G. A., & Mitrovica, J. X. (1996). Postglacial sea-level change on a rotating Earth: First results from a gravitationally self-consistent sea-level equation. *Geophysical Journal International*, *126*(3), F13–F20. https://doi.org/10.1111/j.1365-246x.1996.tb04691.x

Milne, G. A., & Mitrovica, J. X. (2008). Searching for eustasy in deglacial sea-level histories. *Quaternary Science Reviews*, *27*(25–26), 2292–2302. https://doi.org/10.1016/j.quascirev.2008.08.018

Mitrovica, J., & Milne, G. (2002). On the origin of late Holocene sea-level highstands within equatorial ocean basins. *Quaternary Science Reviews*, *21*(20–22), 2179–2190. https://doi.org/10.1016/s0277-3791(02)00080-x

Mitrovica, J. X., Wahr, J., Matsuyama, I., & Paulson, A. (2005). The rotational stability of an ice-age Earth. *Geophysical Journal International*, *161*(2), 491–506. https://doi.org/10.1111/j.1365-246x.2005.02609.x

Paszke, A., Gross, S., Chintala, S., Chanan, G., Yang, E., DeVito, Z., et al. (2017). Automatic differentiation in pytorch.

Patton, H., Hubbard, A., Andreassen, K., Auriac, A., Whitehouse, P. L., Stroeven, A. P., et al. (2017). Deglaciation of the Eurasian ice sheet complex. *Quaternary Science Reviews*, *169*, 148–172. https://doi.org/10.1016/j.quascirev.2017.05.019

Patton, H., Hubbard, A., Andreassen, K., Winsborrow, M., & Stroeven, A. P. (2016). The build-up, configuration, and dynamical sensitivity of the Eurasian ice-sheet complex to Late Weichselian climatic and oceanic forcing. *Quaternary Science Reviews*, *153*, 97–121. https://doi.org/10.1016/j.quascirev.2016.10.009

Peltier, W., Argus, D., & Drummond, R. (2015). Space geodesy constrains ice age terminal deglaciation: The global ICE-6G_C (VM5a) model. *Journal of Geophysical Research: Solid Earth*, *120*(1), 450–487. https://doi.org/10.1002/2014jb011176

Peltier, W. R. (2004). Global glacial isostasy and the surface of the ice-age earth: The ICE-5G (VM2) model and grace. *Annual Review of Earth and Planetary Sciences*, *32*(1), 111–149. https://doi.org/10.1146/annurev.earth.32.082503.144359

Perraudin, N., Defferrard, M., Kacprzak, T., & Sgier, R. (2019). DeepSphere: Efficient spherical convolutional neural network with healpix sampling for cosmological applications. *Astronomy and Computing*, *27*, 130–146. https://doi.org/10.1016/j.ascom.2019.03.004

Pittard, M. L., Whitehouse, P. L., Bentley, M. J., & Small, D. (2022). An ensemble of Antarctic deglacial simulations constrained by geological observations. *Quaternary Science Reviews*, *298*, 107800. https://doi.org/10.1016/j.quascirev.2022.107800

Reichstein, M., Camps-Valls, G., Stevens, B., Jung, M., Denzler, J., Carvalhais, N., & Prabhat (2019). Deep learning and process understanding for data-driven Earth system science. *Nature*, *566*(7743), 195–204. https://doi.org/10.1038/s41586-019-0912-1

Ronneberger, O., Fischer, P., & Brox, T. (2015). U-Net: Convolutional networks for biomedical image segmentation. In *International conference on medical image computing and computer-assisted intervention* (pp. 234–241). Springer.

Roy, K., & Peltier, W. (2018). Relative sea level in the Western Mediterranean basin: A regional test of the ICE-7G_NA (VM7) model and a constraint on late Holocene Antarctic deglaciation. *Quaternary Science Reviews*, *183*, 76–87. https://doi.org/10.1016/j.quascirev.2017.12.021

Sacks, J., Welch, W. J., Mitchell, T. J., & Wynn, H. P. (1989). Design and analysis of computer experiments. *Statistical Science*, *4*(4), 409–423. https://doi.org/10.1214/ss/1177012413

Sefton, J. (2020). Evaluating mangrove proxies for quantitative relative sea-level reconstructions PhD thesis. Durham University.

Simms, A. R., Lisiecki, L., Gebbie, G., Whitehouse, P. L., & Clark, J. F. (2019). Balancing the last glacial maximum (LGM) sea-level budget. *Quaternary Science Reviews*, *205*, 143–153. https://doi.org/10.1016/j.quascirev.2018.12.018

Tarasov, L., Dyke, A. S., Neal, R. M., & Peltier, W. R. (2012). A data-calibrated distribution of deglacial chronologies for the North American ice complex from glaciological modeling. *Earth and Planetary Science Letters*, *315*, 30–40. https://doi.org/10.1016/j.epsl.2011.09.010

Tarasov, L., Hughes, A., Gyllencreutz, R., Lohne, O. S., Mangerud, J., & Svendsen, J.-I. (2014). The global GLAC-1c deglaciation chronology, melwater pulse 1-a, and a question of missing ice. In *IGS symposium: Contribution of glaciers and ice sheets to sea-level change* (pp. 26–30).

Tarasov, L., & Peltier, W. (2005). Arctic freshwater forcing of the Younger Dryas cold reversal. *Nature*, *435*(7042), 662–665. https://doi.org/10.1038/nature03617

Tarasov, L., & Peltier, W. R. (2003). Greenland glacial history, borehole constraints, and Eemian extent. *Journal of Geophysical Research*, *108*(B3), 2143. https://doi.org/10.1029/2001jb001731

Waelbroeck, C., Labeyrie, L., Michel, E., Duplessy, J.-C., Mcmanus, J. F., Lambeck, K., et al. (2002). Sea-level and deep water temperature changes derived from benthic foraminifera isotopic records. *Quaternary Science Reviews*, *21*(1–3), 295–305. https://doi.org/10.1016/s0277-3791(01)00101-9

Wang, Z., & Bovik, A. C. (2009). Mean squared error: Love it or leave it? A new look at signal fidelity measures. *IEEE Signal Processing Magazine*, *26*(1), 98–117. https://doi.org/10.1109/msp.2008.930649

Webster, J. M., Braga, J. C., Humblet, M., Potts, D. C., Iryu, Y., Yokoyama, Y., et al. (2018). Response of the Great Barrier Reef to sea-level and environmental changes over the past 30,000 years. *Nature Geoscience*, *11*(6), 426–432. https://doi.org/10.1038/s41561-018-0127-3

Whitehouse, P. L. (2018). Glacial isostatic adjustment modelling: Historical perspectives, recent advances, and future directions. *Earth Surface Dynamics*, *6*(2), 401–429. https://doi.org/10.5194/esurf-6-401-2018

Whitehouse, P. L., Bentley, M. J., & Le Brocq, A. M. (2012). A deglacial model for Antarctica: Geological constraints and glaciological modelling as a basis for a new model of Antarctic glacial isostatic adjustment. *Quaternary Science Reviews*, *32*, 1–24. https://doi.org/10.1016/j.quascirev.2011.11.016

Whitehouse, P. L., Bentley, M. J., Milne, G. A., King, M. A., & Thomas, I. D. (2012). A new glacial isostatic adjustment model for Antarctica: Calibrated and tested using observations of relative sea-level change and present-day uplift rates. *Geophysical Journal International*, *190*(3), 1464–1482. https://doi.org/10.1111/j.1365-246x.2012.05557.x

Woodroffe, S. A., Long, A. J., Milne, G. A., Bryant, C. L., & Thomas, A. L. (2015). New constraints on late Holocene eustatic sea-level changes from Mahé, Seychelles. *Quaternary Science Reviews*, *115*, 1–16. https://doi.org/10.1016/j.quascirev.2015.02.011

Xu, K., Zhang, M., Li, J., Du, S. S., Kawarabayashi, K.-I., & Jegelka, S. (2020). How neural networks extrapolate: From feedforward to graph neural networks. arXiv preprint arXiv:2009.11848.

Yao, W., Zeng, Z., Lian, C., & Tang, H. (2018). Pixel-wise regression using U-Net and its application on pansharpening. *Neurocomputing*, *312*, 364–371. https://doi.org/10.1016/j.neucom.2018.05.103